University of Texas at El Paso
DigitalCommons@UTEP

Open Access Theses & Dissertations

2019-01-01

Cmas/volcanic Ash Infiltration Performance Of Yttria Rich-Zirconia Thermal Barrier Coatings Produced By Electron Beam Physical Vapor Deposition

Juan Jose Gomez Chavez
University of Texas at El Paso, juanjogch92@gmail.com

Follow this and additional works at: https://digitalcommons.utep.edu/open_etd


Part of the Geology Commons, Materials Science and Engineering Commons, Mechanical Engineering Commons, and the Mechanics of Materials Commons

Recommended Citation
Gomez Chavez, Juan Jose, "Cmas/volcanic Ash Infiltration Performance Of Yttria Rich-Zirconia Thermal Barrier Coatings Produced By Electron Beam Physical Vapor Deposition" (2019). *Open Access Theses & Dissertations*. 75.
https://digitalcommons.utep.edu/open_etd/75

This is brought to you for free and open access by DigitalCommons@UTEP. It has been accepted for inclusion in Open Access Theses & Dissertations by an authorized administrator of DigitalCommons@UTEP. For more information, please contact lweber@utep.edu.

CMAS/VOLCANIC ASH INFILTRATION PERFORMANCE OF YTTRIA RICH-ZIRCONIA THERMAL BARRIER COATINGS PRODUCED BY ELECTRON BEAM PHYSICAL VAPOR DEPOSITION

JUAN JOSE GOMEZ CHAVEZ

Doctoral Program in Mechanical Engineering

APPROVED:

Ramana Chintalapalle, Ph.D., Chair

Ravisankar Naraparaju, Ph.D.

Arturo Bronson, Ph.D.

Stephen W. Stafford, Ph.D.

Charles H. Ambler, Ph.D.
Dean of the Graduate School

Copyright ©

by

Juan Jose Gomez Chavez

2019

Dedication

This work is dedicated to my parents Juana Chavez Valdez and Homero Gomez Alba. Their unconditional support and encouragement have always helped me to follow my dreams.

CMAS/VOLCANIC ASH INFILTRATION PERFORMANCE OF YTTRIA RICH-ZIRCONIA THERMAL BARRIER COATINGS PRODUCED BY ELECTRON BEAM PHYSICAL VAPOR DEPOSITION

by

JUAN JOSE GOMEZ CHAVEZ, B.S., M.S.

DISSERTATION

Presented to the Faculty of the Graduate School of

The University of Texas at El Paso

in Partial Fulfillment

of the Requirements

for the Degree of

DOCTOR OF PHILOSOPHY

Department of Mechanical Engineering

THE UNIVERSITY OF TEXAS AT EL PASO

May 2019

Acknowledgements

I would like to express my gratitude to my Ph.D. Advisor Prof. Ramana Chintalapalle and my co-advisor and supervisor during my stay at DLR Dr. Ravisankar Naraparaju. They kindly introduced me to this topic and gave me the opportunity to join their research teams. Their guidance and support helped me through this fascinating learning process. I want to express also my most sincere gratitude to all the individuals who contributed to the completion of this project. I would like to thank Prof. Uwe Schulz and Dr. Peter Mechnich for their shared expertise and critical feedback to this project. Additionally, to all the DLR researchers and technicians who also provided support during this project, Mr. Christoph Mikulla, Ms. Alexandra Ott, Mr. Peter Bauer, Mr. Vito Liesner, Mr. Anil Sirigiri, Mr. Jan Philipp, Dr. Roussain Lontio and many others. I thank Mr. Daniel Peters and Mr. Jorg Brien for manufacturing the EB-PVD samples and Mr. Andreas Handwerk, Mr. Berndhard Kanka and Mr. Peter Hertzog for their assistance in experimental testing. Special thanks to Dr. Klemens Kelm for his expertise in TEM analysis and to Mr. Frederick Krepps for his assistance in FIB preparation. Thanks to Mr. Philipp Niemeyer by providing support for porosity measurements. Many thanks to Profs. Arturo Bronson and Stephen Stafford for agreeing to be part of my thesis committee.

To the external collaborators to this project from LMU University I express my gratitude, Dr. Kai-Uwe Hess, Dr. Donald Dingwell, Dr. Wenjia Song. Special thanks to Mr. Siddharth Lokachari for providing the contact angle measurement data. Thanks to Mr. Lars Steinberg from TU Dresden for providing the erosion behavior data to this project. Special thanks to Dr. Patrick Hopkins, Dr. John Gaskins and Mr. David Olson form University of Virginia for providing the TDTR data and discussion for thermal conductivity. I thank Mr. Chance Barrett from UCF for his technical support during this project. To our collaborators from CINVESTAV Queretaro, Dr. Juan Muñoz Saldaña and Mr. Marco Antonio Rivera Gil for their support and assistance, I express my gratitude.

I also express my gratitude to all the Dr. Ramana's research team members and former members for providing support during my Ph.D. studies at UTEP, Dr. Paritosh Dubey, Dr. Satya Gulapalli, Dr. Mallesham Bandi, Dr. Lalitha Raveendran, Dr. Gustavo Martinez, Dr. Sandeep Manandhar, Dr. Ernesto Rubio, Mr. Juan Duran, Mr. Christian Orozco, Mr. Nanthakishore Makeswaran, Mr. Anil Battu, Mr. Vishal Zade and many others.

Finally, I express my gratitude to the funding agencies that provided financial support for the completion of this Ph.D. work, The Consejo Nacional de Ciencia y Tecnologia (CONACYT), the German Science Foundation (DFG) and the National Science Foundation (NSF) PREM program.

Abstract

For many years the use of thermal barrier coatings (TBC) in gas turbine engines has allowed a significant increase in engine operating temperatures which are above the Ni-based super alloys' melting point. The base material for TBCs is the state of the art 7 wt % yttria stabilized zirconia (YSZ) which provides the thermal protection. Current industry demands for increased engine efficiency has pushed TBCs to the limits where significant technological constrains have been identified. One of the main ones represents the high temperature corrosion of the TBC material due to the ingestion of silicate based airborne particles commonly referred as CMAS into the engine. Their main constituents represent CaO-MgO-Al_2O_3 and SiO_2 (or CMAS to simplify). The most common CMAS sources represent sand, dust, environmental pollution, runway debris, fly ash and volcanic ash. As they are ingested into the engine, they melt and infiltrate the porous TBC which produces significant corrosion damage to the TBC material and loss of the TBC strain tolerance. These combined CMAS attack mechanisms lead to reduced coating lifetime or even TBC premature failure. Several approaches have been proposed to counteract this corrosion damage. Among one of the most successful approach is based on the use of a sacrificial top coating based on a rare earth (RE) material oxide which can react with the CMAS melt inducing its crystallization into stable products. Therefore, the CMAS glass can be arrested into only a few microns of infiltration. This thesis explores the CMAS and volcanic ash (VA) infiltration performance of a RE based coating made of 65 wt % Y_2O_3-ZrO_2 balanced (65YZ). Electron beam physical vapor deposition (EB-PVD) methods were used to produce the 65YZ coatings. The studies are based on the effects of chemical composition of the RE material and the microstructural influence of the coating for infiltration. The proposed coatings showed promising results as a CMAS/VA resistant material for high temperature regimes (1250 and 1300 °C) by forming stable apatite and garnet crystalline phases. A detailed study on yttria-zirconia ratios is presented for an optimal CMAS resistant coating. The influence of RE oxide and melt chemistry in the phase equilibra and kinetics of reaction was studied in detail for this proposed coating. A corrosion

mechanism study is presented by applying basicity index estimations in the melt which proves to be a good indicator to predict reaction phases and corrosion damage. In addition, comparative experiments with $Gd_2Zr_2O_7$ (GZO) coatings are performed were the 65YZ coating exhibited higher CMAS/VA resistance. The microstructural influence of the 65YZ coatings with infiltration were also assessed showing that microstructures can be tuned specifically to further improve the infiltration resistance of the coating. Additionally, real engine conditions e.g. thermal gradient infiltration testing were studied for a full proposed CMAS/VA resistant coating system which included the Ni-based super alloy, bond coat, thermally grown oxide (TGO), YSZ TBC and CMAS resistant TBC. Finally, an overview of the mechanical properties of the proposed 65YZ coatings (i.e. erosion, thermal conductivity and toughness) is presented.

Table of Contents

List of Tables

List of Figures

Chapter 1: Introduction

Thermal barrier coatings represent state of the art material systems which are used in the hot gas path components of modern gas turbines to provide thermal protection to the underlying metallic components. Therefore, with the help of TBCs, gas turbines can operate at temperatures higher than the Ni-based super alloy materials melting point. Thus, a significant increase in engine thermal efficiency can be achieved [1-8]. The material of selection for the TBC refractory ceramic represents 7 wt % Y_2O_3 stabilized ZrO_2 (7YSZ) which is commonly coated by means of electron beam physical vapor deposition (EB-PVD) or atmospheric plasma spray (APS) on superalloys. These deposition techniques provide a complex network of porous features, which in combination with the low thermal conductivity 7YSZ, acts as an excellent isolator. Additionally, the porous features also provide strain tolerance to the high thermal cycles at which engines are subjected [9]. Furthermore, the current high demands in industry for more fuel-efficient gas turbines that can be operated at temperatures up to 1500 °C has brought the vulnerability of TBC against siliceous melts into attention. Specifically corrosion due to the ingestion of siliceous based air borne debris commonly referred as CMAS [3, 10, 11]. Furthermore, this CMAS attack currently represents one of the main technological limitation to the development of high temperature capable engines based on more sophisticated high temperature ceramic matrix composites (CMC) structural material systems protected with environmental barrier coatings (EBC) [11-16]. CMAS refers to CaO-MgO-Al_2O_3-SiO_2 which represents the main oxides and their sources including: dust, sand, volcanic ash, fly ash, runway debris and environmental pollution. As the debris is ingested into the engines, they melt in the combustion chamber and follow the hot gas path and deposit onto the TBC surfaces, consequently infiltrating into the porous features of the coatings. This infiltration generates chemical degradation of the 7YSZ material and causes loss in the strain tolerance of the coating which leads to a premature coating failure [17]. Due to the serious threats that CMAS attack poses to TBC lifetime, significant research efforts have been made to mitigate CMAS infiltration in gas turbines. One of the most successfully tested CMAS mitigation strategies involves the usage of a

coating material based on RE zirconates or hafnates with a high RE oxide concentration. The enriched RE material reacts with the molten CMAS glass upon dissolution inducing its crystallization into stable crystalline products such as apatite resulting in minimized infiltration [11, 18-30]. More details regarding all the different mitigation strategies and the categorization of CMAS attack in TBCs are presented in the next chapter. Therefore, it has been widely recognized that if a CMAS reactive material is to be effective it must react quickly with the glass melt upon interaction an induce a nucleation of products which can effectively seal the porous TBC features in order to minimize the CMAS infiltration. The aim of this research is to provide a wide and fundamental understanding of the CMAS infiltration performance of a RE based zirconate coating specifically65 wt % Y_2O_3-ZrO_2 balanced, (referred in this study as "65YZ") under the attack of a wide variety of CMAS based compositions (synthetic CMAS and VA). The presented work focuses on infiltration temperatures relevant to standard 7YSZ TBC operating temperatures (1300 °C max.) for various time periods (up to 50 h) under different testing conditions (rapid cooling, slow cooling and thermal gradient testing). A systematic study is presented to determine the optimal RE-Zr ratio in the coating to maximize CMAS resistance potential. The kinetics of reaction is discussed in detail with respect to the composition of the CMAS/VA source and RE material. A detailed study of the influence of coating microstructure on the infiltration behavior is also presented on the basis of coating deposition parameters and substrate roughness preparation. Finally, the study is concluded by presenting the infiltration performance of a proposed multilayer coating system based on TBC and CMAS resistant coating under real engine conditions. A general overview of 65YZ coating's mechanical properties is provided.

1.1 Project Aim

The main goal of this project is to provide a full spectrum view of all the different challenges and considerations that must be taken into account in order to produce an efficient TBC/CMAS resistant integrated coating system. As seen from **Figure 1.1** several design parameters must be considered for an effective CMAS resistant coating. These parameters include

the chemical composition of the coating and the CMAS source since different phase equilibria in the reaction can be produced by varying the compositions. The microstructure of the coating is a critical parameter in mitigating CMAS infiltration as exemplified in previous studies [31, 32]. Since the configuration and tuning of the microstructural features and processing parameters of the TBC can significantly influence the infiltration. In this context, since depositions techniques produce different microstructures, e.g. APS, EB-PVD, SHVOF, LPPS [9]. It is expected that the infiltration behavior will be different for every microstructure. Additionally, it has been reported that sintering also plays an important role on inducing deeper infiltration due to the presence or larger open capillaries. This has been tested in infiltration tests with 7YSZ TBCs produced by EB-PVD and APS (not published) where a clearer deeper infiltration was found for pre-sintered samples. The operating temperature of the engine (very specific for particular engine types) represents another critical factor since CMAS/VA melting ranges vary significantly depending on composition [10, 33] and also the produced reaction phases can vary depending on temperature [11, 34]. Lastly, reaction time has been seen in literature for lab scale tests to shift the reaction products into secondary phases as well showing that some produced phases could be in a metastable equilibria [30].

Additionally, this project aims to understand the importance of every single oxide role on the reaction equilibria with the TBC reactive material since they can lead to formation of other non-desired phases which can significantly influence the reaction. Since most of the literature reported CMAS tests were based only on the effects of the CaO-Al_2O_3-SiO_2 ternary and some subsequent additions of MgO and Fe_2O_3. They do not assess the influence of other oxides present in natural sources such as VA (K_2O, Na_2O, TiO_2, among others). Moreover, another very important factor i.e. microstructure on the infiltration behavior as well as on the local reaction dynamics is also studied. Especially, it is proven (in Chapter 5) that high infiltration rates can be produced in the non-optimized microstructure which makes it significantly less effective regardless of having a highly CMAS resistant TBC material. The microstructural effects also influence the coating wettability by significantly changing contact angles of the molten fluids on the TBC surfaces. All

these microstructural parameters were studies using our concentric pipe approach which exhibited their influence in infiltration. Therefore, in order to produce an efficient multilayer CMAS resistant coating a careful coating controlled and optimized deposition must be achieved.

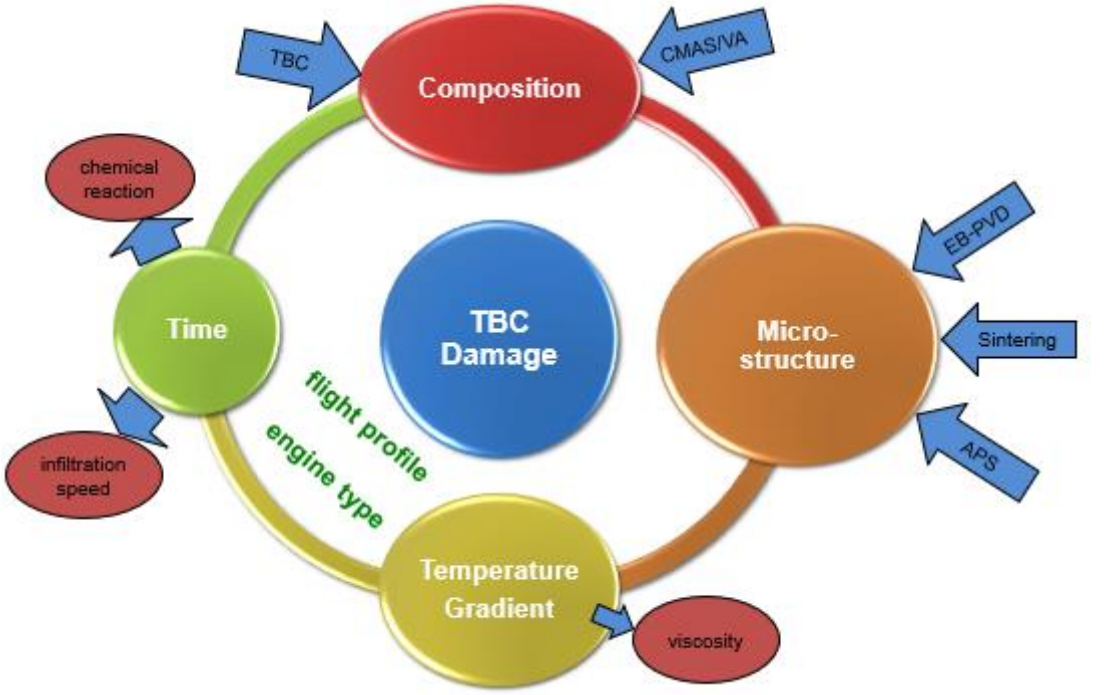

Figure 1.1: Overview of the main parameters that control CMAS attack in TBCs [35].

1.2 Project Significance

It has been estimated that the total industry capital expenditures for only YSZ based TBC coatings for aerospace applications reached $1500 million dollars only in 2015 [36]. The overall gas turbine engine industry worldwide was valued in $42 billion dollars [3]. Since the eruption of the Eyjafjallajökull volcano located in Iceland in 2010, a big concern was brought on air safety due to engine vulnerability to VA based CMAS attack; this eruption event generated a significant air traffic disruption and multi-millions in economic losses [37-44]. The event had so much influence in air safety that a "safe to fly" VA concentration had to be developed by Rolls-Royce with a 2 mg/cm^2 as a safe limit VA concentration for engine

operation [38]. However, this concentration limit does not correlate with long term CMAS accumulations in engines since the CMAS deposits can stick to the surfaces and remain for long periods of time. In addition, VA can be found at very high altitudes (several kilometers) [38] compared to standard CMAS bearing components such as sand or environmental pollution. This increases the VA attack aggressiveness which could lead to engine catastrophic failure. The corrosive potential of CMAS compounds was identified back in the 1990s in military engines operated in middle eastern countries [45] and CMAS attack has been found in industrial gas turbines as well [46]. Therefore, the need for more efficient and CMAS resistant gas turbine engines that operate reliably under high, aggressive environments has significant economic impetus. Thus, this thesis stresses the urgency to develop multilayer TBC systems that incorporate a full TBC coating system (super alloy, bond coat, 7YSZ coating) for thermal protection with a top CMAS resistant TBC based on an yttria rich coating as shown in **Figure 1.2**.

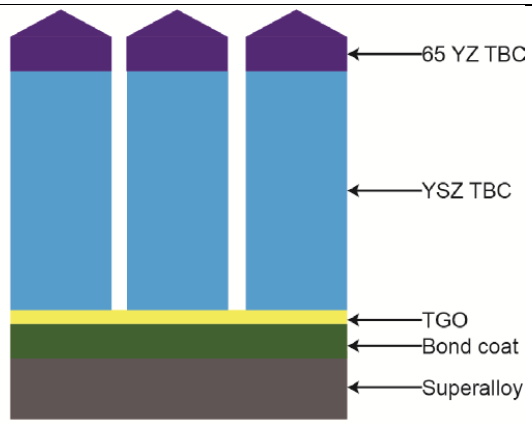

Figure 1.2: Proposed multilayer TBC system that incorporates the standard TBC system with Ni-based super alloy, bond coat, TGO and 7YSZ TBC. Additionally, the CMAS resistant top coat is shown on top based on the 65YZ coating.

Chapter 2: Literature Review

2.1 Gas Turbine Engines General Overview

Gas turbine engines represent heat engines that operate under the principle of the Bryton cycle where power is generated by the compression of air which is then mixed and burned with fuel in a combustion chamber. The energy added to the hot gases during the combustion process is used to drive a turbine where useful power is then extracted due to the rotational motion of the turbine [47]. Gas turbines are applied mainly in the power generation industry to drive electrical generators to produce electricity and in the aviation industry to propel aircrafts. They are commonly integrated by three main components as seen in **Figure 2.1**: (1) compressor, (2) combustor and (3) turbine.

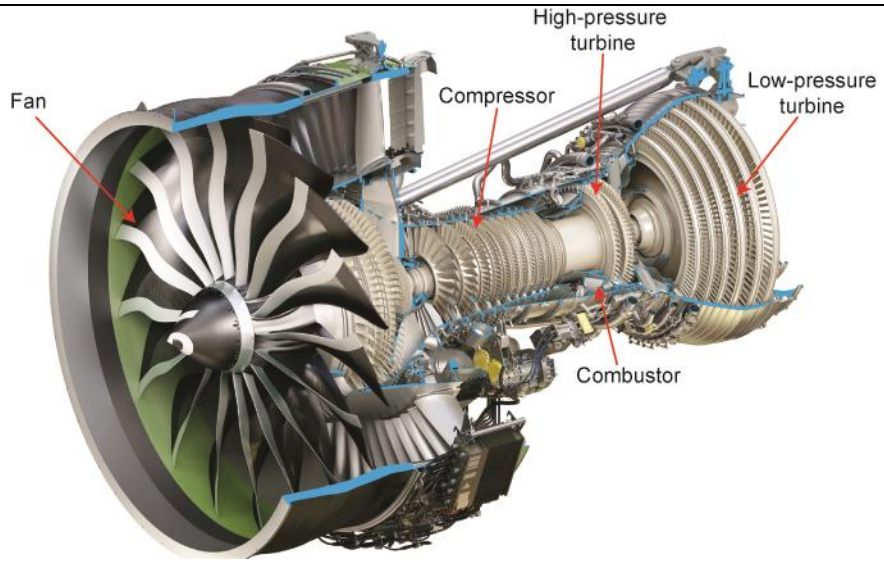

Figure 2.1. Cutaway view of GE9X engine showing its main components (image courtesy of GE aviation).

The parts that compose the combustor and turbine sections are commonly referred as the hot gas path components where TBCs are applied to increase engine's performance and life span. The thermodynamic principle in gas turbines shows that as the engine is allowed to operate at higher temperatures the thermal efficiency is increased as seen in **Figure 2.2** [48]. The benefits of

more efficient engines are translated to higher fuel efficiency and lower emissions. Therefore, the constant demand to reach higher engine temperatures drives the innovations of advanced materials that can withstand high temperatures.

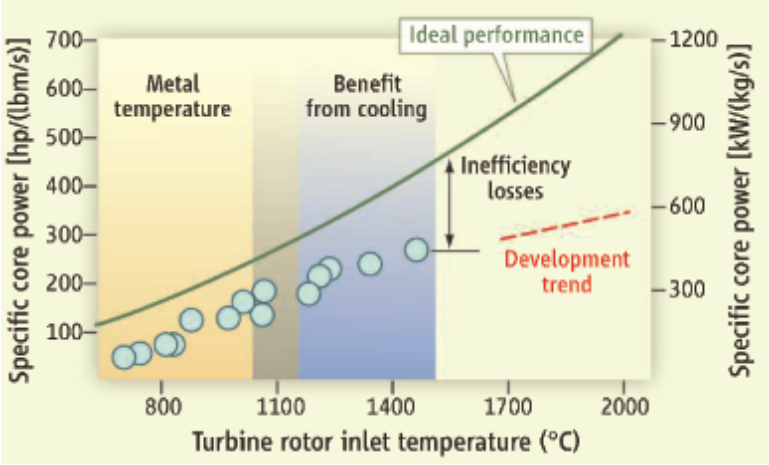

Figure 2.2. Engine efficiency projection with respect to temperature increase.

2.2 Thermal Barrier Coatings

Thermal barrier coatings are multilayer coating systems used mainly to provide thermal insulation to the underlying metallic components used in the engine's hot sections. TBCs allow engines to operate at higher temperatures than super alloys' meting point (up to 1300°C) generating a significant increase in engine efficiency. This has been achieved by a combination of an effective TBC thickness (100-500 µm) and internal cooling of the superalloy components [1-3, 5, 49, 50]. The TBC introduction on engine parts was originally meant to extend the lifespan of engine stationary engine parts such as combustor liners [3, 49]. Progressively, TBCs technology became robust enough to be applied on critical engine components such as first stage nozzles and rotating blades in the late 1980s [51]. Nowadays, in modern gas turbine engines TBCs represent a critical an essential component to ensure high performance and safe operation.

The overall TBC system is integrated by four different layers which have a different functionality and exhibit different chemical and mechanical properties. The layers are the following:

i) Thermal barrier coating (TBC)

ii) Thermal grown oxide (TGO)

iii) Bond coat (BC)

iv) Superalloy

Figure 2.3 [3] shows a representation of a TBC system used in a high-pressure turbine blade with a ceramic top coat deposited by EB-PVD. TBCs operate under harsh conditions, some of these include temperatures above 1300°C, high thermal gradients (up to 1 K/µm), oxidizing/corrosive environments, high pressures and extended service hours [1, 3]. For this reason, the production of advanced TBCs currently represents one of the major areas for increasing engine efficiency in the gas turbine industry as seen in **Figure 2.3**.

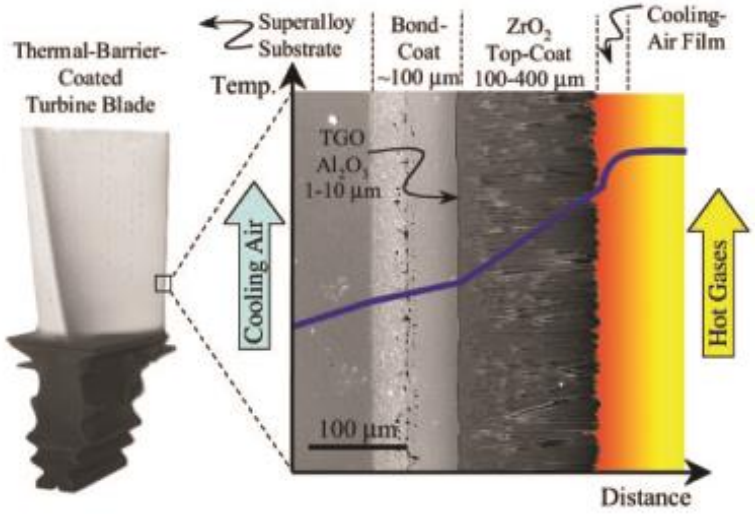

Figure 2.3. Typical cross-sectional scanning electron microscope (SEM) image of the total TBC system used in a turbine blade from an aircraft engine. The TBC was produced by electron beam physical vapor deposition (EB-PVD). The image includes the temperature gradient commonly generated in the system due to the thermal insulation generated by the 7YSZ TBC and the cooling air passages.

2.2.1 Thermal Barrier Coating

The thermal barrier coating itself is the overlaying layer which provides the thermal insulation to the underlying metallic components. This is achieved by the use of a low thermal conductivity material in combination with an engineered porous microstructure. The most widely used material for the TBC is the state of the art 5-8 wt.% Y_2O_3-stabilized ZrO_2 (7YSZ). This material possesses very suitable properties such as low thermal conductivity (λ) at high temperatures (2.3 $W.m^{-1}.K^{-1}$ at 1000°C as a dense material), relatively high coefficient of thermal expansion (CTE) ($11x10^{-6}$ $°C^{-1}$) which reduces residual stresses generated from the thermal expansion mismatch with the higher CTE from the superalloy ($14 x10^{-6}$ $°C^{-1}$), and a melting point of about 2700°C [3]. Due to the high thermal strain generated upon thermal cycling from the engine operating conditions the TBC has to be highly strain tolerant. This is achieved by the combination of two mechanisms: a) the usage of a columnar or porous microstructure with a low in-plane modulus which accommodates the thermal strains associated with the coefficient of thermal expansion (CTE) mismatch between the ceramic and the metal [11]. b) high fracture toughness for a ceramic material generated from a specific ferro-elastic toughening mechanism that YSZ exhibits [52]. This improved fracture toughness is retained at high temperatures which is relevant for TBC applications due to their higher thermal cyclic durability [8, 52]. The discovery of the YSZ composition dates back from the 1970's from the research performed by NASA where this composition showed the best thermal cyclic performance in burner rig testing [53]. The common deposition techniques for 7YSZ coatings are EB-PVD and APS, their characteristics are described in section 2.3. Additionally, the porous microstructure also helps to reduce λ (1.5 and 0.8 $W\ m^{-1}K^{-1}$ for EB-PVD and APS respectively) [54-56]. The λ also vary between each deposition method depending on their deposition parameters which vary their microstructural features.[57]. In contrast, these porous microstructures are unable to prevent oxygen transport into the underlying layers which leads to in service oxidation. Furthermore, the YSZ material possesses a high ionic diffusivity of oxygen which allows higher oxygen diffusion into the underlying layers [58]. To protect the underlying super alloys from high temperature oxidation the TGO layer is generated

during operation which acts as an oxygen diffusion barrier to mitigate the oxidation of the metallic materials.

2.2.1.1 The YSZ System

Ceramic materials are mostly known to be good thermal insulators and to exhibit low CTE, this makes them suitable materials for high temperature applications. YSZ represents a material that does not exhibit a significant change in λ with respect to temperature compared to other refractory ceramics as seen in **Figure 2.4** [7].

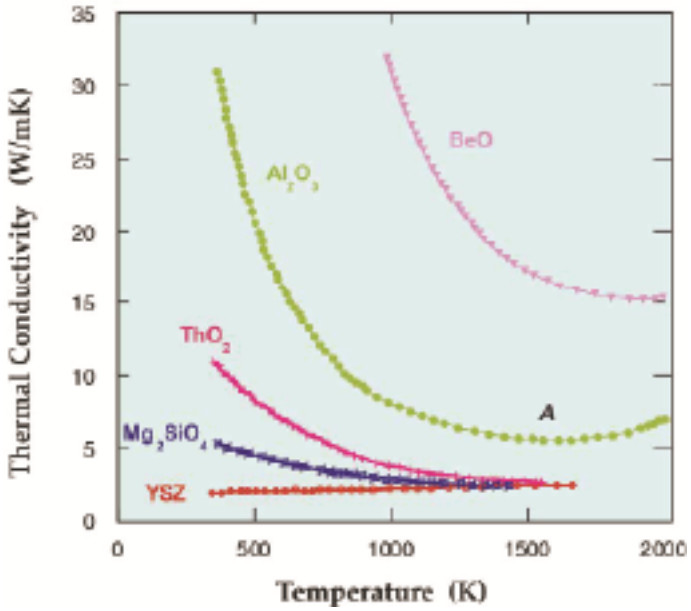

Figure 2.4: Thermal conductivity vs. temperature for several refractory ceramics.

This represents one reason why it is still used as a state-of the art TBC material since 1980's. The second and main reason why YSZ has been a TBC material for decades is its ability to stabilize a *t'* phase with a high variety of dopants (CaO, MgO, Y_2O_3, Yb_2O_3) as yttria is the most effective one to form the stable solid solution phase by being doped in the range of 6 to 11 mol % (or commonly used 7 wt% also referred as 7YSZ) as seen in **Figure 2.5** [49]. Since zirconia exhibits three main polymorph solid nature phases known as: Monoclinic (m)<1170 °C, tetragonal (t) 1170-2370 °C, and cubic >2370 °C [49]. The presence of transformable phases e.g. *t* - *m* at

critical engine operating temperatures generates a disadvantage to zirconia based TBCs since the *t* phase is reversely transformed to the *m* phase upon thermal cycling. This type of martensitic phase transformation produces a lattice volume increase from 3 to 12 % which leads to subsequent residual stress generation upon cooling and coating spallation [49, 59, 60]. The stabilization of the desirable *t'* from the yttria doping into zirconia avoids the undesirable phase transformation upon cooling. Some of the limitations of the desired *t'* phase include accelerated sintering at temperatures >1200 °C and insufficient phase stability [59, 61].

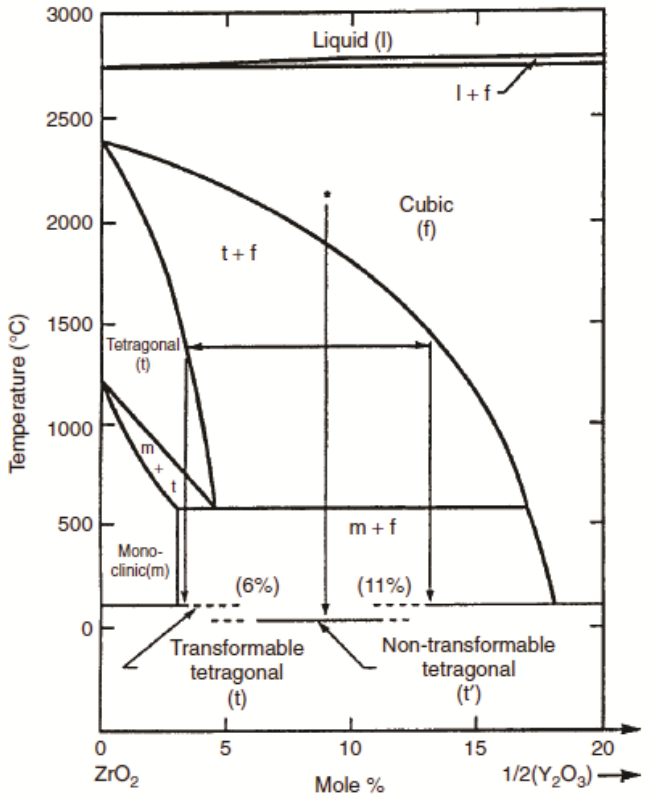

Figure 2.5: Phase diagram for the YSZ system to stabilize the *t'* phase.

2.2.1.2 High Yttria Containing YSZ Systems

YSZ systems in the cubic phase (above 11 mol% $YO_{1.5}$) represent very brittle materials compared to the *t'* tough systems by exhibiting a toughness of Γ=6 Jm^{-2} [62, 63] compared to the 7YSZ used in TBC materials $45 \leq \Gamma \leq 150$ J m^{-2} [52]. It has been reported by Bissom et al. that yttria

additions up to 20 mol % $YO_{1.5}$ in zirconia single crystals lower the λ from 8.2 $W.m^{-1}K^{-1}$ for pure zirconia to 2.0 $W.m^{-1}K^{-1}$ [64]. From there the conductivity started to increase again up to 3.1 $W.m^{-1}K^{-1}$ for 60.8 $YO_{1.5}$ content. In addition, the thermal conductivity reduction up to 20 wt% Y_2O_3 (12 mol % $YO_{1.5}$) is also reported for TBC based microstructures as seen in **Figure 2.6** [54]**.** In theory, the heat is transferred via (i) electrons, (ii) lattice vibrations and (iii) radiation in crystalline solids [54]. Relevant to TBC applications the conductivity is dictated by lattice vibrations (phonons) or by radiation (photons) where the λ contribution by phonons is dictated by [54]:

Equation 1

$$\lambda_p = \frac{1}{3}\int C_v \rho v l_p$$

Where C_v represents the specific heat, ρ density, v phonon velocity and l_p the mean free path for phonon scattering. Thus, the decrease in conductivity for higher yttria contents in zirconia is due to the phonon scattering by point defects directly related to the presence of large concentration of oxygen vacancies [63, 64]. This is explained by the introduction of point defects which are manly oxygen vacancies (Vo) as two Y^{3+} ions are added to substitute two Zr^{4+} an oxygen vacancy is introduced to maintain neutral charge within the lattice as seen in [64, 65].

Equation 2

$$Y_2O_3 \rightarrow 2Y'_{Zr} + V_o + 3O^x{}_o$$

Where Y'_{Zr} is a Y^{3+} ion that substitutes a Zr^{4+} ion, V_o represents the double charged oxygen vacancy produced and O^x_o is an O^{2-} ion located at its respective oxygen site. As explained by Bissom [64] the low λ up to the $20YO_{1.5}$ content is due to the introduced point defects that act as phonon scattering centers, whereas at concentrations >20 mol % the point defects may interact leading to a periodic arrangement which produces less phonon scattering.

The radiation conduction in the yttria-zirconia system is more prominent at higher temperatures (>1200 °C) by exhibiting a 10 % contribution in λ at 1250 °C and increasing at temperatures above [54]. This radiation contribution is written in [54]

Equation 3

$$\lambda_r = \frac{16}{3}\sigma n^2 T^3 L_r$$

Where σ is the Boltzmann's constant, n is the refractive index, T is the absolute temperature and l_r the mean free path for photon scattering. Furthermore, the high yttria contents in the YSZ system are claimed to be sintering resistant compared to standard TBC YSZ [66].

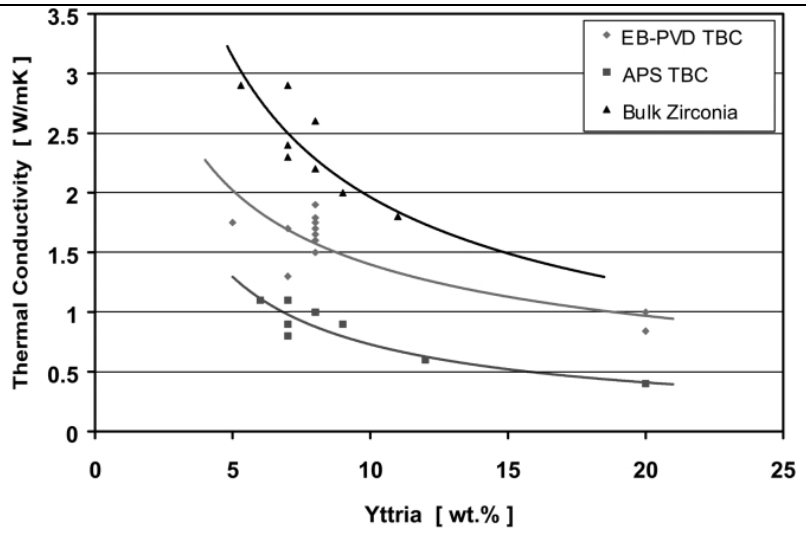

Figure 2.6: Thermal conductivity (λ) as a function of Y_2O_3 content for different processed TBC materials.

2.2.2 Thermally Grown Oxide

The thermally grown oxide layer (TGO) is not generated by the deposition technique. Its growth is generated by the oxygen interaction with the Al rich bond coat (BC) during TBC deposition and engine operation, thereby, generating thin (1-10 μm) α-Al_2O_3 layer between the BC and the TBC [67]. The generated alpha phase in the alumina TGO is due to the processing of the BC and the engine operation which ensures the formation of this phase upon oxidation. However,

intrinsic alumina phases can form during engine cycles (θ, γ and δ) which produce a higher oxidation rate [68]. The α-Al_2O_3 is an oxide that grows very slowly, uniformly and with low defects which makes this material an excellent diffusion barrier. Additionally, in some cases this layer produces an outward diffusion of aluminum which leads to the formation of new phases at the interfaces called an "intermixed zone" [67, 69]. The formation and growth of the TGO have a critical influence in the TBC lifetime since common failure mechanisms are located at this layer [70]. This failure is due to the very high compressive residual stress generated at the interface with the BC. Is has been reported that the strain energy in the TGO increases linearly with its thickness and quadratically with the TGO stress driving the common coating failure at this layer [1].

2.2.3 Bond Coat

The bond coat (BC) is a metallic layer deposited on top of the superalloy which serves mainly as: (i) An oxidation resistance barrier to the superalloy. This is done by the continuous supply of Al (as Al reservoir) to the oxidation front which oxidizes into a continuous, non-porous and uniform alumina TGO layer at the BC/TC interface. (ii) Provides mechanical bonding with the TBC by matching the CTE with the superalloy substrate and by the surface treatment generated from the production technique [71].

The commonly used BC material includes the MCrAlX system where M represents Co, Ni or a combination of both and X is commonly a reactive material Y,Hf. The M and Cr elements are commonly used to form intermetallic phases β and γ to match with the superalloy properties and allow the required surface properties for the subsequent overlay coatings. The common deposition technique includes APS and EB-PVD. Another type of BC system uses Ni or Pt based aluminides where the deposition method includes electroplating and chemical vapor deposition [49].

Some of the major bond coat requirements focus on the very slow growth of the TGO layer, highly chemical stability from impurities such as S and C, high creep strength to suppress rumpling effect and minimal use of expensive precious metals such as Pt, Re and Pd [49]. Additionally, the

Y and Hf additions in low concentrations (0.005-0.3 wt %) are reported to be beneficial for the alumina scale adhesion [68].

2.2.4 Superalloy

The superalloy material represents the critical component which carries the mechanical load exerted from the high pressure, temperature and centrifugal forces at which the engine is exposed. The widely used materials that can withstand these critical conditions are Nickel or Cobalt based superalloys since that exhibit superior mechanical properties that can be maintained at high temperatures [49]. The processing of superalloys evolved over time until reaching single crystal systems that are able to operate at temperatures above 1100°C as seen from **Figure 2.7** [49]**.** Finally, thanks to the implementation of TBC systems in conjunction to advanced superalloy processing techniques that allow production of hollow engine parts with internal cooling passages, the engines' operating temperatures have been increased substantially (about 250 °C higher than superalloy meting point [72]) allowing more efficient operation [71].

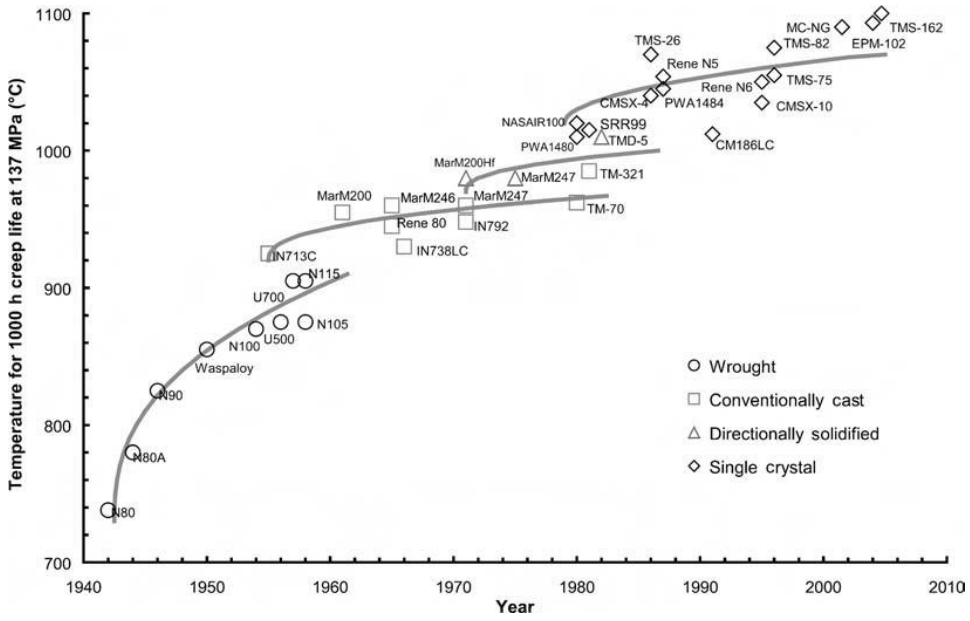

Figure 2.7: Evolution of the temperature capability over time for superalloys.

2.3 Deposition Techniques

Part of the great success of TBCs in gas turbine engines comes from the development of advanced deposition techniques. The most widely used techniques for the TBC top coat materials are EB-PVD and APS. The employment of these technologies is used mostly due to the very high melting point of 7YSZ (about 3000 K) making a requirement of ultra-high temperature plasmas and electron beam sources for effective material processing [9]. The second main attribute that makes these processes the most widely used is the generated microstructural porous architecture as seen in **Figure 2.8** [9]. These porosities usually range in between 10 to 30 percent which reduces significantly the λ thermal conductivity of the coatings. This reduction in λ is mainly attributed by the interfacial porosity generated from the deposition techniques, the normal orientation of these microstructural porosities to the heat flow produce an effective reduction in the thermal conductivity specially for nanosized induced porosities or grain boundaries [6, 54]. The main characteristics of these deposition processes are discussed in detail in the following sections. Other coating methods have been widely studied such as suspension plasma spray (SPS), plasma spray physical vapor deposition (PSPVD), among others. Their main goal is providing a low price deposition solution to incorporate the main characteristics of traditional EB-PVD and APS methods which are high strain tolerance and low thermal conductivity [9]. However, due to their proven operating robustness the EB-PVD and APS methods still currently remain the most widely used for TBC deposition.

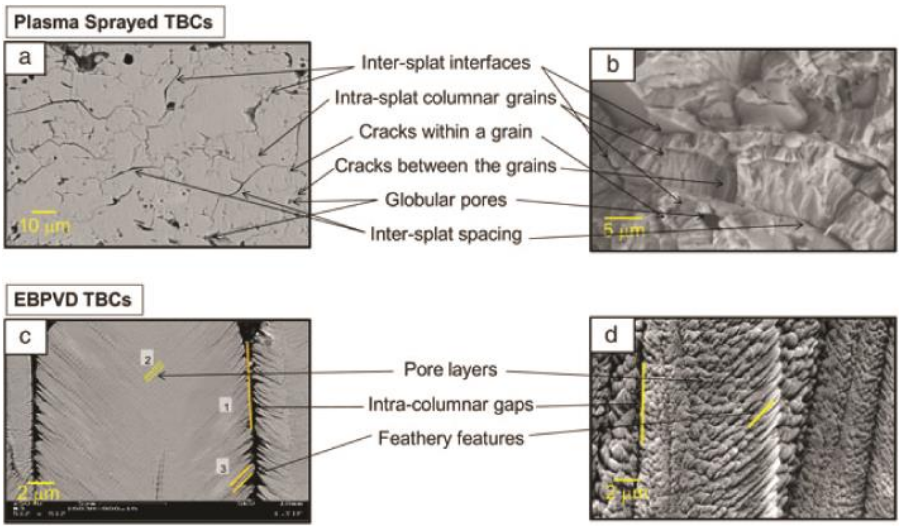

Figure 2.8. Microstructure generated by APS and EB-PVD processing.

2.3.1 Electron Beam Physical Vapor Deposition

The EB-PVD system works under a high vacuum environment, evaporating a ceramic ingot using a high-power electron beam controlled by a specified rastering pattern. This process can be categorized under the coating manufacturing processes that employs the deposition of materials coming from a gas phase commonly referred to as physical vapor deposition (PVD) [57]. The EB-PVD process ensures a uniform evaporation of the ceramic source (ingot) thus, avoiding imperfections generated in the microstructure from non-uniform evaporation [57, 72]. The electron beam source is able to heat up the ceramic ingot high above its melting point where a rate of evaporation becomes appreciable (>3500 °C for 7YSZ) [73]. The ingot is contained in a water-cooled crucible and continuously fed into the process at a desired rate. The evaporated material generates a vapor cloud which consist of atoms, molecules and ions which are subsequently deposited and condense on the surface of the top heated substrates as represented in **Figure 2.9** [57].

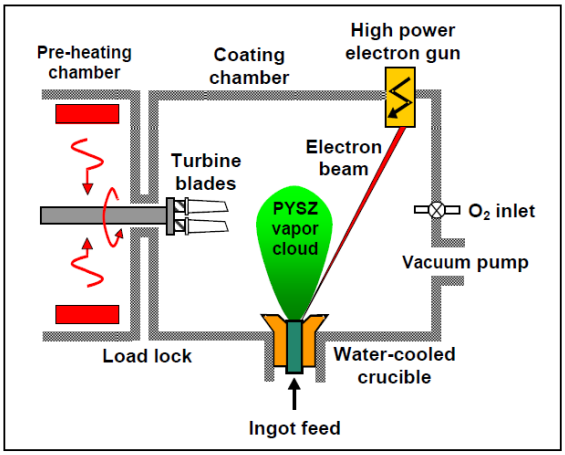

Figure 2.9: Schematic of the principal components of an EB-PVD system.

Lifetime (thermal fatigue) studies performed with burner rig testing comparing EB-PVD and APS TBCs showed superior performance for the EB-PVD microstructure (APS reached 30 to 40 % of the EB-PVD lifetime) [72]. This is due to the high in plane compliance exhibited from the columnar growth of EB-PVD TBCs which are crucial to their high strain tolerance and lifetime [74]. Additionally, it is known that EB-PVD processing generates aerodynamically smooth surfaces of the coated parts which eliminates the need to perform post coating polishing or conditioning of cooling holes [72]. For these reasons the EB-PVD process represents the selected method for critical moving and stationary components in the engine such as nozzles and blades. The coating thickness, density, crystallographic orientation, and microstructure correlate with the deposition parameter, namely deposition rate, substrate temperature, deposition height, chamber pressure, and location in the coating chamber with respect to the evaporation source [75]. The distinguished EB-PVD columnar microstructure is controlled mainly by the unique vapor incidence angle (VIA), rotation of coating components, shadowing effects, deposition rate and substrate temperature [75]. For this work special attention on the microstructural growth is paid on the shadowing effect. It has been reported that substrate roughness plays an important role on the columnar growth since polished substrates generated parallel columns compared to conical cauliflower-like growth generated for rough grounded substrates which grew more

unsymmetrically with increased grid size [76]. It has been reported that surface roughness enhanced the degree of shadowing which leads to cauliflower-like (conical-shaped zone 1 growth as seen from **Figure 2.10** [73]). Therefore, in the absence of substrate roughness a transition to zone 2 (parallel columnar growth **Figure 2.10**) occurs at the limit of no surface diffusion [73]. The effects of substrate diffusion in the growth of multi-layer 65YZ/7YSZ CMAS coatings will be discussed in **Chapter 5**.

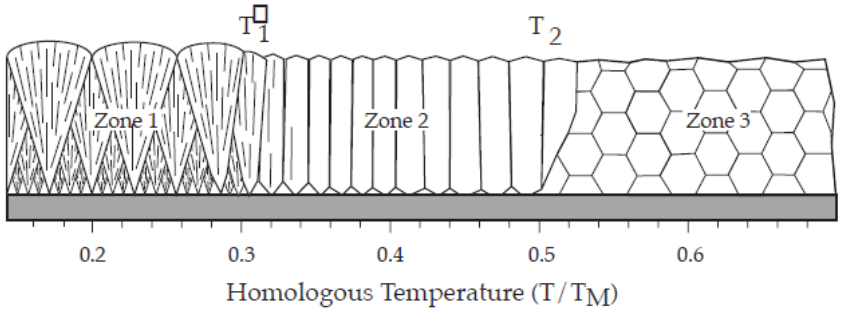

Figure 2.10: Schematic of microstructure produced with respect to homologous temperature (substrate temperature/melting temperature of deposited material) obtained from [73]. T1 and T2 are the zone boundaries in metallic films which correspond to the activation of surface diffusion (T/T_M=0.3) and bulk diffusion (T/T_M=0.5) respectively.

2.3.2 Air Plasma Spray

Air plasma spray (APS) is a deposition method that utilizes a feedstock powder deposition material which is fed into a plasma jet which heats it up to a semi molten state. The semi molten deposition material is carried by the jet and deposited onto the substrate as splats (as shown in **Figure 2.11** [77]). The spraying velocity, powder size and plasma gun position are the prominent factors controlling the coating microstructure [9]. The plasma is generated by a specific gun which uses argon or nitrogen in combination with hydrogen as working gas to generate the high temperature plasma. The resultant microstructure is characterized by a series of "splats" of rapidly solidified materials which configure in a brick-wall type structure as seen in **Figure 2.8a & b [9]**.

Some of the characteristics of this deposition technique are its lower cost compared to the EB-PVD method and lower lifetime. For this reason, this method is commonly used for deposition on non-highly stressed stationary engine parts such as combustor liners. However, the APS microstructural splat architecture provides lower thermal conductivity compared to the EB-PVD process in ranges up to 20 % of the bulk ceramics [9]. A summary of properties of EB-PVD and APS production methods in TBCs is give in **Table 2.1**.

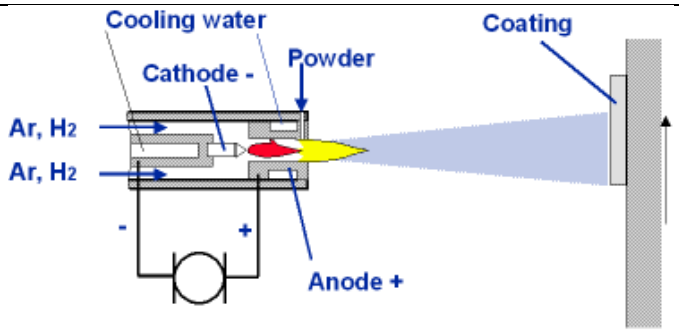

Figure 2.11: Schematic representation of the APS deposition process obtained from [77].

Table 2.1: Summary of TBC properties from EB-PVD and APS deposition methods adapted from [78].

Properties/Characteristics	EB-PVD	APS
λ (W $m^{-1}K^{-1}$)	1.5-1.9	0.8-1.1
Surface roughness (μm)	1	10
Adhesive strength (MPa)	400	20-40
Young's modulus (GPa)	90	200
Erosion rate (normalized to PVD)	1	7

2.4 Prospective TBC Materials

Other material candidates have been considered to replace the state of the art 7YSZwith low λ being the critical parameter sought for prospective materials. Other basic requirements are: high melting point, no unwanted phase transformation between operating temperature and room

temperature, chemical inertness, good thermal expansion mismatch with metallic substrate and low sintering rate for porous microstructures [79]. Several material candidates which include pyrochlores based on the lanthanate series, non-yttria stabilized zirconia materials, hafnia based materials, silicates, lanthanum aluminates, and garnets among others were studied [6, 79-81]. Special attention has been paid to pyrochlore based materials since they exhibit reduced thermal conductivity compared to YSZ as well as improved sinter resistance [6]. A summary of the advantages and disadvantages of the prospective TBC materials with respect to standard 7YSZ is provided in **Table 2.2** [79]. However, since aircraft engine inlets are exposed to any incoming debris toughness represents a very critical parameter to counteract foreign object damage (FOD) and erosion which can impact and remove the TBC coating exposing the bare metal to very high temperatures. Therefore, until today no other prospective TBC material has been able to match the toughness exhibited by 7YSZ which still makes it a material of choice for TBC applications.

Table 2.2: Advantages and disadvantages of TBC materials.

Materials	Advantages	Disadvantages
7YSZ	(1) High thermal expansion coefficient (2) Low thermal conductivity (3) High thermal shock resistance	(1) Sintering above 1473 K (2) Phase transformation (1443 K) (3) Corrosion (4) Oxygen transparent
Mullite	(1) High corrosion resistance (2) Low thermal conductivity (3) Good thermal shock resistance below 1273 K (4) Not oxygen transparent	(1) Crystallization (1023-1273 K) (2) Very low CTE
Alumina	(1) High corrosion resistance (2) High hardness (3) Not oxygen-transparent	(1) Phase transformation (1273 k) (2) High thermal conductivity (3) Very low CTE
YSZ + CeO_2	(1) High CTE (2) Low thermal conductivity (3) high corrosion resistance (4) Less phase transformation between m and t than 7YSZ (5) High thermal-shock resistance	(1) Increased sintering rate (2) CeO_2 precipitation (> 1373 K) (3) CeO_2 loss during spraying
$La_2Zr_2O_7$	(1) very high thermal stability (2) low thermal conductivity (3) Low sintering (4) Not oxygen-transparent	(1) Relatively low CTE
$Gd_2Zr_2O_7$	(1) Very high thermal stability (2) Low thermal conductivity (3) Low sintering	(1) Relatively low CTE (2) Low toughness

Silicates	(1) Cheap, readily available (2) High corrosion resistance	(1) Decomposition into ZrO_2 and SiO_2 during thermal spraying (2) Very low CTE

2.5 CMAS Attack in TBCs

The infiltration of molten silicate-based deposits commonly referred as CMAS into gas turbine engines represents a critical, fundamental barrier for the development of more efficient high temperature gas turbines. This is due to the high temperature CMAS attack generated on the TBC coated materials which represent a critical component for the engine's thermal protection. CMAS damage is present in gas turbines operated in desert-sandy environments, near volcanic ash clouds and highly polluted environments. Additionally, industrial gas turbines operated in integrated gasified combined cycle (IGCC) power plants which use H_2-rich synthesis gas (syngas) obtained from coal and steam [82, 83] as fuel are susceptible to CMAS attack as well [24]. Another important feature of CMAS compounds is their very wide variety of chemical compositions depending on the geographical presence reported in the open literature as seen in **Figure 2.12** [10]**.**

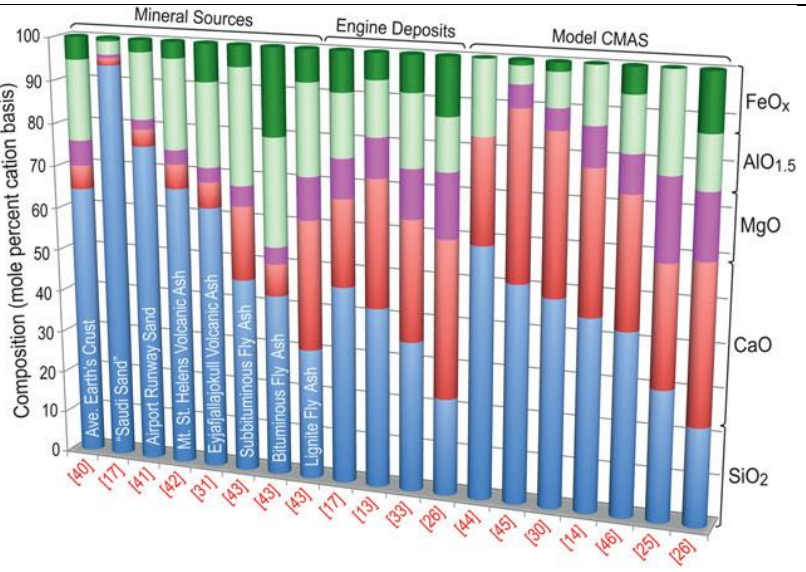

Figure 2.12: Different chemical composition of CMAS sources. The references provided in the figure can be obtained from [10].

These compositions contain significant amounts of FeO_x and small amounts of TiO_2. Additionally, for the tested volcanic ash (VA) sources in this work the content of alkali oxides is also significant as seen in the next chapters. The early reports of the threat of CMAS corrosion in aero-engines was reported for silica rich compounds [10, 45, 84, 85]. Furthermore, special attention has been paid to VA as a CMAS source which has been recognized as a significant threat for aviation safety [38, 41-44, 86-88]. The turning point for VA in aviation safety was from the eruption of the Eyjafjallajökull volcano in Iceland in 2010. This eruption caused a major disruption in the European air traffic exposing the significant threat that large volcanic eruptions represent for airspace safety in addition to the significant economic losses generated from the airspace closure. The glassy nature of volcanic ash sources generate a low glass transition temperature (≤900°C) which produces a softening and partial melting of the glass which could promote infiltration at low temperatures [42]. Additionally, areas with significant volcanic activity are present in western the U.S., central Mexico, central America, southern Japan and south eastern Asia. These areas represent zones with significant air traffic which could be seriously disrupted in the event of a large volcanic eruption.

Furthermore, the common CMAS damage in TBC is characterized in 3 main types. At low temperatures the ingested large particles can produce erosive wear of the TBC due to foreign object damage (FOD) and blocking of the cooling passages of airfoils. At high temperatures >1200 °C the CMAS deposits melt yielding glassy particles which adhere and infiltrate into the porous features of the TBC (regardless of the deposition method) producing two recognized types of attack. These attack mechanisms are commonly referred as thermo-mechanical and thermo-chemical. Their characteristics and mechanisms are described in the next sections.

2.5.1 Thermo-mechanical Attack in YSZ TBC

The molten CMAS glass infiltrates the porous TBC driven by capillary forces (as seen in **Figure 2.13 [35]**) where CMAS viscosity, surface tension and TBC permeability represent the main governing factors (as described in section 2.6). As the CMAS starts to melt at high temperatures (>1200°C) [3], its lower viscosity no longer sustains the capillary forces therefore, it is expected that

an increased infiltration rate will be produced at high temperatures due to the further viscosity reduction of the molten glass. As the CMAS melt flows down the TBC's thermal gradient in gas turbines, its viscosity increases generating a slower infiltration rate and partial crystallization thus, stiffening the t'-YSZ coating. Upon cooling the melt completely solidifies within the columnar gaps generating a fully dense domain which increase the coating susceptibility for spallation [17]. It has been reported that CMAS interactions at the TGO promote creep cavitation in the bond coat inducing delamination cracks propagating within the metal layer [10]. An additional failure mode generated at the TGO layer is reported from the vapor phase transport of CMAS compounds such as Ca and Mg and Si from the top deposit without complete infiltration. This vapor phase transport has been reported for solid CMAS deposits leading to formation of anorhite and spinel at the TGO layer leading to coating delamination at the modified TGO [11]. **Figure 2.14** [11] shows a summary of different modes of CMAS induced thermo-mechanical attack in TBCs [11]. Moreover, as the melt fills the porous features it produces degradation of the insulating properties of the TBC [10, 89]. The thermo-mechanical driven failures are produced by the strain energy accumulated in the coatings upon cooling. The strain energy is high due to the CTE mismatch between the CMAS-stiffened topcoat and the superalloy which promotes coating spallation [11, 90]. It is reported that for fast cooling conditions, the surface cooling induces initially tensile stresses which generate vertical cracks leading to delamination cracks parallel to the coating surface [11]. At slow cooling conditions, the in-plane stress in the infiltrated coating increases as the substrate cools [11]. Thus, since a prospective TBC must incorporate a porous microstructure to accommodate the thermal strains generated from the operating cycles it is highly critical that hotter more efficient engines address effective solutions to CMAS attack at targeted turbine temperatures up to 1500 °C [10].

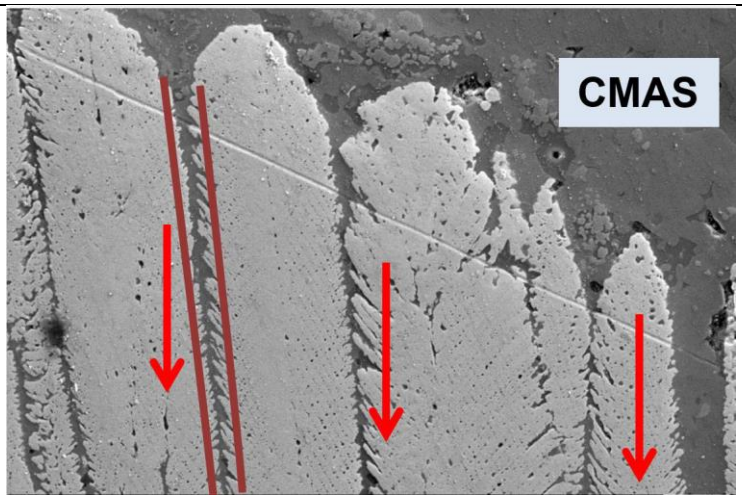

Figure 2.13: CMAS induced thermo-mechanical attack dictated by capillary forces infiltrating the porous features of EB-PVD TBC. The red arrows show the molten glass infiltration direction and the parallel red lines show an infiltrated columnar gap.

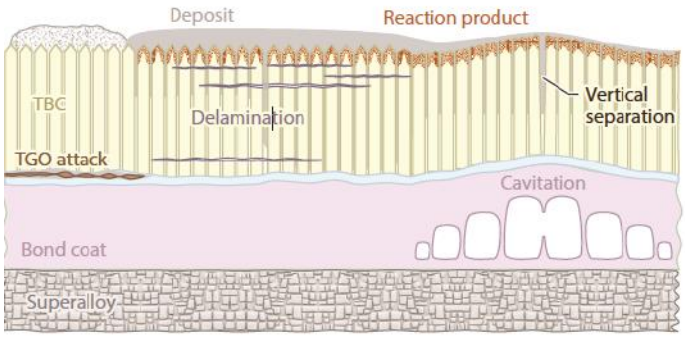

Figure 2.14: Schematic of CMAS induced thermo-mechanical attack in TBC systems.

2.5.2 Thermo-chemical Attack in YSZ TBC

Substantial research efforts have been accomplished in understanding the thermo-chemical aspects of CMAS interaction with t'-TBC [78, 90-106]. Since the reported CMAS bearing sources exhibit a very large variety of compositions it is critical to understand the implications of interaction of TBC oxides with different melt compositions. The main mechanism acting upon CMAS glass/TBC interaction is the dissolution of the coating which upon saturation a re-precipitation of crystalline products is exhibited depending on the melt composition as seen in

Figure 2.15 [10, 96]. The common precipitation reaction phases reported in the reaction is always a type of YSZ polymorph due to the Zr dissolution depending on the melt composition [10]. In interactions with Ca rich or Si rich melts precipitation of $Ca_2ZrSi_4O_{12}$ and zircon ($ZrSiO_4$) respectively has been reported [91, 98]. Furthermore, interactions with more complex melt compositions has shown formation of garnet type phases [93] and zirconolite ($Ca_2Zr_2Ti_4O_{14}$) [102]. Additionally, at deeper CMAS infiltrations the melt can interact with the TGO inducing Al bearing compounds such as anorthite or spinel. This generates pore formation within the modified TGO leading to spallation and crack propagation [11].

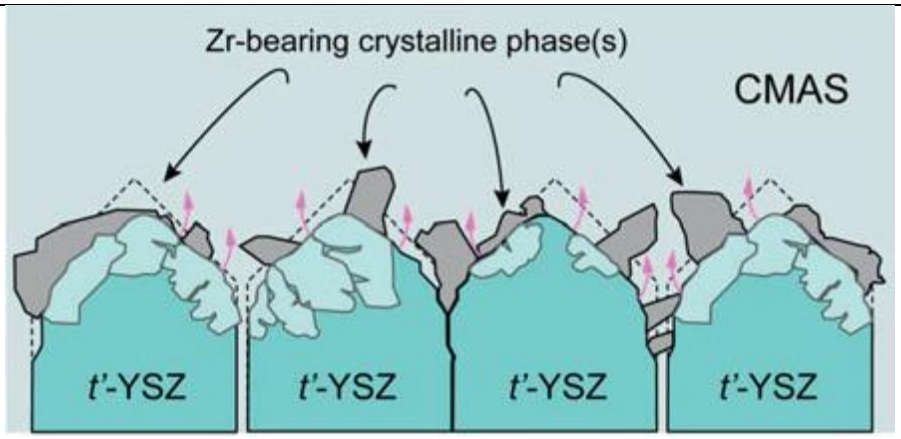

Figure 2.15: Schematic of CMAS melt interaction incorporated from [10] with standard YSZ TBC wherein the coating is dissolved by the glass promoting precipitation of Zr-based phases depending on the melt composition. Some phases can form during high temperature interaction and others during cooling.

2.5.3 CMAS Mitigation Strategies

Since the magnitude of strain energy in infiltrated layers increases nonlinearly with the thickness of melt deposit and infiltrated layer, the mitigation strategies focus mainly on minimize the infiltration depth into the TBC [11]. In this context, numerous CMAS mitigation approaches have been proposed. One general approach focuses on the use of a dense ceramic or non-reactive Pt or Pd layer which can block the CMSA infiltration [11, 106-108]. However, such approach is technically not feasible due to the high cost of thick precious metal layers (Pt or Pd) and the careful

grading for dense coatings to minimize the thermal stresses generated by the produced barrier [11]. The second and most implemented approach is based on the manipulation of the chemical reaction generated from the CMAS melt and TBC interaction using a reactive TBC material which induces crystallization of the melt upon dissolution. As the melt is consumed, the promotion of stable crystalline reaction products can block the porous features avoiding further infiltration of the melt (or keeping a shallow infiltration) in the essence of growing an in-situ barrier against further infiltration. This reaction product layer should be a sacrificial layer which spalls off during cooling allowing the underlying RE coating to continue the reaction with further CMAS interaction [11].

2.6 CMAS Reaction Kinetics

As explained before, the most effective mitigation CMAS strategy was based on the usage of a reactive sacrificial TBC layer. Two main mitigation CMAS reactive layers have been proposed in literature. The first one employs the application of alumina (Al_2O_3) as a reactive material on top of 7YSZ and doped with Ti which, upon reaction with the CMAS melt (rich in CaO and SiO_2) promotes the precipitation of anorthite, $CaAl_2Si_2O_8$ as the primary reaction product for CMAS arrest. In the reported literature alumina was incorporated into 7YSZ in solid solution with a small TiO_2 amount to act as a crystallization catalyzer [109, 110]. Another applied approach was a top EB-PVD alumina layer on top of a standard YSZ TBC [111]. Although, alumina has reacted quite fast, thus promoting anorthite and spinel as primary reaction products, its low sintering resistance has generated larger cracks which allowed deeper CMAS/VA infiltration..

The second and most studied mitigation strategy involves the usage of a reactive top coating based on rare-earth (RE)[1] zirconate or hafnate as a sacrificial layer [18-30, 112, 113]. Since higher RE concentration is exhibited in these coatings compared to standard 7YSZ coatings, their reaction with silicate melts was found to be very different [11]. The reported interactions conclude that upon CMAS dissolution the RE based TBC promotes the precipitation of cubic fluorite from the Zr-Hf dissolution into the melt. Whereas the high RE content promotes precipitation of a stable

[1] All the lanthanide series elements and also including Y^{3+}

apatite phase (nominally $Ca_2RE_8(SiO_4)_6O_2$) which reacts with CaO and SiO_2, promoting glass crystallization and sealing the porous features thus, arresting the melt. **Figure 2.16** shows a comparison of different mitigation scenarios of GZO, 65YZ and alumina coatings where the reaction products are shown. Previous studies performed on 65 wt % Y_2O_3-ZrO_2 balanced (65YZ) EB-PVD coatings have shown promising results as a prospective CMAS resistant coating [26]. However, the use of single coating based CMAS resistant TBCs still remains a challenge for real engine conditions (e.g. under thermal gradients-cycles, under FOD and erosion damage). This is due to the lower intrinsic toughness that pyrochlore or fluorite based TBCs exhibit compared to standard 7YSZ. In this context, the erosion resistance of CMAS infiltrated 7YSZ TBCs has been found to depend on coating microstructure [114]. This erosion resistance information under the effects of different infiltration depths and reaction product formation still remains unknown for CMAS resistant coating systems. Furthermore, it is commonly proposed to incorporate multi-layer CMAS resistant systems with a CMAS resistant top coat with an underlying thin 7YSZ coating. This system is commonly used mainly because of the chemical compatibility that 7YSZ has with the TGO which is not exhibited with pyrochlores (specifically GZO) [112] and the extra protection provided from the underlying 7YSZ higher toughness

Additionally, other materials such as lanthanum hexaaluminate have been explored as candidate materials for CMAS resistant coatings in configuration with underlaying 7YSZ coatings [115, 116]. Other coatings have been explored for their use in EBC systems to also provide CMAS protection [117, 118].

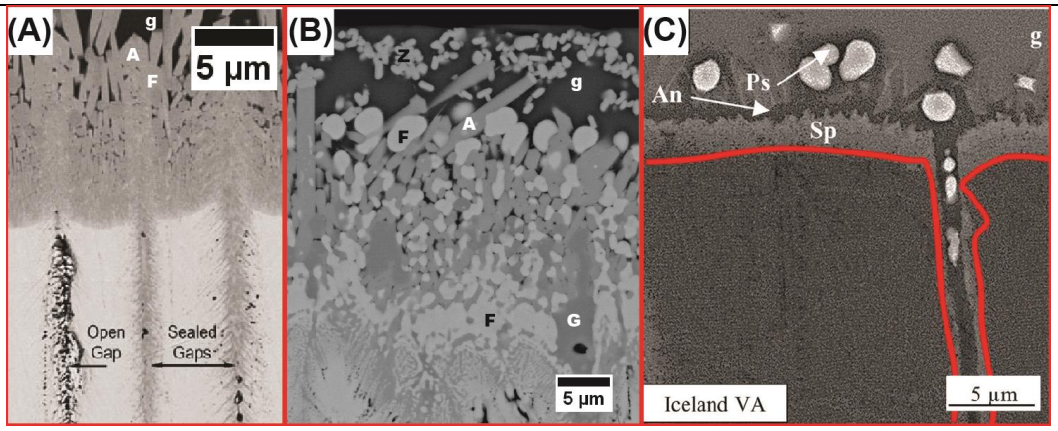

Figure 2.16: Different EB-PVD CMAS reactive sacrificial coatings based on (A) gadolinium zirconate under synthetic CMAS attack for 4 h at 1300 °C [10]. (B) 65YZ under Iceland VA attack for 10 h at 1250 °C. (C) Alumina under Iceland VA attack for 5 min at 1250 °C. The reaction product labels are: A for apatite, An for anorthite, F for fluorite, G for garnet, g for glass, Ps for pseudobruokite and Sp for spinel.

The ideal reaction behavior for CMAS/VA resistant coating is believed to be optimal with quick crystallization of the melt upon saturation of dissolved coating oxides in addition to reduced melt volume and impeded further infiltration [11]. From all the reported literature the most beneficial phase that approximates this ideal reaction behavior represents the apatite phase. Furthermore, the produced reaction products from CMAS glass/TBC interactions can be categorized in three main categories namely: intrinsic crystallization, precipitation and reactive crystallization [11]. The common reaction products reported from these different reaction stages are given in **Table 2.3** incorporated from [11]. Thus, it is idealized that the effective CMAS arrest is proportional to the volume of crystallized Si bearing product with respect to the volume of coating dissolved (V_{crys}:V_{TBC} >> 1), in addition the reaction must produce a beneficial morphology which can effectively block the porous TBC features [11].

Table 2.3: Summary of reaction products that are relevant to CMAS interactions with RE TBCs, EBC and standard YSZ TBC [11].

Type	Name	Nominal formula
Intrinsic crystallization	Anorthite	$CaAl_2Si_2O_8$
	Diopside	$CaMgSi_2O_6$

	Cristobalite, tridymite	SiO_2
	Pseudowollastonite	$CaSiO_3$
	Pseudobrookite	Fe_2TiO_5
	Melillite	$(Ca)_2(Al,Mg)(Al,Si)SiO_7$
	Spinel	$MgAl_{2-x}Fe_xO_4$
Reprecipitation	Fluorite	$(Zr,RE,Ca)O_{1.x}$
	Tetragonal ZrO2	$(Zr,RE,Ca)O_{1.x}$
	Celsian	$(Ba,Sr,Ca)Al_2Si_2O_8$
	Zirconolite	$(Ca,RE,Zr)_2(Fe,Ti,Al,Mg)_2O_7$
Reactive crystallization	Zircon	$ZrSiO_4$
	CaZr-cyclosilicate	$Ca_2ZrSi_4O_{12}$
	Calcium zirconate	Ca_2ZrO_3
	Apatite	$(Ca,RE)_4(RE,Zr)_6(SiO_4)_2O_2$
	Garnet	$(Ca,RE,Zr)_3(Zr,Ti,Mg,Al,Fe)_2(Si,Al,Fe)_3O_{12}$
	Cuspidine	$(RE,Ca,Hf,Mg)_4(Si,Al)_2O_{9.x}$
	CaRE-cyclosilicate	$Ca_3RE_2Si_6O_{18}$
	Silicocarnotite	$Ca_3RE_2Si_3O_{12}$
	yttrium disilicate (YDS)	$Y_2Si_2O_7$

Finally, **Figure 2.17** shows the schematic of the common reaction products produced for CMAS glass interactions with RE based TBCs [11]. The reactions indicated in red arrows are representative for the RE silicate-based reactions and the ones in gray color for the M^{4+} based reactions (where M stands for Zr or Hf). Upon reaction with CMAS these coatings follow a series of sequences which are (i) dissolution of TBC cations (RE^{3+} and M^{4+}) into the melt upon wetting the coating. Consequently, as the TBC cations reach a saturation limit within the melt, they reprecipitate into the fluorite phase with a different composition (being RE lean compared to the original TBC composition). As the melt dissolves more coating, the RE concentration increases until it reaches the saturation limit to promote silicate-based phase formation (such as apatite and garnet). From these phases, apatite represents the first phase to form upon reaching glass saturation limit. The green arrows show the required input of glass elements to promote phase formation. Thus, Ca represents a critical element (besides RE) to promote apatite formation. Then other elements present in the glass promote secondary formation of reactive phases such as garnet or cuspidate. Besides rapid crystallization of apatite phase for CMAS arrest, another important consideration for CMAS resistant coatings is the recession rate (or consumption rate) of the coating

being consumed to promote reaction phases. Very high recession rates would require very high coating consumption and thick CMAS resistant coatings which add extra parasitic weight to the coating system. Additionally, a deeply infiltrated coating or a large reaction zone could also promote larger residual stresses. Finally, from the current studies it is exposed that the chemical composition of the melt also plays a critical role (e.g. Si content, Ti and Fe) in the formation of secondary reaction phases such as garnet or yttrium disilicate (YDS) as discussed in the next sections.

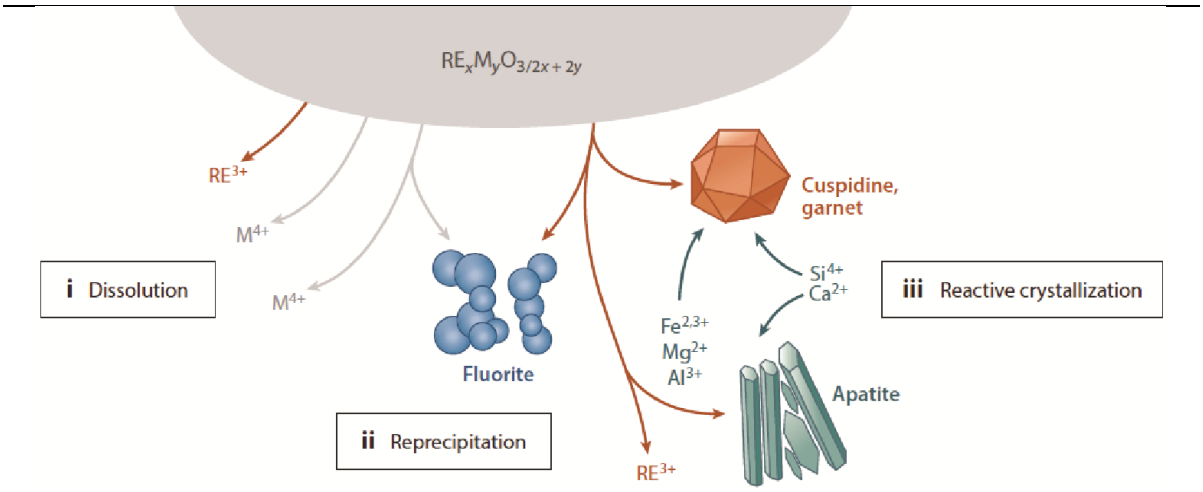

Figure 2.17: Schematic of reaction process of CMAS glass with RE based TBCs. The reaction shows all the stages where first (i) the TBC cations are dissolved into the melt seen in red for RE and gray for M based reactions (where M stands for Zr or Hf). (ii) As the cations reach the melt's saturation limit, they reprecipitate with a different composition and structure and (iii) reactive crystallization is promoted being apatite the primary phase formed upon RE saturation limit in the melt. Green arrows indicate the exchange of elements required to promote other secondary reactive phases such as garnet.

2.6.1 Intrinsic Crystallization

Intrinsic crystallization of silicate melts infiltrated into 7YSZ TBCs has been reported due to the melt undercooling generated from the thermal gradient exhibited in real engine conditions as it infiltrates the porous features [11]. On the other hand, for reactions with RE based CMAS resistant coatings, intrinsic crystallization can also be triggered from the changes in melt

composition as reactive phases are formed (e.g. apatite) which shift the melt equilibria (depleting Si and Ca while enriching Mg and Al commonly) into the areas of stable products (such as anorthite or spinel) at high temperatures. However, these type of crystallization products are not considered as beneficial for CMAS arrest since they are promoted as byproducts of reaction and their produced microstructure is not beneficial to seal the porous TBC features. (See chapter 4 for CMAS 1 reactions producing anorthite as byproduct of reaction).

2.6.2 Reprecipitation and Primary Reactive Crystallization

As explained before as the melt dissolves in the coating it produces reaction products as the melt saturation limit is locally reached (being fluorite and apatite the first crystallization product formation for RE based CMAS resistant coatings). The fluorite formation is considered to be a reprecipitation product since it does not retain any significant Si content to be considered as a reaction phase from melt/TBC interaction making Zr or Hf (M elements) the main elements contributing to its crystallization. On the other hand, the apatite phase represents the first reactive product formed from the RE interaction with CaO and SiO_2. It has been reported for GZO reactions that the apatite phase is promoted within seconds of interaction with CMAS melts producing immediate gap sealing effect [10]. The apatite phase represents a ternary phase from the CaO-SiO_2-$REO_{1.5}$ system which exhibits a nominal composition of $M^I_4M^{II}_6(SiO_4)_6X_2$ where in general the M^I and M^{II} sites correspond to columns of cations along the c-axis of the hexagonal unit cell. The oxygen coordinations of the M^I and M^{II} sites are 9 and 7 respectively [119]. The X site host oxygen anions not covalently bonded to the Si tetrahedra which are located within a ring of M^{II} sites (commonly occupied by a combination of Zr^{4+} and RE^{3+}) as seen in **Figure 2.18a** [119]. The M^I is commonly occupied by Ca^{2+} and RE^{3+}, additionally it has been reported that apatite structures exhibit a solid solution homogeneity ranges enabled by ionic substitutions [119]. Additionally, the apatite structure exhibits a range of compositions as shown in **Figure 2.18b** also depending on the RE cation. In general, without introducing lattice defects such as vacancies or interstitials the charge balance is achieved when the M^I site contains two Ca^{2+} simplified as $Ca_2RE_8(SiO_4)_6O_2$ (as

seen in **2.18b**). Since Ca and RE can be substituted, increasing the Ca content induces oxygen vacancies to balance charges whereas, increasing RE content generates cation vacancies (Ca lean). Finally, from the theoretical stability range in **2.18b** the Ca lean apatite composition can range in between $RE_{9.33}(SiO_4)_6O_2$ and $RE_{10}(SiO_4)_6O_3$ requiring oxygen interstitials for the high RE containing composition.

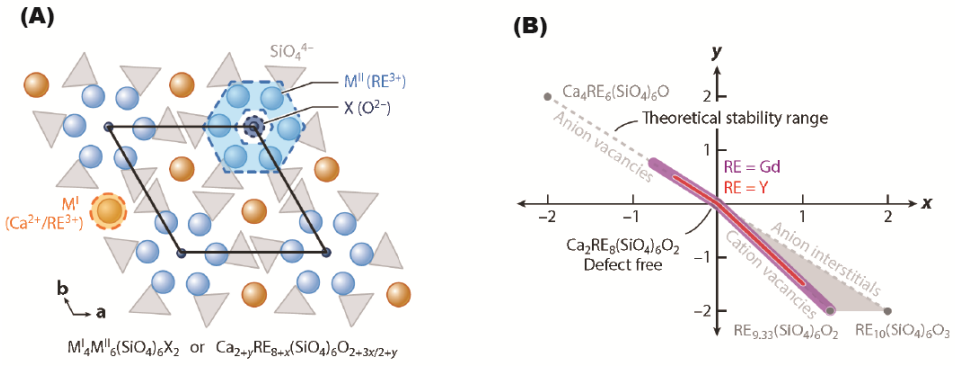

Figure 2.18: (A) Schematic of the apatite structure and (B) range of apatite compositions with respect to Y and Gd [11]. The colored Gd and Y marks indicate the reported ranges of apatite composition in literature.

2.6.2 Secondary Reactive Crystallization

From the literature reports, it is known that the other secondary reactions are produced from the constant glass interaction with the primary reaction products (apatite and fluorite). The common reported secondary phases for RE based TBCs represent garnet, silicocarnotite, YDS and zircon at temperatures ranges between 1200 and 1300 °C [11, 26, 120]. These phases are also reported to not being as effective as the apatite phase for CMAS arrest due to the slow crystallization kinetics and less desirable growing morphologies [11]. The melt composition plays an important role in this secondary phase formation since they are promoted from the constant interaction of the primary reaction products with large glass reservoirs (as discussed in chapter 4). For large Si and low Ca containing melts the formation of YDS and zircon is produced at the expense of apatite and fluorite respectively. Whereas for other element enriched melts (such as Mg, Fe, Ti and Al) garnet formation is promoted. Special attention in this thesis has been paid to

the garnet phase since it exhibits a slow reaction rate and maximizes melt crystallization. The phase exhibits a complex crystal chemistry of which represents a cubic cell containing a very large variation of atoms of various masses (160 atoms for these studies all the available melt/TBC cations) [81].This phase appears to be beneficial to promote slow coating reaction rates for long term infiltration testing (up to 50 h as discussed in chapter 4).

2.7 Basic-Acid Theory for CMAS Infiltration Assessment

Viscosity represents an important fluid property that dictates the infiltration of a CMAS melt into the TBC porosity being low viscous melts more susceptible to exhibit deep infiltration. The concept of basicity has been widely used to estimate the viscosity of slags in steel production which resemble CMAS compositions with Ca and Si as the main components [121]. It has been widely recognized that the viscosity of slags is controlled by the ratio of acid oxides (with SiO_2 being the most dominant) to basic oxides such as CaO, MgO or alkali oxides [78, 122]. This principle is called basicity index (BI) which works on the basis that SiO_2 is a well-known network former. Thus, for glassy silicate-based melts the silica tetrahedra generates chain connections in all directions resulting in SiO_2 complex interconnected networks exhibiting high viscosities.[121] Additions of network modifiers such as Ca,Mg or alkali elements act as chain braking ions which free the silica tetrahedra corners resulting in an overall reduction in melt viscosity [121]. The application of BI to predict reactivity of CMAS melts in YSZ TBC was applied by Craig and Ndamka [78, 122]. Where the BI was estimated as the ratio of basic oxides to acidic oxides as shown in

Equation 4

$$BI = \frac{\sum Basic\ oxides\ (mol\ \%)}{\sum Acid\ oxides\ (mol\ \%)}$$

Where the predominant oxides represent the following [122]:

- Modifiers (basic oxides) – CaO, MgO, Na_2O and K_2O

- Network formers (acidic oxides) – SiO_2 and P_2O_5
- Amphoteric oxides – Al_2O_3, TiO_2 and Fe_2O_3

The amphoteric oxides are believed to act as basic or acid oxides depending on the overall basicity of the melt. The BI correlation with SiO_2 and CaO contents in the melt is shown in **Figure 4.19** where an acid melt is considered until ranges up to 1.75 BI, the neutral range remains in the 1.75 to 2.25 BI and basic melts are considered for BI> 2.25. Thus, is has been reported that the amphoteric oxides behaved as acid until BI ranges > 2. The tested CMAS/VA compounds in these studies are considered as acid since they exhibited BI<1.75. Finally, next sections show the correlation of BI with prediction of expected reaction products at the reaction layer front and melt viscosity.

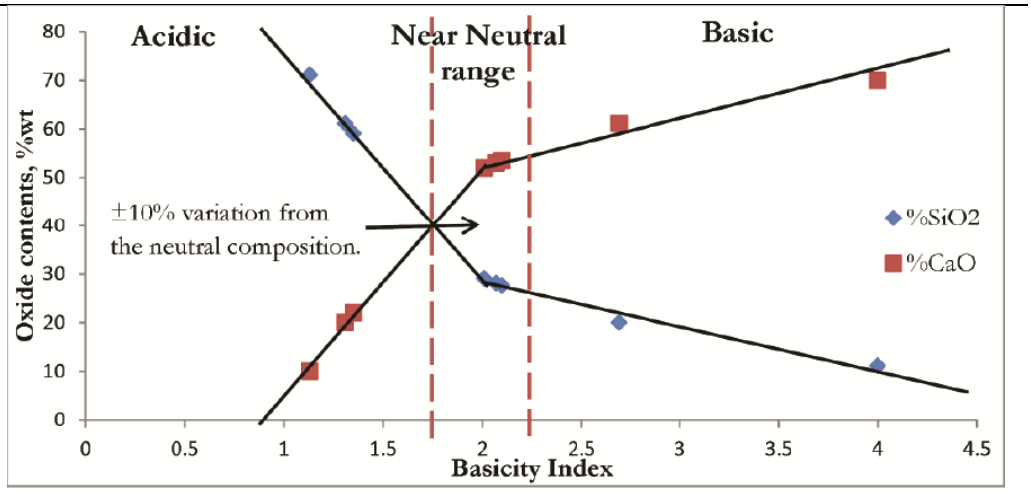

Figure 2.19: Basicity index correlation with respect to CaO and SiO2 contents in the melt [78].

2.8 Kinetics of CMAS Infiltration in EB-PVD TBC.

The essential columnar gaps that provide strain tolerance to EB-PVD TBC represents open capillaries susceptible to CMAS infiltration. The glass infiltration is influenced by capillary forces which act during the wetting of the TBC surface. The main factors governing the CMAS

infiltration are the fluid properties (e.g. viscosity, surface tension and contact angle) and TBC permeability (dependent on geometric factor, pore fraction and column to columnar gap correlation) which can be controlled by tuning the deposition parameters [31, 32]. The CMAS infiltration kinetics in EB-PVD TBCs using a prediction model proposed by Naraparaju et al. named "concentric pipe model" [31, 32] was studied in detail. The model combines the Darcy's law for steady state uni-directional flow into porous media with capillarity theory to correlate time dependence (t) on infiltration depth (h) of a melt with certain viscosity in TBCs [31, 32] where Darcy's equation can be written as:

Equation 5

$$\frac{\partial p}{\partial x} = -\frac{\mu v}{k} = \Delta p = -\frac{\mu}{k}\frac{x\partial x}{\partial t}$$

where k is the permeability of the medium, v is the velocity of the fluid, p is the pressure that drives the fluid, x represents the infiltrated distance and t the infiltration time. The fluid is then assumed to be driven only by the capillary pressure, therefore Δp can be written as:

Equation 6

$$\Delta p = \frac{\sigma cos\theta}{r}$$

where σ is the surface tension, θ is the contact angle and r the capillary radius. By inserting **Equation 6** into **5** and integrating over the whole length of the capillary tube, the time required for a liquid to infiltrate a certain depth h is obtained as shown in

Equation 7

$$t = \frac{\mu r h^2}{2\sigma k cos\theta}$$

where μ, σ, and θ represent the fluid properties viscosity, surface tension and contact angle respectively. The microstructural properties are controlled by k and r. The permeability of the TBC is represented by considering the TBC column and a columnar gap around as a concentric pipe (b)

with a kernel inside (a) as seen in **Figure 2.20** [31]. The permeability equation (k) is described as follows:

Equation 8

$$k = \frac{\varphi}{8\tau^2} b^2 \left[1 + \frac{a^2}{b^2} + \left(1 - \frac{a^2}{b^2} \right) . \frac{1}{\ln \frac{a}{b}} \right]$$

where φ represents the pore fraction of the coating, τ the geometric factor, a radius of the TBC column, and b radius of the TBC column plus column width. Finally, the radius (r) for open infiltration in Equation 5 is calculated as follows:

Equation 9

$$r = \sqrt{b^2 - a^2}$$

by substituting the **equations 7** & **6** in **equation 5** the infiltration depth (h) at a given time can be estimated for EB-PVD based microstructures as given in **equation 8**.

Equation 10

$$t = \frac{\mu \sqrt{b^2 - a^2} h^2}{2\sigma k cos\theta}$$

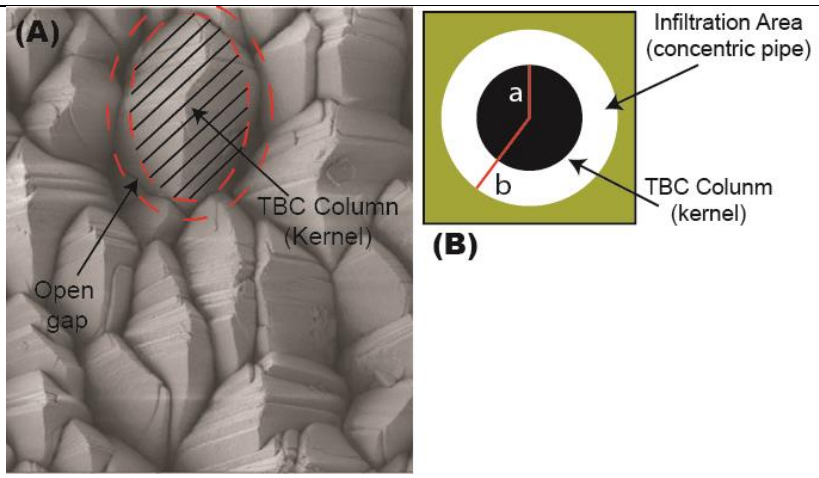

Figure 2.20: Representation of the concentric pipe model assumption for EB-PVD TBCs where (A) shows the top view of a standard YSZ coating exhibiting the columnar arrangement. The shaded area shows the column (or kernel "a") and the area in between the dashed circles represents the columnar gap (or concentric pipe "b") open for CMAS infiltration. (B) shows the representation of the parameters in a simplified schematic [31].

Additionally, the surface tension is usually estimated by the following equation proposed by Kucuck et al. [123] based on the chemical composition of the melt at 1400 °C:

Equation 11

$$\sigma\left(\frac{mN}{m}\right) = 271.2 - 2.22K_2O + 1.96MgO + 3.34CaO + 2.68FeO + 3.47Al_2O_3\ (mol\ \%)$$

It has been reported that no significant variation in surface tension is seen from relevant turbine operating temperatures (1200 °C and above) [96]. The geometric factor τ is believed to highly influence the infiltration in TBCs since it distributes the glass flow more efficiently by splitting the molten glass from the columnar gap into to the feather arm capillaries as shown in **Figure 2.21a [31].** Its estimation is based on the ratio of the open are for infiltration of the feather arm (FA) with respect to the columnar gap area (CG) as seen in **Figure 2.21b**. The current value is usually reported in literature as >1 and for TBC microstructures it is believed to not be higher than 3. At last, since the CG:FA relation varies for different EB-PVD microstructures the highest

parameter is always considered as the numerator and the lowest the denominator to provide a value >1.

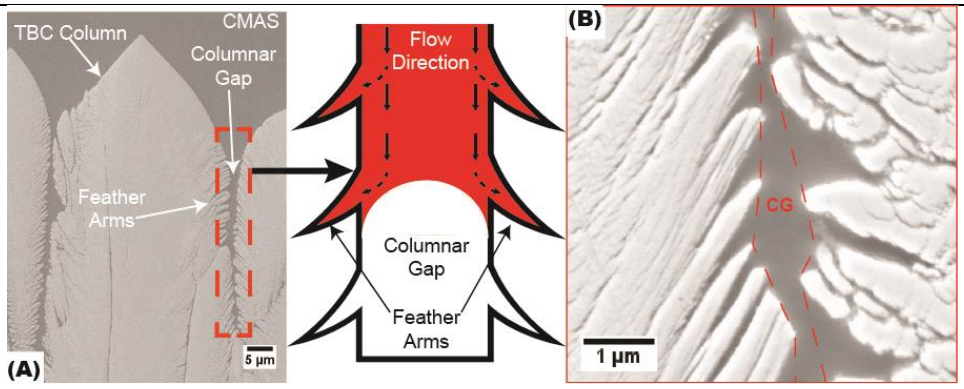

Figure 2.21: (A) representation of the geometric factor effect in CMAS infiltration produced in EB-PVD TBC where glass flow is delayed due to the splitting into the feather arms and (B) high magnification representation of the geometric factor estimation where the columnar gap area (CG) is compared with respect to the feather arm area.

Chapter 3: Effects of Yttria Content on the CMAS Infiltration Resistance of Yttria Stabilized TBC System

The effects of $YO_{1.5}$ doping in the yttria-zirconia based TBCs against the CMAS interaction/infiltration are discussed. The TBCs with $YO_{1.5}$ content ranging from 43 to 67 mol % (rest Zirconia) were produced by EB-PVD technique. The results revealed a trend of higher apatite formation probability with the higher free $YO_{1.5}$ available in the yttria-zirconia system. Additionally, the highest infiltration resistance and smallest amount of consumed coating appears to be strongly dependent on the $YO_{1.5}$ content in the coating. This was supported by the results showing the thinnest reaction layer and lowest infiltration for the highest produced $67YO_{1.5}$ coating. Complementary XRD experiments with $VA/YO_{1.5}$ powder mixtures with higher yttria contents than in the coatings ($80YO_{1.5}$ and pure $YO_{1.5}$) also showed higher apatite formation with respect to yttria content. The threshold composition to promote apatite-based reaction products was found to be around $50YO_{1.5}$ in zirconia proved in the coatings and XRD powder experiments. A Y-Zr-Fe-Ti bearing Zirconolite phase was formed as a reaction product for all the coating compositions which could lead to the conclusion that TiO_2 in the melt acts as a Y sink to promote zirconolite formation. This phase could be detrimental for CMAS/Volcanic Ash infiltration resistance since it can be formed alongside with apatite which controls or limits the amount of Y^{3+} available locally. The garnet phase containing all the possible elements exhibited a slower nucleation compared to apatite and its growth was enhanced with slow cooling rates. The implications of phase stability and heat treatment effects on the reaction products are discussed for test performed at 1250 °C.

3.1 Materials and Methods

3.1.1 Coating Preparation

Yttria-zirconia coatings were prepared by EB-PVD using a jumping beam method with two evaporation sources, one matching the standard 7YSZ composition and the other one being pure Y_2O_3. A schematic of the deposition process is shown in **Figure 3.1**. The produced samples

exhibited an overall thickness of 50 µm ± 3 and were deposited on top of previously developed 65 wt % Y_2O_3-ZrO_2 coating (produced with the same jumping beam procedure as described elsewhere [26]). A further schematic of the complete TBC system with the substrate is shown in **Figure 3.2**. A 1 mm thick Al_2O_3 substrate was used due to the advantages it gives to test high-temperature infiltration (>1250 °C) which cannot be tested if standard Ni-based superalloy substrates are used. Due to the evaporation process, two clouds of different evaporated material e.g. 7YSZ and Y_2O_3 were produced (**Figure 3.1**). These clouds generate a different Y_2O_3 content in the coated sample with respect to how close it was located with respect to the pure yttria ingot in the coating chamber. Therefore, the produced samples exhibited a $YO_{1.5}$ content (ZrO_2 balanced) in between 43 to 67 $YO_{1.5}$ mol % [2]. The deposition parameters are specified in **Table 3.1**.

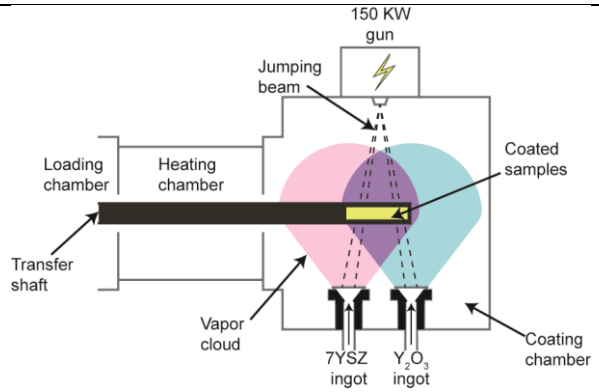

Figure 3.1: Schematic of EB-PVD deposition chamber for the produced yttria rich samples.

[2] The single cation mol % basis will be used to refer to the coating composition in this study with respect to the yttria content.

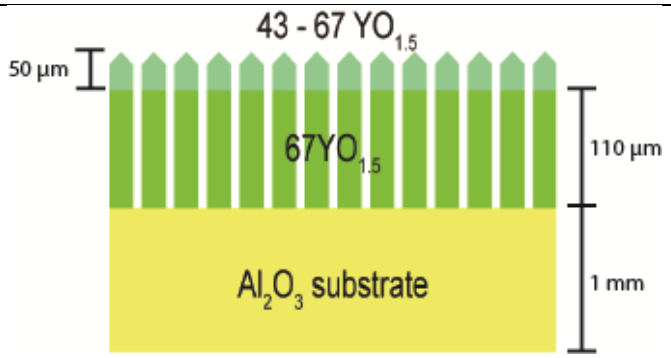

Figure 3.2: Schematic representation of the as coated TBCs used for this study.

Table 3.1: Summary of EB-PVD processing parameters and thickness of $YO_{1.5}$-ZrO_2 top coat.

Pressure (mbar)	RPM	Temp. (°C)	Power (KW)	Thickness (µm)	$YO_{1.5}$ content (mol %)
0.004	30	1030	112	47-53	43-67

3.1.2 Infiltration Experiments

The selected CMAS source was natural volcanic ash (VA) collected from the Eyjafjallajökull volcano. Its composition is given by $C_{11}M_6A_{13}S_{45}F_{16}T_4L_5$ where each letter represents every oxide in mol % using single cation basis (CaO, MgO, $AlO_{1.5}$, SiO_2, FeO, TiO_2, and L which represents the sum of $Na_{0.5}O$ and $K_{0.5}O$). Its composition was determined by energy dispersive X-Ray spectroscopy (EDS) using different powder samples. The estimated melting range of the Iceland VA is in between 1060 and 1150 °C. It was measured via differential scanning calorimetry (DSC) in previous studies [26]. The volcanic ash infiltration experiments were performed by mixing the VA with distilled water with an ash concentration of 20 mg/cm^2. Subsequently, the slurry was deposited on top of the coatings and dried at ambient temperature for 2 h. The heat treatment was performed with a heating rate of about 80 K/min followed by isothermal treatment at 1250 °C for 1 h and subsecuently cooled down (using extra fans) to room temperature at a rate of 18 K/sec. The infiltrated samples were cut in half and prepared

metallographically for microscopy inspection. **Figure 3.3** shows the appearance of the samples before and after infiltration.

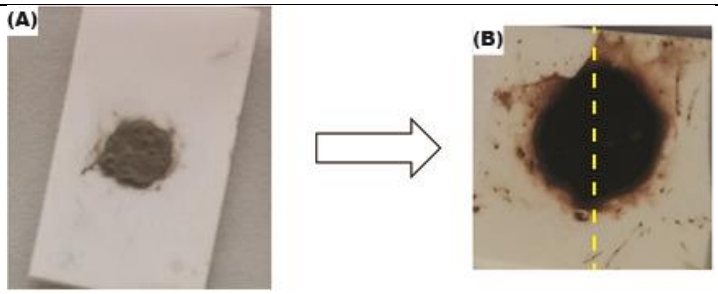

Figure 3.3: Image of the coated sample before infiltration (A) and after infiltration (B). The yellow dotted line represents the area where a cross-section was taken for microscopy.

3.1.3 Characterization

3.1.3.1 Microscopy analysis

Cross-sectional scanning electron microscope images (SEM) were obtained from the infiltrated samples to assess the VA infiltration damage. The infiltrated samples were covered with a carbon-based epoxy (Gatan G2) and cut in half as seen in **Figure 3.3** using a diamond saw automated machine. The cross-sections were then embedded in a conductive epoxy and polished down to a 0.05 µm finish using standard metallographic techniques. A DSM Ultra 55 (Carl Zeiss NTS, Wetzlar, Germany) SEM microscope equipped with an EDS system (Inca, Oxford Instruments Abingdon, UK) was used to determine compositions of the crystalline phases and microstructural analysis. Focused ion beam (FIB) assisted transmission electron microscopy (TEM) was used to analyze the as coated 65YZ coatings. The used equipment were a Strata 205 FIB machine and a Tecnai F30 TEM-STEM utilizing a field-emission gun (FEI Inc., Eindhoven, Netherlands).

3.1.3.2 XRD Studies

Phase identification was done via X-ray diffraction (XRD) of synthesized yttria-zirconia powders mixed with Iceland VA. The process for yttria-zirconia powder synthetization is explained in the next section. The powder mixtures of 60 wt % of Iceland VA and 40 wt % of yttria-zirconia were ground in a mortar with ethanol until homogenization was achieved and heat treated as explained in section 3.1.2 for 10 hours on top of a Pt foil. Then, the heat-treated powder mixture was mechanically removed from the Pt foil and pulverized in a mortar to get a fine powder for XRD analysis. The XRD measurements were carried out using a Si single crystal holder and a Siemens D5000 diffractometer equipped with a CuKα radiation source with a secondary graphite monochromator (EVA/Topas 4.2 software package, Bruker AXS, Karlsruhe, Germany).

3.1.3.3 Yttria-zirconia Powder preparation

Yttria-zirconia powders in the compositions ranging from 50 to 80$YO_{1.5}$ were synthesized by co-deposition of stoichiometric aqueous solutions of $ZrCl_2$*8H_2O and $Y(NO_3)_3$*6H_2O (Alfa Aesar, 99 %+ purity) on a hot plate at 400°C. The obtained composition products were crushed and subsequently heat treated at 1200 °C for 1 h in a chamber furnace. Additionally, pure Y_2O_3 powders (Alfa Aesar 99.9 % purity) were also used to compare the pure $YO_{1.5}$/Iceland VA XRD reactions.

3.2 Results

3.2.1 As Coated TBC Microstructure and Phase Analysis Including that of Synthesized $YO_{1.5}$ Powders

The as-coated samples exhibited the typical parallel columnar structure generated by EB-PVD methods. **Figure 3.4** shows the exhibited microstructure for the as coated samples from the lowest $YO_{1.5}$ (a) and highest (b) with the compositions of 43 and 67 mol percent (ZrO_2 balanced) respectively. Both microstructures exhibited parallel columnar growth with enlarged feather arms (2-5 μm long) compared to standard 7YSZ microstructures (0.5-3 μm) [56]. Both samples showed a 2 μm thick deposited layer of alumina with an approximated composition of 8-15 $AlO_{1.5}$ ($YO_{1.5}$

and ZrO_2 balanced). The uniform alumina layer was a result of the involuntary short evaporation of one alumina substrate that fell into the molten evaporation pool due to the high rotations used during deposition. It is not believed that the addition of such small amounts of alumina into the coatings generate an influence on crystallization behavior. However, the analysis of the alumina effect is discussed in detail in the discussion section.

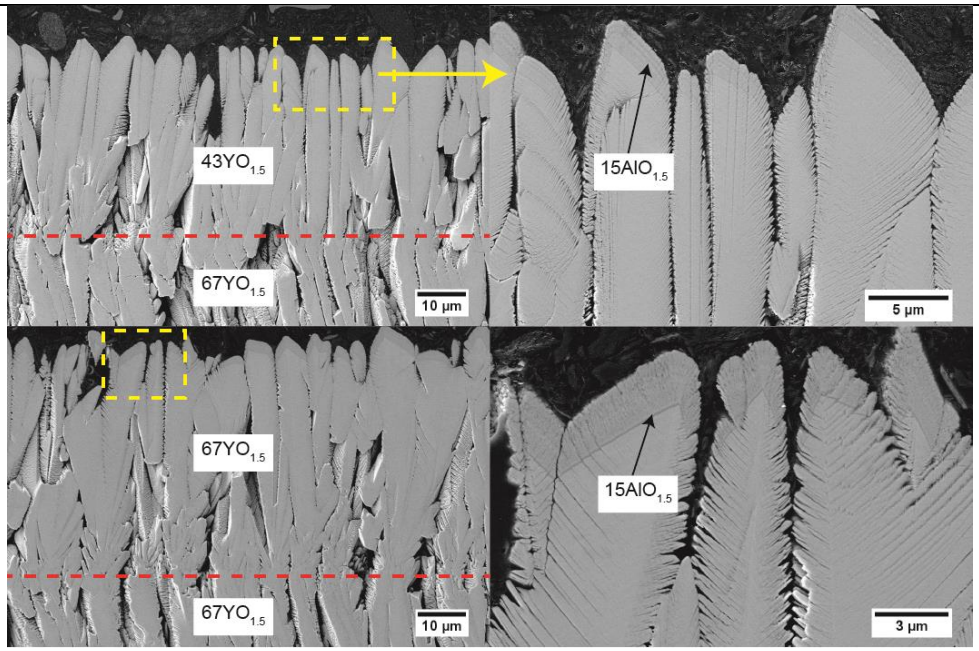

Figure 3.4: SEM cross-section image for the as coated samples from the lowest $43YO_{1.5}$ content to the highest 67 $YO_{1.5}$ content. The dashed red line shows the interface between the underlying previously coated 67 $YO_{1.5}$ and the new layer. High magnification images are shown on the right side for the area delimited within the dotted yellow rectangles.

The XRD plots are shown in **Figure 3.5** for the as coated and as synthesized $YO_{1.5}$-ZrO_2 coatings and powders. The XRD patters for the TBCs show no significant peak from the alumina layer as expected since previous experiments with as deposited EB-PVD alumina produced by EB-PVD generated an amorphous alumina coating [111]. The phases are indexed as a cubic fluorite YSZ phase for the as coated TBCs. In the case of the as synthesized powders (**Figure 3.5b**), the fluorite lattice constant is increased with yttria additions until the $80YO_{1.5}$ composition where the

pure cubic yttria peaks start to appear. These peaks are slightly distinguished in the $67YO_{1.5}$ TBC sample.

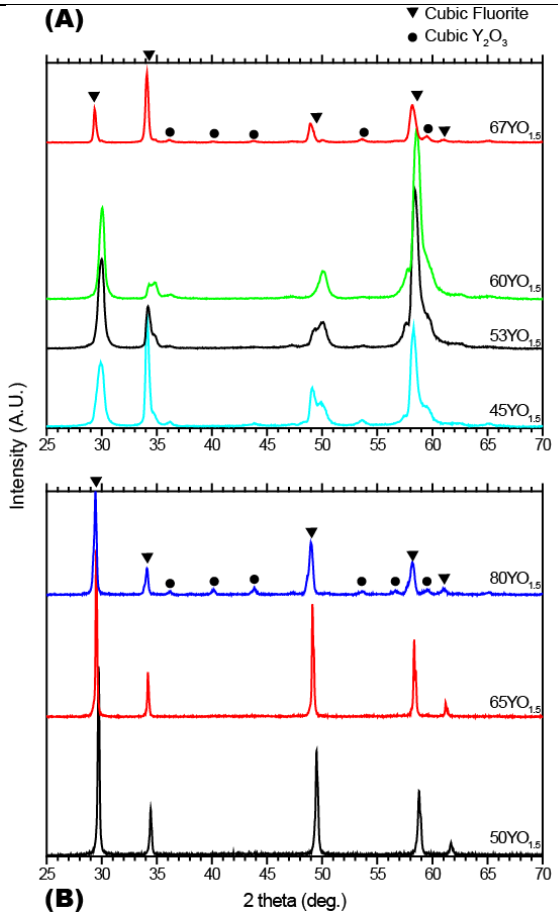

Figure 3.5: XRD plots for the (A) as coated TBCs with different $YO_{1.5}$ compositions and (B) as synthesized $YO_{1.5}$ powders.

3.2.2 XRD Analysis of the CMAS/TBC Interaction

The reaction products that have been produced by the annealing of VA/$YO_{1.5}$ powder mixtures were analyzed by XRD as shown in **Figure 3.6.** The XRD patterns show the apatite (A) and garnet (G) phases as common reaction products among all the reactions involving yttria and VA ($50YO_{1.5}$ to pure $YO_{1.5}$). The XRD peaks clearly show a trend that the probability for apatite formation increases with respect to the yttria content in the coating i.e. availability of yttria as "solute" increases in the glass. This is seen since higher apatite peaks are generated for the pure

$YO_{1.5}$ sample followed consequently by the 80, 65 and 50 $YO_{1.5}$ samples. It seems like 50$YO_{1.5}$ is the limit to promote apatite formation in this study case, the intensity of apatite peaks is so low. The garnet formation seems to be un-affected regardless of the $YO_{1.5}$ content in the reaction. It also appears to be the silicate-based phase with the highest concentration (highest peak formation) in the reaction. The fluorite phase (F) was found for the powder mixtures containing ZrO_2 (80 to 50 $YO_{1.5}$) as expected since it is a zirconate based phase. It is also known that the ZrO_2 solubility in the glass is lower than the $YO_{1.5}$ [124]. This promotes the nucleation of ZrO_2 bearing crystals which capture $YO_{1.5}$ to crystalize as any of the three available YSZ phases (monoclinic, tetragonal or cubic fluorite) depending on the composition of the melt [96-98, 124]. The zirconolite phase (Z) was identified for all the ZrO_2 bearing mixtures only. A summary of the identified reaction products and their theoretical chemical formulas is shown in **Table 3.2**. The Z and F phases can accommodate Y^{3+}, this reduces the amount of Y^{3+} available to promote apatite formation. Finally, it is important to note that all the $YO_{1.5}$ powder was consumed in the crystallization reaction since no traces of the cubic yttria phase (peak) are visible after the heat treatment test.

Table 3.2: Summary of reaction phases for the Iceland VA/ $YO_{1.5}$ powders heat treated for 10 h at 1250 °C.

Phase name	**ID**	**Theoretical formula**
Apatite	A	$(Ca,Mg,RE^{3})_2(RE,Zr)_8(SiO_4)_6O_2$
Garnet	G	$(RE,Zr,Ca)_3(Mg,Al,Fe,Ti,Zr)_2(Si,Al,Fe)_3O_{12}$
Fluorite	F	$(RE,Zr,Ca)O_{1.x}$
Zirconolite	Z	$(Ca,RE,Zr)_2(Fe,Ti,Al,Mg)_2O_7$

[3] RE stands for any rare earth from the lanthanide series, including Y.

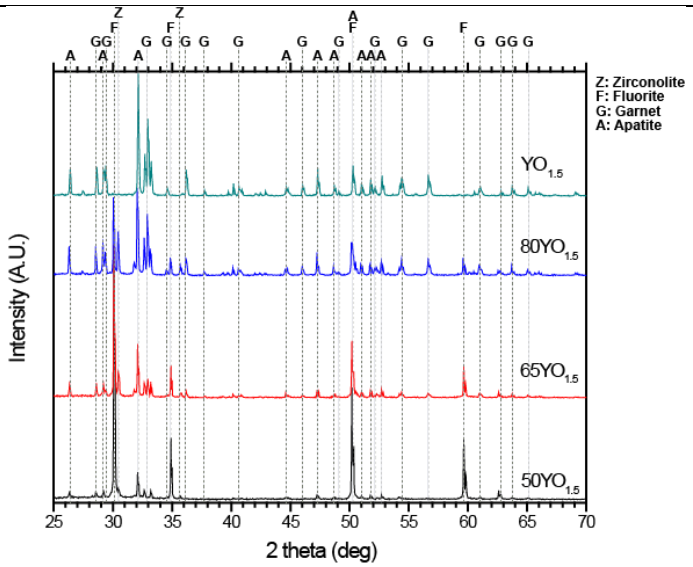

Figure 3.6: XRD plots for the $YO_{1.5}$/Iceland VA mixtures heat treated for 10 h at 1250 °C.

3.2.3 Volcanic ash infiltration

Figure 3.7 shows the cross-sectional image of the Iceland VA infiltrated samples with 4 different $YO_{1.5}$ average compositions (43, 53, 60 and 67 respectively) after 1 h at 1250 °C. The reaction phases are identified as same as for the XRD studies (apatite, garnet, fluorite and zirconolite) with help of the composition measurement using EDS co-relating with the XRD found phases and literature. It is clearly seen that $43YO_{1.5}$ sample (shown in **Figure 3.7a**) has undergone some reaction with the VA, however, no apatite formation (A) was found in the layer. At the reaction front an uniform zirconolite (Z) layer is visible on top of the TBC/glass interface with a thickness of 1 to 2 µm. Large globular fluorite crystals (F) are seen distributed evenly throughout the reaction layer (delimited within the dotted lines in the other figures). Lastly, no garnet phase (G) presence is identified either in the $43YO_{1.5}$ case. In contrast, the 53 to 67 $YO_{1.5}$ reactions exhibited different reaction products than that of $43YO_{1.5}$. Apatite crystals (A) are clearly seen in small confined areas such as small columnar gaps or feather arms and they clearly grow favorably to seal the gaps as shown in Figure 3.7b, c & d and their presence becomes more prominent with the higher yttria content.

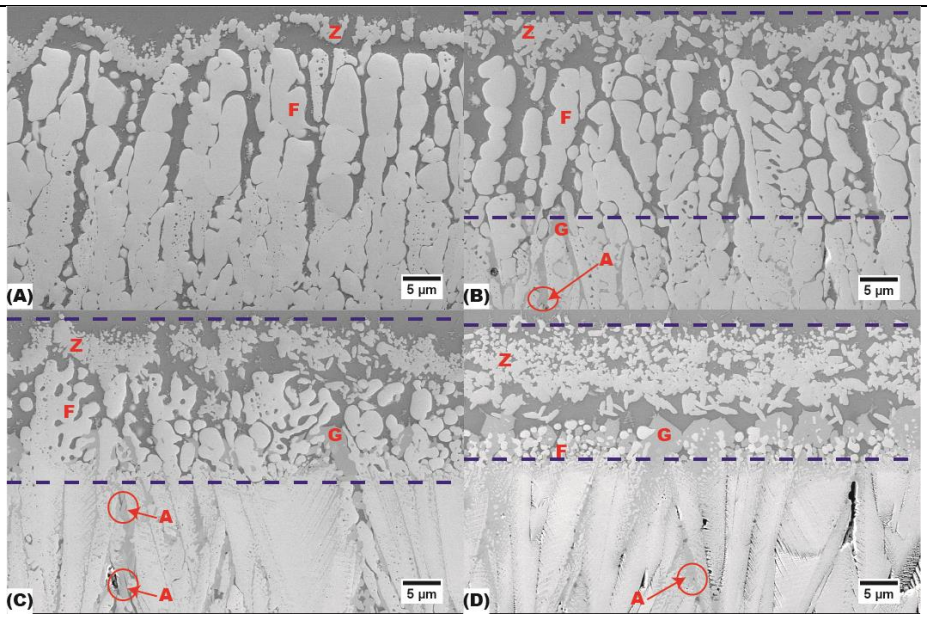

Figure 3.7: Cross-section SEM image of the reacted samples for 1 h at 1250 °C with Iceland VA. The area delimited within the dotted lines represent the reaction zone. A) shows the reaction for the $43YO_{1.5}$, B) for the 53, C) for the 60 and D) for the 67.

The garnet phase appears to be engulfing the other products at the glass/TBC interphase (apatite, garnet and zirconolite) but it seems to consume mainly the apatite phase in the columnar gaps (See 3.7d). This type of growth is in agreement with the hypothesis that the garnet phase represent a secondary reaction product which grows or nucleates slower at expense of other phases from the constant interaction with the glass [34]. Fluorite and zirconolite phases are clearly distinguished in all the reactions however, fluorite concentration goes down and partly appears to transforms in to zirconolite with the increase in the yttria content. The $53YO_{1.5}$ emerges to be the compositional threshold for the apatite. These results are in agreement with the XRD studies which were discussed earlier. The reaction zone gets thinner with respect to the increase in $YO_{1.5}$ content: 23, 20 and 18 µm for the 53, 60 and 67 $YO_{1.5}$ respectively.

The coating containing $YO_{1.5}$ from 47 to 60 percent exhibited full infiltration of the 50 µm thick top coat having an additional reaction at the underneath $67YO_{1.5}$ layer. The $67YO_{1.5}$ top layer was the only one that did not showed complete infiltration as seen from **Figure 3.8** where the Si elemental mapping (given in green color) shows the localized infiltration at large columnar gaps

at about 40 μm maximum. The elemental mapping shows a clear Ti enrichment in the zirconolite layer. This phase was seen in previous experiments at 1250 °C at various heat treatment durations (5 min to 20 h) [26] but it was finally identified in this study. Additionally, the zirconolite phase was also found after long heat treatments (100 h) for $Gd_2Zr_2O_7$ TBCs tested with an artificial volcanic ash produced matching the composition of the Iceland VA collected from a different ash plume event [30]. This phase is believed to be closely related to the pyrochlore structure and is also structurally related to the zirkelite and polymignyte minerals [125-127]. The details on the phase equilibra of this reaction phase will be discussed in detail in the discussion section. The garnet phase showed a characteristic Fe enrichment as seen in **Figure 3.8**. These findings are consistent with previous studies with Iceland VA [26].

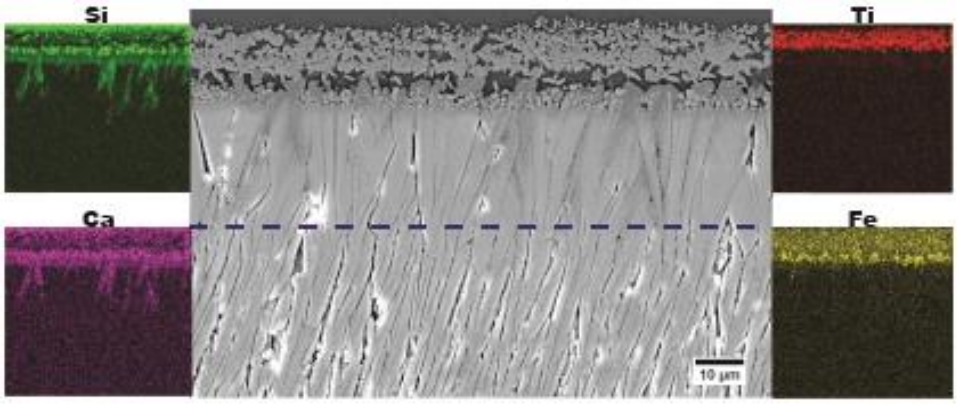

Figure 3.8: Cross-section SEM image of the infiltrated $67YO_{1.5}$ sample showing the elemental mapping for the overall infiltration (seen as Ca and Si mappings) and reaction layer zone with the Ti and Fe concentration. The dotted line shows the interface between the new and old deposited coatings.

3.3 Discussion

3.3.1 As Coated Coatings and $AlO_{1.5}$ Content

The presence of 15 mol % of $AlO_{1.5}$ in the 2 μm thick layer which was accidentally deposited on top of yttria rich layers was found to be in amorphous in nature. As stated before,

previous studies using EB-PVD alumina coatings were amorphous after the deposition and additional heat treatments were needed to stabilize the α alumina phase [111]. The estimated amount of dissolved alumina from the coating would be very minimal which could count about 0.4 vol % of the CMAS deposit (estimated by the average deposited CMAS volume on top the TBC (about 3.51 mm^3) and the alumina volume content in the 2 μm thick alumina bearing layer (0.015 mm^3)). These amounts are essentially neglectable for the VA melt equilibrium. However, this alumina could lead to a form alumina-yttria based phases such as YAG ($Y_3Al_5O_{12}$), YAP ($YAlO_3$) and YAM ($Y_4Al_2O_9$) upon heat treatment [128]. Special interest has been paid to these phases since they have exhibited potential as a CMAS resistant coatings [129, 130]. Since the alumina and zirconia are not expected to form any crystalline phase [131] only attention was paid to the Al-Y mixture. In this context, TEM studies were performed on the 1 h heat treated sample at 1250 °C in the non-VA infiltrated region to look for possible Y-Al phases. The TEM results are shown in **Figure 3.9** for the top alumina mix layer in the $67YO_{1.5}$ sample. The results indicate nonmixing of the alumina and zirconia as expected but it also showed no mixed yttria-alumina phases. The Al was found to be located in small polycrystalline inclusions, presumably as a γ-Al_2O_3 phase. Additionally, cubic fluorite YSZ crystals were found in this region. Furthermore, the TEM results in the column core are also shown. The base material at the column core had a lanthanide cubic type yttria structure with alternating layers of fully stabilized cubic fluorite YSZ phase. This is due to the jumping beam evaporation process which produces an intermixed layer which is the function of the jumping beam frequency [132].

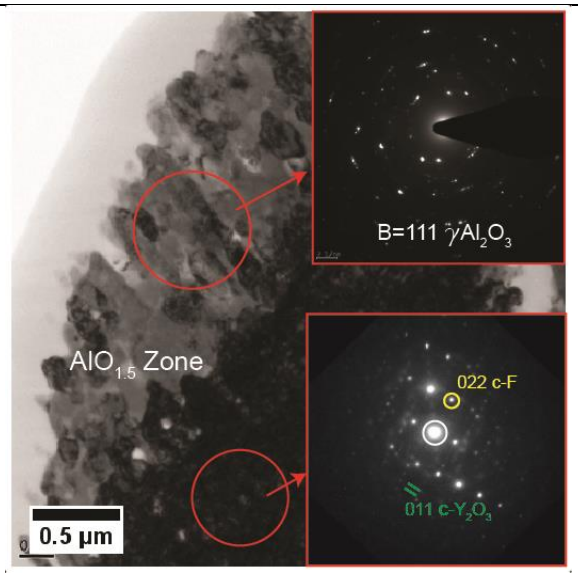

Figure 3.9: Bright field TEM image of the $67YO_{1.5}$ column after 1 h heat treatment at 1250 °C from the non-infiltrated zone. The SAED images show the non-mixed alumina phases at the alumina rich zone and the mixture of cubic fluorite and cubic yttria at the core of the TBC column.

3.3.2 Effect of Reaction Phase Formation with $YO_{1.5}$ content

It is well known that the most desirable phase for CMAS resistance is the apatite since it represents the first and fastest silicate based phase to crystalize upon yttria saturation in the glass [11, 27]. Additionally, its crystallization morphology/configuration within the columnar gaps allows sealing them therefore, no more glass is allowed to infiltrate through the columnar gaps. This crystallization behavior is believed to be beneficial in the initial infiltration stages (first few minutes of interaction) for TBC porous microstructures. However, it is suggested that after long term heat treatment (more than 1 h) it is important that the coating consumption rate (or reaction layer growth) is minimum so the need of thick sacrificial coatings is reduced. Additionally, since reported CMAS glasses and VAs exhibit a large variety of oxides such as Fe, Ti, K and Na. It is important that the reaction phases are able to retain more glass and more oxides per consumed TBC amount (i.e. Y and Zr). In this context, the garnet phase appears to be the most beneficial phase at the long-term infiltration since compared to the other phases it retains less TBC material

i.e. glass g/TBC is highest as seen in **Figure 3.10**. This ratio estimation is based on the percentage amount of glass products "g" (Ca, Al, Mg, Si, Fe, Ti) with respect to the percentage amount of coating material "TBC". Furthermore, studies performed comparing a vigorous apatite former TBC material such as $Gd_2Zr_2O_7$ (referred as GZO) with a good garnet former 67-70 $YO_{1.5}$ rest ZrO_2 coatings infiltrated with CMAS 1 for 50 h at 1250 °C (see chapter 4) have shown a larger reaction layer growth for the GZO. These results support the hypothesis that the garnet phase appears to be beneficial for the long-term infiltration. The composition summary for the reaction products is shown in **Table 3.3** for the performed experiments.

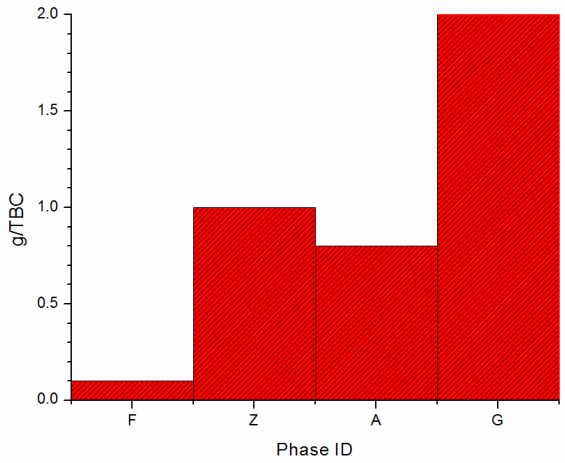

Figure 3.10: g:TBC ratio plot for the produced reaction products. Where the g represents the amount in mol % of the glass oxides and the TBC represents the $YO_{1.5}$ and ZrO_2 contents.

The importance of the early and quick formation of apatite phase was discussed above. Therefore, the current studies prove that in order to have a CMAS/VA resistant $YO_{1.5}$ based coating a minimum amount of 50$YO_{1.5}$ (shown in the XRD and TBC results) is required to promote the formation of this phase. The thinner reaction layer with respect to higher yttria content in the coating leads to the conclusion that more yttria available for reaction is expected to generate more apatite which seals the gaps early as seen in the XRD results. This can be explained from the phase

equilibria of pure yttria and yttria-zirconia coatings seen in the Y_2O_3-ZrO_2 phase diagram shown in **Figure 3.11** and adapted from [133-135]**.** The dashed line in the figure show the $80YO_{1.5}$ composition used in powder mixtures that were analyzed by the XRD. The red dashed line in the figure indicates the testing temperature of 1250 °C. As the coating material is dissolved by the glass, the Zr^{4+} re-precipitates upon reaching a saturation limit (about two times less than Y^{3+}) [124]. Since the glass is enriched in Y^{3+} as well, fluorite phase is promoted which as seen from the phase diagram it can retain about 16 $YO_{1.5}$ percent minimum at 1250 °C. From this point the Y^{3+} ions partition into fluorite and apatite formation. The $80YO_{1.5}$ was the highest tested composition with zirconia, as seen from the phase diagram this leaves more Y^{3+} ions available to divide into apatite and fluorite. However, since the Zr content is reduced for higher $YO_{1.5}$ contents, less fluorite phase can be promoted which allows for more free yttria available for reaction in the system. From this analysis it is then expected that the pure $YO_{1.5}$ composition will maximize apatite formation since the cubic fluorite phase will not be present upon glass dissolution. In this context, it has been proposed that fluorite formation limits apatite formation for RE compositions and this reaction changes with respect of RE ionic radius [34]. The current results show that the limited amount of available yttria for reaction to promote apatite is constrained to the point where the pure fluorite phase (F) starts to form; this is in good agreement with the literature reports. Additionally, we report that the compositional limit to promote glass reaction is with $50YO_{1.5}$ compositions as confirmed from the TBC and XRD experiments. Thus, it is evident that below this $50YO_{1.5}$ amount there is not enough free yttria available to promote apatite formation from its dissolution into the glass. Therefore, the apatite cannot precipitate as seen for the $43YO_{1.5}$ composition. Additionally, similar results were found in experiments performed with Yb-Hf based pellets with similar phase fields as for the $YO_{1.5}$-ZrO_2 (e.g. fluorite and δ phase) performed by Poerschke et al. [19]. In their studies apatite formation in was promoted for the δ Yb-Hf phase ($56YbO_{1.5}$ composition) but it was not promoted for the $30YbO_{1.5}$ tested composition. The study concluded that the low Yb composition did not form apatite since the dissolved Yb was retained in the fluorite phase or in solution in the melt and as more Yb was added the system could saturate

in Yb to promote apatite formation. Our current results are in good agreement with the reported results with Yb-Hf pellets. Besides, it is important to note that the boundary for formation of the δ phase ($Zr_3Y_4O_{12}$) still allows the apatite formation as found in the literature [11, 120] since it exhibits a $57YO_{1.5}$ which still has potential to give out excess yttria for dissolution prior fluorite formation. From this assumption of fluorite limiting or controlling apatite formation one more supporting hypothesis can be drawn from the phase diagram. It is seen at higher temperatures e.g. above 1400 °C approximately the fluorite phase field expands into wider yttria compositions of about 14 mol % $YO_{1.5}$ at the lowest and 61 at the highest. This range expands more with increasing temperature. This leads to the conclusion that the potency of apatite formation for yttria rich-zirconia coatings at temperatures above 1300 °C will be reduced due to the thermodynamic preference to promote fluorite nucleation. In contrast, the pure yttria would promote pure apatite crystallization since it would not produce any fluorite formation upon Y^{3+} dissolution (since no Zr^{4+} is available in the reaction) which theoretically would make a better candidate for CMAS/VA infiltration resistance. On the contrary, experiments performed by Eils et al. [27] using pure yttria and $Y_2O_3.ZrO_2$ coatings showed lower CMAS infiltration for the $Y_2O_3.ZrO_2$ coating than the pure yttria coating. However, the microstructure of both coatings was not analyzed in this study (not providing data for permeability of each coating) which makes it difficult to draw a conclusion from these results. It is important to stress that also that microstructure plays a prominent role in CMAS infiltration (as will be discussed in the next sections) e.g. for EB-PVD coatings the microstructure can be tailored to reduce CMAS infiltration by effectively distributing the flow of the molten glass [31, 32]. Also, very wide columnar gaps may allow large volumes of glass to infiltrate which could shift the saturation limit of the melt retarding the apatite formation. Therefore, a comprehensive study of microstructural infiltration effects is needed to effectively evaluate the infiltration resistance for coatings with different compositions.

Table 3.3: Summary of chemical composition of reaction products and residual glass (g) for the $67YO_{1.5}$ coating. Unless specified in the table, the element composition error was below 1.0 mol %.

	Chemical composition (mol %)									
Phase ID	$NaO_{0.5}$	MgO	$AlO_{1.5}$	SiO_2	$KO_{0.5}$	CaO	TiO_2	FeO	$YO_{1.5}$	ZrO_2
Z	-	1.5	3.5	3.9 ±2.5	-	2.0	19.9	19.3	21.2 ±1.3	28.7 ±1.9
G	-	6.8 ±1.1	7.2 ±2.2	20.7 ±2.2	-	9.6	0.9	21.9 ±6.5	29.4 ±5.1	3.5 ±2.3
A	-	1.7	0.4	30.7 ±3.2	-	10.4 ±1.3	-	0.6	47.8 ±2.1	8.4 ±4.7
F	-	-	-	-	-	0.6	4.5	6.7	23.5 ±2.5	64.8 ±3.2
g	3.7	5.9	13.2	43.6	0.9	10.3	1.9	10.0	7.8	2.7 ±0.2

It is important to know that the drive to use yttria-zirconia based coatings comes from some limitations that pure yttria exhibits y low toughness compared to fluorite YSZ [136] and higher thermal conductivity [54]. It is reported that the increase in yttria in the fluorite lowers the thermal conductivity [54, 65] up to $32YO_{1.5,}$ after that the thermal conductivity starts to increase again [64]. The performed CMAS experiments show the superior protective behavior of the highest yttria bearing coating ($67YO_{1.5}$ or about 65 wt % Y_2O_3). Therefore, this coating composition was selected as our reference coating for further experiments with CMAS infiltration testing.

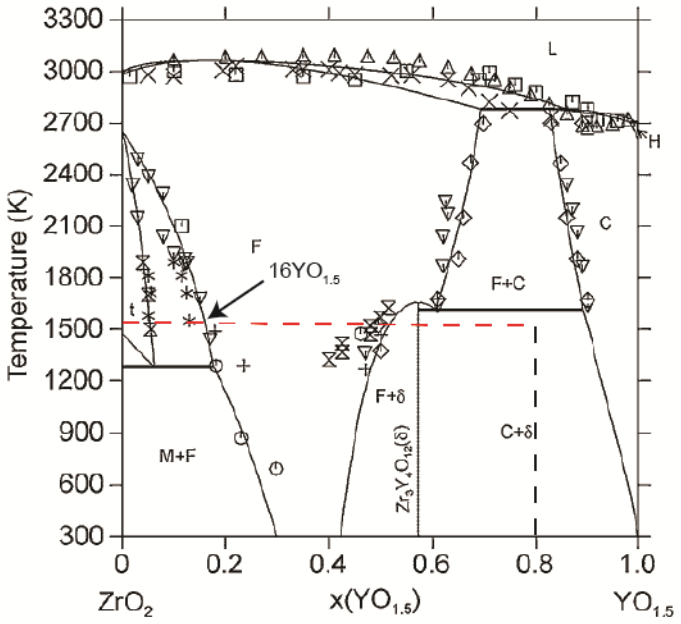

Figure 3.11: Adapted phase diagram from [135] of the ZrO_2-$YO_{1.5}$ system showing the possible phases for the tested system at 1250 °C up to $80YO_{1.5}$.

3.3.3 Effect of Cooling Rate on the Crystallization of the Reaction Products

Since aircraft engines are subjected to very abrupt temperature changes during operation e.g. take-off, cruise and landing [49]. Being the landing stage very critical since it produces a very severe temperature drop in the material from the reverse thrust to the ground idle stages. This makes the use of air quenched experiments a more approximate testing condition for the actual engine operating cycle. Besides, by using this testing approach the high temperature phases are retained so they can be analyzed. Therefore, the CMAS infiltration experiments were performed one more time under slow heating and cooling (10K/min) conditions using a box furnace to study if there is any phase nucleation upon cooling. The reaction layers after the heat treatments are shown in **Figure 3.12** for the 43 and $67YO_{1.5}$ TBCs only. The reaction products consisting of A, G, F, etc. were also found but an additional phase consisting of dendritic particles (d) in the molten glass zone was distinguished compared to the air quenched samples. These dendrites were also found for the Iceland VA in previous tests with slow furnace cooling and they exhibited all

available cations in their composition [26]. This phase retained all possible in it and were identified as garnet dendrites but they exhibited a larger Fe content (21.3 FeO mol %) $Mg_{9.9}Al_{9.9}Si_{29.5}Ca_{11}Ti_{1.2}Fe_{21.3}Y_{17.3}$. The current experiments prove that the nucleation of these particles is driven by the slow diffusion control growth from the slow cooling rate of 10 K/min. Additionally, very small dendrites were also found in the air quenched case samples with sizes below 1 µm (**Figure 3.12c**) which supports the findings on their diffusion enhanced growth due to the slow cooling process.

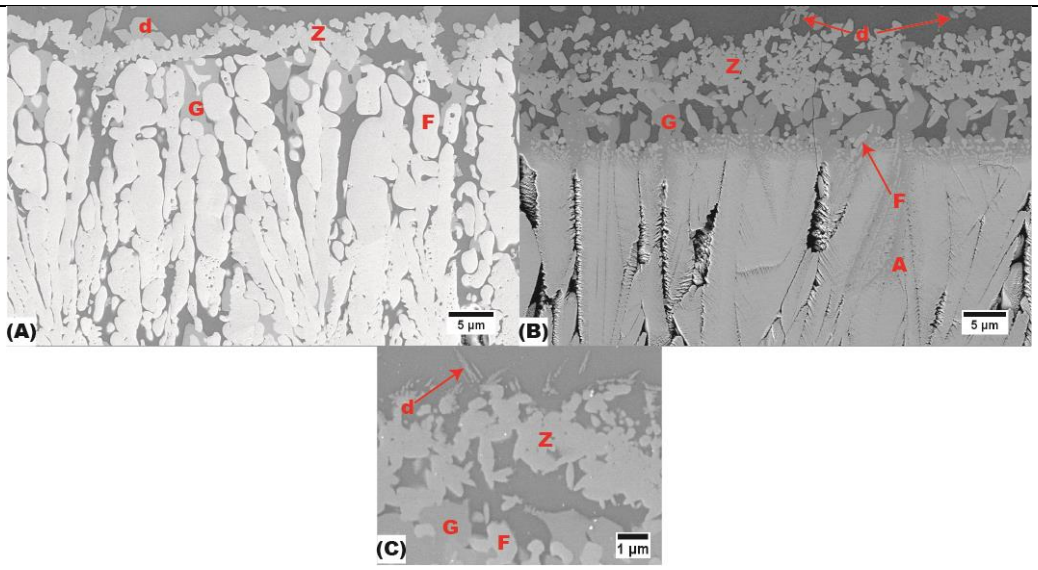

Figure 3.12: SEM image of the (A) $43YO_{1.5}$ sample after slow cooling, (B) $67YO_{1.5}$ sample after slow cooling and (C) 67 $YO_{1.5}$ sample from the top reaction zone after air quenching showing the small dendrite particle formation d. All the samples had the same infiltration time for 1 h at 1250 °C.

Furthermore, a clear formation of garnet crystals is seen in the $43YO_{1.5}$ sample (**Figure 3.12a**) which were not seen in its counterpart under air quenched condition (**Figure 3.7a**) . Here the garnet crystals appear to be nucleating at the expense of the fluorite globular particles. Also, more accumulated and larger garnet crystals are seen for the slow cooled samples. These findings are in agreement with the reported garnet growth behavior in literature from slow cooling and

consumption of apatite and fluorite phases [11]. The garnet phases produce for the air and slow cooled tests did not vary significantly which proves no phase transformation.

Finally, the zirconolite phase appears to nucleate from the Zr dissolution in the Ti-rich glass which promotes this phase formation regardless of the heat treatment. Its composition did not vary significantly with respect of the heat treatment cooling phase. A similar Zr-Ti bearing phase identified as calzirtite ($Ca_2Zr_5Ti_2O_{16}$) with a diffraction match with zirconolite was identified by Vidal-Setif et al. [102] in high pressure turbine blades removed from military plane engines under CMAS attack. This phase exhibits a general stoichiometry of $A_2B_2X_7$ where A= Ca, Na, RE, Zr, Ti and actinoids (ACT). B= Ti, Nb, Ta, Al, Mg and Fe and X= O or F [125, 126, 137, 138]. It is seen that a wide variety of elements can be accommodated in solid solution but the main constituents appear to be Zr and Ti [126]. It is believed that trivalent Ti can be incorporated in the A site in small amounts [139] but due to the large content of available cations in these experiments Ti is assumed to only occupy the B site. Additionally, no reports in literature were found about the possible site that Si would occupy.

It is important to note that the zirconolite phase needs less yttria compared to apatite and other garnet as seen for the $43YO_{1.5}$ sample. Additionally, it retains a significant amount of Y^{3+} (up to 23 mol percent as seen from **Table 3.3**) which could be problematic since it represents a sink for Y^{3+} which cannot be used for apatite formation. These results show how dynamically complex these reactions are and the big influence in the phase equilibira that other cations such as Ti have. Therefore, a comprehensive understanding on the thermodynamic influence that different cations have in the system could significantly help in predicting the CMAS/VA infiltration resistance of TBCs.

3.4 Conclusion

Experiments were performed using Iceland VA as CMAS bearing source in interaction with TBCs produced by jumping beam evaporation with varying $YO_{1.5}$ content at 1250 °C. The infiltration resistance of the coatings was assessed with respect of the $YO_{1.5}$ content in the coating

and supplemental studies with VA/$YO_{1.5}$ synthesize power mixtures were performed for phase identification. The results have given the following conclusions:

- The results from XRD powder mixtures and TBC coating experiments showed that higher VA infiltration resistance is expected with higher $YO_{1.5}$ as solute to promote apatite formation in order to seal the columnar gaps. Thinner reaction layer is also expected with higher yttria contents.
- The reaction showed that $50YO_{1.5}$ contents in the coating appears to be the compositional limit to promote apatite formation as reaction product. This phase reaction exhibits a correlation with the fluorite phase formation and free yttria available for reaction which is also function of infiltration temperature.
- The growth of the garnet phase is enhanced due to the diffusion-controlled growth mechanism produced during slow cooling. Additionally, the garnet dendrite phase also exhibited the same slow controlled growth process. Their compositions did not vary significantly with respect of heat treatment.
- The high Ti contents in the glass promote the zirconolite phase formation which accommodated large amounts of Y^{3+} and nucleates with lower yttria contents in the coating ($43YO_{1.5}$) compared to apatite. This shows the urgency to understand the effects of other cations not only CMAS in the phase equilibria to effectively predict phase formation.

Chapter 4: Kinetics of Reaction of CMAS/VA Interactions with Yttria-Zirconia TBC

This chapter presents the detailed study on the kinetics of chemical reactions and phase equilibria of the CMAS/VA interaction with 65 wt % Y_2O_3-ZrO_2 balanced (65YZ) EB-PVD coatings. The infiltration experiments were performed for different time durations and infiltrating temperatures (1250 and 1300 °C). The reactions were also compared with GZO and the infiltration performance for both samples was evaluated with respect to the reaction kinetics and melt equilibration due to rare earth element (RE) dissolution. The results showed the increased infiltration resistance and slower reaction layer growth for the 65YZ coatings than the GZO. The main mechanisms for its CMAS protection behavior are: i) The efficient phase reaction mechanism which promotes high glass arrest via quick apatite formation in combination with a synergetic mechanism that promotes the formation of garnet phase which consumes less RE from the coating and enforces the further melt crystallization. ii) The effect of the viscosity changes in the residue CMAS melt due to RE dissolution which might reduce the viscosity of the melt. This effect is seen predominantly for the GZO layers. A system to predict phase evolution in the reaction zone is used based on basic-acid theory to estimate the basicity index of the melt (BI). This BI approach appears to be effective in predicting formation of garnet or YDS as main secondary reaction phases based on melt chemistry.

4.1 Experimental Approach

4.1.1 TBC Deposition

Yttria-zirconia samples with a nominal composition of 65 wt. % Y_2O_3 and rest ZrO_2 (65YZ) were prepared by means of electron beam physical vapor deposition (EB-PVD) on top of 1 mm thick Al_2O_3 substrates. The evaporation was performed using a single ingot source with a nominal yttria-zirconia composition as specified above. The substrates were selected to allow higher temperature infiltration testing (1250 °C or higher) where Ni-based superalloy substrates would not withstand for longer time periods (up to 50 h). Additionally, GZO were also prepared

by means of EB-PVD on top of alumina substrates for complementary experiments. The deposition parameters and microstructural features for both samples are specified in **Table 4.1**.

Table 4.1: Summary of deposition parameters and microstructural features for the as coated EN-PVD coatings.

Coating	Thickness (µm)	RPM	Substrate Temp. (°C)	Chamber Press. (mbar)	Porosity[4] (%)	Feather arm length (µm)	Column width (µm)	Columnar gap width (µm)
65YZ	92-100	12	950	6×10^{-3}	29.7 ±2.5	3.7 ±0.6	6.1 ±1.8	0.8 ±0.4
GZO	330-340	12	1000	6×10^{-3}	23.2 ±1.4	3.7 ±1.5	15.6 ±1.0	1.7 ±1.3

4.1.2 CMAS/VA Sources

The summary of the used CMAS/VA compositions is given in **Table 4.2**. The synthesized CMAS sources have been used extensively in a large variety of studies and are commonly referred as CMAS 1, CMAS 2 and UCSB [26, 27, 32, 99, 100, 111, 114]. The CMAS 1 chemical composition was obtained by screening of real engine hardware which was operated in middle-eastern countries, its production method is specified elsewhere [99]. The CMAS 2 compound essentially represents CMAS 1 with extra CaO [99]. UCSB CMAS represents a widely used CMAS standard compound first generated by studies of the University of California at Santa Barbara (UCSB) [96] and its production method is specified elsewhere [27]. The volcanic ash sources were collected from volcanic ash plumes events from the Eyjafjallajökull volcano located in Iceland (ICE), the Nevado de Colima Volcano located in central-pacific Mexico (COL) and the Popocatépetl volcano located in central Mexico (Popo). These volcanos represent very active volcanos which are located in highly transited air traffic corridors. A schematic summary of their chemical composition is given in **Figure 4.1**.

Table 4.2: Summary of CMAS/VA sources including basicity index (BI) and Si:Ca ratios.

Source	ID	Melt Composition[5]	Melting Onset (°C)	BI	Si:Ca
CMAS 1	CMAS 1	$C_{22}M_{11}A_{20}S_{38}F_8T_1$	1243-1250	1.4	1.7

[4] Determined by imaging software Image J

[5] Composition is provided in single cation mol % basis which is abbreviated by the first letter of the cation such as: C= CaO, M=MgO, A=AlO1.5, S=SiO_2, F=FeO, T=TiO_2 and L=sum of $NaO_{0.5}$ and $KO_{0.5}$

CMAS 2	CMAS 2	$C_{28}M_{10}A_{18}S_{35}F_7T_1$	1215-1225	1.7	1.3
UCSB CMAS	UCSB	$C_{33}M_9A_{13}S_{45}$	1233-1249 [33]	1.1	1.4
Eyjafjallajökull VA	ICE	$C_{11}M_6A_{13}S_{45}F_{16}T_4L_5$	1060-1150	1.0	4.0
Colima VA	COL	$C_5A_8S_{69}F_3T_1L_{14}$ (M<0.5 %)	900-1060	0.3	13.8
Popocatepetl VA	Popo	$A_6S_{59}F_7T_1L_{26}$ (C&M<0.5%)	N/A	0.4	197.0

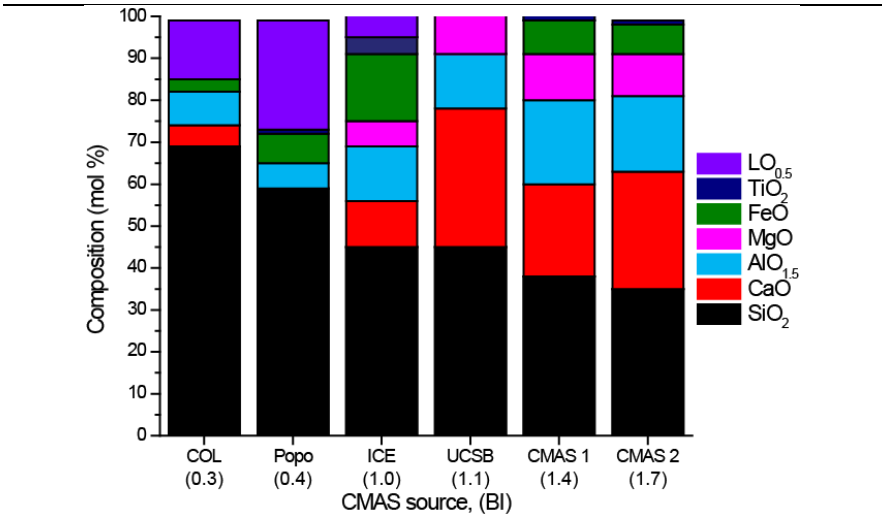

Figure 4.1: Graphical representation of CMAS/VA chemical composition.

4.1.3 Infiltration Experiments

The infiltration experiments were carried out by depositing the pulverized CMAS/VA mixed with distilled water compound on top of the TBC coated sample in the amount of 20 mg/cm^2. The heat treatments were performed in two sets. The first one (air quenched) was done using a cyclic furnace held isothermally at 1250 °C for 5 min to 50 h followed by rapid air cooling (using extra fans) to room temperature with a cooling rate of 18K/sec average. The second set was performed using a box furnace with a heating rate of 10 K/min followed by isothermal heating for 5 and 50 h finalizing with furnace cooling at 10 K/min (slow cooled). The heat treatment used in this case was at 1250 and 1300 °C.

4.1.4 Characterization Techniques

4.1.4.1 Microscopy Analysis

After infiltration tests, the samples were mounted in a low viscosity carbon-based epoxy (Gatan G2) and cut in cross-sections using a high-speed diamond saw. The cross-sectioned samples were mounted in a conductive epoxy and polished using standard metallographic techniques to a 0.05 μm surface finish. Scanning electron microscopy (SEM) was performed for the samples using a DSM Ultra 55 (Carl Zeiss NTS, Wetzlar, Germany) SEM microscope. The microscope was equipped with an energy dispersive X-Ray spectroscopy (EDS) system (Inca, Oxford Instruments Abingdon, UK) which was used to determine compositions of the crystalline phases and microstructural analysis. Focused ion beam (FIB) assisted analytical transmission electron microscopy (TEM) for phase identification was done using a Strata 205 FIB machine and a Tecnai F30 TEM-STEM utilizing a field-emission gun (FEI Inc., Eindhoven, Netherlands).

4.1.4.1 XRD Analysis

Additional phase identification was done via X-ray diffraction (XRD) of synthesized yttria-zirconia powders with compositions of $65YO_{1.5}$ and CMAS/VA power mixtures as specified in **Chapter 3**. The powders were mixed in a mortar with ethanol for 1 hour and heat treated via air cooling method for 10 hours on top of a Pt foil. Then, the heat-treated powder mixture was mechanically removed from the Pt foil and pulverized in a mortar to get a fine powder for XRD analysis. The XRD measurements were carried out using a Si single crystal holder and a Siemens D5000 diffractometer equipped with a CuKα radiation source with a secondary graphite monochromator (EVA/Topas 4.2 software package, Bruker AXS, Karlsruhe, Germany). Additionally, in-situ high-temperature XRD was performed using a Bruker D8-Advance equipment to identify the evolution of the garnet phase for the CMAS 1 65YZ interactions at the early infiltration stages. For this experiment an as coated sample with the CMAS 1 deposit on top was used for analysis (the same as for infiltration experiment approach). The CMAS deposited TBC coating was placed on top of a 1 mm thick Pt strip heating source. The sample was rapidly

heated up to 1250 °C with a ramp rate of 200 K/min. After 2 min of temperature equilibration, the XRD measurement was performed within 5 min. One additional measurement was performed without changing sample increasing the temperature at 1300 °C to study phase formation during the high-temperature regime.

4.2 Results

4.2.1 Microstructure and Composition of As Coated TBCs

The SEM images for the as coated 65YZ EB-PVD coatings in both cross-sectional and top view are shown in **Figure 4.2**. The coatings exhibited a parallel columnar microstructure which is a characteristic property of EB-PVD deposition method similar to that of standard YSZ coatings. The overall porosity was measured using an imaging software (Image J) on a cross-sectional view of the coatings giving porosity values of 29.7 ±2.5 and 23.2 ±1.4 for 65YZ and GZO respectively. The thickness of the samples was measured in ranges of 92-100 µm 330 to 340 µm for GZO. The information summary of the microstructural features for the produced coatings is given in **Table 4.1**.

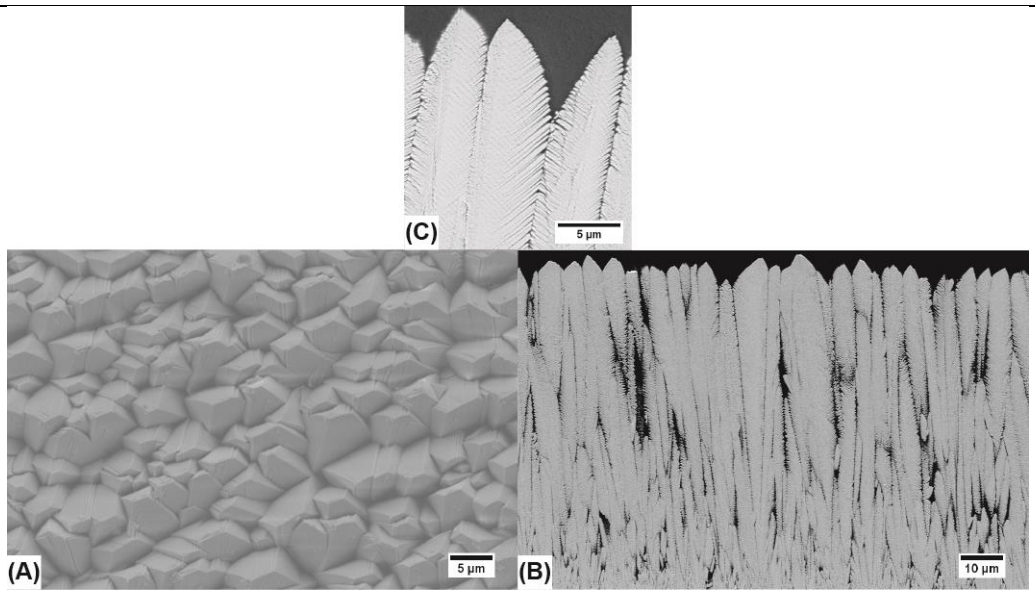

Figure 4.2: SEM images for the as coated 65YZ samples for the (A) top view, (B) cross-section and (C) high magnification cross-section at the top showing the microstructural features.

The intra-columnar gaps (feather arms) generated in the 65YZ samples appear to be more pronounced (3.7 µm long) when compared with standard 7YSZ coatings (3 µm long max.) produced under similar deposition parameters [56, 57]. The surface view of the 65YZ samples exhibits a pyramidal arrangement of columns distributed asymmetrically. The columns and columnar gaps had an overall width of 6.1 and 0.8 µm respectively. The chemical composition of the 65YZ columns was measured using EDS analysis on a TEM lamella. The composition was consistent at 65 wt. % Y_2O_3-ZrO_2 balanced (about 67 to 70 $YO_{1.5}$ mol. %) with the overall composition of the ingot evaporation source. The diffraction patterns of the as coated 65YZ samples (shown in **Figure 4.3**) confirmed a lanthanide yttia cubic type homogeneous structure with zirconia in solid solution. The samples exhibited a planar arrangement along the [100] similar to that of MOCVD yttria rich-zirconia and pure yttria coatings produced by Eils et al. [27].

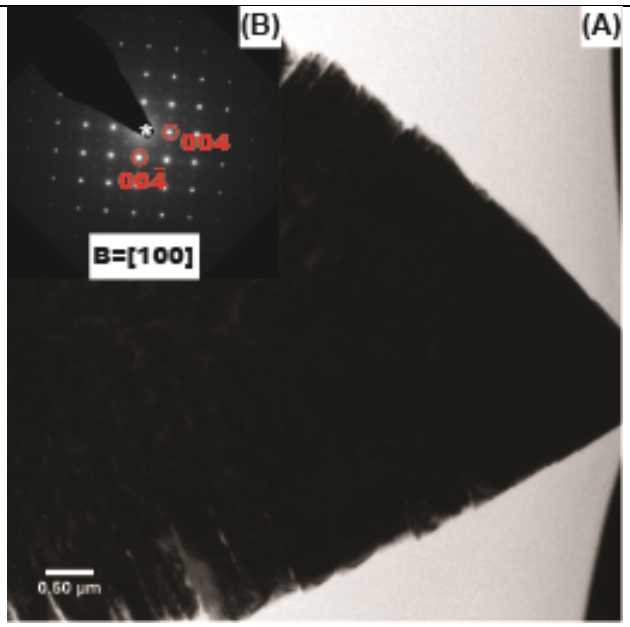

Figure 4.3: (A) TEM dark field image of the as coated 65YZ coating at the top section. (B) SAED pattern showing the cubic yttria base phase.

The as coated GZO cross-section and top view images are shown in **Figure 4.4.** They also showed a similar pyramidal arrangement as seen in their 65YZ. The average columnar gap widths were 15.6 and 1.7 µm respectively. The samples exhibited the standard pyrochlore cubic phase for $Gd_2Zr_2O_7$ confirmed by XRD (not shown here).

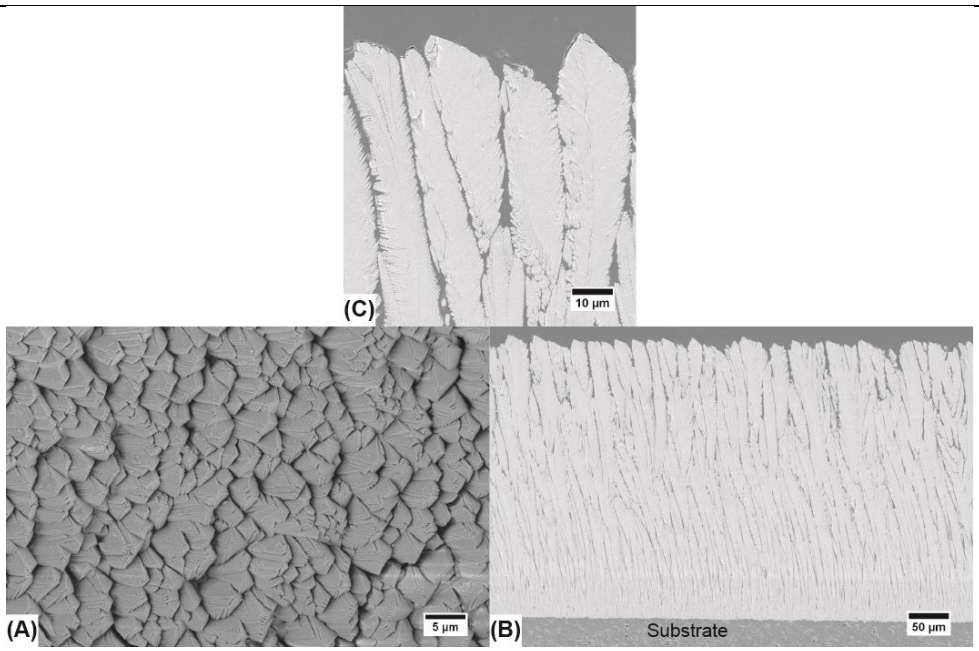

Figure 4.4: SEM image for the as coated GZO samples in the (A) top view and (B) cross-section. (C) Shows a higher magnification cross-section view of the upper coating area showing its microstructural features.

4.2.2 Phase Identification Using XRD Analysis of $65YO_{1.5}$ Powders and CMAS/VA Interactions

The reaction products that were produced in the reactions between CMAS/VA and $65YO_{1.5}$ powder mixtures (after 10h at 1250°C) were analyzed by XRD as shown in **Figure 4.5**. All reactions exhibited fluorite (F) and apatite phases (A) as common phases which confirms that these phases are the primary reaction (reactive crystallization) products produced upon interaction of the CMAS source with the 65YZ TBC [11]. The UCSB CMAS exhibited the highest intensity peaks corresponding to apatite formation whereas the Popo and Colima (COL) VA exhibited the least intensity peaks of apatite. This behavior suggests that apatite formation is strongly dependent of Ca content in the melt (more apatite with higher Ca content) as also reported in literature [120]. It appears that no garnet formation (G) was produced for the COL and Popo VA since no significant peak was found. Instead, yttrium disilicate (YDS) peaks are distinguished for these phases. Garnet peaks are formed for the other mixtures but CMAS 1 and CMAS 2 exhibited the highest peak intensity for this phase. Additionally, the zirconolite peak (Z) was only identified for the case of

the Iceland VA (ICE) as expected due to its high Ti content (Previously discussed in **Chapter 3**). Finally, small traces of intrinsic crystallization phases from the glass were found as anorthite (A) for CMAS 1. The kinetics of reaction will be explained on the basis of the interactions with the TBCs in the discussion section. The summary of the produced reaction products with their respective theoretical formula is given in **Table 4.3**.

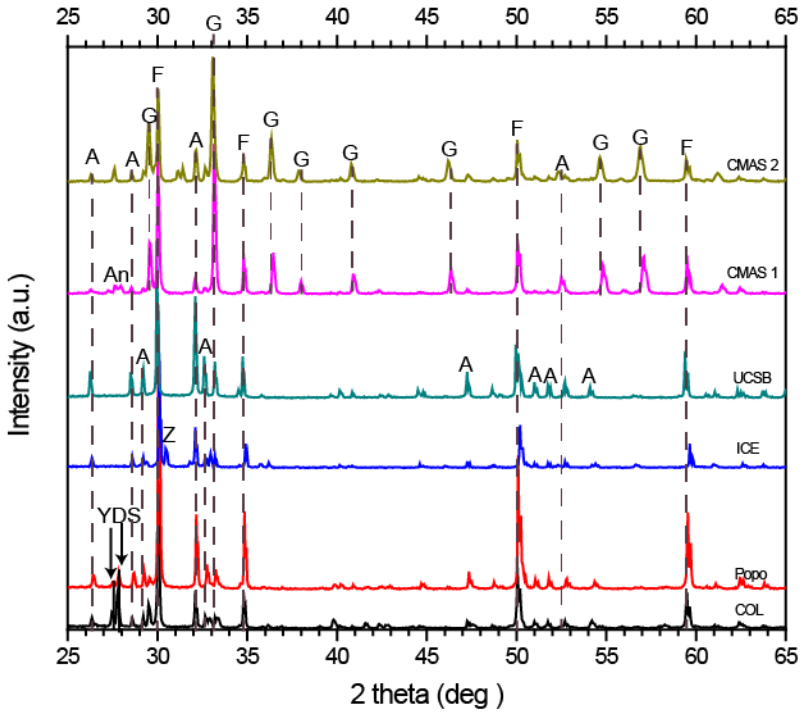

Figure 4.5: XRD plot for the CMAS/VA powder mixtures with $65YO_{1.5}$ for 10 h at 1250 °C after air quenching. Only the main characteristic peaks are shown.

Table 4.3: Summary of reaction products found for all CMAS/VA reactions for this study.

Phase	ID	Theoretical formula	Type of reaction
Anorthite	An	$CaAl_2Si_2O_8$	Intrinsic
Fluorite	F	$(RE,Zr,Ca)O_{1.x}$	Re-precipitation
Apatite	A	$(RE,Ca)_4(RE,Zr)_6(SiO_4)_6O_2$	Reactive crystallization

Garnet	G	$(RE,Zr,Ca)_3(Mg,Al,Fe,Ti,Zr)_2(Si,Al,Fe)_3O_{12}$	Reactive crystallization
Zirconolite	Z	$(Ca,RE,Zr)_2(Fe,Ti,Al,Mg)_2O_7$	Reactive crystallization
Zircon	Zi	$ZrSiO_4$	Reactive crystallization

4.2.3 CMAS/VA Interaction for Air Quenched Samples

4.2.3.1 Infiltration Attack under fast cooling conditions

The cross-sectional image of the infiltrated CMAS 1 sample after 50 h at 1250 °C is shown in **Figure 4.6a** containing its respective Ca and Si elemental mapping used for determination of infiltration depth. These mappings clearly show a discontinuous infiltration due to the variation of columnar gaps in width. This behavior was also distinguished in previous experiments due to large columnar gaps which exhibited deeper infiltration [26]. An overall infiltration zone is delimited up to the dotted white lines in the Si and Ca mapping to evaluate the infiltration depth and was measured as 58 µm ±5. This represents a vast improvement in comparison with the 155 µm infiltration that CMAS 1 produced in a standard YSZ coating after 30 sec of infiltration at 1250 °C [31]. Besides, the microstructural improvement achieved via single source evaporation compared with dual source (jumping beam evaporation) has also shown an enhanced resistance (65 µm infiltration depth after 20 h at 1250 °C with CMAS 1) [26]. **Figure 4.6b** shows a high magnification of a deeply infiltrated columnar gap delimited with a red rectangle in **4.6a**. The dashed black rectangle shows a sealed columnar gap with a deep infiltration which was used to obtained a TEM lamella for subsequent analysis in **Figure 4.8**.

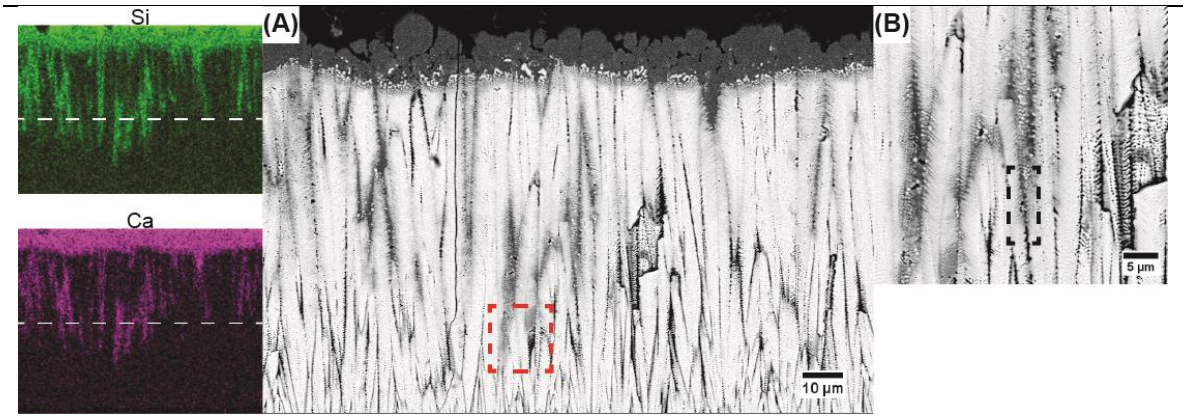

Figure 4.6: (A) Cross-section SEM image of the CMAS 1 sample infiltrated for 50 h at 1250 °C. The Si and Ca elemental mapping for estimation of infiltration are shown on the left. (B) High magnification image of a deeply infiltrated columnar gap..

Furthermore, the infiltration kinetics (depth vs time) of all the studied CMAS/VA compositions on 65YZ is plotted in **Figure 4.7**. The sample that exhibited the deepest infiltration (~58 µm) after 50 h was CMAS 1 followed by ICE (56 µm), CMAS 2 (53 µm), UCSB (51 µm), Popo (51 µm) and COL (49 µm). The appendix A shows the rest of the 50 h infiltrated samples for all the CMAS/VA sources. It is distinguished that the infiltration clearly progresses continuously from the 5 min testing to 5 h in all cases and then starts to equilibrate by showing no significant infiltration depth changes up to 50 h. Additional TEM studies are shown in **Figure 4.8** which were performed on the CMAS 1 infiltrated sample after 5 h. The TEM lamella was obtained from an infiltrated columnar gap located at the area where the deepest infiltration was found (as explained before in **Figure 4.6b**).

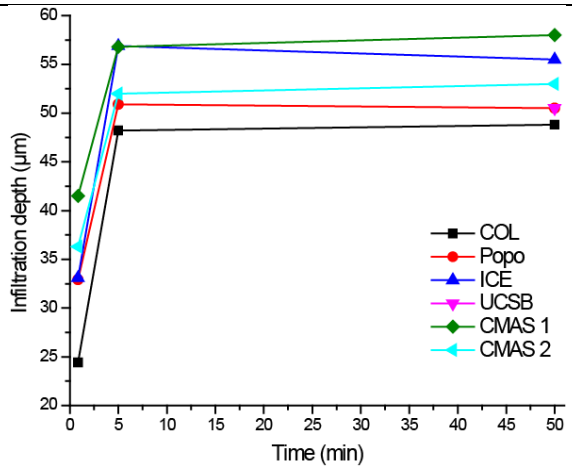

Figure 4.7: Infiltration depth vs time for the air quenched CMAS/VA samples tested at 1250 °C.

The reaction products found in between two feather arms (from the TEM studies) indicate the presence of completely crystallized products with no residual glass left since all the analyzed area exhibited diffraction contrast. The found products were identified as garnet and fluorite in **Figures 4.8b** and **c** respectively. The apatite crystals were found in very small quantities (**Figure 4.8d**) compared to the enlarged garnet phase identified from the Fe mapping. The apatite crystals appear to be consumed by the garnet phase in Figure 4.8d, this was also seen for the ICE samples in the previous chapter. These crystalline products that are forming in between columnar gaps block or completely arrest (reaction) the molten glass after 5h. For this reason, no further infiltration is seen after 5 hours since the glass was completely reacted and no more liquid phase is present.

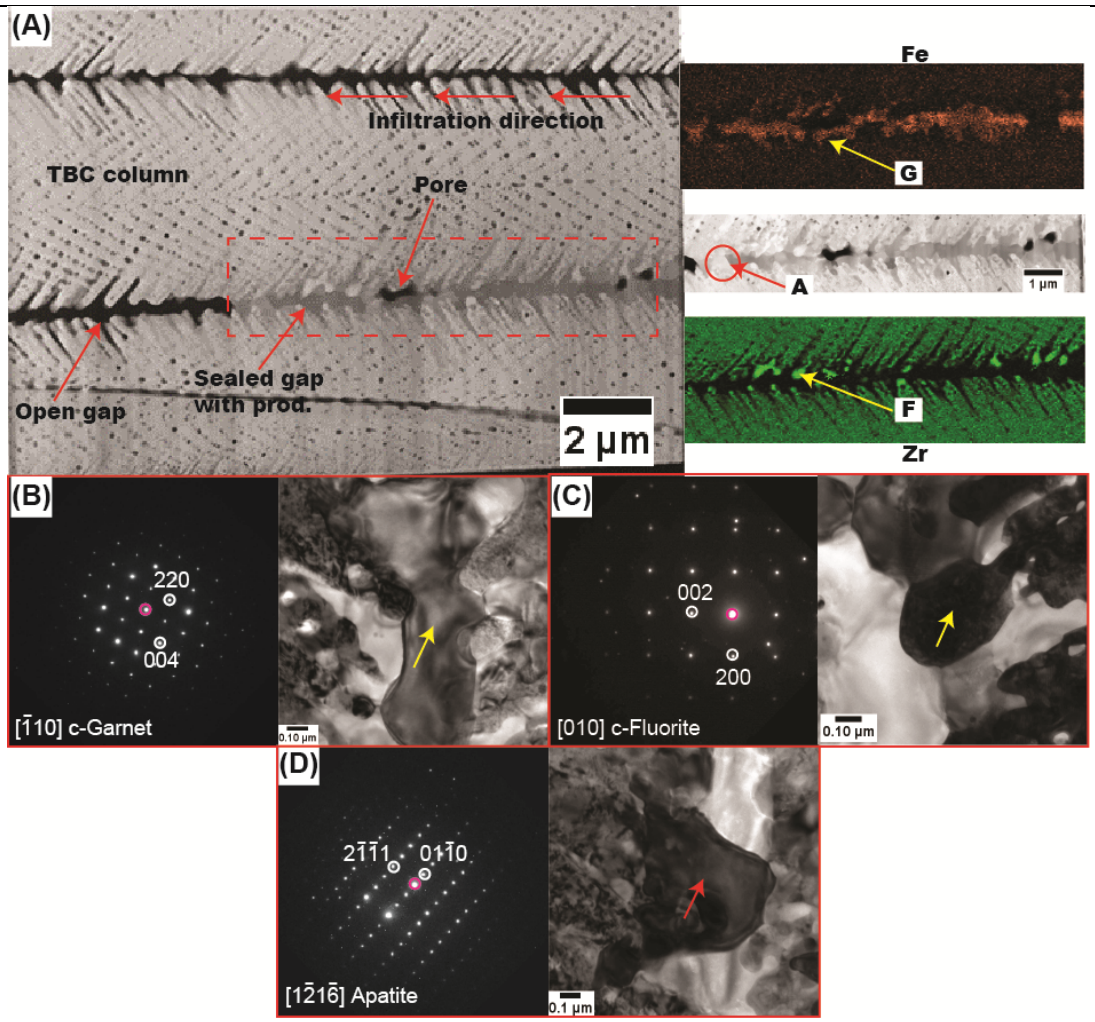

Figure 4.8: TEM image (A) of the analyzed area obtained from the bottom part of the infiltrated columnar gap and higher magnification image (top right side) from the dotted rectangle with included Fe and Zr mapping. (B) SAED pattern identifying the cubic garnet structure with its respective bright field TEM image. (C) SAED pattern identifying the cubic fluorite structure with its respective bright field TEM image. (D) SAED pattern identifying the hexagonal apatite structure with its respective bright field TEM image.

4.2.3.2 CMAS/VA Reaction Layer Behavior

The reaction layer that has formed on 65YZ for different CMAS/VA compositions is shown in **Figure 4.9** within the time intervals of 5 min, 5h and50 h. These time intervals were selected to study if there is any change in reaction products from the initial infiltration stages (5 min) to long term infiltrations (5 and 50 h). The formed reaction phases were identified by

comparing the EDS compositions with the XRD studies, TEM for CMAS 1 case and phases reported from literature. The XRD identified phases matched the infiltration experiments. The only exception was the ICE VA which shows formation of YDS after 50 h which was not found in the 10 h XRD experiments. However, this large YDS crystal was the only evidence of YDS crystallization found throughout the sample compared to all the other reaction products which were found in abundance all over the reaction zone. Additional formation of YDS is only seen in the other VAs as expected from the XRD results. The YDS crystals seem to grow at the expense of the apatite phase from the constant interaction with the Si rich glass. This phase was found in previous studies with interactions with Si rich VA only collected from the Sakurajima volcano located in southern Japan [26] and it was also found in interactions with Si rich CMAS sources in literature [120]. The fluorite formation (F) appears to be suppressed for the CMAS 1 and 2 samples since it is clearly seen from the figure how the VAs produce larger amount of globular fluorite particles through the time progression compared to the CMAS 1 and 2 samples. Furthermore, the apatite formation for all samples at the initial 5 min infiltration is concentrated at the columnar gaps and small localized pockets such as feather arms. Only the ICE and UCSB samples exhibited more pronounced faceted apatite crystals (see appendix A for UCSB figure after 50 h) which come out of the reaction zone into the unreacted glass deposit. As expected, the zirconolite phase (Z) was only found in the ICE case due to its high Ti content (4 times higher than the other sources) as explained in the previous chapter. Finally, an exclusive garnet phase formation was found at the reaction zone only for the BI>1 source. Its presence in the reaction layer seems to increase with respect to BI from being found as localized enlarged globular particles (ICE and UCSB) to a complete uniform product layer (CMAS 1 & 2) taking over the reaction front.

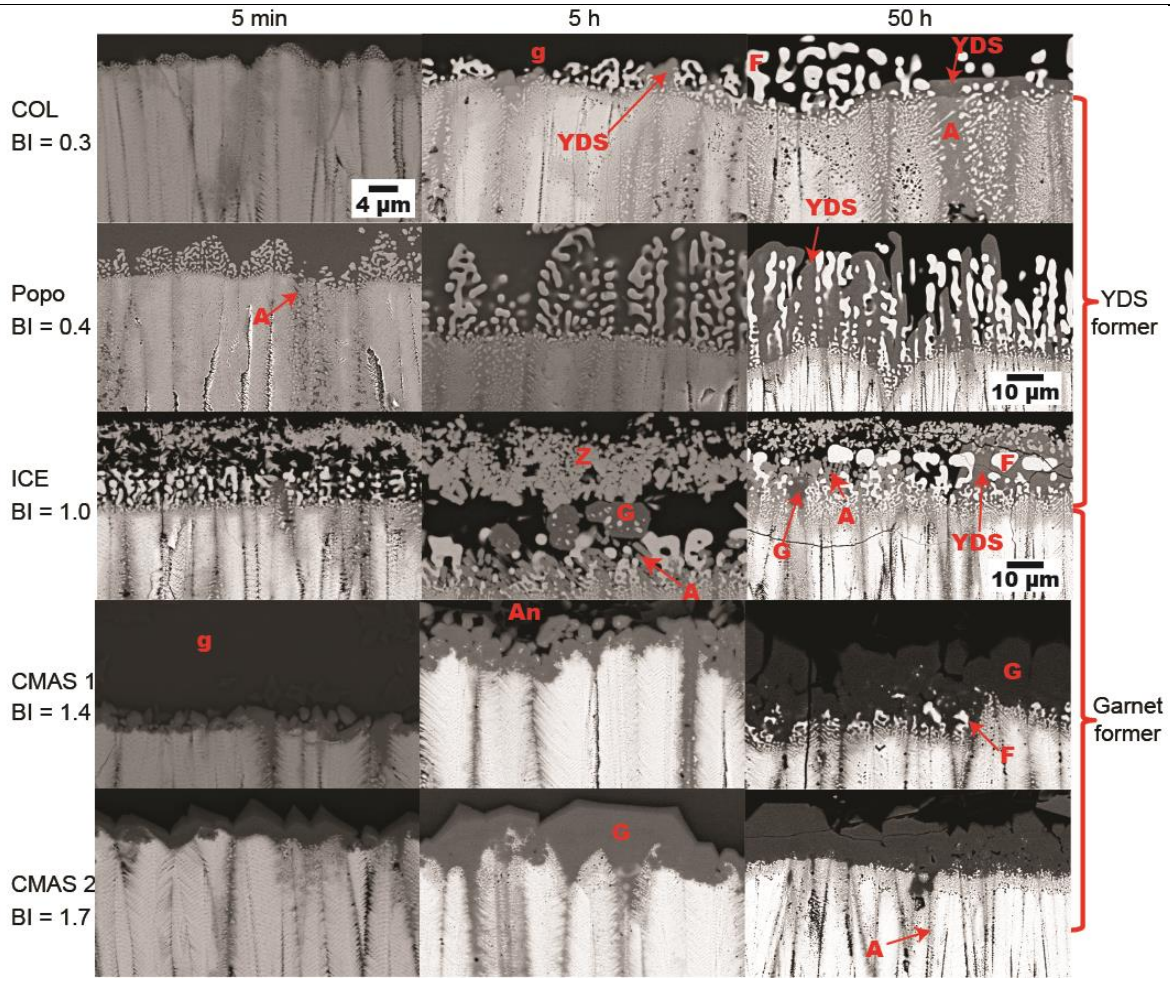

Figure 4.9: SEM cross-sectional images of the reaction layer with respect to time for all tested CMAS/VA samples at 1250 °C under air quenching. Note that only the Popo and ICE case after 50 h have a different scale due to its thicker reaction layer produced.

It is evident from the exhibited reaction zone among all the samples that a steady progressive growth in the reaction layer is distinguished with respect to time. This reaction layer progression is plotted for all the studied cases as shown in **Figure 4.10** where the highest reaction layer growth (after 50 h) was produced by the Popo VA by reaching up to 30 µm layer. It is followed then by the ICE (28.5 µm), CMAS 2 (17.5 µm), CMAS 1(16.4 µm) and COL (11.8 µm). The plot shows how the Popo VA is the only sample that shows a large increase in reaction layer thickness after 50 since at the 5 min and 5 h the ICE VA exhibited the thickest reaction layer and then it is surpassed by the Popo VA after 50 h. The effects of composition on the reaction layer

growth and infiltration behavior will be assessed in detail in the discussion section. More elaborated results on each composition is given below.

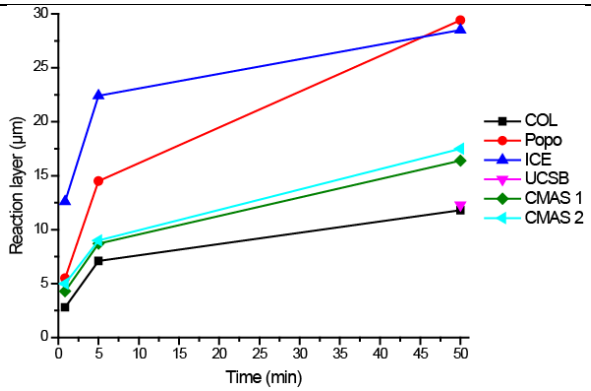

Figure 4.10: Reaction layer growth with respect to time for all the tested CMAS/VA samples at 1250 °C air quenched.

4.2.3.3 CMAS 1 Reaction

The reaction layer for CMAS 1/65YZ sample which is infiltrated for 5 min and 50 h is shown in **Figure 4.11**. The yellow arrow indicates the sealed columnar gap by the reaction products after 5 min which were found to be a mixture of apatite and garnet crystals as previously confirmed from TEM analysis. It is seen from the large columnar gap in **4.11a** that the garnet phase is progressively forming in a columnar gap opening larger than 1.5 µm and slowly crystallizing the left-over unreacted glass. The apatite phase is seen in small amounts located in gaps having thicknesses lower than 1 µm. Enlarged rectangular shaped anorthite crystals are seen uniformly embedded in the unreacted glass on top of the reaction layer as sign of intrinsic crystallization of the glass. No significant fluorite formation is seen at the reaction and was mostly found in the large gaps. The garnet phase ~ 4 µm thick has formed uniformly on top of the coating at the reaction front interface between the coating and glass deposit after 5 minutes. Consequently, the garnet layer thickness increases to 16.4 µm ±2.2 after 50 h. The globular fluorite particles are distinguished after 50 h especially localized between the garnet layer and the unreacted coating in combination with apatite crystals. This zone shows a thin layer of uniformly distributed fluorite

and apatite particles (A&F) with a thickness of about 4 µm as seen in **4.11b** delimited within the red dotted lines. No significant change in morphology is seen for the anorthite crystals which are still embedded in the unreacted left-over glass on top of the reaction layer (nor clearly seen in the figure due to image contrast to show the A&F layer). The columnar gaps still exhibit a mixture of garnet (in majority) and apatite crystals with minimal fluorite formation. Additionally, the summary of chemical composition for all the reaction products at the reaction layer including the unreacted glass (g) is shown in **Table 4.4** for CMAS 1 after 5 min and 50 h.

Table 4.4: Chemical composition summary for the reaction products located at the reaction zone for CMAS 1 infiltrated at 1250 °C for 5 min and 50 h. (unless specified in the table the chemical composition deviation is less than 1 mol %).

Time	**ID**	**Chemical composition (mol %)**							
		MgO	$AlO_{1.5}$	SiO_2	CaO	TiO_2	FeO	$YO_{1.5}$	ZrO_2
5 min	An	1.8	30.8	40.8	23.3	0.2	3.0	0.0	0.0
50 h	An	0.5	35.1	40.3	22.1	0.0	1.7	0.0	0.2
5 min	G	7.7	8.8	26.6 ±4.5	22.2 ±3.7	2.5	15.1	11.8 ±7.4	5.3 ±2.2
50 h	G	7.7	11.7	23.8	19.6	1.7	17.3	16.7	1.6 ±1.4
5 min	A	4.9 ±1.5	6.8	18.8 ±1.6	11.7 ±1.9	1.3 ±0.4	5.2 ±1.1	35.3 ±5.6	16.1 ±2.7
50 h	A	1.4	1.9	30.1 ±2.3	15.0	-	0.4	42.9 ±1.5	8.4
5 min	F	4.0	5.7	10.4 ±4.3	8.8 ±2.9	1.8	5.3	19.0	45.1 ±8.5
50 h	F	2.9	4.3	6.6	7.5	1.4	6.1	17.7	53.3
5 min	g	8.8	18.3 ±1.8	37.4 ±2.7	24.3	1.3	9.0 ±2.9	0.4	0.4
50 h	g	13.1 ±4.0	12.7	37.5 ±1.4	23.6 ±1.4	1.7	6.3	2.4 ±2.1	2.7

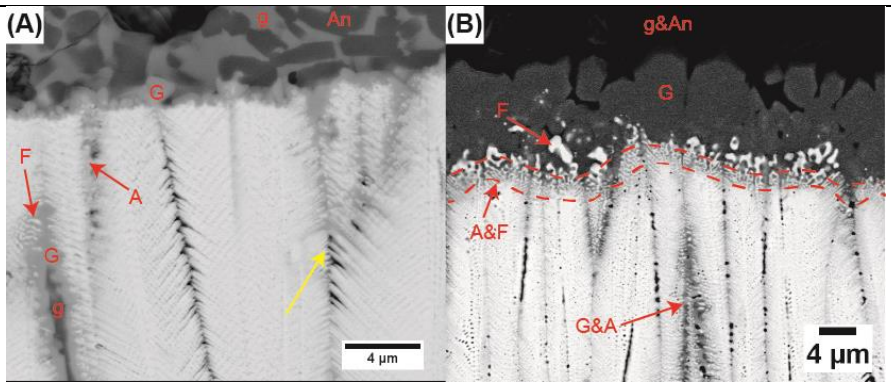

Figure 4.11: SEM cross-sectional image of the reaction layer formed on CMAS 1 (air quenched samples) infiltrated sample at 1250 °C for (A) 5 min and (B) 50 h.

4.2.3.4 CMAS 2 Reaction

The reaction produced for the CMAS 2/65YZ sample which is infiltrated for 5 min and 50 h is shown in **Figure 4.12**. The 5 min reaction layer exhibits a similar scenario as the CMAS 1 case except the intrinsic glass crystallization phases. The garnet layer still exhibits a uniform formation with a thickness of ~ 5 µm slightly higher than the CMAS 1 case (4 µm max.). The higher magnification image of a large sealed columnar gap (**4.12b**) shows the formation of majorly garnet which is crystallizing the glass and small contents of apatite and fluorite. The apatite phase appears to be engulfed by the large garnet particle as also seen for the CMAS 1 case and for the ICE VA in the previous chapter. Furthermore, less unreacted glass is seen in the columnar gap of about 2 µm width compared to the CMAS 1 case. From this result it is apparent that the higher Ca content in the CMAS 2 promotes higher garnet formation/growth as seen from the columnar gap and the reaction layer. After 50 h the garnet phase exhibits a significant increase in thickness (17.5 µm±2.6) compared to the 5 min case. Additionally, a dark contrast color is distinguished on top of the garnet layer at the interface with the unreacted glass reservoir (marked with a yellow arrow in **4.12c**). EDS analysis revealed a composition gradient at this interface with respect to the core garnet composition. The top layer revealed lower $YO_{1.5}$ (2 mol % less) and FeO (4.5 mol % less) contents and higher CaO (1 mol % more) and SiO_2 (2.5 mol % more) contents compared to the

core garnet. The same behavior was found for the CMAS 1 garnet as well. This compositional gradient could be indication of a diffusion-controlled growth for the garnet layer. Furthermore, apatite and garnet layer were formed with a slight increase in thickness compared (about 5 μm) to the CMAS 1 case after 50h. The CMAS 2 sample formed a larger amount of apatite crystals in general (at the A&F layer and the columnar gaps) compared to the CMAS 1 case. This is consistent with the increased Ca content in the glass for CMAS 2, more apatite formation is expected. The summary of chemical compositions for the reaction products at the reaction layer for 5 min and 50 h is given in **Table 4.5**.

Table 4.5: Chemical composition summary for the reaction products located at the reaction zone for CMAS 2 infiltrated at 1250 °C for 5 min and 50 h. (unless specified in the table the chemical composition deviation is less than 1 mol %).

Time	**ID**	**Composition (mol %)**							
		MgO	$AlO_{1.5}$	SiO_2	CaO	TiO_2	FeO	$YO_{1.5}$	ZrO_2
5 min	G	5.3	4.3	29.3 ±2.0	31.7	3.3	17.9 ±1.4	5.4 ±2.3	2.8
50 h	G	8.5 ±1.6	5.4	27.8 ±2.0	25.2 ±2.2	1.8	14.2 ±3.1	13.4 ±2.3	3.7 ±3.3
5 min	A	1.1	1.2	26.7 ±1.9	19.7 ±1.9	0.3	1.3 ±1.3	38.0 ±2.2	11.7
50 h	A	1.7	1.8	29.5	16.5 ±5.1	-	2.1	40.3 ±2.4	8.1
5 min	F	-	-	-	-	-	-	-	-
50 h	F	3.1	2.3	13.2	12.7	1.4	2.4	24.4	40.6
5 min	g	8.4	7.1	36.9	34.8	1.4	8.0	2.0	1.4
50 h	g	8.9	9.4 ±3.5	39.8 ±6.6	30.9 ±5.3	0.9	4.6 ±4.5	3.3 ±2.8	2.0

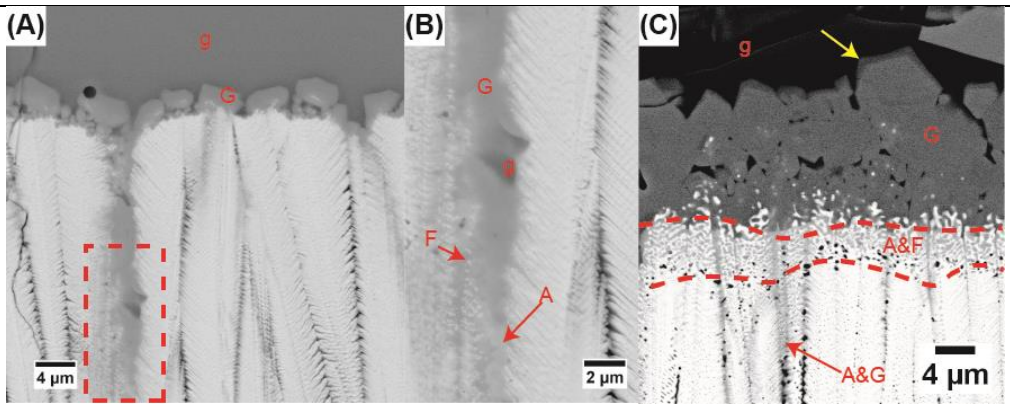

Figure 4.12: SEM cross-sectional image of the reaction layer formed on CMAS 2 (air quenched samples) infiltrated sample at 1250 °C for (A) 5 min. (B) high magnification image of the area delimited in the dotted red rectangle in (A). (C) Reaction layer zone for 50 h.

4.2.3.4 UCSB Reaction

The reaction for the UCSB/65YZ sample is only shown after 50 h at 1250 °C in **Figure 4.13**. Here the reaction exhibits a very different morphology compared to the other CMAS samples. A significantly less amount of garnet particles is seen in this case. The garnet phase still appears to be consuming the apatite crystals as described for the other CMAS cases. The apatite phase is primarily the main reaction product found in this reaction layer. It is exhibited as enlarged faceted crystals which protrude outwards towards the glass reservoir. No formation of intrinsic glass crystallization is seen in this phase as well as very thin layer of unreacted glass was found for this CMAS compound. Larger fluorite crystals are produced in this reaction as compared to the other CMAS compounds. The reactions products found at the columnar gaps are primarily apatite and fluorite with small localized garnet products. The summary of chemical composition for the reaction products is shown in **Table 4.6.** It is interesting to see that the garnet phase still has all available cations in its composition (Mg, Al, Si, Ca, Y and Zr). In contrary, in the CMAS 1 and 2 cases, the garnet phase has all the available cations but a significant Fe enrichment is seen (more than 14 mol %). From these results it could be concluded that the garnet phase appears to nucleate at expense of the apatite (consuming its Ca, Si, Y and Zr) but sufficient amounts of Mg and Al are required to promote its growth. Furthermore, as seen from the Fe carrying CMAS 1 and 2 sources,

Fe is a key element in addition to Al and Mg for the growth of a different type of garnet phase. More additional analysis on the garnet formation is provided in the discussion section.

Table 4.6: Chemical composition summary for the reaction products located at the reaction zone for the UCSB infiltrated at 1250 °C for 50 h. (unless specified in the table the chemical composition deviation is less than 1 mol %).

Time	ID	Composition (mol %)					
		MgO	$AlO_{1.5}$	SiO_2	CaO	$YO_{1.5}$	ZrO_2
50 h	G	11.4	16.5	31.2	22.5	18.4	0.0
50 h	A	0.4	0.7	33.8	18.8	40.9	5.4
50 h	F	0.0	0.0	0.0	3.9	24.7	71.3
50 h	g	7.5	13.6	36.7	34.0	6.1 ±1.5	2.1

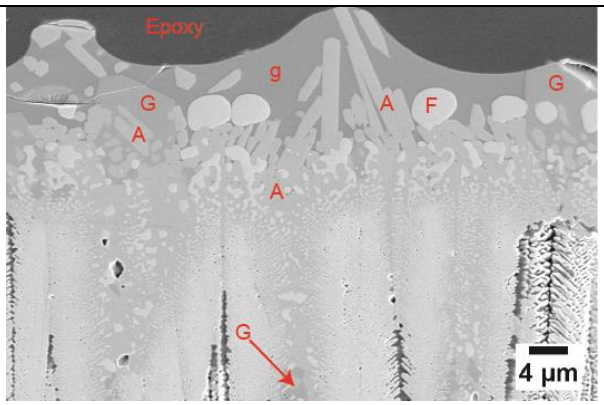

Figure 4.13: SEM cross-sectional image of the reaction layer formed on UCSB CMAS (air quenched) infiltrated sample at 1250 °C for 50 h.

4.2.3.5 ICE Reaction

The ICE/65YZ reaction is shown for 5 min and 50 h in **Figure 4.14**. The reaction sequences were found to be similar to that of the coatings produced by the jumping beam as shown in **Figure 3.7d.** In both cases zirconolite, fluorite, garnet, apatite phases were formed and a single YDS localized crystal was observed only after 50 h from the scanned zone which covered about 1 cm (see **Figure 4.8)**. Small dendrites are seen as small protrusions in interaction with the fluorite and zirconolite phases as seen in **Figure 3.7**. These phases also exhibited all available cations but could

not be identified with EDS analysis and TEM is needed for proper identification. It is believed that their nucleation would have been promoted during the cooling phase of the samples which is discussed in the next section for slow cooled tests. Thus, For the 50 h case sample in **4.14b** if the zirconolite phase is excluded, the reaction phase appears to be similar to the UCSB by showing the same localized garnet products with the reaction layer primarily made of the enlarged faceted apatite and globular fluorite phases. However, the ICE VA exhibits higher formation of fluorite crystals compared to the UCSB. The summary of composition for the formed reaction products is given in **Table 4.7**.

Table 4.7: Chemical composition summary for the reaction products located at the reaction zone for ICE infiltrated at 1250 °C for 5 min and 50 h. (unless specified in the table the chemical composition deviation is less than 1 mol %).

Time	ID	Composition (mol %)								
		LO0.5	MgO	AlO1.5	SiO2	CaO	TiO2	FeO	YO1.5	ZrO2
5 min	G	0.0	6.5	10.3 ±2.9	18.9 ±2.5	8.7	0.9	25.5 4.7	26.6 ±3.7	2.5 ±2.5
50 h	G	0.0	8.7 ±1.9	11.7 ±1.5	17.8 ±1.8	7.7	0.9	23.5 ±2.4	27.0	2.8 ±1.8
5 min	A	0.0	2.0	0.4	29.3 ±1.3	9.9	0.4	1.2 ±1.1	46.4 ±2.7	10.4 ±1.9
50 h	A	0.0	1.0	0.0	32.8 ±3.8	10.7 ±2.0	0.3	0.3	49.1 ±1.6	5.8 ±5.6
5 min	F	0.0	1.2	2.9	8.5	2.3	5.7	8.6 ±1.3	22.1	48.8 ±3.4
50 h	F	0.0	0.0	0.0	0.0	0.0	3.6	4.7	24.5	67.2
5 min	Z	0.0	1.4	3.4	4.6 ±3.3	2.3	20.4	20.9	21.0	25.9 ±3.2
50 h	Z	0.0	0.4	4.3	3.5	1.5	20.5 ±1.8	18.3 ±1.9	23.5	27.9 ±2.4
5 min	g	3.8	5.3	12.3	42.6	10.9 ±1.3	2.8	12.5 ±1.2	8.3 ±2.5	1.6 ±1.4
50 h	g	0.5	5.1	16.2	43.1 ±1.8	9.1	2.1	10.9	12.1	0.9 ±1.6
5 min	d	3.0	5.7	10.4	36.0	6.4	3.2	26.0	6.7	2.5
50 h	d	0.0	12.7	11.0	28.0	8.8	0.6	17.2	21.6	0.0
50 d	YDS	0.0	1.2	0.9	44.4 ±2.2	1.4	0.0	1.4	43.8	6.7 ±2.1

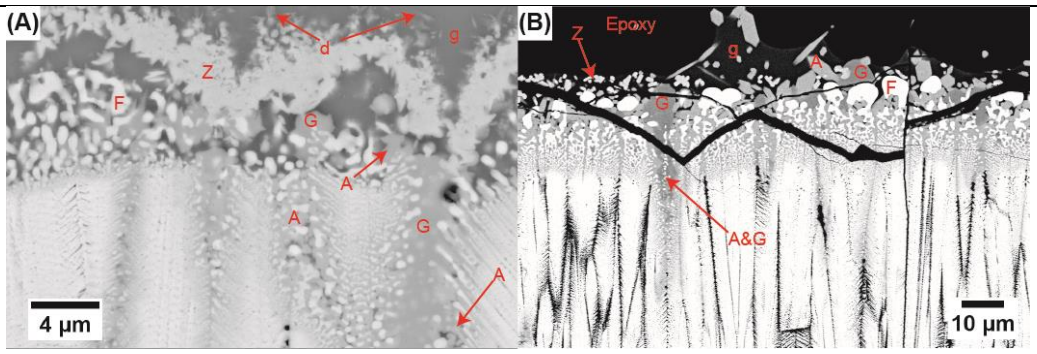

Figure 4.14: SEM cross-sectional image of the reaction layer formed on ICE VA (air quenched) infiltrated sample at 1250 °C for (A) 5 min and (B) 50 h.

4.2.3.6 Popo Reaction

The reaction with the Popo/65YZ is seen in **Figure 4.15** for 5 min and 50 h. The high magnification image **4.15a** shows the large coalesced fluorite particles embedded in the glass deposit. These particles were found to be swimming/floating on the molten glass up to 40 µm from the reaction interface and were evenly distributed throughout the glass. The high magnification image of the reaction zone (**4.14b**) shows quite different behavior compared to the ICE VA and the CMAS sources. The coating consumption by the glass leaving behind fluorite particles which follow the original faceted shape or foot print of the TBC column. No apatite presence is seen at these degraded column tips and it was only found in the columnar gaps interacting with unreacted glass and small fluorite globular particles. The apatite crystals have grown as facets perpendicularly to the opposite column which appears to be favorable for sealing the gap. It is seen how the feather arm features of TBC columns appear to vanish by being dissolved in the molten glass leaving globular shaped sharp fluorite particles. This increased dissolution behavior appears to be due to the very minimal CaO (very traceable in less than 1 mol %) and high SiO_2 (59 mol %) presence in the melt which requires higher amounts of $YO_{1.5}$ from the coating to be dissolved before the glass can be locally saturated to promote apatite formation. Additionally, at this early stage no signs of other reaction phases such as garnet or intrinsic crystallization were found for this reaction. In the 50 h infiltration case the coating microstructure has changed abruptly and

undergone the highest coating consumption of about 30 µm having large globular fluorite particles in interaction with pseudo-globular shaped YDS layer as reaction products. A thin apatite and fluorite mixed layer was found in between the YDS layer and the unreacted coating similar to the configuration of the CMAS 1-2 case, an additional complementary image of this layer for the Popo VA case is provided in the appendix A section. Additionally, the fluorite particles are seen to coalesce into bigger globular particles on the top zone of the glass reservoir (marked with yellow arrows in 4.15a and c). The embedded fluorite particles within the glass interact and a zircon phase is seen to nucleate out of the reaction. The zircon formation has been found for high Si bearing glasses and interactions with YSZ TBCs [98, 120, 140]. Among the studied compositions zircon formation was only observed in case of the Popo VA. These results show that the YDS and zircon phases require some extended heat treatment to form since they were only found after 5 h onwards in these studies, though, previous test with VA from Japan promoted YDS formation after 1 hour at 1250 °C [26]. The summary of chemical composition of the reaction products from the reaction zone is given in **Table 4.8**.

Table 4.8: Chemical composition summary for the reaction products located at the reaction zone for Popo infiltrated at 1250 °C for 5 min and 50 h. (unless specified in the table the chemical composition deviation is less than 1 mol %).

Time	**ID**	**Composition (mol %)**								
		$Na_{0.5}O$	MgO	$AlO_{1.5}$	SiO_2	CaO	TiO_2	FeO	$YO_{1.5}$	ZrO_2
5 h	YDS	0.0	2.0	0.3	43.7	1.5	0.0	1.0	41.5 ±1.9	9.8 ±4.7
50 h	YDS	0.0	1.8	0.5	47.0	1.7	0.0	0.4	43.3	5.3
5 min	A	0.9	3.4	4.1 ±1.6	33.4 ±1.8	8.6	0.0	2.2	36.5 ±5.4	11.0 ±1.1
50 h	A	0.0	2.2	0.0	32.7 ±1.8	7.4	0.0	0.0	51.8 ±1.5	5.9 ±3.4
5 min	F	0.6	2.8 ±1.4	4.7 ±2.4	14.7 ±10.1	2.7 ±2.0	0.5	3.4 ±2.0	13.8 ±3.8	56.8 ±23.3
50 h	F	0.0	0.0	0.0	0.0	0.0	0.0	2.2	23.9 ±1.3	73.8 ±1.3
5 h	Zi	0.0	0.0	1.7	49.8	0.8	0.0	0.0	0.0	47.7
50 h	Zi	0.0	0.0	0.0	48.9	0.0	0.0	0.4	0.0	50.7
5 min	g	4.1	7.1	14.3	49.7	8.3	0.5	6.7	7.0	2.4
50 h	g	5.1	5.4	18.2 ±1.6	52.8 ±2.1	7.5	0.4	4.8	4.3 ±3.8	1.4 ±1.3

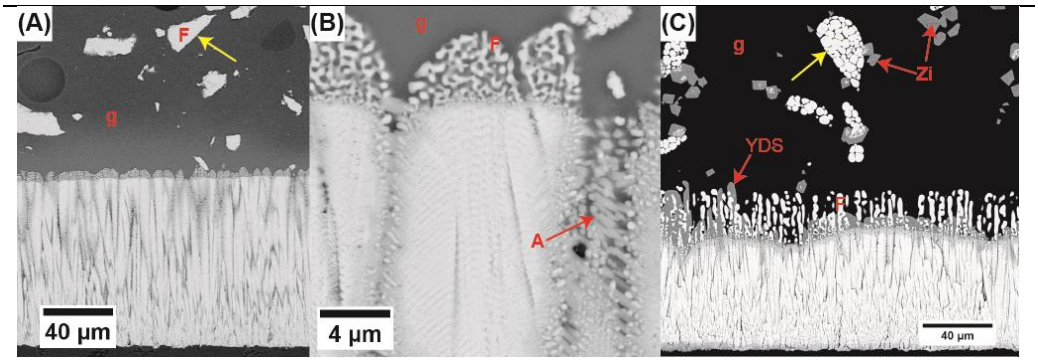

Figure 4.15: SEM cross-sectional image of the reaction layer formed on Popo VA (air quenched) infiltrated sample at 1250 °C for (A) 5 min. (B) high magnification image of the reaction zone generated from the 5 min testing. (C) 50 h infiltration image.

4.2.3.7 COL Reaction

Lastly, the COL/65YZ reaction is shown in **Figure 4.16** for 5 min and 50 h. The COL reaction exhibited a similar configuration as Popo with the only difference being the non-presence of fluorite particles embedded far into the glass reservoir after 5 min (see **4.15a**). A lower coating consumption was seen in COL case and more apatite formation was noticed. This is consistent with the Ca content in the COL glass about (5 mol %) which is in one order of magnitude higher than the Popo VA therefore, there is more tendency to form quicker apatite without having to dissolve as much coating as for the Popo case. This behavior is clearly seen in the reaction zone scenario after 50 h since the COL reaction (11.8 µm) exhibited almost 3 times less thick layer than the Popo case (29.4 µm). Finally, a small unidentified phase was found in the columnar gaps after long term infiltration (U) with a dark and sharp faceted configuration. This phase was found in very minimal amounts and it is presumed to be nucleated due to the local Al enrichment produced in the glass after precipitation of apatite and fluorite (since the phase shows very high $AlO_{1.5}$ contents above 27 percent). The chemical composition of the unidentified phase exhibits all available cations excluding Mg which is closer to that of garnet phase and does not show a composition close to a known phase such as anorthite ($CaAl_2Si_2O_8$) or spinel ($MgAl_2O_4$). It has

exhibited a significant change in composition specifically two times in $AlO_{1.5}$ content and depletion in CaO and SiO_2 content from 5 min to 50 h as shown in **Table 4.9**. Since it retains significant amounts of Si it should be based on a silicate phase expected from the CMAS/TBC interactions which leads to the assumption to be a variation of garnet. Since its presence in the reaction is very small it is neglected as a relevant reaction phase.

Table 4.9: Chemical composition summary for the reaction products located at the reaction zone for COL infiltrated at 1250 °C for various time lines. (unless specified in the table the chemical composition deviation is less than 1 mol %).

Time	ID	Composition (mol %)								
		$LO_{0.5}$	MgO	$AlO_{1.5}$	SiO_2	CaO	TiO_2	FeO	$YO_{1.5}$	ZrO_2
5 min	YDS	-	-	-	-	-	-	-	-	-
50 h	YDS	0.0	0.7	0.7	46.3 ±3.0	2.0	0.0	0.0	43.5	6.8 ±1.6
5 min	A	1.6	1.2	5.2 ±3.5	35.0 ±6.6	9.5	0.0	1.0	37 ±7.3	9.5 ±5.2
50 h	A	0.0	0.9	0.0	32.8 ±2.1	9.5	0.0	0.0	51.3	5.5 ±2.3
5 min	F	2.4	0.7	7.5	28.6	4.8	0.0	2.7	23.8	29.5
50 h	F	0.0	0.0	0.0	0.0	0.0	0.0	2.5	23.4	74.1
5 min	g	6.9	1.7	17.9	59.9 ±1.2	6.2	0.4	3.0	2.6	1.3
50 h	g	6.2	2.1	19.2 ±2.6	58.2	5.9	0.3	3.4	3.0 ±2.6	1.7 ±1.7
5 h	U	2.0	0.0	27.3	36.9	14.0	0.0	1.4	11.6	6.8
50 h	U	0.0	0.7	69.2	5.4	1.7	0.0	2.5	15.6	4.9

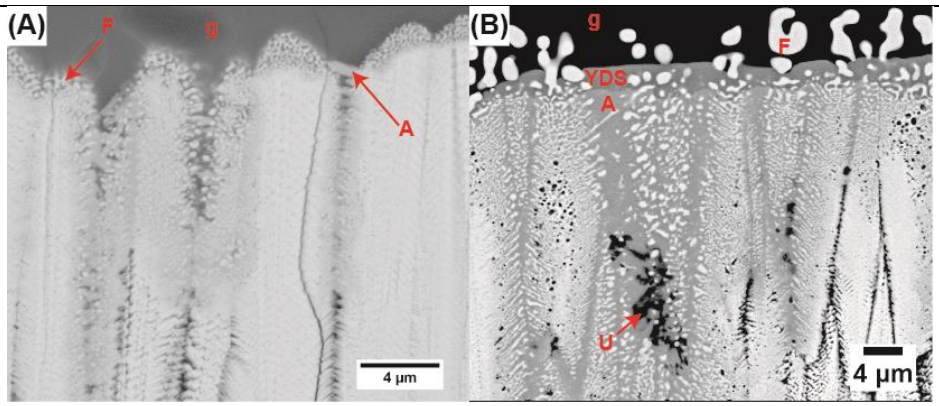

Figure 4.16: SEM cross-sectional image of the reaction layer formed on COL VA (air quenched) infiltrated sample at 1250 °C for (A) 5 min and (B) 50 h.

4.2.4 CMAS/VA Interaction for Slow Cooled Samples

The slow cooling experiments were performed to investigate if there was a secondary phase formation upon cooling. Additionally, the tests were performed at 1300 °C with slow cooling only due to the cyclic furnace limitations (air quenching) to test maximum at 1250 °C. In this way the infiltration resistance was also tested at higher temperature regimes. The experiments were performed with the same approach as in the previous section for 5 and 50 h by using a heating and cooling rate of 10K/min. Then, 5 CMAS compositions were tested (CMAS 1-2, ICE, Popo and COL) The infiltration test results at 1250 and 1300 °C are provided in the following sections.

4.2.4.1 Infiltration and Reaction Layer for Slow Cooled Experiments at 1250 °C

The infiltration produced for all the samples with the slow cooling did not show any variation in the depth after 5 h and 50 h as expected. The only distinguished variation from the slow cooling treatment for all the samples was the formation of larger amounts of the garnet phase in the ICE and CMAS samples as shown in **Figure 4.17**. The composition of these garnet phases did not vary significantly from the air quenched compositions. CMAS 1 and 2 samples have exhibited a thicker reaction layer (uniform garnet phase) compared to their air quenched counterparts. The reaction layer after 50 h (slow cooled) for the CMAS 1 and 2 samples was found to be 17 and 21 µm respectively. In contrast their air-cooled counterparts for CMAS 1 and 2

samples exhibited a reaction layer of 16 and 17.5 μm respectively. It is evident from these results that the garnet phase exhibits a favorable growth during slow cooling. This is in agreement with reports from literature where an increased garnet growth is exhibited due to slow cooling [34]. Additionally, the ICE VA exhibits formation of dendrite particles after slow cooling embedded in the unreacted glass. These products were also found in previous studies with ICE VA and 65YZ jumping beam samples [26]. In the previous studies they were identified as garnet dendrites since they have exhibited all the available cations in their composition with a particular Si and Fe enrichment as seen in **Table 4.7.** Since these products were not exquisitely seen in the air quenched samples (found as less than 0.5 μm long particles protruding from the Z and F phases) they were concluded to be diffusion growth-controlled particles due to the slow cooling. The rest of the SEM images of the infiltrated 65YZ samples at 1250 °C after 50 h in slow cooking conditions are provided in the appendix B section.

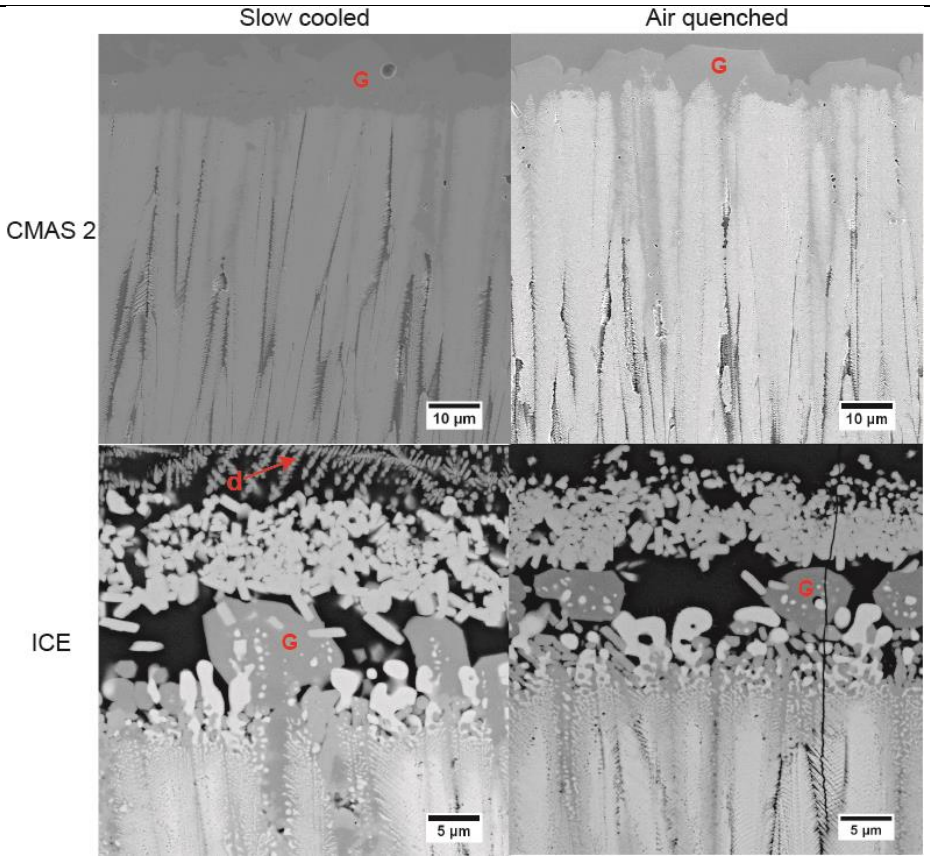

Figure 4.17: Cross-section SEM image comparison for the slow cooled and air quenched samples tested for 5 h at 1250 °C.

4.2.4.2 Infiltration Behavior for Slow Cooled Tests at 1300 °C

Complementary infiltration experiments were performed at 1300 °C for 5 h followed by slow cooling only to see the evolution of the reaction products and infiltration behavior at higher temperature regimes. The reaction layer cross-sectional images are shown in **Figure 4.18** for the tested CMAS/VA samples. The reaction configuration for all the samples is still similar to those of 1250 °C cases and the composition of the products did not vary significantly. The CMAS 2 case is not shown due to the large spread of the melt on top of the sample which did not generate a significant reaction layer (the figure has been included in the appendix B section). The CMAS 1 case (**4.18a**) showed a significant increase in size for the garnet layer (about 32 µm average over 17 µm at 1250°C) as seen from **Figure 4.18** and subsequent formation of dendrites (d) in interaction with the garnet layer which are embedded in the glass. This dendritic formation with

Fe bearing CMAS sources has been found with GZO interactions [112]. Additionally, no signs of the anorthite phase within the glass were seen as in the 1250 °C case.

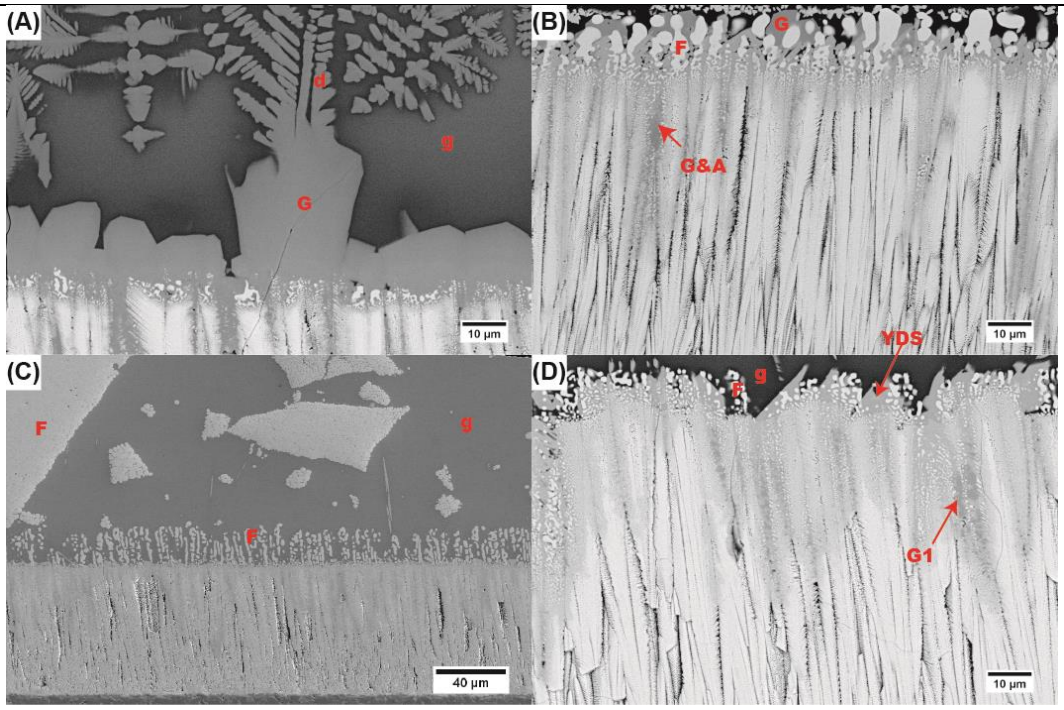

Figure 4.18: Cross-sectional images for the infiltrated samples tested at 1300 °C for 5 h for (A) CMAS 1, (B) ICE VA, (C) Popo VA and (D) COL VA.

EDS analysis performed on the produced dendrites for the CMAS 1 case showed a significant $YO_{1.5}$ deficiency in this phase and a high increase in CMAS elements were observed which are given in Table **4.10**. The reaction products found in the CMAS 1 sample still represented the same and had the same configuration as in the 1250 °C case. The apatite phase was found still in the columnar gaps in combination with fluorite and garnet particles. Thus, the only main difference from the 1250 °C case was only in the enlarged garnet formation with exhibited dendrites. The ICE VA sample did not show any formation of dendrites in the glass: Reason can be the wide spreading or high wetting of the glass on the coating which did not allow accumulation as a glass pile of unreacted glass as can be seen from **4.18b.** This effect is clearly seen form the reaction layer thickness since a thicker reaction is seen for the 1250 °C (22.4 µm) compared to the

1300 °C case (17.8 μm) as shown in **Figure 4.19b.** This lower reaction layer at 1300°C is possibly due to the significant drop in viscosity which allowed the molten glass to spread throughout all the TBC sample, therefore, reducing significantly its concentration < 20 mg/cm^2 as for the 1250 °C case. In both Popo and COL cases a phase bearing all available cations as seen from **Figure 4.18d** was found in the columnar gaps which is assumed to be a garnet type (the phase is labeled G1 in 4.18d). This G1 phase composition exhibits all available cations but a low Ca content (as sown in **Table 4.10**) of 0 to 3.9 CaO for Popo and COL respectively. In contrast, this phase was not found at 1250 °C for Popo and COL samples. However, one unidentified phase (U) was found for the COL case with a particular $AlO_{1.5}$ enrichment 27.3 mol % after 5 min (**Table 4.9**) which appears to be close to the composition of this G1 phase (27.7 and 28. 6 mol % for Popo and COL respectively). It could be possible that these phases are correlated and that its bigger growth seen in the 1300 °C case could be attributed to the slow cooling. However, since this phase could not be identified by XRD and no literature reports have been found additional TEM studies are required to properly identify it. Additionally, the reaction layers appear to be the same having the same reaction products in both cases. The Popo VA case exhibits a very large fluorite product accumulation in the glass reservoir compared to that of 1250 °C sample. This is expected as the temperatures rise viscosity of the melt goes down creating a widespread of glass on top of the coating, therefore, more coating dissolution is produced. The zircon products were still found as small accumulations engulfing the glass embedded fluorite particles. The coating reaction layer growth is clearly higher for the 1300 °C cases due to the increased reaction activity at higher temperatures and to the increased cooling time that is generated at 1300 °C. Finally. the infiltration depth is clearly seen to increase at1300 °C compared to 1250°C for all cases as shown in **Figure 4.19a**, expected due to the drop in melt viscosity.

Table 4.10: Chemical composition summary of the samples tested for 5 h at 1300 °C after slow cooling. The exhibited products represent the ones found with different compositions compared to 1250 °C tested samples.

		Composition (mol %)							
Source	ID	MgO	$AlO_{1.5}$	SiO_2	CaO	TiO_2	FeO	$YO_{1.5}$	ZrO_2
CMAS 1	d	10.3	11.3	29.3	23.7	2.2	10.8	8.4	3.9
CMAS 1	G	7.6	15.8	20.9	16.3	1.1	16.8	19.2	2.4
COL	G1	6.4	28.6 ±2.0	15.6 ±3.1	3.9	0.0	8.9 ±2.0	34.8 ±3.9	1.8 ±2.5
Popo	G1	7.3	24.7	16.3 ±1.3	0.0	4.0	5.5 ±2.7	36.0 ±1.6	6.2 ±3.5

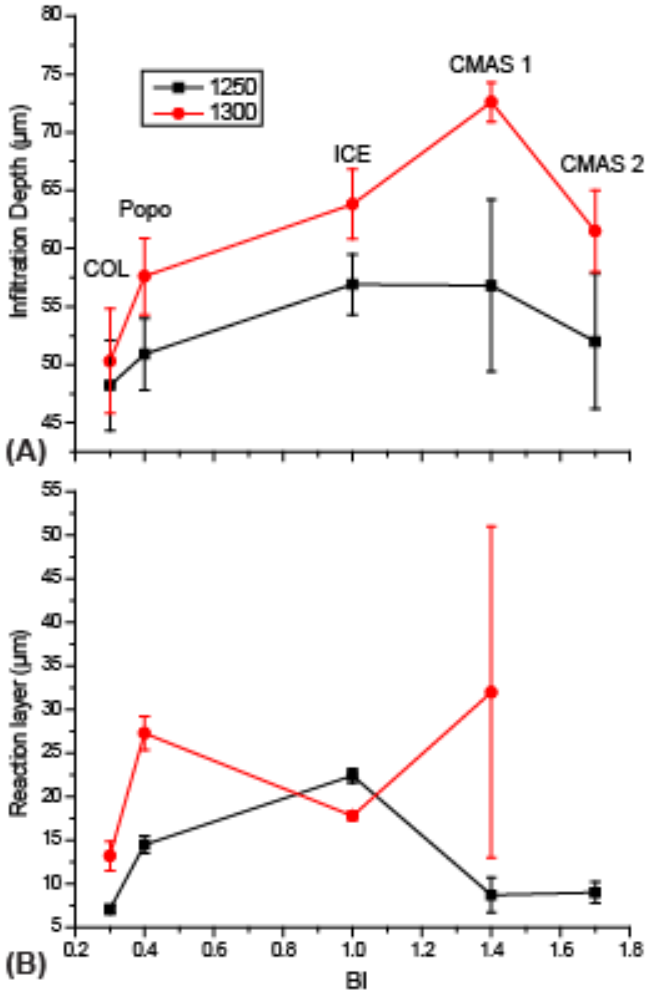

Figure 4.19: Infiltration depth plot (A) and reaction layer (B) for the 5 h tested samples at 1300 and 1250 °C samples using slow cooling.

4.2.5 CMAS/VA Interaction for GZO Samples

The GZO samples were tested at 1250 °C for 50 followed by air cooling using CMAS 1-2, ICE VA and UCSB CMAS to compare its infiltration resistance with 65YZ under the same testing conditions. **Figure 4.20** shows the SEM cross-sectional images of GZO infiltrated samples by CMAS 1, ICE VA, CMAS 2 and UCSB after 50 h at 1250 °C. The infiltration depth was found to be significantly higher (150, 168, 147 and 80 μm for CMAS 1, CMAS 2, UCSB and ICE respectively) and the reaction layer thickness (60, 55, 25 and 66 μm for CMAS 1, CMAS 2, UCSB and ICE respectively) compared to all the 65YZ samples (see **Figure 4.27** in the discussion section). All the samples exhibited a uniform layer with intermixed apatite and fluorite phases delimited within the red dotted bars in **Figure 4.20**. This intermixed layer represents most of the reaction zone for the CMAS 1, CMAS 2 and ICE samples. For the UCSB case it represents all the reaction layer since no other secondary phase was formed such as garnet. The thicknesses of these intermixed layers were about 45, 30 and 58 μm for CMAS 1, CMAS 2 and ICE respectively. Comparing the thickness of these intermixed layers exhibited for the 65YZ samples (about 4 μm for CMAS 1, 4 μm for CMAS 2 and 15 μm for ICE) the GZO layers are significantly thicker. This could lead to the conclusion that more apatite and fluorite formation is promoted for GZO. This is in agreement with literature reports about higher apatite crystallization potential for GZO than δ-$Y_3Zr_2O_{12}$ [11, 34, 120]. In general, the GZO samples exhibited very minimal amounts of unreacted glass deposits on top. It varied from being almost absent for the ICE case to localized 20 μm thick max deposits for CMAS 2. Compared to their 65YZ counterparts at 1250 °C only the ICE VA left small amounts of glass until the top zirconolite layer as also exhibited for the GZO case. On the contrary, all the other samples left a glass deposit on top being 25 μm max for CMAS 2, 42 μm max for UCSB and 100 μm max for CMAS 1. A detailed analysis about the infiltration and reaction products is given in the discussion section comparing the GZO and 65YZ results. Additionally, the CMAS 1 and 2 reactions showed garnet formation in small amounts at the columnar gaps as well as an uniform garnet layer on top of the reaction zone similarly as exhibited for 65YZ/CMAS 1-2 case. The garnet layer has exhibited similar engulfing behavior into other phases such as apatite

and fluorite. The ICE VA did not exhibit formation of garnet crystals. Both samples exhibited the formation of small dark prismatic crystals with Al, Mg and Fe enrichment. They were identified as spinel (Sp) and exhibited the same composition ($(MgAl_{2-x}Fe_x)O_4$). This phase has been reported previously in literature but without the Fe enrichment [29]. This spinel phase is believed to be formed as intrinsic crystallization due to the Ca and Si depletion in the glass which promotes precipitation of the Al, Mg, Fe rich spinel phase. Therefore, this phase is not promoted in the 65YZ case since the garnet phase acts as a sink for Mg and Fe.

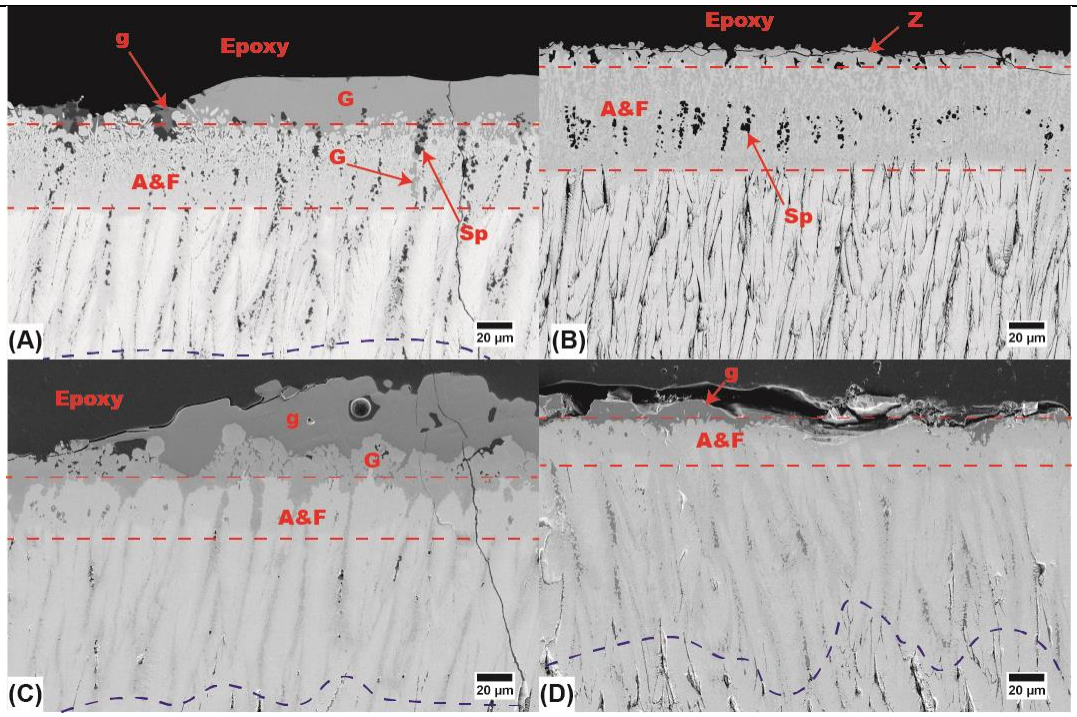

Figure 4.20: SEM cross-sectional image of the (A) CMAS 1 (B) ICE (C) CMAS 2 and (D) UCSB infiltrated GZO samples for 50 at 1250 °C (air quenched). The blue dotted line at the bottom of shows the discontinuous infiltration.

The reaction products produced for the CMAS 1 at the columnar gaps showed that the garnet phase is promoted with large glass accumulations since it precipitated at large open gaps only. The spinel was also found in interaction with the garnet phase at large gaps but it was mainly found in small confined areas. The summary of the reaction product composition is given in **Table 4.11**.

Table 4.11: Summary of composition for the reaction products formed for the GZO samples tested for 50 h at 1250 °C.

	ID	MgO	$AlO_{1.5}$	SiO_2	CaO	TiO_2	FeO	$GaO_{1.5}$	ZrO_2
CMAS 1	A	0	0	31.9	14.5	0	0	49.4	4.2
CMAS 2	A	0	0	30.3	14.4	0	0	49.7	5.6
ICE	A	0	0	30	8.7	0	0	54.3	6.9
UCSB	A	0	0	31.2	16.8	0	0	47.3	4.8
CMAS 1	G	4.5	9.7	18.8	21.6	2.1	20.2	16.9	6.2
CMAS 1	g	6.9	15.8	33.9	29.7	1.3	4.8	4.8	2.8
CMAS 1	Sp	27.6	57.8	0	0.3	0	14.3	0	0

4.3 Discussion

The current results have shown that the CMAS/VA interaction with TBC is a very complex and dynamic system where every single element has an influence on the overall reaction and can shift the equilibria depending on its concentration. Additionally, it is well known that effective CMAS arrest for any TBC is highly dependent on the composition of the local melt and the reactive oxide used to saturate the glass to promote its crystallization [11]. In addition, the reaction products must be able to seal the columnar gaps effectively by producing a beneficial crystallization morphology that seals the gaps fast so that no more glass phase can penetrate further into the porous features. This study proves that the reaction products are clearly changing with the composition of the melt as also mentioned in literature [120]. Furthermore, as the current studies focused on a large range of compositions of CMAS/VA, a mapping of the expected reaction phases with respect of basicity index (BI) is developed as seen in **Figure 4.21.** Since the BI represents an effective system to trace the composition of the melt and its viscosity, these studies also show that BI could be applied as a screening parameter to predict reaction product formation at the reaction front. The overall reaction kinetics for CMAS/RE based TBC systems can be described by the initial dissolution of the TBC materials into the molten glass followed by the simultaneous re-precipitation and reactive crystallization of products (being fluorite and apatite the main formed products respectively). Consequently, secondary reactive crystallization is promoted due to the

constant interaction of varied oxides from the rich composed glass (Mg, Al, Fe, Ti, etc.) with the primary products promoting subsequent phase formation. The intrinsic crystallization behavior can be promoted from the pure chemical composition of the initial melt which can favor formation of mineral compounds such as anorthite, melillite among others [11]. Besides, it can be promoted due to the depletion of elements to promote reactive crystallization (Si and Ca to form apatite). This was found in the GZO samples where the depletion in Ca and Si to promote apatite within the gaps shifted the residual glass composition to promote spinel formation. Therefore, this **Figure 4.21** divides this figure divides the first reactive crystallization products expected to form upon glass saturation from the 65YZ TBC cations (Y^{3+} and Zr^{4+}). The first phases that are expected to be formed are fluorite and apatite from the main network former oxides which represent zirconates or silicates. Their formation is promoted from the constant dissolution of Y^{3+} and Zr^{4+} from the coating into the glass which upon reaching local glass saturation they precipitate with respect to their favorable element interaction (e.g. Ca and Si for apatite). The apatite phase represents the most beneficial phase in the initial infiltration stages since it is the first silicate based phase to form upon reaction and also represents the most favorable energetically silicate phase to from [34]. The fluorite phase is promoted from the Zr dissolution into the melt which promote its re-precipitation capturing other fluorite stabilizers such as Ca and RE [27, 30, 34]. The zirconolite phase appears to be a special case phase which forms due to the Ti and Fe enrichment in the glass in large quantities e.g. big glass reservoirs in interaction with the TBC material. As seen from these results the secondary reaction phases appear to nucleate at expense of a parent phase: apatite as the parent phase for garnet and YDS and fluorite for zircon. This is in agreement with literature reports that the garnet phase nucleates at expense of apatite [18, 19, 120]. Additionally, as seen from the reaction product composition for CMAS 1, 2 and ICE VA small concentrations of Mg, Al, and Fe in the apatite phase also show evidence of subsequent transformation into garnet from interaction with large glass deposits. Literature reports on the YDS-apatite phases expose that yttrium monosilicate and disilicate are believed to be decomposition products from the Ca-lean apatite phase [141-143]. Besides, the YDS phase also requires a high Si glass concentration and long time

periods to nucleate. The zircon phase appears to be a special case where it requires a high Zr and Si activity and longer time periods to nucleate. In this context, the garnet phase appears to be the fastest forming secondary reaction phase since it was found in 5 min test right after apatite formation as shown in **Figure 4.9**.

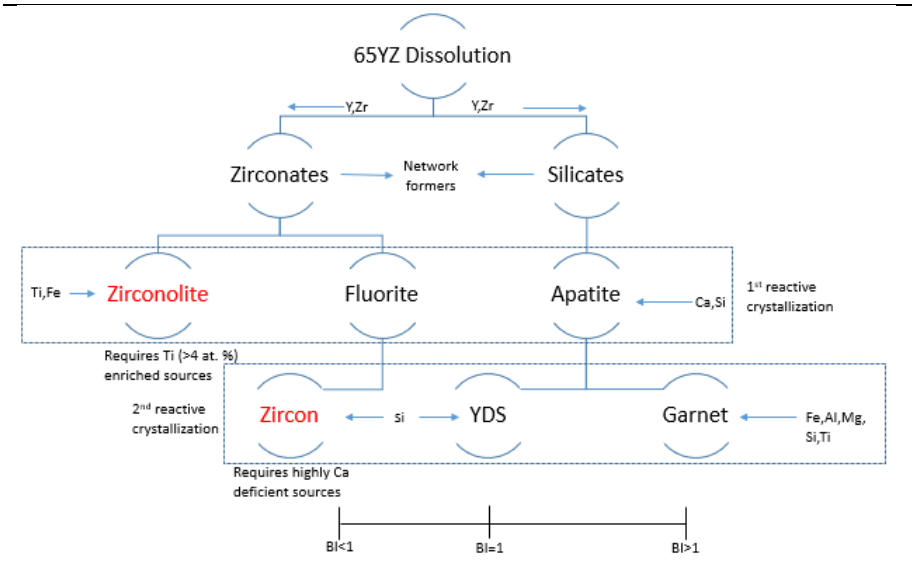

Figure 4.21: Mapping for reaction products produced at the reaction layer for 65YZ reactions with respect to basicity index (BI).

Furthermore, from the current study, it can be said that two main mechanisms are governing the infiltration and reaction behavior of 65YZ coatings. They are classified as a) the reaction kinetics of phase formation which promote the crystallization of the glass into stable products as a uniform layer and its slow growth. b) The viscosity variation of the melt with respect to coating dissolution (RE and Zr) which controls the infiltration depth and glass concentrations.

4.3.1 Reaction Kinetics

4.3.1.1 1st Reactive Crystallization

From the results it is clear that the apatite formation is favorably promoted in smaller pockets (e.g. feather arm gaps) where the high Y^{3+} saturation limit can be easily achieved requiring

less coating dissolution than at the reaction front where the large glass reservoir makes it more difficult to reach this saturation point. In this context, Krause et al. performed studies with $2ZrO_2.Y_2O_3$ powders in interaction with CMAS, and found that the apatite formation was only promoted in small glass pocket areas [124]. Additionally, it was found that Y^{3+} solubility in the glass was 2 times higher than Zr^{4+}. It was also reported that Y^{3+} showed concentration gradients mainly in small pocket areas due to apatite concentration. Their conclusion was that Y^{3+} confinement in the CMAS melt played a critical role in promoting apatite formation. Consequently, since the apatite phase accepts Zr contents max. in between 11 to 16 mol %, (as seen from product compositions in the results section) the excess dissolved Zr is precipitated into the fluorite phase which also retains significant amounts of Y^{3+}. In contrast, literature reports of the apatite phase show a maximum content of 7 mol % of ZrO_2 for GZO reactions [120].

The apatite phase formation is clearly important in crystalizing the melt and it is believed that it is critical to quickly arrest infiltration in the early stages (first few minutes of infiltration). The main cation that is required for apatite formation is Ca^{2+} and its solubility limit in the apatite phase is dictated by its theoretical formula $M^{I}_4M^{II}_6(SiO_4)_6X_2$ where Ca^{2+} and Mg^{2+} are assumed to occupy the M^{I} site and the RE^{3+} the M^{I} and M^{II} sites [144-148]. Then, the Zr^{4+} cation is believed to substitute the RE^{3+} at the M^{II} site [11]. Finally, the Al contents in the apatite are believed to be accommodated in the Si tetrahedral [30] and X represent the oxygen anion. **Figure 4.22** exhibits the ternary plot for the $CaO\text{-}SiO_2\text{-}YO_{1.5}$ where the apatite phase compositions which were identified in this study are plotted for 65YZ with respect to the Si:Ca ratio of the melt and BI. In the diagram the plotted phases were normalized only to the SiO_2, CaO and $YO_{1.5}$ contents. The ternary plot exhibits a trend of increased Ca content (M^{I} site cations) with respect to higher CaO content in the original melt (lower Si:Ca ratio). This trend has been found in CMAS reactions with other RE oxides as well [34]. Thus, by only looking into reaction kinetics (i.e. potency to promote apatite formation to seal the gaps) it could be predicted that melts with low Si:Ca ratio (e.g. UCSB) would be expected to exhibit low infiltration compared to high Si:Ca melts (Popo VA) on reactive TBCs such as 65YZ. Surprisingly, this has not been the case as seen in **Figure 4.6** where the UCSB

source did not exhibit the lowest infiltration. It even showed the similar infiltration depth to that of the Popo VA. This clearly proves that the infiltration behavior is not only influenced by the chemical composition but other factors have a significant impact in the infiltration behavior such as melt viscosity and coating microstructure. Therefore, all these parameters must be considered as a whole for an ideal CMAS/VA resistant system. The viscosity effect will be discussed in the following sections and the microstructural effect will be studies in the next chapter. Next, the garnet compositions in **Figure 4.22** show large ranges of Ca-Y contents. The YDS range zone given in 4.22 was incorporated from the ternary plot provided in ref [11] where the YDS compositions obtained from these studies fitted within the YDS region. It is important to note that the YDS layer precipitates from a smaller range of Ca lean apatite phases compared to the garnet phase which is promoted from higher Ca bearing apatite phase.

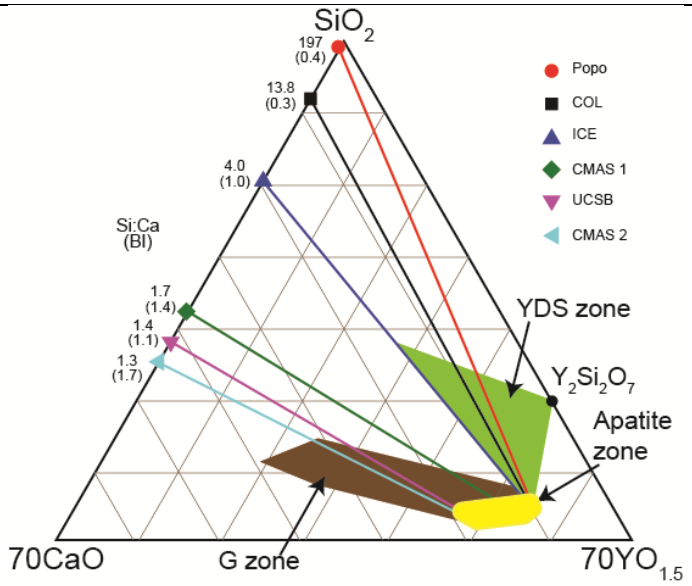

Figure 4.22: Ternary plot for the found reaction phases in the 65YZ interactions with different CMAS/VA sources at 1250 °C after 50 h. Their Si:Ca and BI are plotted from the CaO-SiO_2 axis.

A special case is seen for the ICE VA where the zirconolite phase was promoted due to the high Ti enrichment in the melt. This phase was found to have an indirect influence on the reaction

products formation at the reaction front: especially on the apatite formation. Complementary experiments were performed with the mixtures of ICE:CMAS 1 in ratios of 1:3, 1:1 and 3:1 to identify the amount of threshold TiO_2 required for zirconolite formation. Additionally, the Fe content in the glass is also of importance since the ICE VA exhibits larger Fe contents than the CMAS 1-2 cases but the garnet layer does not form continuously. These powder mixtures were used in the infiltration tests which were performed at 1250 °C for 5 h (air quenching). The formed reaction zones are shown in **Figure 4.23**. The SEM images show how the reaction layer behaves more like CMAS 1 with a uniform garnet layer in the 1:3 mixture case. After the compounds are mixed in a 1:1 ratio higher fluorite formation is distinguished in the reaction layer with initial formation of localized large garnet crystals still with no zirconolite formation. Then, the reaction is shifted to form the zirconolite phase on top of 3:1 mixture in the glass reservoir when high ICE content (3:1)in the mixture exhibits a Ti content of 3.40 mol % which appears to be the threshold for zirconolite formation with a composition of $Mg_{1.9}Al_{3.9}Si_{2.9}Ca_{2.8}Ti_{20.1}Fe_{18.1}Y_{20.2}Zr_{30.2}$. However, since no more tests were performed in between 1:1 and 3:1 (2.50 and 3.40 Ti content respectively) it is still possible that zirconolite could be promoted in compositions between this range. The zirconolite phase did not show variation in the Fe and Ti (18.1 and 20.1 respectively) compared to the 50 h zirconolite formed for pure ICE after 50 h at 1250 °C in the previous section. The garnet composition for the 1:3 mixture was $Mg_{8.4}Al_{11.4}Si_{21.9}Ca_{16.4}Ti_{1.7}Fe_{19.5}Y_{18.2}Zr_{2.4}$, the other garnets exhibited variations in the Ca, Fe and Y with respect to mixing ratio as seen in **Figure 4.24**. The compositions changed to $Mg_{8.2}Al_{12.1}Si_{21.2}Ca_{14.1}Ti_{1.7}Fe_{20}Y_{20.8}Zr_{1.8}$ for the 1:1 mixture and $Mg_{8.7}Al_{9.8}Si_{19.7}Ca_{10.7}Ti_{1.4}Fe_{22.2}Y_{23.4}Zr_{4.2}$ for the 3:1 mixture.

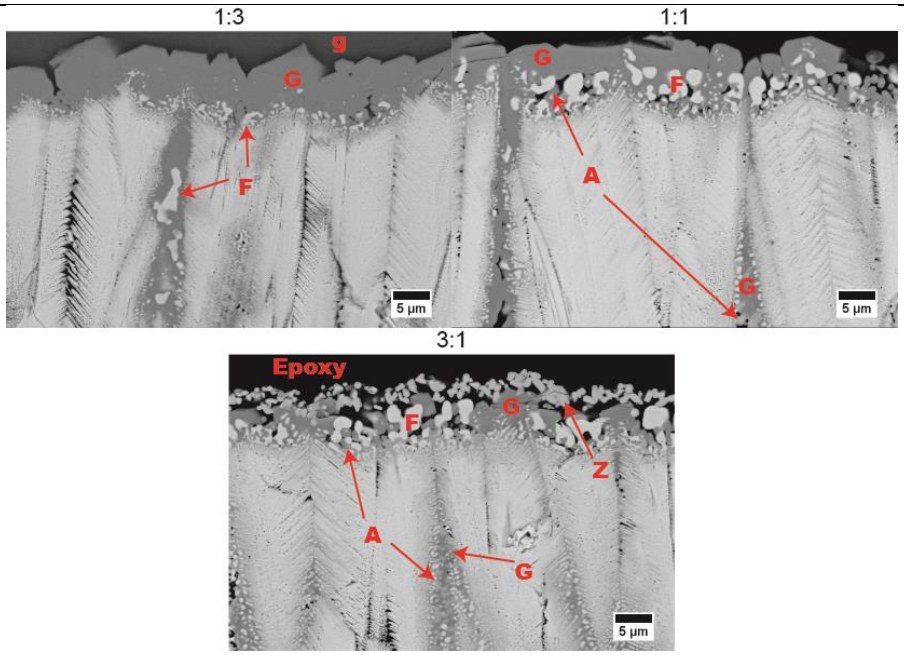

Figure 4.23: Reaction layer cross-section image of the ICE:CMAS 1 mixed compounds tested for 5 h at 1250 °C under air quenching.

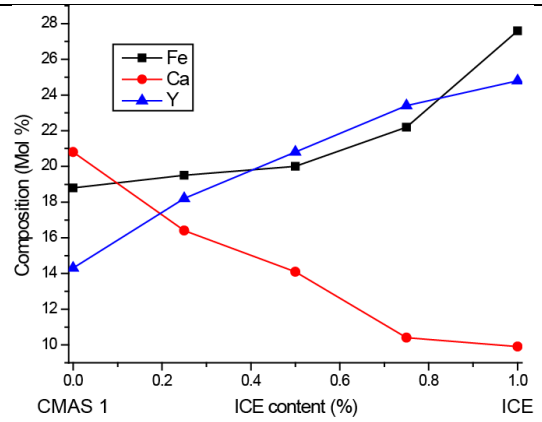

Figure 4.24: Element composition of the garnet phase with respect to ICE:CMAS 1 mixture.

The **Figure 4.24** plot shows the variation of Fe, Ca and Y composition in the garnet phases with respect to the ICE:CMAS1 mixing ratio for samples tested at 1250 °C for 5 h (air quenched). The garnet produced in the pure CMAS 1 case (0 percent ICE content in **4.24**) shows the lowest Fe and Y contents but the highest Ca. As the ICE VA is mixed a clear increase in Y and Fe is

distinguished with a Ca depletion until reaching pure ICE (or =1 in the plot) for the garnet phase. This variation in garnet compositions was already reported in the literature [19, 27, 34, 120, 129]. Additional tests also showed that the garnet melting point is decreased with increasing Ca content. Additional, tests also showed that the garnet melting point is decreased with increasing Ca content. One interesting feature from these experiments was the increase in the Fe content in the garnet phase as more Fe was available in the melt. The extra Fe in the ICE case was not accommodated in other Fe bearing phases such as zirconolite (since its composition did not vary). Thus, the results for these specific garnet types showed that there appears to be a complex interaction of elements specifically Fe, Ca and Y in the system. Fe and Y appear to substitute Ca in the garnet phase for high Fe containing melts such as ICE VA as seen in **4.24.** These results lead to the conclusion that besides Fe the presence of CaO appears to be important for enhanced garnet formation as a continuous layer.

4.3.1.2 2nd Reactive Crystallization

The secondary reaction phases based on silicates (garnet, YDS and zircon) nucleate at expense of other phases being apatite as the "parent" phase for garnet and YDS and fluorite for zircon. These secondary phases are believed to have a sluggish formation which makes them not suitable as efficient CMAS blocking??phases. This has been suggested for Yb based garnet formation in experiments performed with model CMAS sources [18, 34]. The garnet phase is believed to be promoted from the high local concentration of MgO, $AlO_{1.5}$ and FeO in the glass reservoir (mainly large columnar gaps and the reaction front) [26, 129]. This hypothesis is supported from the mentioned cation concentration in the apatite phase for the CMAS and ICE samples from the results section and the garnet formation seen at the reaction layer and in between large columnar gaps. There is a current debate if the garnet phase is beneficial for long term CMAS arrest over apatite phase due to its slow precipitation rate. Although in the current study, evidence of garnet formation has been found in the early stages specifically after 5 min along with the apatite phase. In order to study its formation complementary in-situ high temperature XRD analyses were performed on a 65YZ as coated sample deposited with CMAS 1 to track the garnet formation with

respect to time. The XRD plots obtained at 1250 and 1300 °C are shown in **Figure 4.25** where clear formation of the garnet phase is seen in the very initial heating stages after just a few minutes of interaction as also found in the short-term experiments. Additionally, the garnet concentration is clearly higher than apatite in this reaction. The results confirm that the garnet phase is generated as a reaction phase during the high temperature interactions of the TBC material and the CMAS melt and not during the cooling phase.

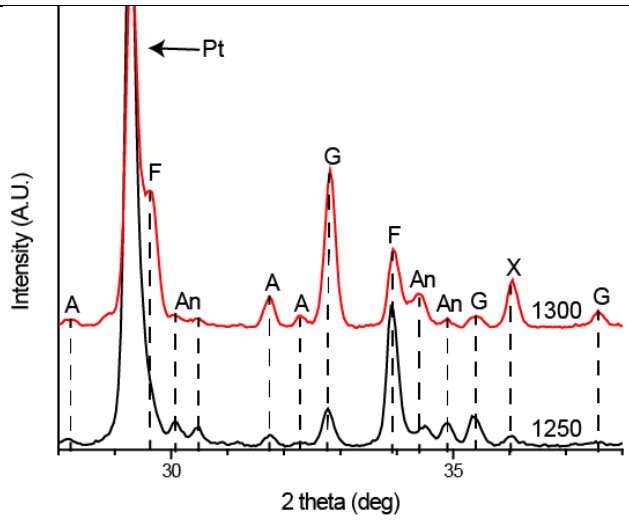

Figure 4.25: HT-XRD pattern for the in-situ experiments performed for CMAS 1 deposited on a 65YZ sample for 1250 and 1300 °C.

Furthermore, a continuous garnet formation is only exhibited for the CMAS 1 and 2 samples and its presence at the reaction layer is reduced for the ICE and UCSB samples then being completely suppressed at the reaction layer for the Popo and COL VAs. It is reported in literature that small RE cations e.g. Yb^{3+} and Y^{3+} exhibit higher tendency for garnet formation in silicate based melts due to the higher partition coefficient (D) generated as compared to larger RE cations e.g. Gd^{3+} or La^{3+} [34]. The partition coefficient is defined as the concentration of a specific compound in two phases that are in equilibrium with each other [149]. Besides, it has been reported that the enthalpy of formation for the apatite phase decreases with low RE cations making it less stable thus, promoting more decomposition phases such as garnet [34, 150]. **Figure 4.26**

incorporates the estimated partition coefficients of the garnet and apatite phases found for 65YZ and GZO in these studies after 50 h at 1250 °C. The plot was modified from [34] where a large mapping of apatite and garnet phase partition coefficient based on their RE content with respect of the RE ionic radius was provided. The plot predicts that for D>1 values the substitution of the RE cation is favorable into the crystallographic site of the phase of interest and for D<1 is not [34]. The results are in good agreement by showing all the found garnet phases within the expected zone delimited for the silicate garnet in the 65YZ case. Only the ICE VA apatite phase was extended into the phosphate apatite region. It is important to note that the phosphate apatite is crystallographically identical to the silicate oxyapatite as reported in the literature [34, 151]. The GZO garnet (D cry/melt=3.52) was found in the upper limit of the silicate garnet formation which confirms that the CMAS 1 compound would produce stable garnet in interaction with GZO. The plot also confirms a higher potency of garnet formation for the 65YZ phase due to D values that extend significantly into the upper values and overlap higher with the apatites. More details in the comparison of reaction phases for GZO and 65YZ are provided in the following sections.

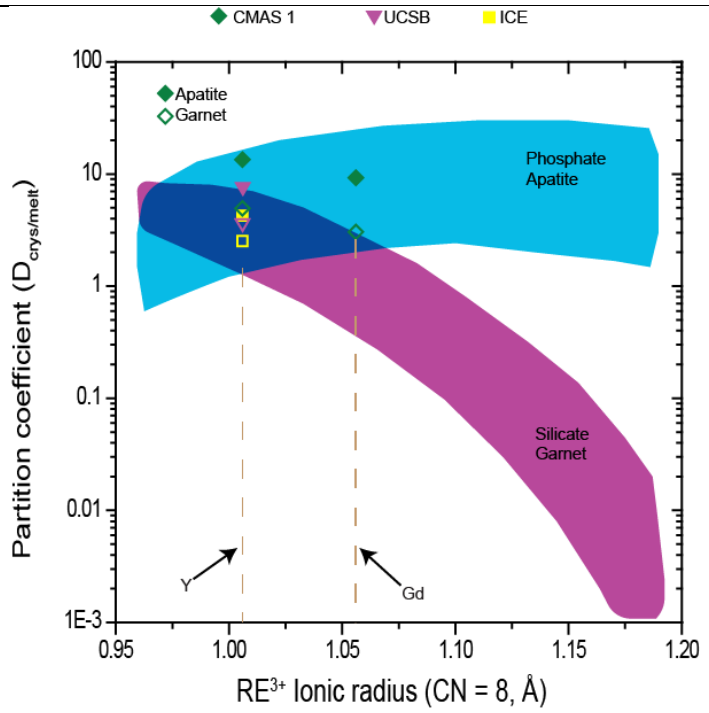

Figure 4.26: Partition coefficient plot vs RE ionic radius for CMAS/VA compositions with 65YZ and GZO. The literature values provided in the plot are obtained from ref [34].

The YDS phase is only expected to evolve in silica rich melts only as seen from the results (Si:Ca 4.0 or higher) at expense of the apatite phase. From the phase diagram shown in **Figure 4.22** the YDS range is shown for the VA sources and how they overlap with the apatite phase. As the reaction is supersaturated in Si (requires at least time periods of 1 h) the apatite phase decomposes possibly into Ca lean apatite ($Y_{9.33}(SiO_4)_6O_2$) progressively into YDS. This Ca lean apatite decomposition is known to happen when the melt is deficient in Ca [11]. The zircon phase exhibits a similar precipitation behavior to that of YDS and its nucleation is only promoted from the fluorite crystals. This phase has been also seen to form in CMAS interactions with standard YSZ TBCs [98]. Its formation also requires minimum reaction times of at least 30 min as found in Popo/COL interactions with APS YSZ (paper submitted to Surf. And Coat. Technology). Additionally, its formation was only promoted from fluorite particles that are embedded in the glass and remaining contact with the glass reservoir. As fluorite nucleation is far from the reaction front it leads to a conclusion that the Popo VA needs to dissolve the largest amounts of coating

material to promote apatite formation (proved from thickest reaction layer exhibited). This high dissolution is due to the very low Ca content in the glass which does not promote efficient apatite formation. Therefore, the excess dissolved Zr is then accumulated throughout the glass until a saturation limit is reached to nucleate $YO_{1.5}$ fluorite. Consequently, the Si rich glass interaction with the low Y fluorite crystals promote the zircon formation. In contrast, the YDS phase is formed in the areas close to the coating (see **Figure 4.15**) compared to the zircon phase. This is due to the fact that the YDS phase nucleates at expense of the apatite. On the contrary, the zircon phase is promoted from the fluorite. Thus, since the apatite phase requires enclosed glass areas which can only be found in the columnar gaps, the YDS formation is then found close to the coating where it is in interaction with the fluorite phase.

4.3.1.3 Viscosity Variation

Figure 4.27a shows the different predicted viscosities of the used CMAS/VA melts using the Giordano et al. model (GRD) with respect to their BI. The GRD model is a statistical method used to determine viscosity based on the chemical composition of siliceous melts [152]. The plot clearly shows a correlation of higher BI corresponds to a lower viscosity of the melt. Therefore, by looking into the infiltration depth progression with respect to BI at 1250 °C (**4.27b**) a trend is seen for higher infiltration depth for lower melt viscosity (higher BI). Only the CMAS 2 sample did not follow this trend by exhibiting a lower infiltration than the CMAS 1 sample. This shows that also the Ca content in the melt plays an important role in infiltration since for higher Ca containing melts (CMAS 2) lower coating amounts are dissolved to promote apatite formation to arrest the glass faster. the use of BI as a screening parameter for CMAS/VA sources for infiltration damage is an efficient method. This method or correlation with the reaction layer growth (**4.27c**) does not seem to have agreement with respect to BI. However, it does not exhibit any correlation with Si:Ca ratio either since if this assumption is followed it would mean that the highest reaction layer thickness following Popo must be COL which is not the case.

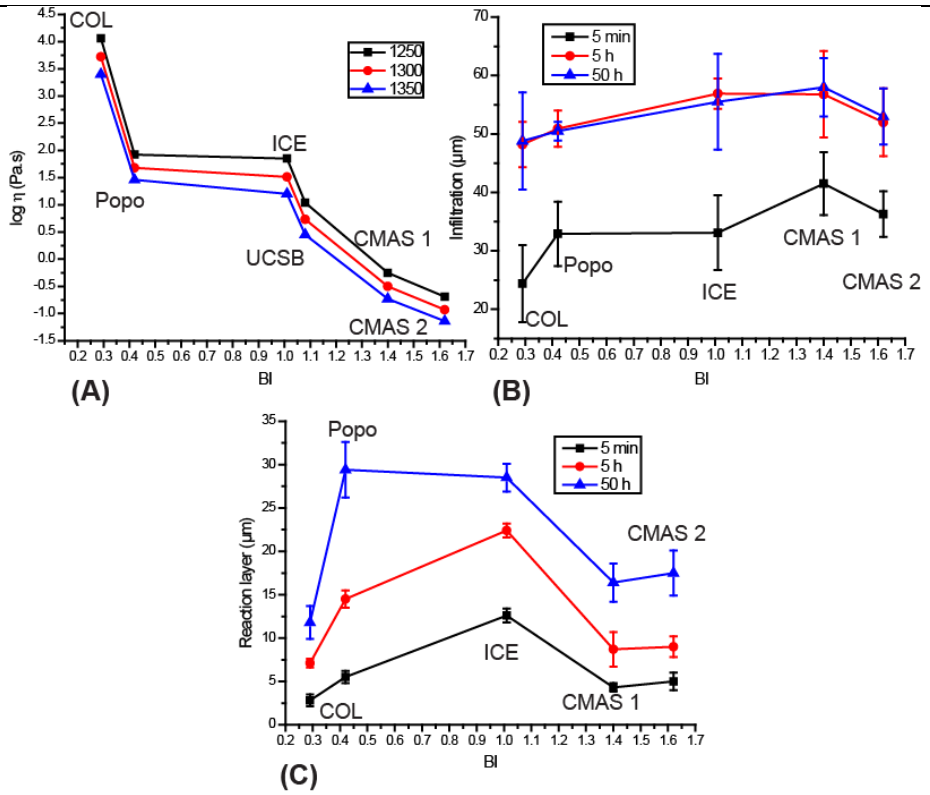

Figure 4.27: (A) Predicted GRD viscosity vs BI for all the CMAS/VA compounds. (B) Infiltration depth vs BI for the experiments performed at 1250 °C. (C) Reaction layer thickness vs BI for the experiments performed at 1250 °C.

Furthermore, due to the dissolution of the TBC material into the melt, it is expected that the composition will change as it gets enriched with RE and Zr. It is known form the literature that the dissolution of Y and Gd elements into glassy melts reduce its viscosity being Gd more effective in reducing the viscosity than Y, whereas Zr increases the viscosity [153, 154]. Since it is known that the RE solubility is higher than the Zr in the melt, the viscosity of the melt is expected to decrease as it starts to dissolve TBC material prior reaction phases formation. This effect can also shift the phase equilibria at long term infiltration (possibly more than 10 h) at the reaction layer since an enhanced low viscosity melt can spread more easily and wet a larger coating surface. This means that the melt concentration per unit area at the contact will be reduced: therefore, lower formation of secondary reaction phases which are enhanced by the interaction with large glass deposits can be suppressed. This phase suppression could be more prominent for the garnet phase

formation since it is promoted with melts of low viscosity (BI>1). Thus, if the melt spreads in larger areas the deposit concentration would be lower generating lower phase precipitation. On the other hand, this effect will be expected to be less prominent for the zircon and YDS phases since they are promoted with high viscosity melts (BI<1). In this case the reduction in melt viscosity from coating dissolution will not affect significantly its wetting behavior. This effect was seen in the 50 h reactions by showing that the COL and Popo VA still retained very large glass deposits compared to the other tested samples.

4.3.2 65YZ and GZO CMAS Interactions Comparison

The infiltration depths and reaction layer growth are compared for GZO and 65YZ in **Figure 4.28**. It is clear from the results that 65YZ appears to outperform GZO in reducing the infiltration depth and reaction layer growth after 50 h. The GZO exhibited a significantly thick intermixed zone of apatite and fluorite in all cases. For the CMAS 1 and 2 samples a continuous garnet layer formation at the reaction front was observed (even though the thickness is at the higher end. As seen previously in **Figure 4.26**, the partition coefficient of the garnet formation was highly promoted for the yttria based silicate reactions by covering larger stable ranges (D>1) than for GZO. On the other hand, the GZO garnet formation for CMAS 1 (D_{CMAS1}=3.52) was located at the limit interface with the apatite phase region which suggest that the RE substitution in the GZO based garnet is not as stable as for the 65YZ case (D_{CMAS1}=4.51). Additionally, the apatite formation for the CMAS 1 case for both samples showed a higher partition coefficient (D=11.6 for 65YZ and D=10.3 for GZO) for the 65YZ apatite. This same case is seen for the Y based garnet compared to the Gd based one. This could be interpreted as more favorable accommodation of the Y^{3+} cation into the crystalline phases compared to the larger Gd^{3+}. Since only the CMAS 1 sample showed small unreacted glass deposits on top of the reaction zone for GZO the D values could be estimated only for this mixture. It is also important to note that the garnet phase exhibits the highest potential to crystalize all the glass constituents products than all the other reaction phases as seen in **Figure 3.10** due to its highest g/TBC ratio. This glass encapsulation mechanism in combination

with a slower growth rate than the apatite appears to make the garnet phase a beneficial reaction product for long term infiltration since it appears to give an advantage for less consumption of the coating as seen for the 65YZ case. However, it is important to note that the GZO microstructure was not optimized leaving larger columnar gaps than the 65YZ case which means that deeper infiltration can be promoted for the GZO case.

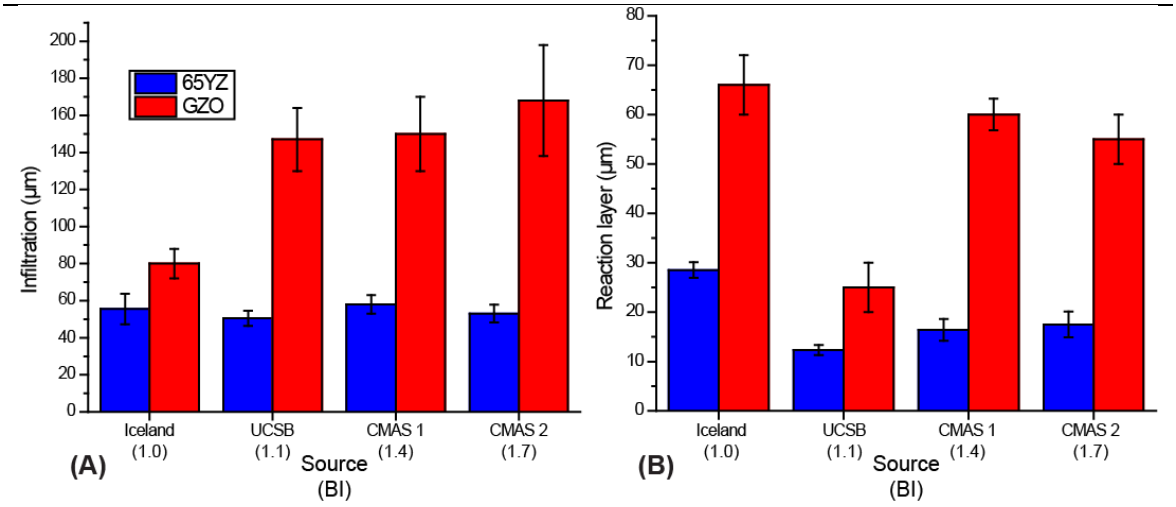

Figure 4.28: Comparison of (A) infiltration depth and (B) reaction layer thickness for the 65YZ and GZO samples tested for 50 at 1250 °C.

The change in the infiltration kinetics was obvious during the initial 5 minutes and up to 5h in case of 65YZ see (**Figure 4.6**). No big change was observed after 5h until 50h. Thus, the quick apatite phase formation is critical for rapid crystallization of the glass during the initial infiltration stages. In this context, the same infiltration kinetics for GZO is assumed since only infiltration experiments were performed for 50 h it cannot be estimated how the infiltration proceeded. The comparison of the M^{I}:M^{II} composition ratios ((Ca+Mg)/(RE+Zr)) for both GZO and 65YZ samples is shown for the tested CMAS samples at 1250 °C in **Figure 4.29**. This ratio represents an effective measurement system to quantify the amount of consumed coating to crystalize the melt as apatite i.e. the higher this ratio is less TBC cations are required to promote apatite formation. This approach has been used in the literature but only considering Ca in the M^{I}

site [34]. The ratios for the compositions are closer to the defect free $M^{I}_{2}M^{II}_{8}(SiO_4)_6O_2$ apatite phase as expected from literature [119] (0.25) and only the Ca rich deposits (UCSB) come close to the ideal $M^{I}_{4}M^{II}_{6}(SiO_4)_6X_2$ phase (0.66) which maximizes the glass crystallization. The plot also shows for all the other reactions a higher M^{I}:M^{II} ratio for the 65YZ case which leads to the conclusion that Y based apatite requires less TBC material to precipitate hence, the 65YZ consumption will be less than the GZO. This hypothesis is supported by similar studies performed by Drexler et al. [146] where the comparison of GZO and $Y_2Zr_2O_7$ pellets under CMAS attack at 1200 °C showed higher infiltration for the GZO pellet. Their results showed increased CMAS resistance for $YO_{1.5}$-zirconate with less yttria contents than in these studies. They have concluded that the larger Gd^{3+} cation would have a higher tendency to occupy also the M^{I} site which increases the amount of Gd^{3+} dissolution to promote apatite formation. Their claim was supported by XRD studies which showed the formation of Ca lean apatite for GZO and Ca rich for $Y_2Zr_2O_7$. This hypothesis is supported in these studies from the compositions of these apatites which give a higher M^{I}:M^{II} ratio and higher partition coefficients for the yttria case. Besides, the Zr content in the 65YZ apatite is higher compared to the GZO which might reduce the amount of Y that is consumed to form apatite since the Zr^{4+} cation occupies the M^{II} site which in theory would be otherwise occupied by the RE^{3+} cation

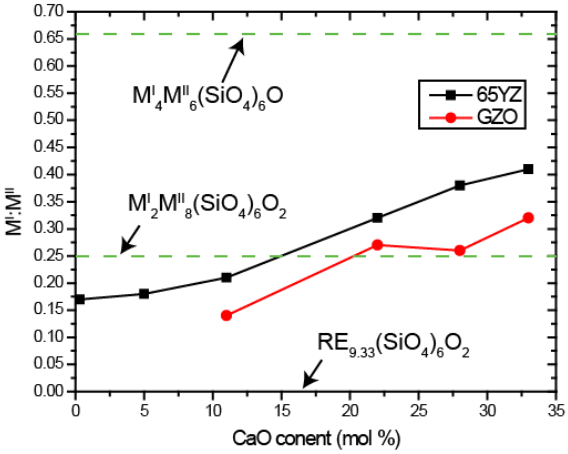

Figure 4.29: M^{I}:M^{II} ratio plot vs CaO content of the melt for the 65YZ and GZO tested samples for 50 h at 1250 °C.

Finally, the viscosity contribution from the dissolved RE in the melt plays an important role in the infiltration. As explained before Gd can reduce the viscosity of the melt more than Y. This is believed to also influence the deeper infiltration and formation of a thicker reaction layer for the GZO sample. The infiltration prediction model proposed for EB-PVD microstructures called "concentric pipe model" (as explained in Chapter 2) [31, 32] was used to estimate the infiltration of the CMAS 1 glass using all the microstructural parameters for 65YZ and GZO coatings given in **Table 1**. The viscosity of the melt at 1250 °C was 6.9 Pa.s (determined experimentally), the surface tension was 0.44 J/m^2 as estimated before [31]. The geometric factor was calculated to be 2.1 for 65YZ (using the approach from [31]) and 1.25 for GZO. The infiltration prediction assuming full wetting of the melt (zero contact angle for the melt with the TBC top surface) for 5 min is 501 and 241 µm of infiltration for GZO and 65YZ respectively. This prediction shows that the GZO microstructure promotes higher infiltration without considering any reaction. By comparing the 50 h results where the GZO was infiltrated 168 µm and the 65YZ 53 µm is clearly seen that these coatings are highly resistant to CMAS infiltration. Furthermore, the predicted values show that GZO coating would be infiltrated 2.1 times more than the 65YZ and the experimental infiltration actually indicates that GZO infiltrates 3.2 times more than 65YZ. It is believed that the increased infiltration effect for GZO in the experiments could be due to the

higher reduction in melt viscosity that Gd generates compared to Y upon dissolution. The lower viscosity of the glass should make it spread and infiltrate more into coating's porous features which means that more coating material can be dissolved promoting more reaction products. This type of behavior is in agreement with the significantly higher reaction zone produced for the GZO sample. Finally, the CMAS 1 residual melt exhibited higher Gd concentration than Y (4.8 and 2.4 mol % respectively) for the 1250 °C samples after 50 h. This shows evidence of higher Gd dissolution into the glass which could explain the significant melt spread exhibited for the GZO samples compared to the 65YZ samples due to the lower induced melt viscosity.

4.4 Conclusions

65YZ single layer coatings were tested with different CMAS/VA compounds at 1250 and 1300 °C for various time scales and with different cooling regimes. The coating exhibited coatings vigorous reaction with the CMAS/VA compounds producing primarily apatite as CMAS arresting phase including secondary reactions made of Fe rich garnet, YDS and zirconolite. Intrinsic crystallization was found in the CMAS 1 case only producing anorthite formation. The slow cooling testing process proved that the garnet phase growth is enhanced from cooling possibly due to a slow diffusion mechanism. Additionally, the formation of dendrites was also proven to form during cooling process. The 1300 °C infiltration tests for 65YZ did not show significant changes in the phase equilibria. However, only the CMAS 1 case has exhibited enlarged dendrites and highly enhanced garnet growth. The infiltration depth was higher as expected since the viscosity of the melt drops significantly compared than at 1250 °C. The 65YZ samples exhibited higher infiltration resistance and thinner reaction layer compared to GZO for all tested CMAS bearing compounds after 50 h at 1250 °C. The GZO samples exhibited also apatite as primary crystallization and secondary phases such as garnet. Additionally, is exhibited spinel phase formation as intrinsic glass crystallization. The reaction mechanisms were studied based on the phase equilibria of the reaction products used to determine which phase is more beneficial for glass

arrest and viscosity changes due to the dissolution in the melt. The current concluding remarks can be drawn from this study:

- The reaction kinetics are governed by the dissolution of the coating into the glass which upon reaching saturation limit it triggers the formation of primarily fluorite and apatite phases. The apatite phase represents the required crystalline product to quickly arrest the glass in the initial infiltration stages. Its precipitation is promoted in small glass pockets where the RE saturation limit can be achieved faster.
- Secondary reaction phases are promoted at expense of primarily reaction phases from the constant interaction with large glass deposits. The apatite phase represented the phase that allowed secondary nucleation of the garnet and YDS, whereas the fluorite phase promotes nucleation of zircon for Ca deficient deposits. A special zirconolite phase was promoted due to the high Ti concentrations that the ICE VA exhibited. Thus, for the secondary reactions Fe, Mg and Al appear to promote garnet formation whereas high Si contents promote YDS and zircon.
- The use of BI represents an effective approach to predict reaction phase formation based on the melt composition. Additionally, the Si:Ca content in the melt dictates the potency of the reaction to promote apatite formation.
- For reactions comparing GZO and 65YZ a complex synergetic mechanism that incorporates formation of slow growing garnet and higher potency of apatite formation for the 65YZ case appears to promote lower infiltration and reaction layer than for GZO. This mechanism correlates the RE ionic raidii for smaller RE cations such as Y^{3+} with formation of more stable apatite and garnet phases.
- It could be hypothesized that Gd dissolution into the molten glass would reduce the local melt viscosity more than its Y counterpart. This effect could possibly induce more infiltration in the GZO case upon dissolution into the glass.

Chapter 5: Effects of Single-layer and Multi-layer 65YZ Coatings' Microstructure on the Infiltration Mechanism

The effects of the coating microstructural features such as column configuration, columnar gap width and feather arm length in the infiltration of single and multi-layer 65YZ/7YSZ TBC produced by EB-PVD are discussed in detail. The results show that the microstructure plays a critical role in dictating the glass infiltration in addition to coating composition. In the studied coatings, the multilayer-coatings have exhibited wider columns and columnar gaps which have shown an increase in the permeability of the 65YZ top layer producing a more prominent infiltration behavior. The single layer 65YZ coatings exhibited the highest infiltration resistance (where the multi-layers were completely infiltrated) due to their more refined microstructure which incorporates thin-parallel columns (< 6.1 μm with thin columnar gaps<1 μm). In contrast the multi-layer coating exhibited columns of 11.9-9.9 μm width and wider columnar gaps of 1.1-1.5 μm width. Additionally, the column nucleation on the smooth alumina substrate (single 65YZ layer) enhances a parallel columnar growth due to the maximization of perpendicular surface interaction with the incoming deposition vapor. For rough interfaces the vapor interacts at different locations generating an irregular columnar growth, this effect is known as shadowing. Grid blasting treatment was applied on 7YSZ prior to the top layer application to achieve a smother surface. This multi-layer coating has exhibited an improved infiltration behavior due to its enhanced nucleation which generated parallel thinner columns and columnar gaps. These results prove that for an effective CMAS resistant multilayer system, the microstructure of the underlying 7YSZ coating is very critical to avoid enhanced infiltration as it was found out that the roughness of the coated surface defines the micro-structure of the top layer. A detailed study on the effects of coating microstructure and growth with respect on the glass infiltration and coating dissolution mechanism is presented.

5.1 Experimental methods

5.1.1 Coating Deposition

65YZ/7YSZ multilayer coatings were prepared by single source EB-PVD methods on 1 mm thick alumina substrates as described in **Chapter 4.** At first a 7YSZ layer of (165-220 µm)was deposited by using standard conditions denominated as "normal" in previous studies [31]. After the 7YSZ deposition, the samples were removed from the coating chamber to introduce the 65YZ evaporation source and start the 65YZ top coating deposition. Two different deposition parameters were used for the 65YZ top coatings as specified in **Table 5.1** and the produced multilayers were specified as multi-layer 1 and 2 (M1 and M2). Additionally, single layer 65YZ coatings were prepared using the same deposition conditions as reported in **Chapter 4,** and the coating was identified as single layer 1 (S1). The single layer coatings were used to compare the infiltration behavior with multilayer coatings. The deposition parameters for the single layer coating are also given in **Table 5.1**. Please note that samples S1 and M1 used the same deposition parameters for the 65YZ coating.

A set of samples were produced to analyze the effects of substrate roughness on coating microstructure. The first sample was produced by depositing a 65YZ coating on one M2 sample as substrate, the sample was denominated as "N1". An additional multi-layer coating (M3) was produced using the same S1 and M1 deposition parameters for the 65YZ layer. The M3-65YZ layer was deposited on a N1 sample. Prior its deposition, part of the top N1-65YZ overlay layer was removed via grid blasting using alumina particles at a 5 bar air pressure with a standoff distance of 15 cm. Next, the samples were ultrasonically cleaned in ethanol for 30 min and air dried for subsequent 65YZ deposition. Finally, thin 30 µm 65YZ coatings were deposited using the M1-S1-M3 deposition parameters on top of polished 7YSZ coatings. The 7YSZ underneath layer was polished with a 2500 grid size prior 65YZ layer deposition and subsequently ultrasonically cleaned as explained for the M3 sample.

Table 5.1: Summary of deposition parameters and microstructural features of the as coated 65YZ single and 65YZ/YSZ multi-layer coatings. Please note that all the deposition and microstructural parameters provided in the table are given for the 65YZ layer only.

ID	65YZ Thickness (µm)	7YSZ Thickness (µm)	RPM	Substrate Temp. (°C)	Deposition Press. (mbar)	Porosity (%)	Feather arm length (µm)	Column width (µm)	Columnar gap width (µm)
M1	81-90	165-170	12	950	6×10^{-3}	26.6 ±2	4.0 ±1.5	9.9 ±4.4	1.1 ±0.4
M2	115-125	210-220	30	850	6×10^{-3}	24.8 ±1.4	4.7 ±0.7	11.9 ±3.2	1.5 ±0.7
M3	90-100	210-220	12	950	6×10^{-3}	24.4 ±1.0	3.2 ±0.6	6.0 ±2.0	0.9 ±0.7
S1	92-100	-	12	950	6×10^{-3}	29.7 ±2.5	3.7 ±0.6	6.1 ±1.8	0.8 ±0.4
N1	100-110	210-220	6	1000	6×10^{-3}	-	-	-	-

5.1.2 Infiltration Experiments and Characterization

Short term infiltration experiments for 5 min at 1250 °C were performed under air cooling (quenching) as specified in the previous chapters. The tested CMAS sources were the same as used in the previous chapter (CMAS and VA). SEM assisted cross-section imaging was used to determine infiltration depth of the molten glass into the coatings as specified in the previous sections.

5.1.3 Contact Angle Measurements

High-temperature in-situ contact angle measurements of the melts on the coatings were performed by monitoring the molten CMAS 1 droplet with respect to temperature using a heating microscope (EM301 Hesse instruments). The CMAS 1 compound was pressed (with a stress of 1.5 $N.mm^{-2}$) into a cylindrical shaped pellet with dimensions of 3 mm diameter by 3 mm height. The pellet was placed on top of the as coated TBC samples and heated up to 1300 °C at a rate of 10 K/min in air ambient pressure. The contact angle on the sides of the samples was monitored using a 1 Hz sampling rate by a charge-coupled device camera (CCD) which captured 2D cross-sectional silhouette images of the decomposing pellets. Then, the contact angle was estimated via imaging software. More details on this method are specified elsewhere [31, 42-44, 155].

5.2 Results

5.2.1 As Coated Multi-layer TBC

The SEM images of the as coated multi-layer coatings are shown in **Figure 5.1** in both top view and cross-section. Both coatings exhibited the same type of unsymmetrically distributed pyramidal arrangement of the columnar tips similar to that of the single layer 65YZ coating (**Figure 4.1**). The cross-sectional image shows larger columnar gaps for the multi-layer coatings compared to the single layer. Besides, the columns are clearly thicker for the multilayers compared to the single layer as seen from the cross section and top view images (Figures 5.1 & 4.1). **Table 5.1** shows the summary of the microstructural features for the multi and single layer coatings. The measurements shown for the coatings clearly show an increased columnar gap width and column thickness for the multilayer coatings even though the S1 and M1 samples had the same 65YZ coating deposition parameters. The feather arm length is larger for the M2 sample case as expected since previous studies showed that high RPM (30) and low substrate temperature (850 °C) gave longer feather arm length for 7YSZ coatings [32].

The interface between the 7YSZ and the 65YZ for the multilayer coatings showed a uniform composition for each layer ($7YO_{1.5}$ mol % for 7YSZ and 67 $YO_{1.5}$ mol % for the 65YZ) as expected since it is known that the yttria diffusion into zirconia is a sluggish process [63]. Additionally, the interphase between both layers is quite difficult to distinguish (marked with arrows in figure) as seen from **Figure 5.2** which shows evidence of a smooth transition of layers or uniform 65YZ coating nucleation starting at the 7YSZ interface. Furthermore, the 65YZ columnar gap for the multi-layer coatings showed a uniform thickness throughout the 65YZ coating following the columnar gap width produced from the 7YSZ layer. This was not the case for the single layer coating (S1) by showing very thin columns (average of 2.4 ±0.6 μm thick) and columnar gaps (below 0.5 μm wide) at the alumina substrate interface as seen from **Figure 5.2c**.

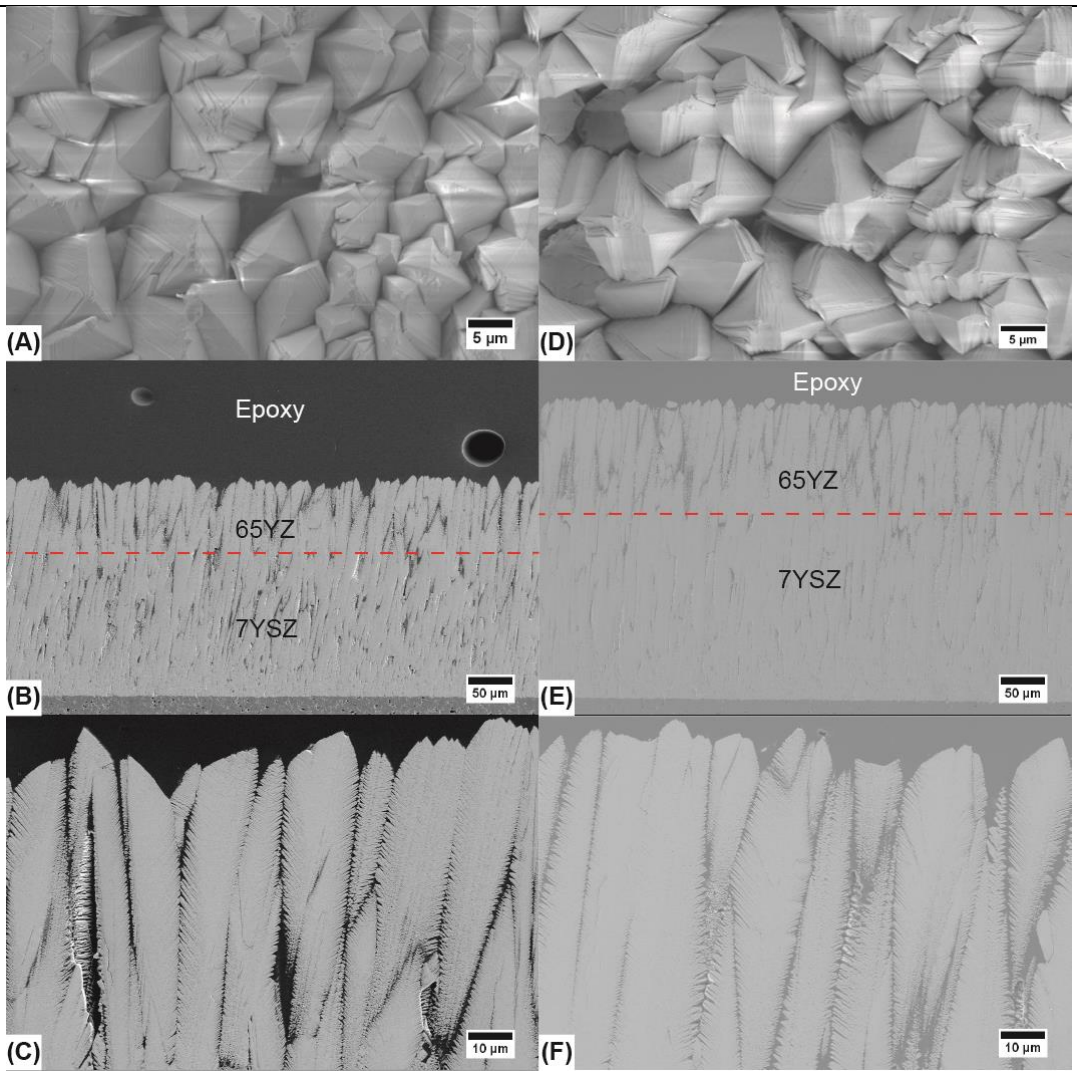

Figure 5.1: SEM imaging of the as coated multi-layer 65YZ/YSZ samples. (A, B and C) show the top view, low magnification cross-section and high magnification cross-section views respectively of the multi-layer 1 sample "M1". (D, E and F) shows the same specified views of the multi-layer 2 sample "M2". The red dashed line in B & E shows the interphase of the 65YZ/YSZ coatings. C & F show the top section of the 65YZ coating microstructure in high magnification.

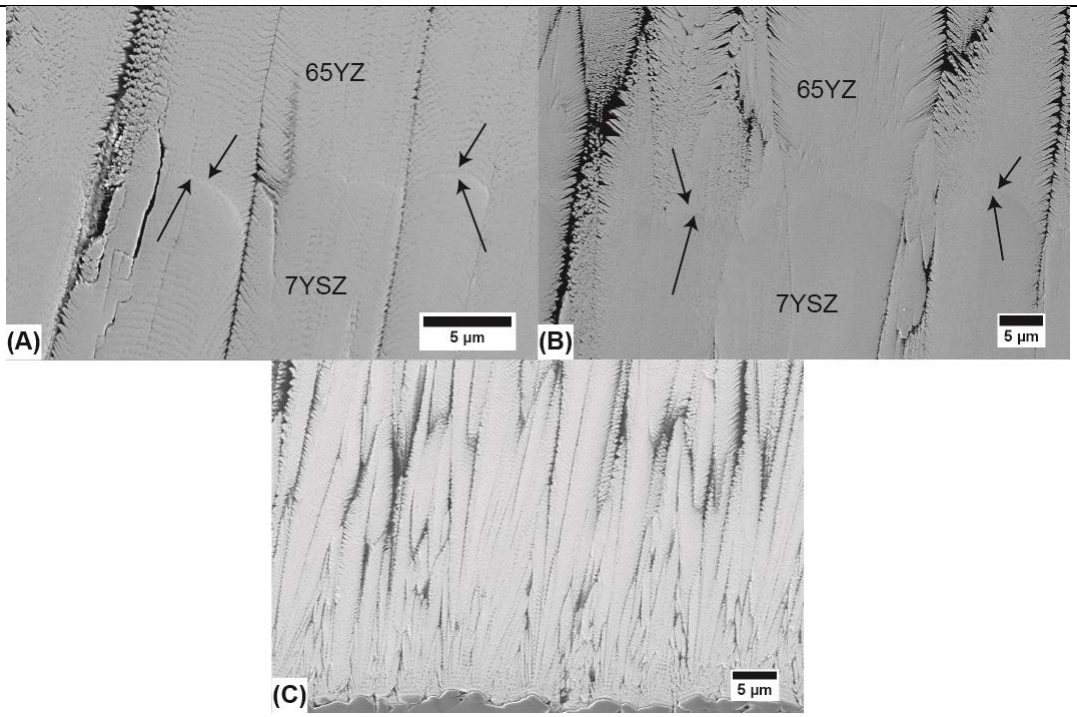

Figure 5.2: Cross-sectional SEM view of the 65YZ/YSZ interface for the M1 (A), M2 (B) samples. (C) S1 sample interface with the alumina substrate. The arrows point interface area of the YSZ columns with the 65YZ columns.

Furthermore, in localized areas for the M1 and M2 samples the 7YSZ/65YZ interface exhibited an irregular transition as shown in **Figure 5.3a**. This transition had a conical cauliflower like shape in the columns (marked in the black arrows in **5.3a**). Additionally, irregular growth of interrupted columns was detected at areas with large roughness difference (8 to 10 µm) from the column pyramidal tips with respect to the base of the pyramid as shown in **5.3a** (marked in a black rectangle). The effect controlling this irregular growth is known as shadowing and its characteristics are discussed in more detail in the discussion section. At these areas, large columnar gaps (>2 µm) were distinguished. In this context, the 65YZ/65YZ interface of the N1 sample also showed this irregular cauliflower like growth as seen in the black arrows in **Figure 5.3b**. From this figure is seen that the larger feather arms from the 65YZ M2 layer appear to act nucleation sites for the new 65YZ columns. As these columns grow in the lateral rough areas of the column tips (marked in the red dashed circle in **5.3b**) their growth is interrupted leaving a columnar gap.

These larger gaps (>2 µm marked with a black rectangle in the figure) appear to be more prominent in the irregularly nucleated N1 layer. In contrast, the test multi-layer sample produced by the deposition of the 65YZ coating on a 7YSZ polished sample is shown in **Figure 5.3c**. The figure shows a parallel columnar growth at the flat polished zone (black arrows) compared to the irregular growth produced at the rough area (red arrow). This shows that surface preparation of the substrate is required to produce parallel columnar growth with reduced columnar gap thickness.

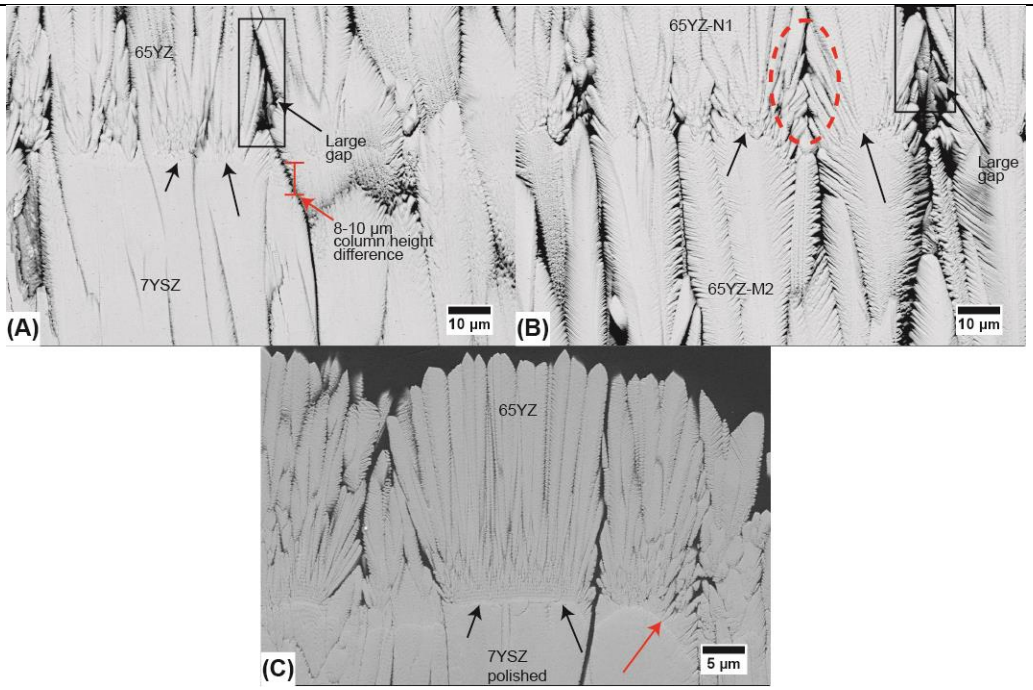

Figure 5.3: Cross-sectional SEM image of the as coated M2 sample at the 7YSZ/65YZ interface (A), N1 sample at the 65YZ/65YZ interface (B) and polished sample at the 7YSZ/65YZ interface (C). .

Finally, the grid blasted M3 multi-layer sample microstructure is shown in **Figure 5.4**. It is seen from **5.4a** and **b** that the 65YZ top layer appears to grow more parallelly with thinner columns and columnar gaps compared to the other multilayers. The nucleation site shown in **5.4c** (black arrows) exhibits a similar nucleation of thin more parallel columns with lesser shadowing influenced growth as also exhibited for the S1 sample (**Figure 5.2c** and **4.1**). The sample exhibited in general close column and columnar gap width compared to the S1 samples as shown in **Table**

5.1. The columnar gaps at the nucleation area (at the grid blasted surface) shown in **5.4c** exhibited a width of ~0.62 µm which is a slightly higher value than the S1 sample (0.55 µm max).

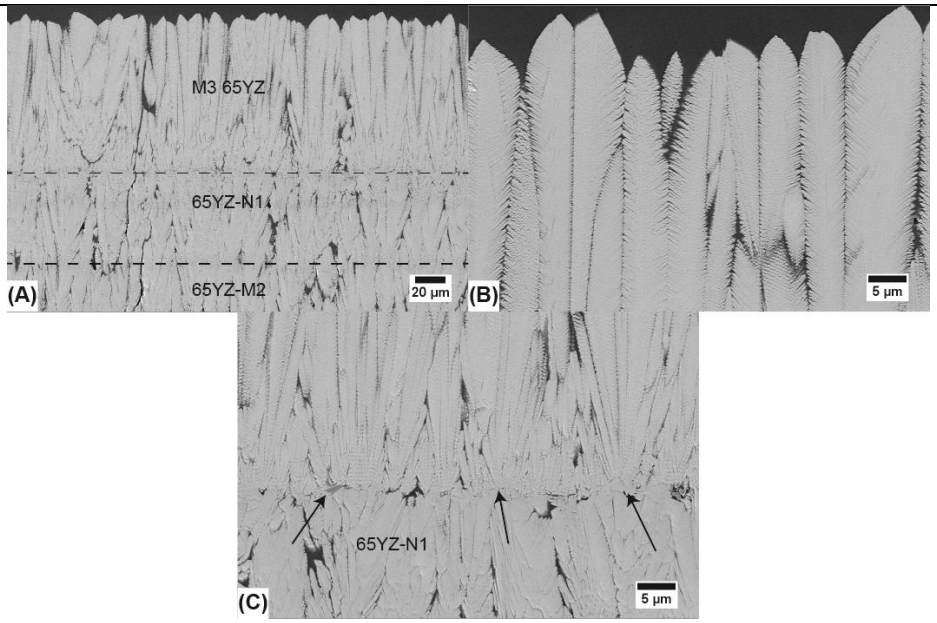

Figure 5.4: Cross-sectional SEM images for the ass coated M3 sample in (A) low magnification, (B) high magnification at the top columnar zone and (C) high magnification at the interface with the grid blasted 65YZ N1 layer.

5.2.2 CMAS/VA Infiltration

The microstructures of CMAS 1 and COL infiltrated multilayer coatings are shown in **Figure 5.5** after 5 min at 1250 °C (air quenched). The rest of the SEM images of the tested CMAS/VA for 5 min are provided in the appendix C section. Both multi-layer samples exhibited full infiltration of the complete coating system (65YZ and YSZ) reaching even the alumina substrate in case of CMAS 1. This represents a poor infiltration resistance compared to the single layer coating which exhibited an overall infiltration depth of 42 µm even with the same 65YZ deposition parameters used for M1 coating. However, it is clearly seen from the figure that the smaller gaps (marked with arrows) did not show complete infiltration whereas all the larger columnar gaps allowed the infiltration. Only the Popo and COL VA which exhibited the lowest

viscosity (as seen in **Figure 4.27**) did not fully infiltrate the 65YZ layer. For the M1 case the overall infiltration depth was 75 μm. The Popo sample showed an overall infiltration of 80 μm and in some wider gaps it reached the 7YSZ coating about 10 μm. For the M2 case the COL VA showed an overall infiltration of 82 μm. Since the M2 sample had a 130 μm thick max 65YZ layer, the Popo VA was found to infiltrate 110 μm in average and also reached the 7YSZ layer in some of the wider gaps. Furthermore, the area marked in the red rectangle in **Figure 5.5b** for the COL VA shows a large columnar gap with consequent severe columnar degradation due to the VA glass dissolution. This was also found for the Popo VA (see appendix C). Both the CMAS compounds and ICE VA have not shown such severe columnar consumption upon glass dissolution compared to that of POPO and COL. A detailed explanation of this enhanced column degradation with respect to TBC microstructure is given in the discussion section.

Next, the same reaction products were found in both the single and multi-layer coatings i.e. apatite and fluorite as the primary reaction products and garnet as the secondary product[6]. **Figure 5.6** shows the reaction formed at the 7YSZ/65YZ interphase for CMAS 1 after 5 min at 1250 °C for the M2 sample. It is distinguished in the figure how the formation of reaction products is generated only in the 65YZ layer, whereas in the 7YSZ layer no reaction product formation is distinguished. This shows evidence of the poor ability that 7YSZ exhibits to promote glass reaction. The glass composition at the infiltrated columnar gap right at the 65YZ/7YSZ interface yielded $Mg_{1.8}Al_{4.4}Si_{8.1}Ca_{6.6}Fe_{3.2}Y_{7.5}Zr_{68.3.}$ This shows that the dissolved yttria is not enough to promote apatite formation. In contrast, the Zr content dissolved in the glass is very high compared to the other oxides which promotes formation of YSZ based phases possibly monoclinic or tetragonal.

[6] Note that YDS and zircon were not found as secondary reaction products for these 5 min infiltration tests since their nucleation time requires long term infiltration as presented in the previous chapter.

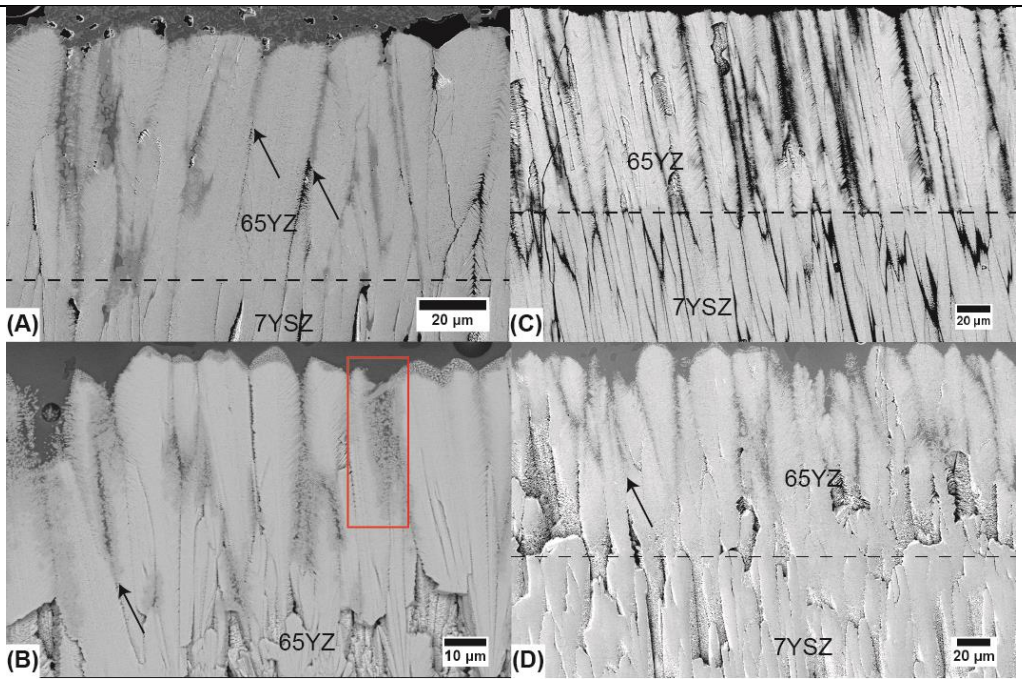

Figure 5.5: Cross-section SEM images of the M1 samples infiltrated by (A) CMAS 1 and (B) COL VA. (C) and (D) represent the M2 samples infiltrated by CMAS 1 and COL respectively. The infiltration tests were performed for 5 min at 1250 °C followed by air quenching. The dashed line in A, B and D show the 65YZ/7YSZ interface. The arrows point partially infiltrated columnar gaps.

The infiltration of the M3 grid blasted sample with CMAS 1 only at 1250 °C for 5 min is provided in **Figure 5.7**. The CMAS 1 glass infiltrated only about 65 µm in average as shown delimited by the red dashed line. It is seen that at the area close to the 65YZ/7YSZ interface (marked with black arrows in **5.7**) the infiltration is arrested due to the thinner columnar gaps closer to the interface. In comparison with the other multi-layer samples tested with CMAS 1 (complete infiltration of 65 and 7YSZ layers), the M3 sample exhibited a significant resistance. However, the M3 infiltration was higher compared to the S1 sample (42 µm) which still shows higher resistance for the single layer coatings. Finally, the infiltration resistance of the M3 sample was only tested against CMAS 1 just to quickly compare how surface treatment of the substrate influences the infiltration.

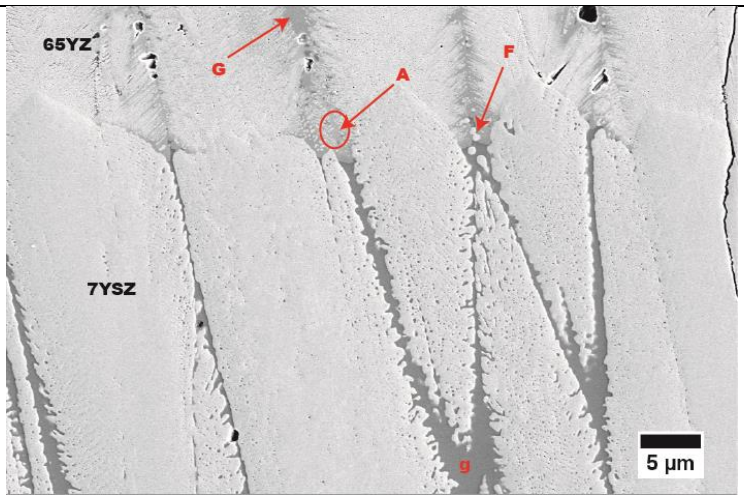

Figure 5.6: SEM cross-sectional image of the CMAS 1 infiltrated 65YZ/YSZ interface for the M2 sample. The sample was infiltrated for 5 min at 1250 °C followed by air quenching.

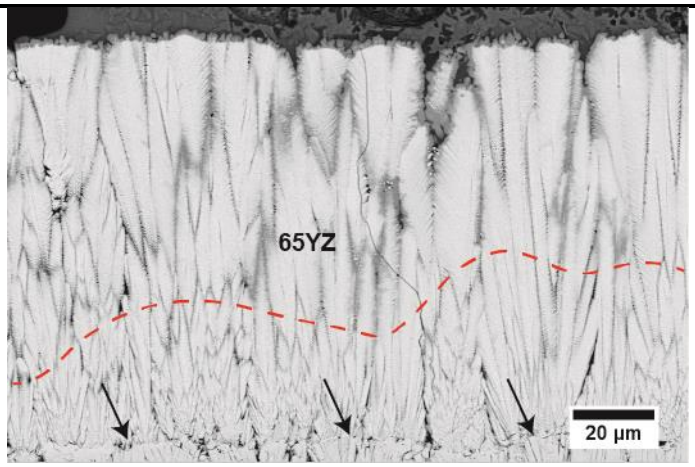

Figure 5.7: SEM cross-sectional image of the M3 sample infiltrated by CMAS 1 at 1250 °C for 5 min.

5.2.3 Contact Angle for Single and Multi-layers

The contact angle images are shown in **Figure 5.8** for the CMAS 1 pellets on top of the S1, M1 and M2 samples at temperatures ranging from 1268 to 1277 °C. The results clearly show that for the same testing temperature the single layer coating (S1) produced a higher contact angle (less wetting) compared to the multi-layer samples (both M1 & M2). At 1268 °C the cylindrical pellet shape was partially lost giving a contact angle (CA) of 54° for the S1 sample. At this same

temperature the shape of the multi-layer samples is completely lost forming a hemisphere with a 40° and 48° CA for the M1 and M2 samples respectively. The higher CA is still produced for the S1 sample at 1277 °C (22°) compared to the M1 (17°) and M2 (19°). This reduced CA with CMAS 1 was also reported previously in YSZ samples with two different microstructural conditions [31]. In those studies, the YSZ coating with thinner TBC columns (denominated as feathery) yielded a CA of 53° at 1266 °C. This was higher compared to its counterpart with thicker columns (denominated as normal) which produced a CA of 35° at 1266 °C. Thus, by producing a thinner columnar structure a reduced wetting on the coating can be achieved which could be beneficial for infiltration resistance. This CA effect in infiltration will be addressed in detail in the discussion section.

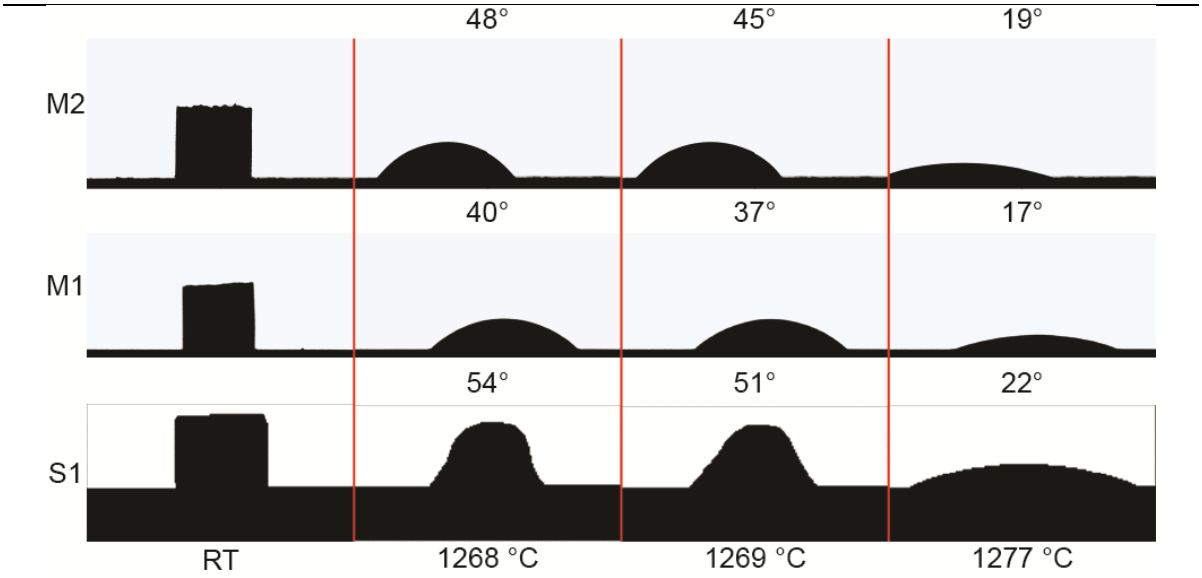

Figure 5.8: Heating microscope imaging for the CMAS 1 on top of the single and multi-layer TBC coated samples at room temperature (RT) and high temperatures.

5.3 Discussion

As mentioned before an effective CMAS resistant coating requires a reactive material that upon interaction with the molten glass promotes its crystallization into phases that grow beneficially sealing the gaps. The most recognized reactive phase with such characteristics in the

initial stages is apatite. Furthermore, our current results show that the microstructure configuration of the TBC plays the most important role in reducing infiltration kinetics of the melt. This claim is supported by the complete infiltration of the CMAS/VA glass into the 65YZ layer in multilayer-configuration compared to the single layer coating which was not completely infiltrated. This effect is directly compared with the M1 and S1 samples which had the same deposition parameters but exhibited an infiltration difference of 1.6 times more for the M1 sample with the COL VA. By varying the deposition parameters in the M2 case the COL infiltration is increased 1.7 times more compared to the S1 case. From **Table 5.1** it is seen that the 65YZ coating for the multi-layer case exhibited thicker columns and columnar gaps. These variations in microstructure appear to be critical to control the glass infiltration. Conversely, the overall porosity for the S1 sample was the highest which leads to the conclusion that the interplay of columnar gap-column dimensions is more critical for infiltration.

Additionally, the coating dissolution rate to promote apatite formation will be expected to vary with respect to columnar gap width since large glass volumes (exhibited in large columnar gaps) will require larger TBC dissolution to promote apatite formation. This is expected to play also an important role in infiltration.

5.3.1 Microstructural Effect on Infiltration

The permeability (k) of the coating represents a critical parameter that controls how fast the coating will be infiltrated i.e. higher k means faster infiltration as seen in **Equation 7**. Additionally, this value represents a variable that can be controlled from the deposition technique in the case of EB-PVD TBCs therefore, by tuning the TBC microstructure increased infiltration resistance can be achieved [31, 32]. The concentric pipe model approach was used to determine the permeability of the coatings with respect to a varying columnar gap and column radius which is shown in **Figure 5.9**. The values were estimated using **Equation 8.** in conjunction with the microstructural parameters estimated for the tested coatings (porosity, column width and columnar gap width) given in **Table 5.1.** The geometric factor (τ) was estimated as described in the previous

chapter for each coating giving the values of 2.7, 1.31 and 2.1 for the M1, M2 and S1 samples respectively. It is important to stress that τ also represents a critical parameter which is believed to be controlled by the distribution of feather arms to split the glass flow more efficiently thus, delaying gap infiltration. Besides, the *k* values shown in **Figure 5.9a** are estimated by keeping the column width (or diameter assuming the column as a kernel "a") as a constant parameter and the columnar gap width (or diameter assuming the gap as a concentric pipe "b") as a varying parameter. The figure clearly shows that the variation of the columnar gap has a high influence in the overall coating permeability. In this context, *k* was estimated as well for each coating using the opposite approach (**Figure 5.9b**) by keeping now the columnar gap constant and the column width as a varying parameter. The results showed negligible changes in permeability with respect to a large varying column width (from 4.3 to 15.5 μm) since the highest variation was exhibited for the M2 sample giving *k* values ranging from 6.775×10^{-3} to 6.784×10^{-3} μm^2. Furthermore, the actual *k* for each coating with their estimated column and columnar gap radius is provided in **Figure 5.9a** where it can be seen that *k* for the M2 sample is 6.8×10^{-3} which represents the same estimated value seen in **Figure 5.9,** the same case was noticed for the other coatings. This shows that for an EB-PVD coating system that the columnar gap radius is orders of magnitude more critical for infiltration than the column size referring to permeability only. The *k* estimation in **5.9a** for the M1 and S1 coatings (which had the same deposition parameters for the 65YZ layer) showed that the M1 permeability in general is lower than the S1 (i.e. higher infiltration would be expected for the S1 sample). However, for the current estimated column and gap parameters for each sample the *k* was lower for the S1 sample (9×10^{-4} μm^2) compared to its M1 counterpart (9.2×10^{-4} μm^2).

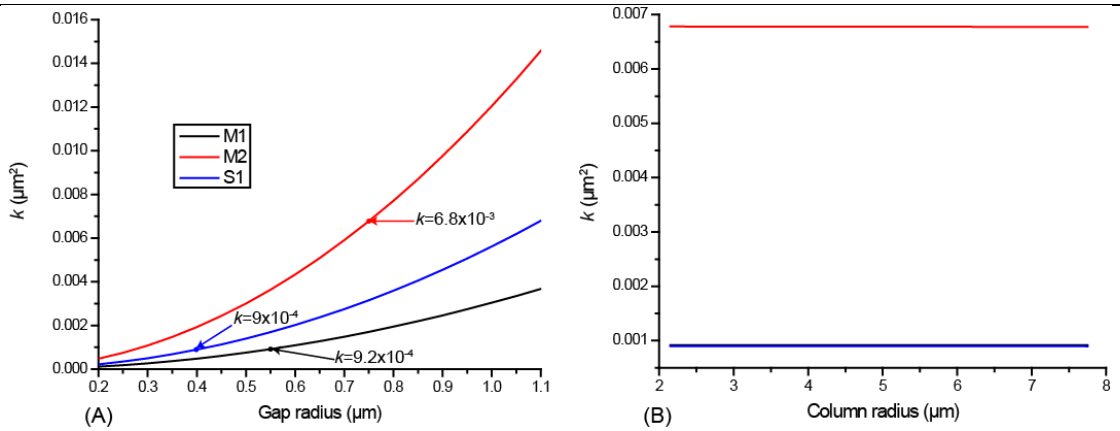

Figure 5.9: Calculated permeability (k) for the tested samples by (A) varying columnar gap radius and (B) varying column radius. The k values are provided in (A) for the specific microstructural parameters for each coating provided in **Table 5.1.** The k values in (B) represent the same specific value for each coating given in (A). Please note that the M1 and S1 samples values in (B) are overlapping since they are very close to each other ($9x10^{-4}$ for S1 and $9.2x10^{-4}$ for M1).

Although permeability represents an important factor controlling the glass infiltration, other fluid properties also play a prominent role in infiltration such as viscosity and contact angle (CA) as seen in **Equation 7**. The CA varies with respect to the TBC column width, e.g. giving a higher CA for the thicker columns of the multi-layers (M1 and M2) than the thinner columns of the single layer coating (S1) as presented in **Figure 5.8**. Thus, the infiltration model (**Equation 7**) predicts that coatings with lower wetting (e.g. higher CA) would be more resistant to infiltration. This CA effect is believed to partially influence the higher infiltration resistance of the S1 sample compared to the multi-layer samples. The CMAS 1 infiltration prediction for 5 min heat treatment at 1250 °C is shown in **Figure 5.10** a varying the contact angle on the X-axis (assuming no coating dissolution)[7]. Since the CA results showed that the coatings were not fully wetted (CA=0) the prediction shows a significant variation in infiltration depth with respect to CA from full wetting (zero degrees) to 70°. The heating microscope tests did not show a CA at 1250 °C for all of the tested samples, this could be due to the temperature calibration setting in the instrument which

[7] The prediction was only given for CMAS 1 since the CA data was obtained only for this compound. Besides, its viscosity was determined experimentally at various temperatures in previous studies [31].

could be off by 10 to 15 K higher. However, since infiltration was generated at 1250 °C of all the samples considerable wetting must be produced on the top surface generating a CA which promotes infiltration. Therefore, the estimated infiltration values for each sample provided in **5.10** are given for the CA generated at 1268 °C in **Figure 5.8**. Additionally, the viscosity considered for the estimation at 1250 °C was obtained from the extrapolated values obtained from the experimentally estimated viscosity for CMAS 1 (6.8 Pa.s) [31]. These predictions are quite close with the multi-layer coatings which showed complete coating infiltration (260 and 345 μm for M1 and M2 respectively) assuming no reaction with yttria. For the S1 case sample, the infiltration depth was clearly improved since the CMAS 1 sample was infiltrated 42 μm after 5 min. This represents 4.4 times less compared to the 184 μm predicted. This improved infiltration resistance is believed to be due to the enhanced sealing of columnar gaps by reaction products for the S1 samples close to the substrate due to thinner columns produced at this zone (promoted by low shadowing from the smooth substrate). Furthermore, the infiltration depth was predicted as well for 5 min using the experimentally determined viscosity at 1300 °C for CMAS 1 (2.5 Pa.s) [31] to compare how the infiltration changes at lower viscosity regimes. The predicted values at 1300 °C assumed a full wetting of the coating (CA=0) since the highest CA reported for S1 at 1277 °C was 22°, thus, it is expected that at such high temperature the CMAS 1 compound will completely wet the TBC surface. The infiltration estimation for M1, M2 and S1 was 334, 797 and 401 μm. Compared to the infiltration at 1250 °C with a CA=0 (201 μm for M1, 480 μm for M2 and 241 μm for S1) this represents a 67 % increase in infiltration at higher temperatures. Since current industry goals to push engine operating temperatures ≥ 1500 °C [10], a high importance on optimized coating microstructure must be addressed to meet safe engine operation against CMAS attack.

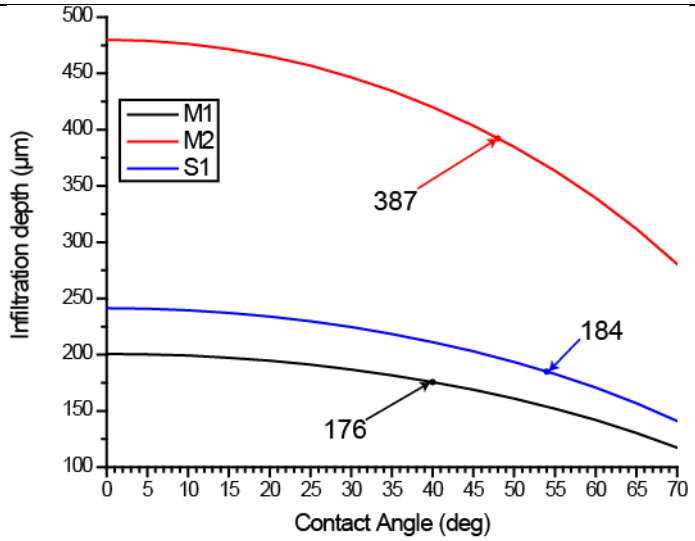

Figure 5.10: CMAS 1 infiltration prediction of the tested 65YZ single and multi-layer samples at 1250 °C for 5 min. The prediction is also given with varying contact angles and the actual infiltration predicted values for the CA specified at 1268 °C in **Figure 5.8** are marked.

The infiltration prediction for the M1 sample was lower (176 µm) compared to the infiltration prediction estimated for the S1 sample (184 µm) using all the estimated variable parameters (CA, τ and *k*). Although, the predictions were very close still the S1 sample exhibited much higher infiltration resistance (42 µm after 5 min at 1250 °C) than the M1 sample regardless of the fact that both 65YZ layers were coated under the same conditions but with different substrate roughness (1-2 and 5-7 µm for S1 and M1 respectively). This increased infiltration resistance for the S1 sample is believed to be due to the thinner columnar gap exhibited at the alumina substrate interface (0.55 µm thick max). In contrast, the multi-layer coatings exhibited the same columnar gap width as of the 7YSZ layer which ranged above 1 µm thick in average. As seen in **Figure 5.9a** the permeability at low gap radius <0.25 µm compared to radius> 0.5 µm varies by one order of magnitude. Therefore, the very low *k* exhibited for the S1 sample as it gets close to the alumina substrate due to its thin columnar gaps improves its infiltration resistance compared to the multi-layer coatings. It is important to note that thinner columns promote enhanced crystallization of the apatite phase (as discussed in the next section). This is believed to be the key factor dictating the lower CMAS infiltration for coatings with thin columnar gaps.

It is well known that rougher substrates produce lower coating refinement by leading to coarser columns and larger gaps in the case of EB-PVD TBCs. These non-refined coating characteristics are controlled by the induced uneven column growth at rough interfaces. At these interfaces (e.g. column feather arms and rough generated hills on the substrate) the incoming vapor produces initial column nucleation at the top hill areas in the substrate (highest points). As the columns located at the upper areas start to grow, they block the incident incoming vapor for the other growing columns located at the lower hill areas restricting their growth. Thus, formation of a large columnar gap is generated and subsequently the upper columns begin to coarsen as they accumulate more area of vapor deposition. This effect is known as "shadowing" and it is commonly controlled by the substrate surface preparation which requires a smooth surface to provide even column nucleation and lower shadowing effect. **Figure 5.11** shows the S1 as coated sample on a smooth alumina substrate (1-2 μm roughness) compared to the same S1 as coated sample on a rough steel substrate (>7 μm roughness). It is clearly seen how the sample produced on the rough steel substrates generated a cauliflower-like growth with large columnar gaps compared to the alumina substrate samples In addition, this irregular growth appears to be suppressed when polishing or grid blasting of the rough 7YSZ-65YZ layer is done prior 65YZ deposition as shown in figures **5.3** and **5.4**. As shown before, the CMAS 1 infiltrated sample exhibits an improvement in the infiltration behavior compared to the other multi-layers by arresting the CMAS glass within the outer 65YZ coating exhibiting an overall infiltration depth of 65 μm. This proves that coating microstructure (i.e. columnar gap thickness and parallel columnar growth) has a critical impact in the overall infiltration. Therefore, from these results it is concluded that an effective multi-layer CMAS resistant system must incorporate an optimized 7YSZ layer with parallel columns to avoid uneven shadowing growth and small columnar gaps < 1 μm so the 65YZ layer can follow a similar coherent growth maintaining a small gap. In this context, experiments performed on multi-layer 7YSZ-GZO EB-PVD systems show that using a smooth transition in evaporation source (from 7YSZ to GZO) inside the coating chamber in a single run rather than using two different runs for 7YSZ and GZO individually (avoiding the vacuum and temperature

breaks) avoids the cauliflower growth [156]. Additionally, a thinner 7YSZ layer (50-90 μm) should be used so the 65YZ top coating can grow more parallel. This use of thin 7YSZ under layer for multi-layer coating systems has been reported in literature [112].

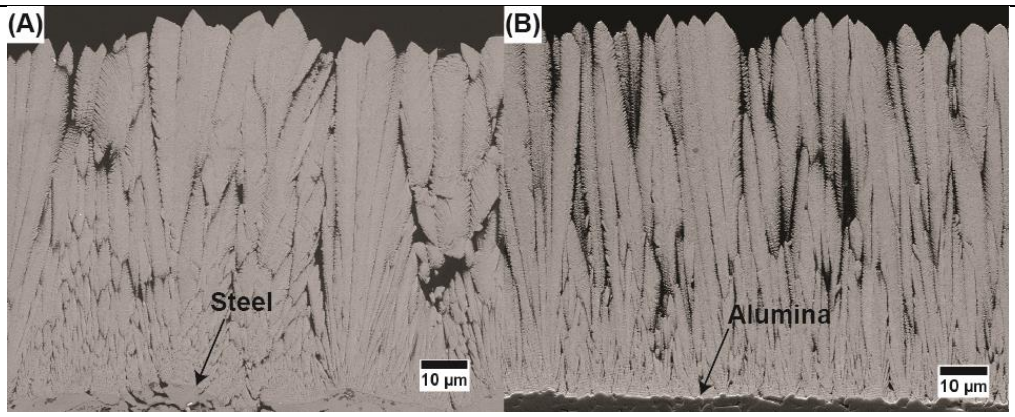

Figure 5.11: Cross-section SEM images for the as coated S1 samples on (A) steel and (B) alumina substrates.

5.3.2 Microstructural Effect on Dissolution

The microstructure plays an important and equivalent role in the dissolution mechanism of the coating in to the melt during the glass/coating interaction. A clear example of this effect can be seen for large glass volumes accumulated in large columnar gaps which require larger amounts of dissolved TBC to promote apatite and fluorite formation than in small gaps. **Figure 5.12** shows the initial reaction scenario after the infiltration of CMAS 2 (**5.12a**) and Popo VA (**5.12b**) at 1250 °C after 5 min in S1 samples. It is clearly seen that the smaller gaps were sealed by the reaction products and did not experience deeper penetration. (marked with single black arrows) for both compounds. In contrast, larger columnar gaps as shown in the red dotted rectangle exhibit deeper infiltration and more coating consumption. This is due to the higher dissolution of coating required to crystallize a specific glass volume. Additionally, a large apatite crystal appears to cross and partially block the columnar gap in the CMAS sample marked in the red dotted rectangle. In contrast, the Popo VA exhibits smaller faceted apatite crystals which seem to be dissolved in the

large glass pocket (large columnar gap). This effect on apatite crystallization can be explained by using mass balance for the chemical reaction at the large gap glass interaction.

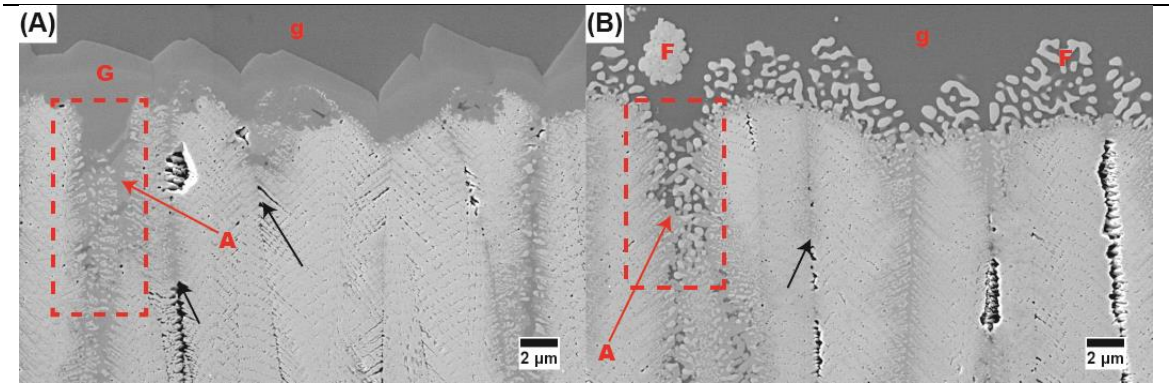

Figure 5.12: Cross-sectional SEM image of the S1 samples reaction zone of the 5 min infiltrated at 1250 °C for (A) CMAS 2 and (B) Popo VA.

The theoretical chemical reaction generated at columnar gaps with varying thicknesses as seen in **Figure 5.13** is approximated for CMAS 2 and Popo reacting with 65YZ below in **Equations 12 & 13**. They are used as examples since they represented the melts with the highest (CMAS 2) and lowest (Popo) Ca content from the tested compounds. The mass balance estimations assume a control volume of 1:1 (CMAS:65YZ) for simplification which represents a large columnar gap scenario as seen in **5.13a**. Besides, the reaction was simplified to only apatite and fluorite crystallization. The defect free $Ca_2Y_8(SiO_4)_6O_2$ apatite is assumed as primary reaction product. It is seen for this control volume that the reaction yields larger apatite crystallization (9 times more) for CMAS 2 compared to Popo VA due to its very high Ca content. Besides, the glass residue from the Popo VA is 2.1 times higher in volume than CMAS 2 and a larger content of retained Y in the glass. By comparing the amount of Y in the apatite and in the glass residue (Yap:Yres) the CMAS 2 an estimation of seized Y for apatite formation can be provided i.e. high Yap:Yres means less coating is consumed for apatite crystallization. The ratios for CMAS 2 and Popo were 3.3 and 0.7 respectively. Henceforth, the higher Ca bearing CMAS/VA melts require less coating dissolution to promote apatite formation. Furthermore, by comparing these ratios for

columnar gaps 4 times thinner (e.g. CMAS to TBC content equal to 0.25:1 as shown in Figure **5.13b**) using the same approach as shown in the mass balance, the ratios increase to 23.8 for CMAS 2 and 1.7 for Popo VA. These results prove that the microstructural configuration of columnar gap width plays a critical role as well in the dissolution in order to arrest the glass faster requiring lesser amount of dissolved coating.

Equation 12

$$C_{28}M_{10}A_{18}S_{35}F_7T_1 + Y_{67}Z_{33}$$
$$\rightarrow 0.9C_{12.5}Y_{50}S_{37.5}(apatite) + 0.4Z_{84}Y_{16}(fluorite)$$
$$+\ 0.7C_{24.2}M_{16.3}A_{26.7}F_{10.4}T_{1.5}Y_{20.8}(residue)$$

Equation 13

$$C_{0.5}M_{0.5}A_6S_{59}F_7T_1L_{26} + Y_{67}Z_{33}$$
$$\rightarrow 0.1C_{12.5}Y_{50}S_{37.5}(apatite) + 0.4Z_{84}Y_{16}(fluorite)$$
$$+\ 1.5A_{3.9}S_{36.7}F_{4.6}T_{0.7}Y_{37.1}L_{17}(residue)$$

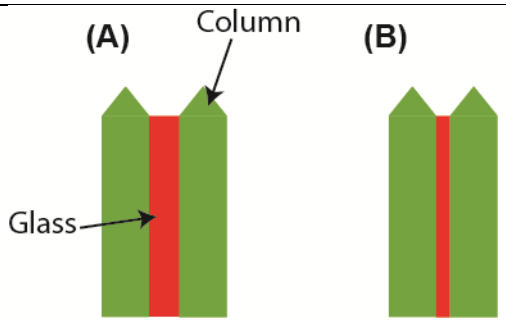

Figure 5.13: Schematic of control volumes used for mass balance estimations for (A) glass-TBC mixtures of 1:1 and (B) 0.25:1

Finally, the feather arm length and distribution with respect to the columnar gap width (or radius assuming a concentric pipe) represents a critical variable that controls the permeability of the coating, this parameter was identified as geometric factor (τ). Previous experiments with 7YSZ

samples with different feather arm configurations showed that the TBC with longer feather arms exhibited lower glass infiltration. It was reported that this infiltration resistance was enhanced by the distribution or splitting of the melt into the feather arm capillaries which reduce the glass volume that flows in to columnar gaps and delays infiltration time [31, 32]. Conversely, for the 65YZ samples the M2 sample which has exhibited larger feather arms compared to M1 and S1 (4.7 μm long) were dissolved very fast by the low Ca bearing VA such as COL and Popo. **Figure 5.14** shows the M2 sample after Popo VA infiltration for 5 min at 1250 °C. The figure shows a large gap with a degraded column (marked in the red dotted rectangle in **5.14a**) and needle like shaped apatite crystals protruding out from the side of the column coming following the foot prints of feather arms. As shown before from the mass balance, the Popo VA requires a large amount of coating dissolution to promote apatite crystallization due to its low Ca content. Since the long feather arms represent the zones with higher specific surface area compared to the overall column, it is expected that their dissolution rate will be faster compared to the column core. This increased dissolution mechanism increases the columnar gap width (b parameter) further and reduces the column radius (a parameter) as shown in the **5.14b** schematic. Thus, this enhanced dissolution at the feather arm could generate an increase in the overall coating permeability enhancing its infiltration. This case was not very prominent for CMAS 2 since from the Yap:Yres ratio for small gaps CMAS 2 exhibits a 14 higher ratio than Popo meaning that in theory it would require 14 times less coating dissolution to promote apatite formation at the feather arms than the Popo VA. For this reason, this feather arm dissolution for high Ca bearing compounds is not as prominent as for COL and Popo VA as seen in **Figure 5.12a** for the CMAS 2 compound which clearly shows formation of large apatite crystals and garnet.

Since CMAS/VA sources exhibit a varied chemical composition it is seen from these results that microstructure plays a prominent role in overall infiltration with respect to different Ca bearing compounds. Therefore, for an aero-engine that can be exposed to different CMAS melts, it is critical to develop CMAS resistant systems with engineered microstructures that are able to provide a robust operation under a wide spectrum of chemical compositions. This enhanced

infiltration due to microstructure has been reported as well for GZO produced by APS and solution precursor plasma spray (SPPS) where complete infiltration in gaps/cracks thicker than 1 µm was found [113]. From the exposed results, enhanced infiltration resistance can be achieved by producing small gaps (<1 µm) in conjunction with a controlled growth of the 7YSZ layer, in addition to providing shorter feather arms (for special cases with low Ca compounds).

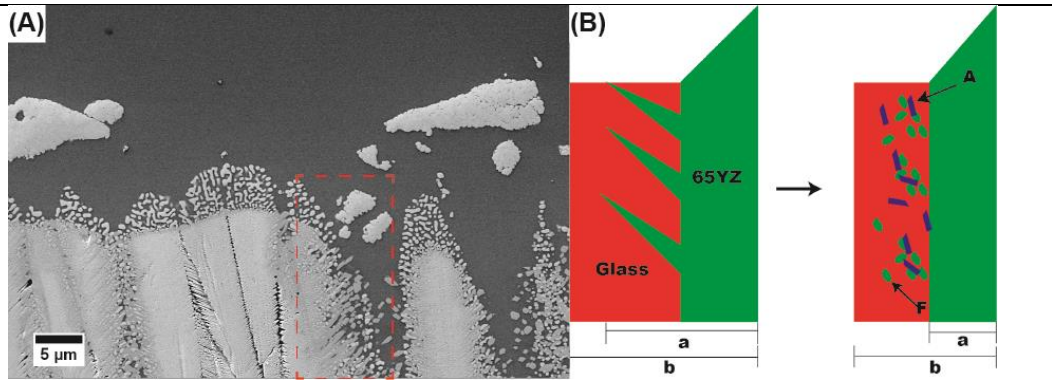

Figure 5.14: (A) Cross-sectional SEM image of the M2 Popo infiltrated sample for 5 min at 1250 °C. The red dashed rectangle shows a large columnar gap dissolving the feather arms. This are is exemplified in (B) where the radius of the column including its feather arm length (a) and the radius of the column plus the columnar gap width (b) are shown at the initial infiltration for a symmetrical columnar section. Then the dissolved feather arms show dispersed reaction products and increase the b parameter.

5.4 Conclusion

The effects of coating microstructure on the infiltration behavior of different CMAS/VA compounds for single and multi-layer 65YZ-7YSZ coating systems was studied in detail for short term infiltration regimes (5 min) at 1250 °C. Several multi-layer coatings were tested against CMAS infiltration and have resulted in full infiltration of the (65YZ) coating. Only exception was the high viscous COL and Popo VA which did not completely infiltrate the top 65YZ layer for the tested multi-layers. In comparison, the single layer sample as shown in previous chapters as well has exhibited much better infiltration resistance (less than 50 % of coating infiltration for all the CMAS/VA compounds). This is due to the thinning of the gaps close to the substrate from the

controlled coating nucleation produced from the smooth alumina substrate. These thinner columns generate lower coating permeability and enhanced apatite phase formation which promote faster CMAS arrest. The infiltration resistance was improved in the multilayers (65 μm deep into the 65YZ top layer) by using surface modification via grid blasting the coating prior deposition. This treatment promoted the nucleation of thinner columns and gaps at the deposited interface. The results showed that microstructure plays a critical role in dictating glass infiltration and dissolution rate in the system. The following conclusions can be drawn from these experiments:

- The columnar gap plays a more prominent role than the column radius in increasing-reducing the coating permeability which enhances the glass infiltration.
- For an effective CMAS resistant multilayer system a functional combination of thin columnar gaps (< 1 μm) for the 7YSZ and 65YZ layers is required so the driving force for reaction kinetics can surpass the infiltration kinetics.
- Special attention has to be paid to the engine operating temperature since very low viscous melts at temperatures > 1400 °C exhibit very large driving force for infiltration kinetics which might not be counteracted by the reaction kinetics of the CMAS resistant layer.
- The nucleation of the top CMAS resistant layer must be coherent with the lower 7YSZ layer by using surface treatment of underlying coating prior deposition or by fast change of evaporation source within the coating chamber.
- The dissolution rate is also controlled form the microstructure by showing that higher amount of coating must be dissolved to promote apatite formation for large columnar gaps. The feather arm length appears to promote larger columnar gap upon dissolution for low Ca bearing compounds leading to enhanced coating infiltration.

Chapter 6: Thermal Gradient Testing of Multi-layer TBC systems Under CMAS/VA Attack

Multi-layer 65YZ/7YSZ coatings produced by EB-PVD were tested under thermal gradient conditions in the as coated and CMAS 1/ICE infiltration attack. The as coated double layer coating was tested under thermal cycling conditions. The samples were heated for 5 min (1250 °C and 1100 °C being the TBC and TGO temperatures respectively) with an oxygen methane burner rig and cooled down to room temperature and kept for 3 mins. i.e. one cycle means 5 min. heating time and 3 min. cooling time. 30 % spallation of the total coating surface area was considered as the failure of the coating and cyclic testing was stopped. The results show relatively good cyclic life time for one tested multi-layer coating by lasting up to 1425 cycles. The CMAS 1 infiltrated sample (1250 °C for 1 h) showed only a partial infiltration of the 65YZ layer (about 40 μm). However, the 65YZ top layer spalled off at the 65YZ/7YSZ interface after the cooling phase due to the cold shock. This interface represented a weak area where cracks were promoted easily. Additional infiltration tests at 1300 °C with ICE and CMAS 1 for1 hour were performed. The results showed an increased damage exhibiting the complete 65YZ coating spallation for the ICE case and even the underlying 7YSZ coating failure for the CMAS 1 case. The results show that the CMAS damage under thermal gradient conditions for multi-layer systems are purely thermo-mechanical in nature dominated by the high residual stress produced from the coating stiffening generated upon infiltration which led to cold shock spallation during the cooling phase.

6.1 Experimental Approach

6.1.1 As Coated Multi-layer TBC Systems

Multi-layer 65YZ-7YSZ coatings were prepared by EB-PVD using the same deposition parameters for the 65YZ samples as used for samples S1 and M1 in the previous chapter. The underlying 7YSZ coating was produced separately in a different coating run using standard deposition conditions described elsewhere as “feathery” [32]. The produced multi-layer samples for these studies were denominated as “M4”, the summary of the deposition parameters and

microstructural features for the 65YZ layer are provided in **Table 6.1**. The selected substrates were Inconel 100 (IN 100) circular buttons with a 1-inch diameter. The buttons were coated with a standard (150 μm) NiCoCrAlY bond coat (BC) via EB-PVD deposition. Prior to the deposition of the 7YSZ coating, the BC coated substrates were surface treated to densify the columnar microstructure of the BC via shot peening the surface and subsequent heat treatment was performed at 1080 °C under H_2 rich atmosphere for 4 h in order to achieve relaxation and re-crystallization of the BC. Next, the substrates were oxidized in the pre-coating chamber to promote the formation of a dense α-Al_2O_3 TGO layer. Subsequently these samples were deposited by a 7YSZ top layer to emulate a complete TBC system incorporating the superalloy substrate, BC, TGO and 7YSZ TBC. Afterwards, the 65YZ layer was deposited on top of the 7YSZ coating. A schematic of the produced multi-layer buttons is given in **Figure 6.1**. The buttons have a 1 mm diameter hole drilled at 1 mm below the BC to insert a thermocouple device (TC) to monitor the BC temperature under thermal gradients

Table 6.1: Summary of deposition parameters and microstructural features of the 65YZ layer produced in the multi-layer M4 samples.

ID	65YZ Thickness (μm)	7YSZ Thickness (μm)	RPM	Substrate Temp. (°C)	Deposition Press. (mbar)	Porosity (%)	Feather arm length (μm)	Column width (μm)	Columnar gap width (μm)
M4	100	175	12	950	6×10^{-3}	28.5 ±1.7	4.8 ±1.0	10.3 ±3.3	1.4 ±0.4

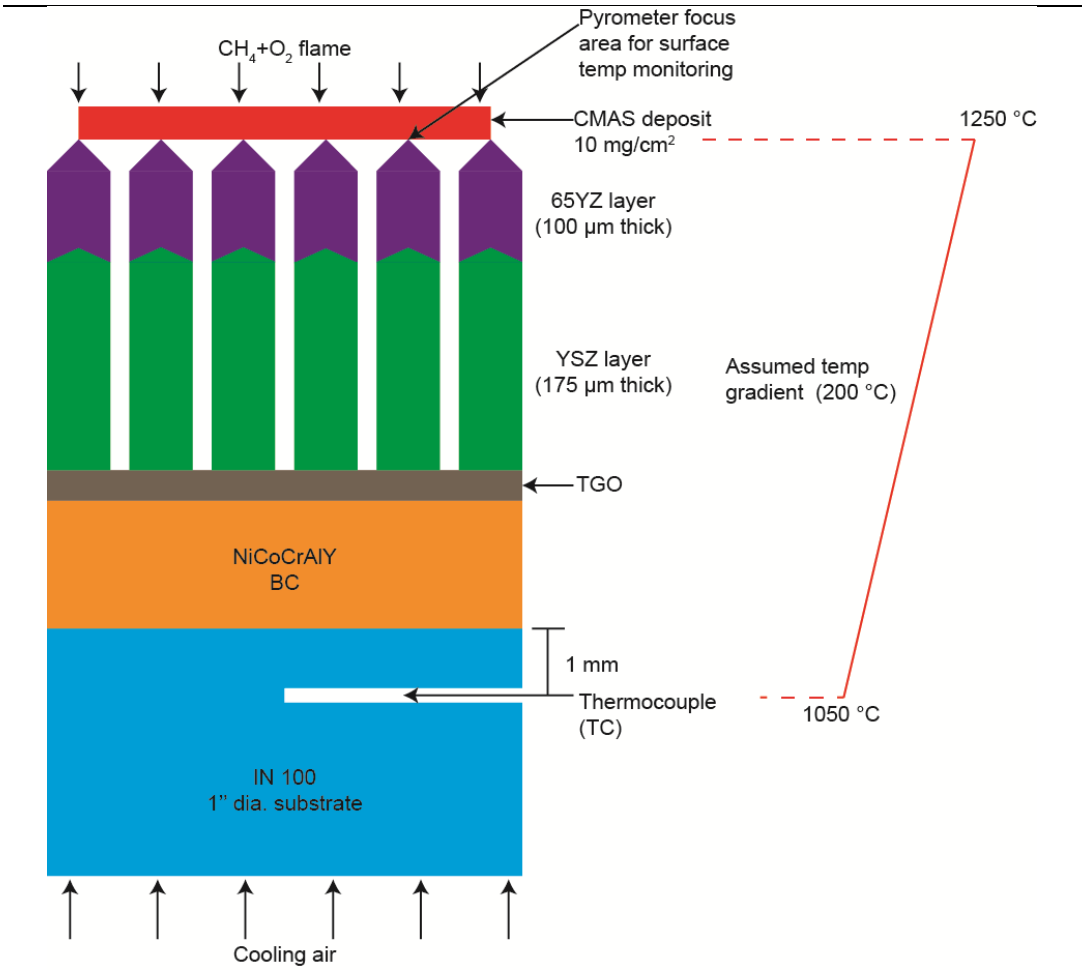

Figure 6.1: Schematic of the produced multi-layer TBC system tested under thermal gradients.

6.1.2 Thermal Gradient Test and Characterization

The procured TBC coated buttons were specially prepared to be tested in a special testing rig which simulates thermal gradient conditions. This system holds the button in place and heats up the top TBC surface using a CH_4+O_2 burner. Additionally, it provides back side air cooling to the tested specimen as shown in **Figure 6.1** so a thermal gradient is established within the coating as experienced in a real gas turbine. Additionally, **Figure 6.2a** shows the actual TGT system set up with all its main components (pyrometer, TC, burner and tested sample). **Figure 6.2b** shows an actual CMAS infiltration test in progress where the coated coupon is seen on top with the deposited CMAS layer on its surface. All the specimens were tested at temperature ranges of 1250 °C-1300°C

of surface temperature and the back-side cooling was adjusted to provide a 200 degree gradient between the top surface and the TC insert (as shown in **6.1**). This gradient represents a common temperature difference exhibited in real engine conditions [49]. The top surface temperature was monitored using a long wavelength (9-11 μm) pyrometer for which the emissivity radiation was calibrated for the as coated 65YZ top coat. This calibration process was performed at 1100 °C for 1 h to avoid substrate damage. Isothermal and cyclic testing were performed under CMAS attack as well as in the as coated state. The heating profile of the conducted experiments is shown in **Figure 6.3**, where for both isothermal and cyclic tests the heating and cooling rates were the same (approx. 10K/sec for heating and cooling). The isothermal heating was performed for 1 h whereas the cyclic tests consist of 5 min heating and for 3 min cooling cycles. Additionally, the red lines in **6.3** show the TBC surface temperature monitoring from the pyrometer. Whereas the black lines represent the BC temperature monitoring recorded from the inserted TC device.

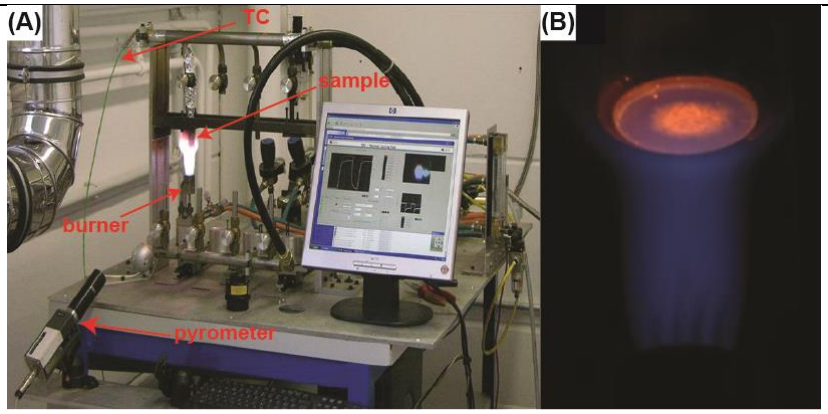

Figure 6.2: (A) TGT system set up with main components indicated. (B) Close up image of running test showing the CMAS deposited layer in the sample and burner flame.

SEM analysis of the top and cross-sectional view was used to assess infiltration and reaction products as described in the previous chapters. Standard metallographic techniques were used for preparation of cross-sections. The selected CMAS bearing compounds were CMAS 1 and ICE VA and were deposited as a slurry on top of the TBC in concentrations of 10 mg/cm^2 using

distilled water. One additional CMAS 1 infiltration test was performed at 1300 °C for the top surface and 1150 °C for the BC. This test was performed to compare the extent of damage at higher temperature regimes under thermal gradients.

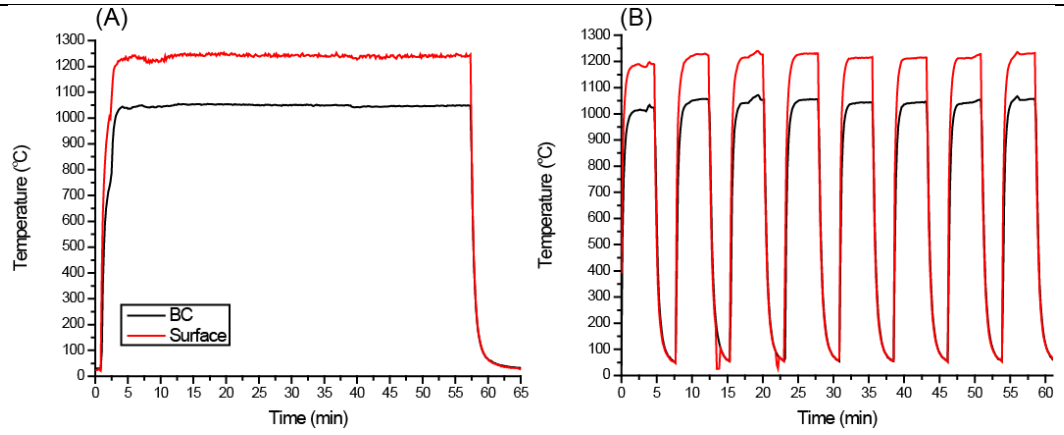

Figure 6.3: Heating profile for the (A) isothermal heat treatment for CMAS/VA infiltration and (B) cyclic heat treatment used for the as coated multi-layers.

6.2 Results

6.2.1 Cyclic Thermal Gradient Testing of As Coated Multi-layers

The as coated M4 sample images at different cycle intervals under thermal gradient testing (TGT) are shown in **Figure 6.4**. First signs of coating spallation have been observed after 700 cycles. This spallation has progressed up to the 30% of the total area which has been considered as the sample failure. This was reached after 1425 cycles (shown in **Figure 6.4d**) which represents 166 hot hours in total[8]. It is seen from **6.4b** that the initial coating spallation starts at the rounded edges of the sample. Additionally, a crack is seen at the TC hole area which starts to propagate into the sample, this is more visible after 1000 cycles (**6.4d**). The optical microscope image (**6.4e**) shows the TC crack propagation into the coating (marked with single red arrows) and **6.4f** shows the coating spallation along the rounded edge and a crack propagation along the edge. The brown

[8] Please note that after 800 cycles the TC failed and could not be replaced therefore, only the top surface temperature was monitored thereafter.

spots exhibited after TGT are stuck molten particles possibly originated from the burner or the test rig set up since they exhibited high Cr contents from EDS spot analysis.

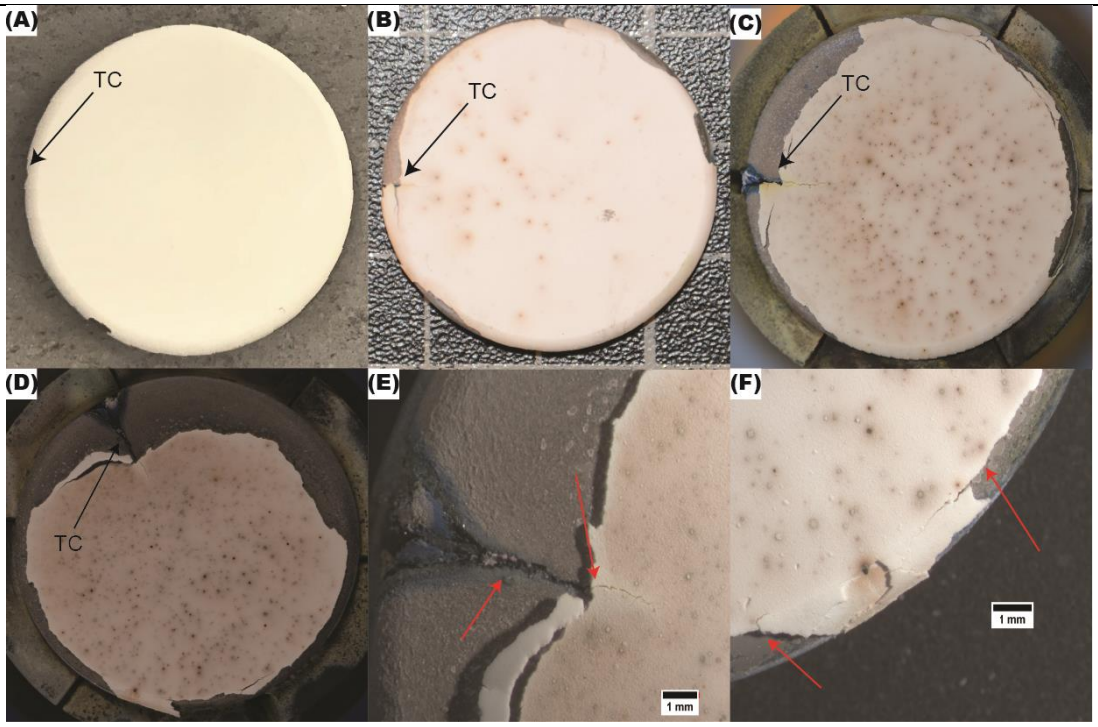

Figure 6.4: Top view images of the (A) as coated M4 sample before TGT, (B) after 700 cycles, (C) 1000 cycles and (D) after failure at 1425 cycles. (E) shows an optimal microscope image from the failed sample at the TC crack. (F) shows an optical microscope image of the failed sample at the edges showing coating spallation.

Furthermore, the SEM cross-sectional images of the failed M4 sample (after 1425 cycles) are shown in **Figure 6.5**. The image from the edge of sample (**6.5a**) exhibits severe BC oxidation due to the absence of TBC. The image obtained from an area closer to the center (opposite to the edge) shows no bonding between the BC and TBC (**6.5b**). Severe BC cavitation and deformation is seen where the TGO also appears to be separated from the TBC. However, the actual TBC layers (7YSZ/65YZ) do not show signs of cracking or degradation. The 65YZ coating nucleation exhibited the same cauliflower like growth behavior influenced by shadowing due to the substrate roughness (7YSZ layer) as described earlier. The TGO exhibited an overall thickness of 3.5 µm

after 1425 cycles. Its overall composition showed stoichiometric Al_2O_3 (40 atomic percent Al and 60 O). It showed very small localized formation of Y bearing particles (presumably YAG) with a mol % composition of 18.4 $YO_{1.5}$ and 81.6 $AlO_{1.5}$. On the other hand, the heavily oxidized BC layer exhibited an overall thickness of 57 μm and a composition of $Al_{7.5}Ti_{0.9}Cr_{21.5}Co_{24.9}Ni_{45.1}$ (single cation mol % basis).

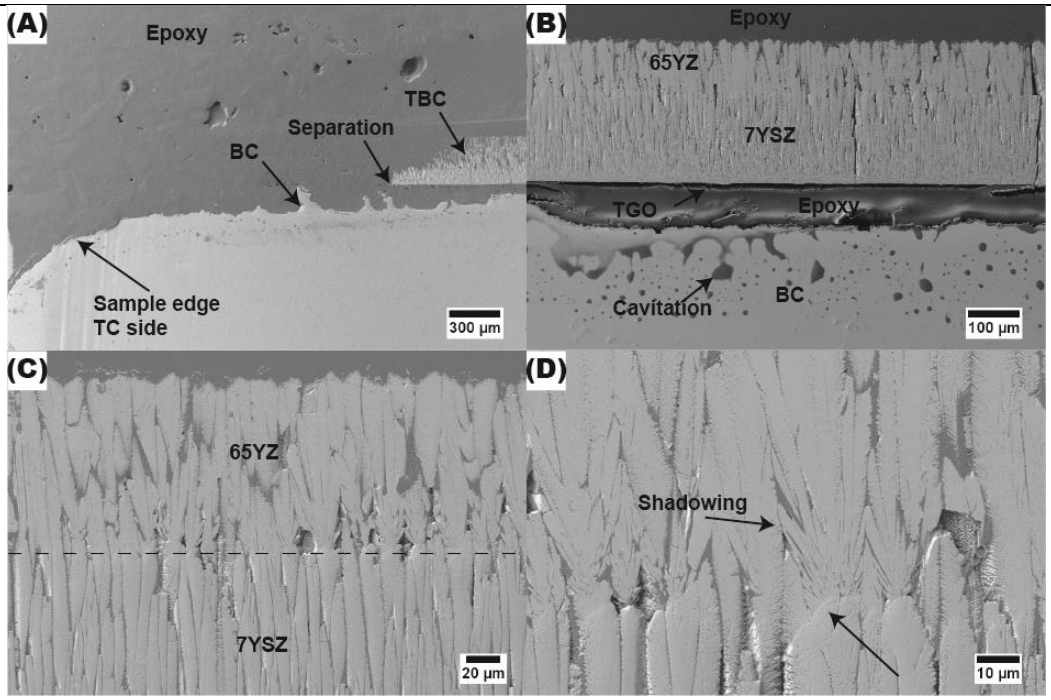

Figure 6.5: (A) SEM low magnification of the failed zone close to the TC edge location. (B) low magnification image of the central area location. (C) SEM image of the 65YZ/7YSZ coating interface (delimited with the dashed line). (D) High magnification image of the 65YZ/7YSZ interface.

6.2.2 CMAS/VA Infiltration of 65YZ/7YSZ Multi-layers under TGT

CMAS 1 and ICE VA were used for isothermal infiltration tests at 1250 °C (surface temp.) for 1 hour. Additionally, one more CMAS 1 specimen was tested at 1300 °C (surface temp.) with a BC temperature of 1150 °C.

6.2.2.1 CMAS 1 Infiltration at 1250 °C

The top view image and cross-sectional SEM micrographs of the CMAS 1 infiltrated M4 sample at 1250 °C are shown in **Figure 6.6**. The 65YZ coating spalled off at the interface of the infiltrated/non-infiltrated zone as seen in **6.6a.** Large amounts of glass deposits were seen to spall off the sample after cooling leaving small localized glass deposits on top of the coating as seen in **6.6a, b** and **c**. The SEM cross-sectional image of the spalled zone (**6.6b**) shows a large crack propagating at the 65YZ/7YSZ interphase. This crack was seen to propagate quite extensively throughout the sample. The infiltration depth has varied as expected due to the uneven columnar gap thickness as shown in (**6.5c** and **d** where the sealed gaps are marked with single arrows) and the overall infiltration zone is delimited within the red dotted lines whose thickness has ranged from 64 to 30 μm. In contrast, the multilayer tested samples on alumina substrates have experienced a completely infiltration at 1250 °C even after 5 min under isothermal conditions (see chapter 5). In other words, the TGT sample has showed an improved infiltration resistance showing that under thermal gradients the infiltration is partially suppressed. The reaction products still exhibited same phases such as garnet (G) located in large glass reservoirs, fluorite (F) as re-precipitation product and apatite (A) located within the feather arms in small glass pockets (**6.6f**). The summary of reaction product composition is provided in **Table 6.2**. The apatite composition exhibits a close composition as for the 5 min reported in **Table 4.4**. However, it is seen that all the CMAS cations are present in small amounts for this product. Thus, this leads to the conclusion that this apatite phase could represent the transition to a garnet phase from the interaction the glass reservoir. The garnet and fluorite phases fall within the compositional range reported in **Table 4.4**. This apatite transition to garnet was found more clearly in the next section for ICE VA. Finally, it is seen in **6.6e** that the crack propagated through the 65YZ nucleation sites (which are controlled by shadowing). This shows that this type of nucleation is not desired since it represents a weak interface susceptible to failure.

Table 6.2: Summary of chemical composition of CMAS 1 reaction products at 1250 °C under TGT.

ID	MgO	$AlO_{1.5}$	SiO_2	CaO	TiO_2	FeO	$YO_{1.5}$	ZrO_2
An	0.9	32.2	40.3	22.9	0.0	2.4	0.5	0.8
A	3.0	6.0	24.1	14.6	1.5	2.2	35.8	12.8
G	9.6	7.6	28.8	23.1	2.5	14.4	14.1	0.0
F	2.4	2.7	9.5	7.6	1.3	3.0	17.1	56.3
g	11.0	11.9	37.8	25.8	1.8	9.1	1.2	1.4

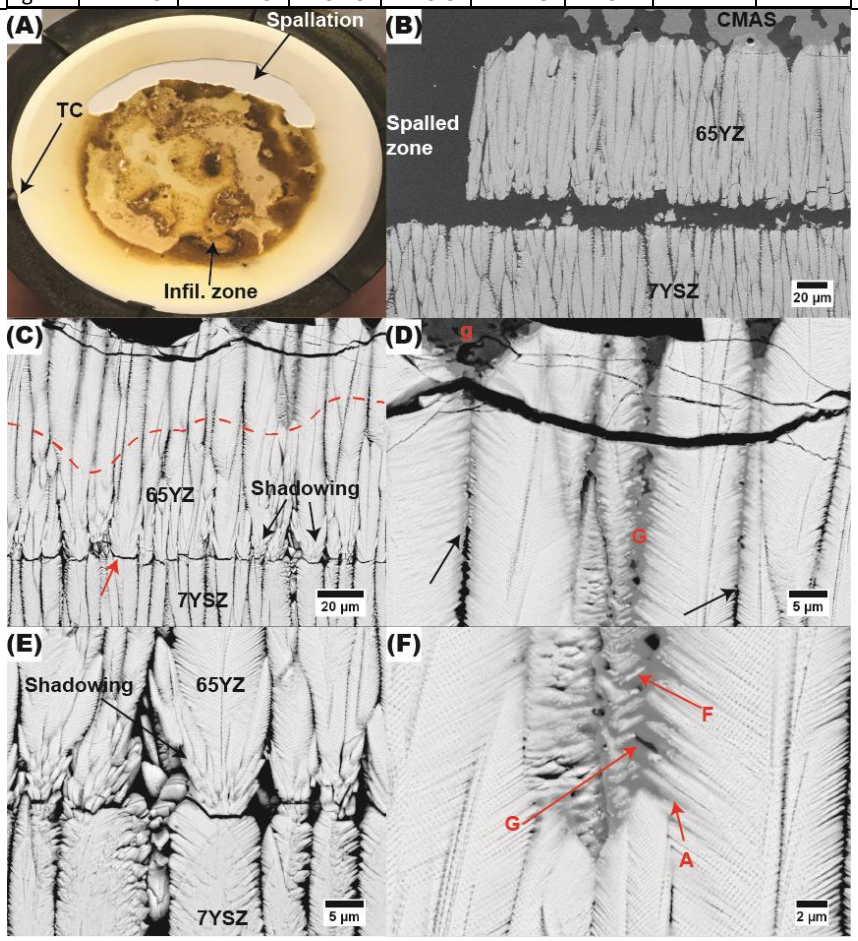

Figure 6.6: (A) top view image of the CMAS 1 M4 sample after 1 h of infiltration at 1250 °C under TGT. (B) SEM cross-sectional image of the 65YZ spalled zone. (C) Higher SEM magnification image of the CMAS 1 infiltration zone where the red arrow indicates the propagated crack at the 65YZ/7YSZ interface. (D) SEM image of the top CMAS 1 infiltrated zone. (E) High magnification image of the 65YZ/7YSZ interface. (F) High magnification image of a wide infiltrated columnar gap.

6.2.2.2 ICE VA Infiltration at 1250 °C

The ICE VA infiltrated images for the macroscopic and SEM top view are shown in **Figure 6.7**. The sample exhibited much higher infiltration damage than the CMAS 1 case (**6.5a**) by showing almost complete spallation of the 65YZ layer. The central area of the button shows a darker coloration at the 7YSZ layer which appears to be mud like cracks. The top view SEM image (**6.6b**) from the area located on the edges where remains of 65YZ coating showing a clear interface of the infiltrated and non-infiltrated zone. The higher magnification image shown in **6.7c** shows a complex network of molten particles and faceted particles crossing the columnar gap from column to column. From **6.7d** the facets are more easily distinguished crossing the gap as trying to seal it. EDS spot analysis confirmed that the apatite phase (A) represents the large facets sealing the gaps. Additionally, it is clearly seen how a small garnet product is nucleating from the apatite crystal engulfing it. The EDS composition of the apatite crystal that is being engulfed by the garnet shows traces of Fe (provided in **Table 6.3**). In contrast, the apatite composition of a large apatite crystal with no signs of garnet nucleation does not show Fe traces ($Mg_{1.5}Al_{1.9}Si_{29.3}Ca_{9.2}Y_{47.8}Zr_{10.3}$), this shows evidence of the garnet growth at expense of the apatite phase. The apatite phases reported in **Table 4.7** for ICE exhibited also small traces of Fe and a composition similar to the one reported in **Table 6.3**. The garnet phase in comparison with the ones reported in **Table 4.7** exhibit much lower Fe contents (less than half) and higher Y (about 10 mol % more). Due to the small traces of glass deposits on top of the coating it was difficult to find zirconolite and fluorite particles, for that reason their composition is not reported in **Table 6.3**.

Table 6.3: Summary of chemical composition of ICE VA reaction products under TGT.

ID	MgO	$AlO_{1.5}$	SiO_2	CaO	TiO_2	FeO	$YO_{1.5}$	ZrO_2
A	1.5	2.0	32.8	9.1	0.0	1.7	49.5	3.4
G	5.0	16.6	17.4	4.9	1.1	9.7	38.1	7.3

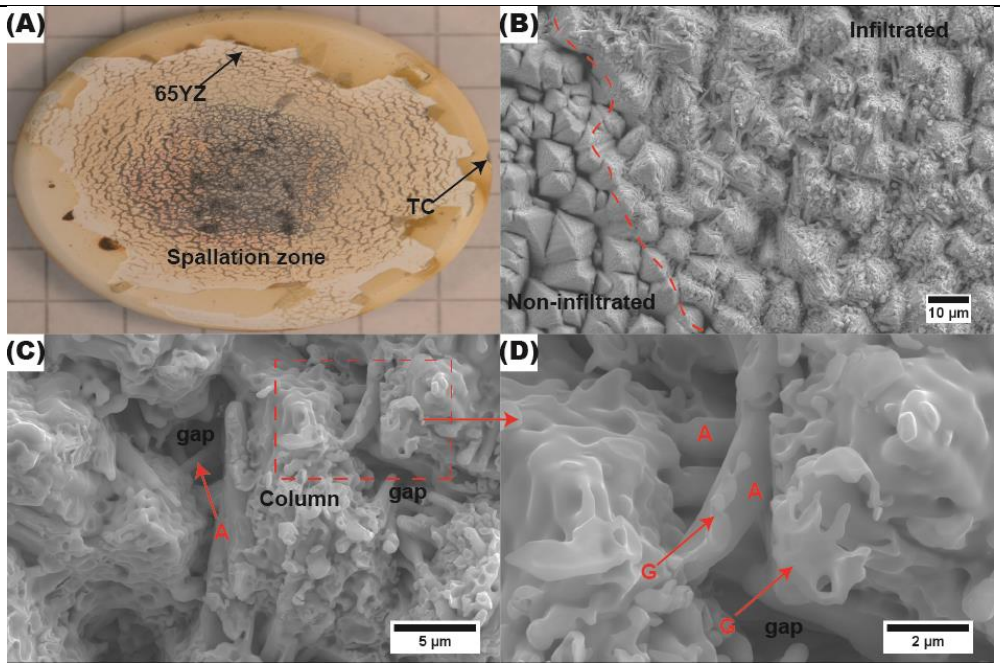

Figure 6.7: (A) Top view macroscopic image of the ICE VA TGT sample. (B) SEM top view image obtained from the zone where the 65YZ coating was still remaining. (C) High magnification image of the ICE VA infiltrated region. (D) Higher magnification image representing the red dotted rectangle in (C).

The cross-sectional SEM images of the ICE VA infiltrated sample are given in **Figure 6.8**. The **6.8a** image shows the central region where both TBC spallation and the remaining 7YSZ layer is present. The presence of TGO suggests that the failure might have started at the TGO/7YSZ interphase. The cross-sectional image at the 65YZ/7YSZ interface (**6.8b**) shows a complete infiltration of the whole 65YZ layer and reaction product formation at the interface. EDS spot analysis into the 7YSZ layer showed traces of Ca, Si, Mg and Fe up to 40 µm above the TGO (e.g. the ICE VA infiltrated ~235 µm). This infiltration behavior does not correlate with the infiltration exhibited for the single layer samples in chapter 4 by showing deeper CMAS 1 infiltration than ICE VA due to its lower viscosity. Thus, it is concluded that the measured temperature at the top surface was higher than 1250 °C (possibly higher than 1300 °C). In contrast, the CMAS 1 composition can serve as a good reference for sample surface temperature since it is reported to exhibit a melting onset starting at about 1243 °C [31] and extending to full melting at about 1265

°C [99]. Thus, from the generated infiltration for the CMAS 1 it can be concluded that its testing temperature was within the expected 1250 °C (± 20). These ICE VA infiltration results show that at high temperature regimes the thermal gradient has not significant effect in infiltration mitigation since the sample almost reached the TGO.

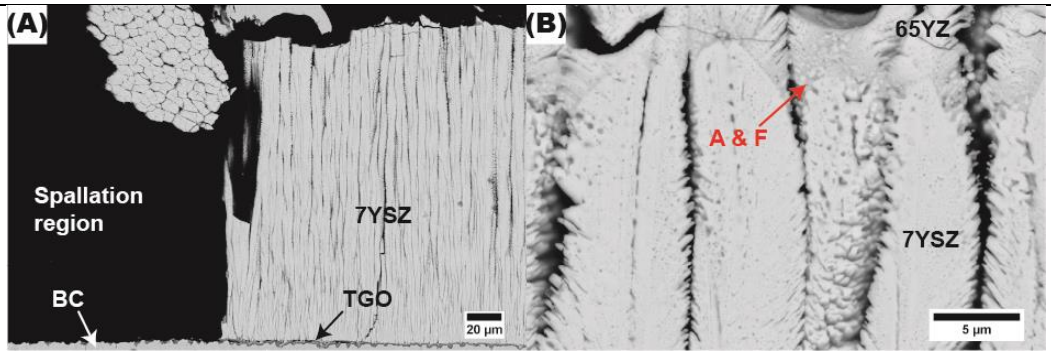

Figure 6.8: (A) low magnification SEM cross-section image of the 7YSZ spalled region. (B) High magnification image of the 65YZ/7YSZ interface.

6.2.2.3 CMAS 1 TGT Infiltration at 1300 °C

The infiltration attack at higher temperatures for CMAS 1 is very significant as seen from **Figure 6.9**. The 65YZ layer spalled off completely from the coating after testing (**6.9a**) and remains only at the sample edges where the infiltration remained low. The SEM cross-section image (**6.9b**) shows delamination of the 7YSZ coating at the TGO/BC interface and the failure appears to be located at the BC area as a large crack is seen to propagate. The high magnification SEM image (**6.9c**) reveals that the TGO remains attached to the 7YSZ coating. EDS spot analysis at the TGO reveals traces of Mg, Ca, Si and Fe which confirms that the glass completely infiltrated the coating reaching the TGO. **Figure 6.10** shows the high magnification SEM image at the TGO zone where small reaction products from CMAS interaction are marked with red arrows. The SEM image from the top reaction layer shows (**6.9b**) the expected reaction products (fluorite, anorthite, garnet, and apatite). **Table 6.4** shows the chemical composition summary of the found reaction products at the reaction layer. The compositions did not vary significantly as for 1250 °C testing

conditions (given in **Table 6.2**). The garnet phase exhibits a Ca depletion (4 mol. %) and Y enrichment (5 mol. %) compared to 1250 °C. The fluorite phase shows lower amount of glass products (Mg, Al, Si) but the Zr to Y ratio is still close (3 and 3.3 for 1300 and 1250 °C respectively).

Table 6.4: Summary of chemical composition of the CMAS 1 reaction products tested at 1300 °C under TGT.

ID	MgO	$AlO_{1.5}$	SiO_2	CaO	TiO_2	FeO	$YO_{1.5}$	ZrO_2
An	0.0	33.6	40.7	24.4	0.0	1.3	0.0	0.0
A	2.0	4.4	30.1	15.7	0.7	1.7	32.2	13.2
G	9.3	11.9	26.5	18.0	1.3	12.7	19.1	1.3
F	0.0	1.3	1.4	2.6	2.1	1.8	22.7	68.2
g	6.9	14.3	38.9	24.2	1.5	4.2	6.6	3.4

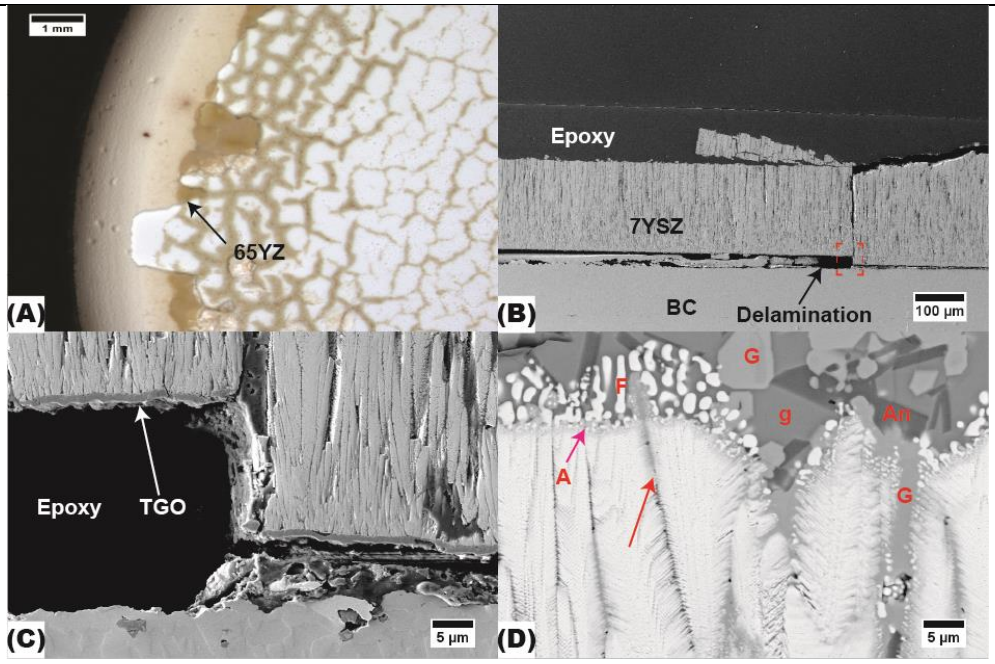

Figure 6.9: (A) optical microscope image of the 1300 °C TGT CMAS 1 infiltrated sample. (B) Low magnification SEM cross-section image of the failed CMAS 1 infiltrated sample. (C) High magnification SEM image from the area marked in a red dotted square in (B). (D) High magnification image of the reaction zone at the top 65YZ coating.

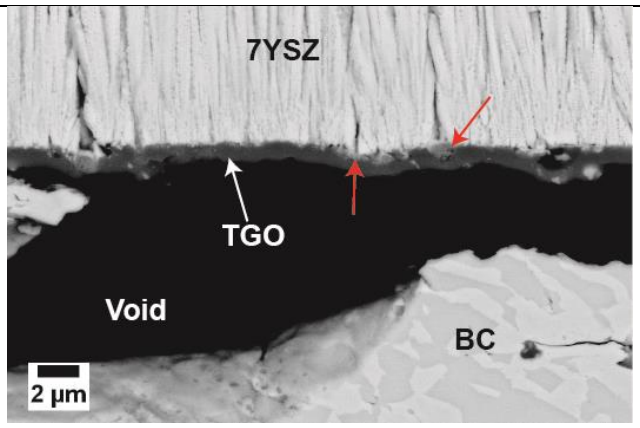

Figure 6.10: Cross-sectional SEM image of the CMAS 1 infiltrated sample at 1300 °C at the TGO zone.

6.3 Discussion

The performed experiments were intended to gain an insight on the TGT life behavior of the proposed multi-layer TBC system under cyclic lifetime and CMAS attack. Special attention in the discussion section will be given to the failure produced in the samples at different temperature regimes and extended cycles. Additionally, the learned concepts in this thesis about the kinetics of chemical reaction and microstructural influence of infiltration will be used to provide a wide view of the overall performance of the system under thermal gradients.

6.3.1 Failure of As Coated Multi-layer Coating

The results from the cycled M4 sample clearly showed that the initial coating delamination at the rounded edges (**Figure 6.4**) of the sample which subsequently progresses into the flat sample surface. It is known that curved surfaces represent areas where higher stresses can be developed and higher stress distribution and energy release rates can be produced [157, 158]. Thus, the initial coating failure starts at the rounded edge presumably at the TGO interface due to the higher stress concentration produced compared to the flat areas. Previous experiments performed in DLR [156, 159] with standard 7YSZ coatings under TGT also have shown initial coating delamination starting at the rounded edges. Subsequently, a large bucking crack is seen to propagate inside the flat surface coating originating from the TC insert. This area appears to be a weak interface since the

drilled hole could produce internal deformation of the BC and can also act as an extra oxidation source inducing higher stresses. As seen from the SEM image the BC produces excessive cavitation and consequent coating delamination from the BC/TGO interface. This type of BC failure is believed to occur due to the BC overheating in combination with through-thickness and in-plane thermal stresses [11]. Thus, it is reported that the BC cavitation is influenced by the cyclic thermal field which induces hydrostatic stresses in the softened overheated BC which drives the formation of voids as seen in **Figure 6.5b**. Here the voids act as areas where the stain energy can be released producing cracks at this interface.

Furthermore, the 65YZ/7YSZ system did not show significant coating degradation or sintering. The nucleation interface exhibits excessive shadowing influenced columnar growth (which is seen for all the CMAS/VA tested samples as well). As explained in chapter 5 the shadowing is influenced by the height difference (or roughness) in the 7YSZ columns which is in the range of about 8 to 10 μm (producing a rough substrate). Additionally, since 7YSZ 'feathery' coating used for the M4 deposition run exhibited more feather arms and intra-columnar porosities compared to the 'normal' (see ref [32] for the microstructural differences of the normal and feathery microstructures), these features act as extra nucleation sites which induce more shadowing. The multilayer 65YZ sample has exhibited higher cyclic lifetime than the single GZO sample, this could be explained by the significantly reduced compatibility that GZO has with the TGO which promotes formation of reaction phases leading to premature failure [112]. For that reason, a thin 7YSZ layer is usually deposited below the GZO to act as a diffusion barrier with the TGO and to provide a tougher layer in case of GZO delamination. The increased M4 lifetime compared to the normal 7YSZ coating could be related to the more feathery features and the extra porosity that 65YZ processes in addition to the underlying more feathery 7YSZ coating that the M4 consists of. Since the normal 7YSZ coating is in principle denser, cracks can propagate faster than in the more porous feathery structure [114]. In this context, the feathery 7YSZ coating lifetime tests under TGT was performed by Naraparaju (not published) showing comparable data with the

multi-layer M4 sample which was stopped after 1000 cycles due to the low coating spallation exhibited[9].

6.3.2 Failure of CMAS/VA infiltrated Multi-layer Coatings

The driving force of coating delamination is mainly related to the strain energy stored in the coating being the thermal expansion mismatch between the coating and the metal substrate its major source [10]. For CMAS infiltrated coatings the failure is purely thermo-mechanical in nature driven by the tensile stresses generated upon rapid cooling which produce vertical cracks and, in some cases, drive delamination cracks parallel to the surface (this is also known as cold shock) [11]. The CMAS 1 sample infiltrated at 1250 °C exhibits delamination cracks parallel to the surface at the 65YZ/7YSZ interface and at the top infiltrated zone. These type of cracks are characteristic of cold shock CMAS failure produced from the high in plane stiffness generated from cooling [17]. The crack propagates at the CMAS infiltrated stiffened zone and it is seen that the 65YZ/7YSZ layer provides a week interface which generates crack propagation. The exhibited delamination crack in **Figure 6.6c** & **d** represents the ideal infiltration performance of a CMAS resistant coating. Since the magnitude of strain energy increases non-linearly with the thickness of the penetrated layer a shallow infiltration is required to minimize the failure upon cooling [11] as seen in **6.6c** & **d**. Thus, upon coating spallation after cooling, more 65YZ coating can be available for reaction. Additionally, since the combustion of methane and oxygen generate water vapor as by product, it would be expected to see accumulation of Mg, Ca and Si at the TGO. This transport mechanism has been reported before for moisture-laden atmospheres suggesting that water vapor could transport hydroxides based on Mg, Ca and Si and accumulate them at the dense TGO layer [11]. However, EDS analysis at the TGO did not show any traces of such elements which proves no vapor transport into the TGO.

[9] Please note that the cyclic lifetime results for the 65YZ/7YSZ coatings only consider one tested sample therefore, there is currently no available data for statistical analysis for effective comparison with other tested TBC under cyclic lifetime.

The CMAS 1 case at 1300 °C exhibited a different type of CMAS failure mode which appears to be related with the TGO reaction with the infiltrated CMAS melt. The EDS analysis showed evidence of CMAS infiltration at the TGO by exhibiting a modified composition of $Mg_{3.1}Al_{74.7}Si_{1.3}Ca_{1.1}Fe_{1.6}Y_{2.1}Zr_{16.1}$. The composition of the modified TGO is comparable with studies with 7YSZ TBCs infiltrated with CMAS 1 at 1300 °C after 96 cycles ($Mg_{3.1}Al_{75.1}Ca_{0.4}Cr_{0.7}Fe_{1.7}Ni_{1.5}Zr_{17.5}$) [159]. This interaction is reported to increase the thermal stress and promote pore formation within the modified TGO. This type of failure appears to the dominating in this case since the coating delamination reached the TGO. Besides, coating spallation at the 65YZ/7YSZ interface was also seen possibly corelated to the weak interface. The TGO thickness in this sample ranged from 1.5 to 2.1 μm. In comparison with the non-infiltrated sample at 1250 °C (TGO thickness of 3.5 μm after 1425 cycles or 119 hot hours), it appears that CMAS infiltration increases the TGO growth. Additionally, for the previous tests at 1300 °C after 96 cycles (8 hot hours), the TGO exhibited a 3 μm thickness which appears to be consistent with the enhanced TGO growth due to CMAS infiltration. However, it is important to note that the temperatures of the CMAS 1 infiltrated samples (from this test and literature report) have a difference of 50 °C higher than the non-infiltrated sample. Thus, it is expected that a slightly higher TGO will be produced at 1300 °C which is not considered in this analysis.

The ICE VA case, failure appears to be due to the cold shock dominated mechanism. In this case, the high infiltration depth which has reached almost the TGO substrate (about 40 μm away from the TGO max infiltration) producing an increased strain energy. In this case also, delamination was found at the 65YZ/7YSZ interface. The current TGT results prove that the CMAS attack under thermal gradient conditions appears to be purely thermo-mechanical in nature since the failure always happened from the high strain energy produced from the CTE mismatch of the coating and the CMAS melt upon cooling. Thus, for effective CMAS resistant systems the shallow infiltration represents the most critical parameter to consider. Then, from the performed experiments an effective microstructure plays a critical role in maintaining the infiltration as minimal as possible. A smooth or epitaxial layer transition from the 7YSZ to the 65YZ is required

to avoid a weak shadowing induced nucleation. Therefore, thin columnar gaps < 1 μm thick can be produced which would exhibit enhanced CMAS crystallization as discussed in chapter 5. This enhanced CMAS crystallization can significantly increase the lifetime of multilayer coatings by maintaining the infiltration in a shallow region thus, minimizing coating spallation upon cold shock.

6.4 Conclusion

Multi-layer full TBC systems based on 65YZ/7YSZ TBC were prepared on Ni based-superalloy substrates to test their lifetime under thermal gradient and cyclic conditions with/out CMAS/VA infiltration at different surface temperatures. The cyclic life time of the as coated multi-layer system has shown good performance by failing after 1425 cycles. In the all tested CMAS/VA infiltration cases, the coating has exhibited same failure by showing 65YZ spallation at 1250 °C and complete coating delamination at 1300 °C. The results showed that the CMAS/VA attack is thermo-mechanical in nature under thermal gradient conditions. This is characterized by the cold shock generated form the large in plane stiffened coating due to infiltration which spalls upon cooling due to the CTE mismatch of the CMAS layer and the TBC. Thus, for effective CMAS infiltration resistance the promotion of shallow infiltration is critical for robust operation under real engine conditions. In this context, the coating microstructure for multi-layer CMAS resistant architectures must be optimized to ensure high infiltration resistance. Additionally, the nucleation interface of the CMAS resistant/7YSZ layer must be coherent to avoid weak zones susceptible to failure.

Chapter 7: Mechanical-Physical Properties of 65YZ Coatings

The erosion behavior of 65YZ as coated coatings in single and multi-layer configuration as well as the CMAS infiltrated coatings (multi-layer only) was tested using alumina particles as erodent. Additionally, the thermal conductivity of 65YZ was measured and compared with standard 7YSZ and GZO using time-domain thermoreflectance (TDTR) methods. The 65YZ samples exhibited poor erosion resistance about 2.3 times lower compared to the standard 7YSZ coatings. The shadowing influenced growth from the 65YZ layer at the 7YSZ interface represents a weak zone where cracks propagate faster which generated an increase erosion rate than in single layer 65YZ cases. For CMAS 1 infiltrated samples, the cracking propagates faster than in single layer cases due to the complete infiltration of the coatings which makes them behave as a continuously dense brittle material. The thermal conductivity results show comparable thermal conductivity for the 65YZ TBC (1.5 W $m^{-1}K^{-1}$) to standard 7YSZ (1.4 W $m^{-1}K^{-1}$). However, GZO still shows the lowest thermal conductivity under cross-sectional TDTR testing (1.1 W $m^{-1}K^{-1}$). The implications of the reported mechanical properties for CMAS environments are discussed in this section.

7.1 Experimental Methods

7.1.1 Sample Preparation for Erosion Testing

Rectangular alumina substrates (30mm x 20mm x 1 mm) were coated with single layer 65YZ and multi-layer 65YZ/7YSZ by means of EB-PVD method. The single layer and multi-layer coatings were produced in the same deposition run as in the case of S1 and M1 samples respectively. The deposition conditions and microstructural parameters for the as coated samples are provided in **Table 5.1**. The single layer S1 samples were used for erosion testing in the as coated conditions whereas the multi-layer samples were CMAS infiltrated prior erosion testing and also eroded under as coated conditions. The CMAS 1 compound was used for infiltration in concentrations of 10 mg/cm^2. The infiltration tests were done at 1250 °C for 20 h at a heating/cooling rate of 10 K/min (slow furnace cooling). This process was used to keep

consistency with previous erosion experiments performed by colleagues on feathery and normal 7YSZ as coated and infiltrated TBCs [114].

7.1.2 Erosion Testing

The erosion testing was performed at the Technische Universität Dresden using a house-built erosion testing rig at room temperature. The erosion concentration spot had an overall diameter of 12.4 mm and alumina particles with a particle size distribution of 54.5 μm (d10), 92.5 μm (d50) and 142.7 μm (d90) were used as erodent at a feeding rate of 0.25 g/min. The particles were accelerated using a focused high-pressure air stream which reached a mean velocity of 125 m/s. The impingement angle for erosion was set at 90 °C with respect to the coated sample. The samples were initially weighed prior erosion testing and at erosion intervals of 8x60 s for the non-infiltrated samples whereas 6x60s for the infiltrated ones. Finally, the coating volume loss was measured via confocal microscopy (μscan; Nano foucus). More details about the erosion testing and 7YSZ erosion results are provided elsewhere [114].

7.1.3 Thermal Conductivity Measurements

Time-domain thermoreflectance (TDTR) approach was used to measure the thermal conductivity (λ) of as coated single layers of 65YZ, 7YSZ and GZO deposited on alumina substrates. The 65YZ sample correlated to the S1 sample run (**Table 4.1** & **5.1**), the 7YSZ sample was produced under the normal 7YSZ conditions [32] and the GZO correlated to the same run of samples provided in **Table 4.1**. The as-coated samples were cross-sectioned and embedded in a conductive epoxy to facilitate polishing. Standard metallographic techniques were used to polish the samples to a 20 nm finish prior TDTR testing. Additionally, top surface samples were also polished using the same conditions as described previously to map λ at the in-plane section. The TDTR measurements were performed at the University of Virginia and the experimental approach details were kindly provided by them. To characterize the thermal conductivity of the TBCs a nominal 80 nm Al transducer was deposited on the coatings. Then, the TDTR was employed to spatially probe the sample surface to determine microstructural effects on thermal conductivity.

TDTR represents an optical-pump probing technique that utilizes a Ti:Sapphire oscillator with an 80 MHz repetition rate and about 100 fs pulses. Using a two-tint setup, the 808.g nm output of the oscillator is spectrally separated into a high energy pump path and a low energy probe path. The pump is electro-optically modulated at 8.4 MHz, and creates a frequency-dependent heating event at the sample surface. The probe is mechanically delayed in time, and monitors the thermoreflectance at the sample surface. Both beams are concentrically focused through a 20x objective to create $1/e^2$ radii of ~ 3.5 μm. By monitoring the in-phase (V_{in}) and out-phase (V_{out}) voltages and subsequently comparing their ratios ($-V_{in}/V_{out}$) to a radially symmetric heat diffusion model, various thermal properties can be extracted such as seen in **Figure 7.1**. The data shown represent the raw data and best-fits for the spots proved on the cross-section TBCs. The insert shows the picosecond acoustic response at earlier time delays [160, 161], which is used to derive the thickness of the Al coated layer using the longitudinal speed of sound of 6.24 nm ps^{-1}. The volumetric heat capacities used for 7YSZ [162, 163], 65YZ [164] and GZO are 2.86 MJ $m^{-3}K^{-1}$ [163], 2.39 MJ $m^{-3}K^{-1}$ and 2.4 MJ $m^{-3}K^{-1}$ respectively[10]. From a practical standpoint, interrogating a single point of a sample using TDTR is tedious and time consuming. In this context, various works have been proposed to spatially mapping the thermal properties of a given system using pump-probe techniques [165], and have specifically been implemented to TBCs [166]. Thus, a similar technique is applied in this work where the thermal conductivity can be mapped by mounting the sample on a 2-axis stage where we raster the sample across regions of interest to spatially understand the λ in that region. The pump-probe delay is held to a 2000 ps, so it can be far enough from the Al relaxation time and a good sensitivity of thermal conductivity can be provided.

[10] Note that the volumetric heat capacities for 65YZ and GZO are estimated from rule of mixtures of the constituent materials.

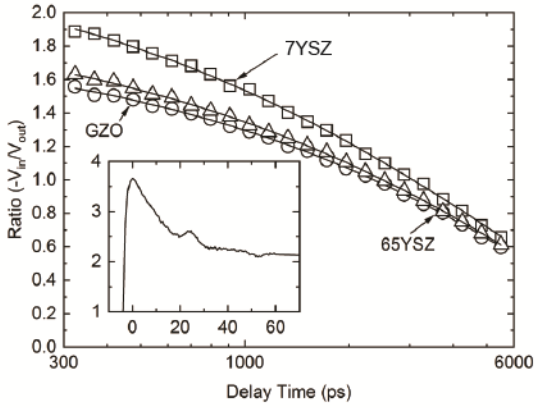

Figure 7.1: Time-domain thermoreflectance data for 7YSZ, 65YZ, and GZO cross-sections. The symbols show the raw data while the lines represent the associated best fits. The inset shows the early time delay, with which is used to extract the thickness of the Al layer. The similar decay curves of GZO and 65YZ suggest that their thermal conductivities are comparable.

7.2 Results

7.2.1 Erosion Tests of 65YZ Single layer(as-coated)

The samples exhibited and erosion of about 3.6 mm^3 of removed material after 120 sec of erosion where the samples spalled off the substrate. The SEM cross-sectional images of the eroded 65YZ S1 samples after the very first erosion interval (about 15 sec) is shown in **Figure 7.2**. The low magnification image (**7.2a**) exhibits the initial cracking of the TBC columns at the upper zone from the first erosion stage. The high magnification image (**7.2b**) of the top layer cracking reveals the crack initiation at the feather arm location with a characteristic V shape crack. This type of cracking is due to the notching effect which concentrates high stresses at the edges of the feather arms [114]. The low magnification image given in **7.2c** shows the evidence of densification of the eroded surface as seen also in the high magnification image (**7.2d**). The densified zone exhibits large crack propagation though several columns. The crack propagation due to densification is believed to be an erosion mode of foreign object damage (FOD) [114].

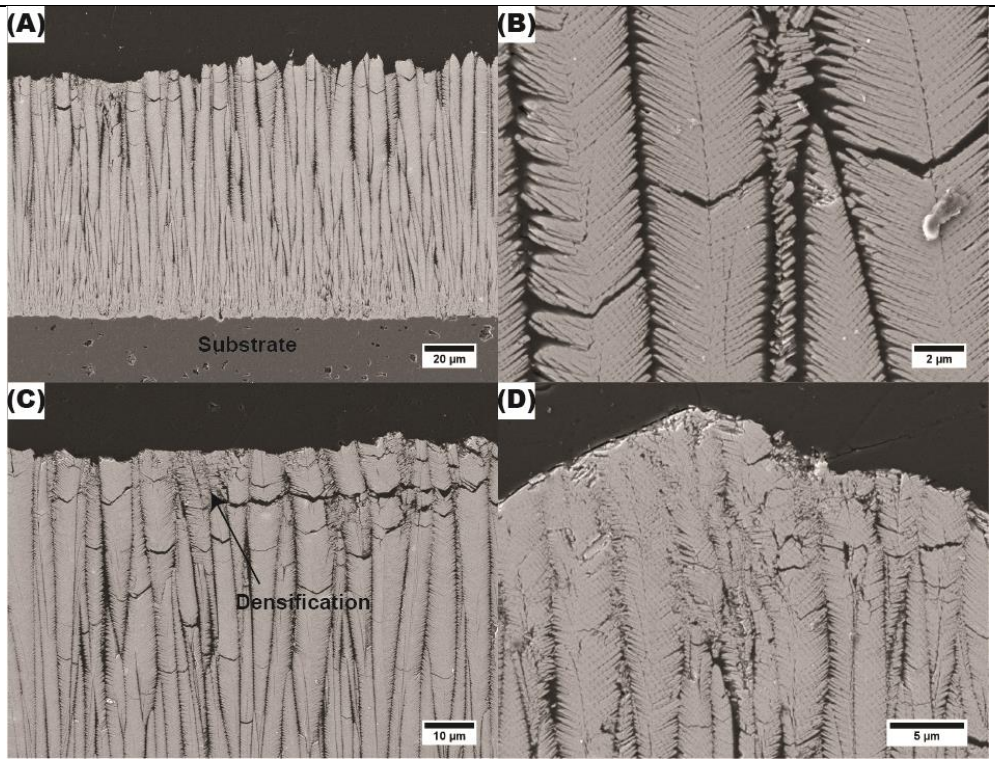

Figure 7.2: (A) SEM cross-sectional image of the eroded S1 65YZ coating at the initial erosion stage of 15 sec. (B) High magnification image of the V shape cracks starting at the feather arm ends. (C) Eroded area showing signs of coating densification. (D) High magnification image of the densified zone.

Additional SEM cross-sectional images of the samples after failure (120 sec of erosion) are shown in **Figure 7.3**. It is seen that left over coating close to the alumina substrate in **7.3a** exhibits high densification and what appears to be cross plastic deformation of the columns. **Figure 7.3b** shows evidence of kink bands (or shear band) forming in an angular direction with respect to the coating surface (marked with single arrows). This type of bands formation also shows evidence of a change in erosion damage characterized by foreign object damage (FOD) [4, 114]. It is important to note that the erosion mechanism is dependent on the erosion parameter (such as particle size and velocity) as well as the coating properties (column diameter, toughness, feather arm length) [114]. Where for small column diameter the bending of the column can be supported by other neighboring columns more effectively [114].

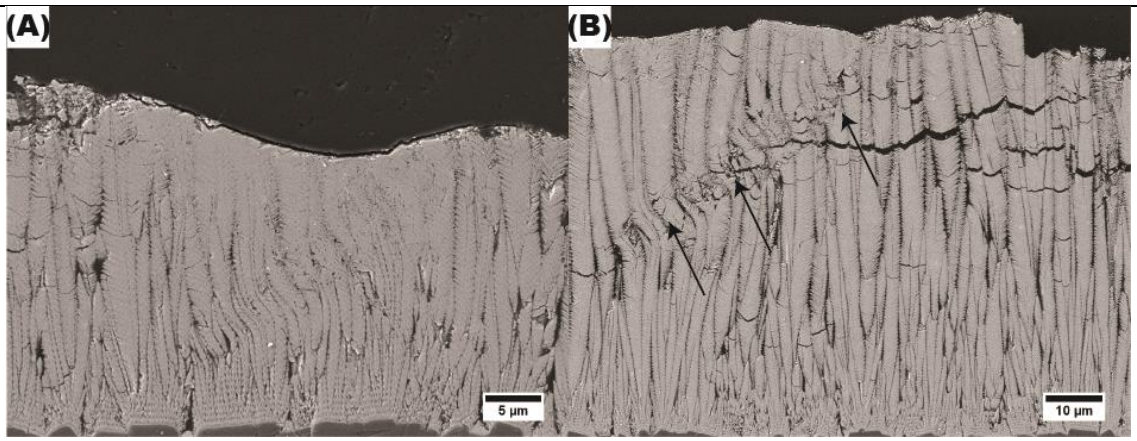

Figure 7.3: (A)Cross-sectional SEM image of the left-over coting after 120 sec of erosion showing column bending and densification. (B) SEM image showing evidence of kink band formation.

7.2.2 Erosion Tests of 65YZ Multi-layer (as-coated)

The erosion exhibited for the M1 samples was slightly higher than in the S1 case sample by exhibiting a total volume loss of about 4.1 mm^3 after 120 sec. The SEM cross-sectional image of the eroded samples after the initial 15 sec of erosion is given in **Figure 7.4a**. The initial crack propagates similarly in the top coating compare to the S1 samples. However, some deeper cracks (marked in single arrows in figure) close to the 7YSZ interface were seen for the M1. After 120 s of erosion the SEM image given in **Figure 7.4b** shows the 65YZ layer complete spallation in some places. The higher magnification image (**7.4c**) shows the crack propagation at the interface with the 7YSZ layer. No further signs of coating densification were found due to the complete 65YZ layer spallation in the M1 sample case.

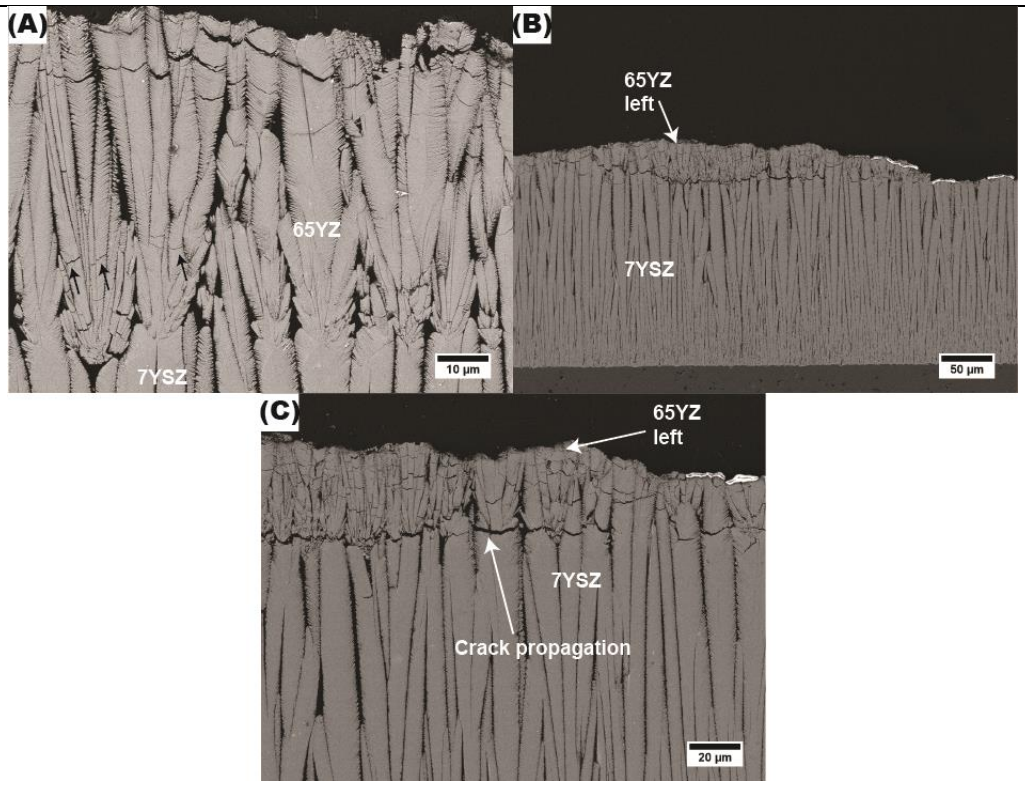

Figure 7.4: (A) Cross-sectional SEM image of the multi-layer M1 sample eroded after 15 sec showing the initial cracking similar for the S1 case. (B) SEM image after 120 sec of erosion showing almost complete spallation of the top 65YZ layer. (C) High magnification image after 120 sec showing the crack propagation at the 65YZ/7YSZ interface.

7.2.3 Erosion Testing of the CMAS Infiltrated Multi-layer Coatings

The samples exhibited complete infiltration after 20 h and even significant reaction of the underneath 7YSZ layer. This is expected since previous test for the M1 samples under CMAS 1 infiltration after 5 min showed complete infiltration of the coatings. Thus, for the long-term infiltration testing it is expected that the infiltrated glass reacts significantly with the underlying 7YSZ layer. The SEM images of the as infiltrated samples are given in **Figure 7.5**, where only a small CMAS 1 deposit is left (g) after 20 h (about 20 µm max as shown in **7.5a**) on top of the coating. The high magnification image of the 65YZ layer (**7.5b**) shows the reaction at the interface with the 7YSZ layer and areas of unreacted glass left in between the 7YSZ and the 65YZ layer (marked with single black arrows).

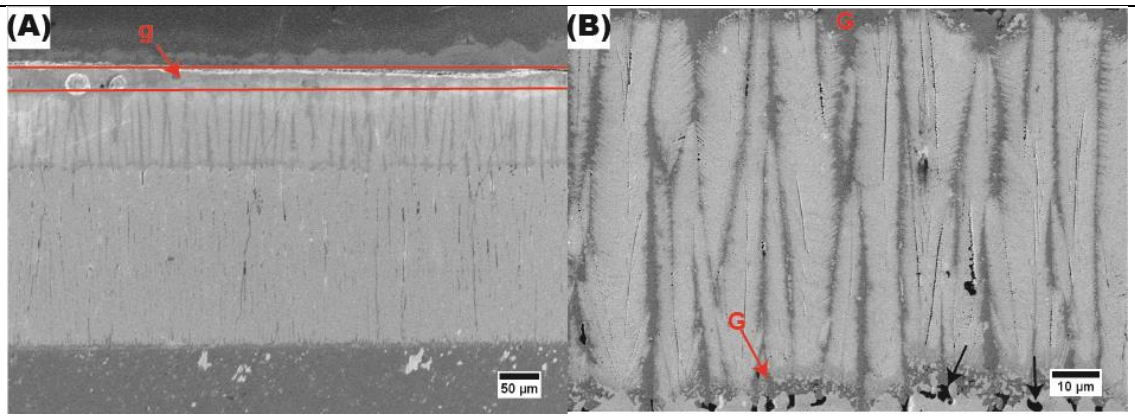

Figure 7.5: (A) SEM cross-section image of the CMAS 1 infiltrated M1 sample after 20 h at 1250 °C. The sample shows complete infiltration and severe reaction with the underlying 7YSZ layer. The glass (g) deposit is delimited within the red lines. (B) High magnification of the top 65YZ layer showing reaction with CMAS 1. Reaction is also seen at the 65YZ/7YSZ interface.

The striking results from the erosion tests revealed that the eroded coating after 120 sec is close (3.8 mm^3 of eroded material) to the value of the single-layer (as coated) sample and even lower than the as coated multi-layer sample. The SEM images of the eroded sample after 120 sec are shown in **Figure 7.6**. In **7.6a** a large crack was found to be propagating through the coating and the cracks appear to be largely connected possibly due to the CMAS interconnected columns which makes the coating behaves as a continuum material. Additionally, it is seen that the cracks only appear to be present within the top 65YZ layer. The high magnification image of the cracks located above the 7YSZ interface (**7.6b**) show that the cracks do not seem to propagate through the 65YZ/7YSZ interface. This indicates that the CMAS infiltration appears to strengthen the interface. The severe 7YSZ coating degradation due to the reaction with CMAS 1 is seen from the exhibited loss of columnar shape and formation of YSZ destabilized (presumably cubic due to the Ca content in the glass) globular enlarged particles. Finally, the high magnification image also shows very large cracks (or vigorous fragmentation) of the top coat after CMAS infiltration compared to the as coated cases.

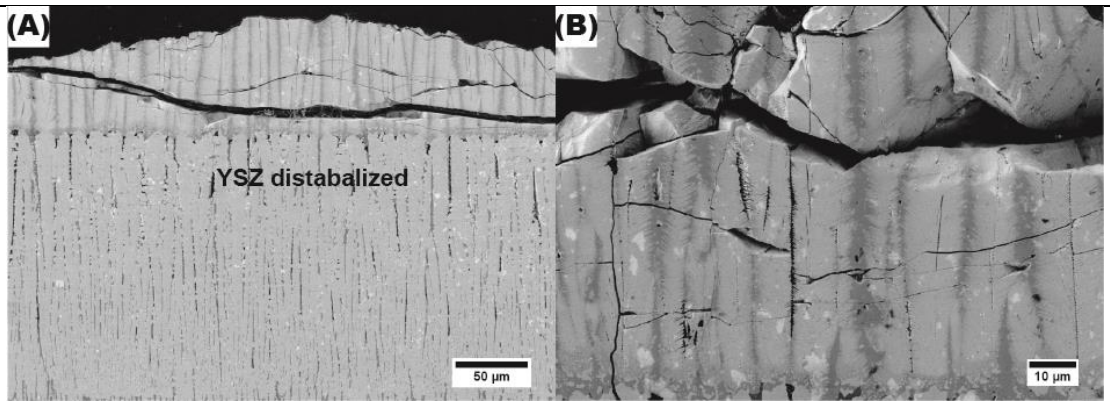

Figure 7.6: (A) SEM cross-section image of the 120 sec eroded CMAS 1 infiltrated M1 sample. (B) High magnification image at the top 65YZ layer showing severe crack propagation above the 65YZ/7YSZ interface.

7.2.4 Thermal Conductivity Results

The thermal conductivity mappings for the top plane-sections and cross-sections are provided in **Figure 7.7** along with their distributions where the map scale size for positions is given in µm. It is chosen to analyze the ratio V_{in}/V_{out} provided in **Figure 7.1** using the estimated heat capacities for each sample to provide the thermal conductivity results. The maps are given at the central area of the plan-view samples, while for the cross-sections they cover the entire coating thickness. The distributions provided encompass the thermal conductivity points at which the probe is secularly reflected in a way that the reflected signal is not influenced by diffuse scattering at the sample surface. The planar section mappings show larger area distributions with λ values above 1.5 W $m^{-1}K^{-1}$ for 7YSZ compared to the 65YZ and GZO cases. For the cross-sectional mapping case, all samples exhibited a drop in λ close to the substrate. Additionally, an average thermal conductivity value (λ) is provided summarizing the distribution for each planar and cross-section measurement in **Table 7.1**. These reported λ at the surface and cross-section values are in close agreement with each other being the GZO the value with the closest agreement. By taking an average of the reported values an overall thermal conductivity is estimated to be 1.8 ±0.1, 1.4 ±.2 and 1.1 ±0.1 for 7YSZ, 65YZ and GZO respectively. These estimations are in good agreement with the reported in literature for EB-PVD 7YSZ (reported as 1.5 W $m^{-1}K^{-1}$) [54] and EB-PVD

GZO (reported as 1 W $m^{-1}K^{-1}$) [112] proving the validity of the TDTR method used. For the best of our knowledge there is not reported thermal conductivity data available for the EB-PVD 65YZ in the open ligature. However, Krause et al.- reported the λ for $2ZrO_2.Y_2O_3$ APS coating (close composition to our 65YZ) at about 0.75 W $m^{-1}K^{-1}$ at room temperature. Which would be expected to have a lower λ for APS coatings than for EB-PVD due to its microstructural configuration [9].

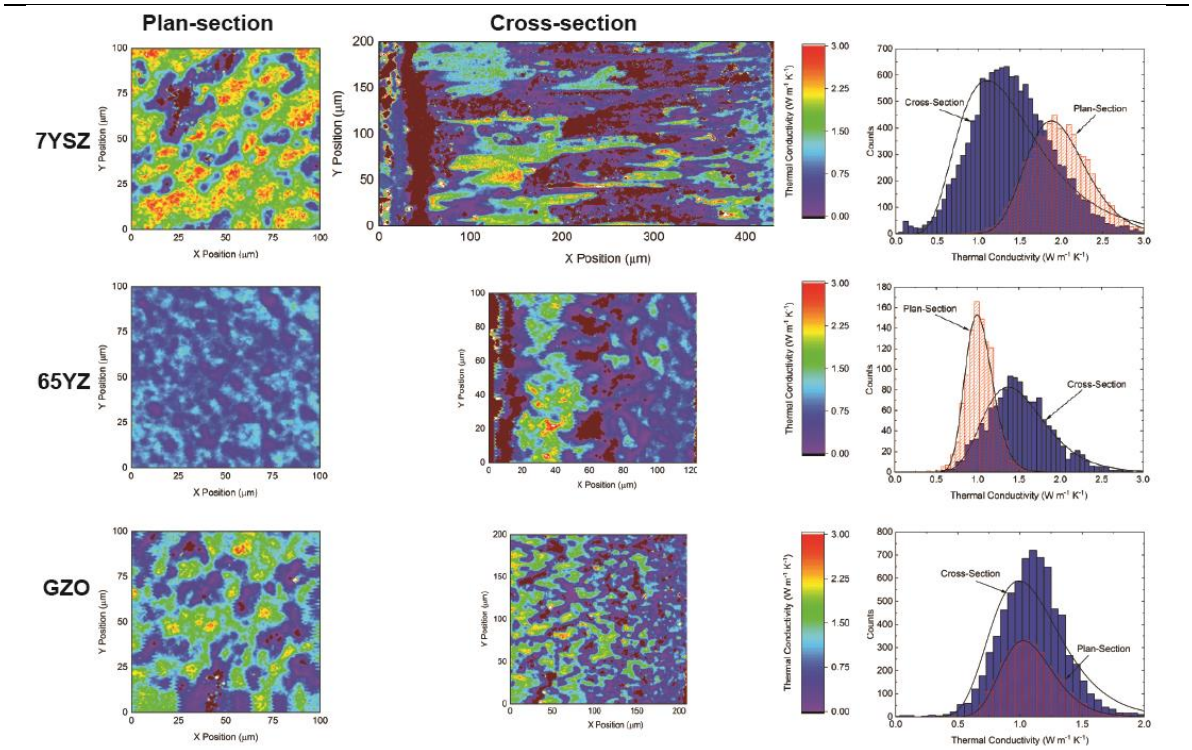

Figure 7.7: Thermal conductivity mappings and distributions for the plan- and cross-sectioned samples.

Table 7.1: Summary of measured λ from plan- and cross-sectioned maps.

Section type	7YSZ	65YZ	GZO
$\lambda_{Plan\text{-}section}$ (W $m^{-1}K^{-1}$)	2.0 ±0.4	1.0 ±0.2	1.1 ±0.2
$\lambda_{Cross\text{-}section}$ (W $m^{-1}K^{-1}$)	1.4 ±0.6	1.5 ±0.4	1.1 ±0.2

7.3 Discussion

7.3.1 Observations on the Erosion Behavior of 65YZ TBC

The erosion resistance represents a critical requirement that a TBC system must have since gas turbines experience erosive wear from larger particles ingested into the engine (commonly referred as FOD). For CMAS environments infiltration and erosive wear come together since at low temperatures the CMAS particles can produce erosion damage whereas at high temperature they can infiltrate the porous TBC [10]. In addition, it is also important to understand the erosion mechanics for cases where CMAS infiltrated coatings are under erosive damage. In this context, experiments performed by Steinberg et al. [114] using normal and feathery 7YSZ microstructures under CMAS/VA infiltration showed that the denser normal microstructure provided higher erosion resistance than the feathery. This was due to the deeper glass infiltration into the column core which generated the production of more brittle YSZ destabilized phases that propagate cracks easier. On the contrary, the erosion resistance for the as coated conditions showed higher resistance for the feathery structure due to its finer microstructure which requires multiple cracks to ensure materials loss and produced lower column bending.

Figure 7.8 shows the mapping of area depth produced from the localized erosion jet for the S1, M1 and M1-CMAS 1 coatings. It is seen that the as coated M1 sample generated the highest erosion. This is believed to be due to the weak nucleation interface between the 65YZ and the 7YSZ coatings. Therefore, as the erosion starts the crack propagates faster at this weak interface thus, generating an increase in the erosion rate until the 65YZ layer spalls off completely reaching the tougher 7YSZ. In contrast, the CMAS 1 infiltrated M1 sample showed lower erosion rate, this is contradictory to the 7YSZ erosion results where the erosion rate was significantly increased after CMAS infiltration [114]. From **Figure 7.6a** the crack no longer propagates at the 65YZ/7YSZ interface unlike the non-infiltrated sample, this leads to the conclusion that the interface is strengthened from the CMAS infiltration/reaction promoting less material removal than in the as coated M1 case. This increased erosion resistance from CMAS infiltration for the M1 case sample can be seen in **Figure 7.9a** where the total volume lost is plotted vs the erosion time for all the

tested 65YZ bearing coatings. In the plot, the M1 sample exhibits the highest erosion rate due to the cracking at the interface which promotes more material removal. Until 65YZ layer spallation (about 120 sec marked in the figure) only the underlying 7YSZ layer is left for erosion. Then, the erosion rate for the CMAS infiltrated sample is clearly seen to increase compared to the as coated M1 after about 350 sec as expected from the 7YSZ infiltration exposed in [114]. By comparing the 65YZ eroded material after 60 sec where the 65YZ did not spall off the substrate yet (2.0 mm^3 for single layer S1) with respect to 7YSZ normal (1.0 mm^3) and feathery (0.6 mm^3), the 65YZ has 2 and 3.3 times less erosion resistance than normal and feathery 7YSZ respectively. This is expected since yttria represents a brittle material and YSZ materials in the cubic system also exhibit lower toughness than standard 7YSZ [112]. Thus, the emphasis on careful tuning of the microstructural parameters for the multi-layer configurations becomes more critical in order to ensure superior mechanical resistance to erosion. Being the nucleation site of the 65YZ layer a very critical zone to control effectively during deposition of multi-layer TBC systems. In this context, it would then be expected that the erosion of an optimized microstructure after CMAS infiltration such as the S1 configuration would be lower than for the M1 sample case. This is due to the thinner columnar gaps of the S1 sample compared to the M1 (see **Table 5.1**) which would arrest the CMAS glass at shallow zones. This means that cracks would propagate faster at the deeper infiltrated M1 sample due to the higher microstructural stiffening generated.

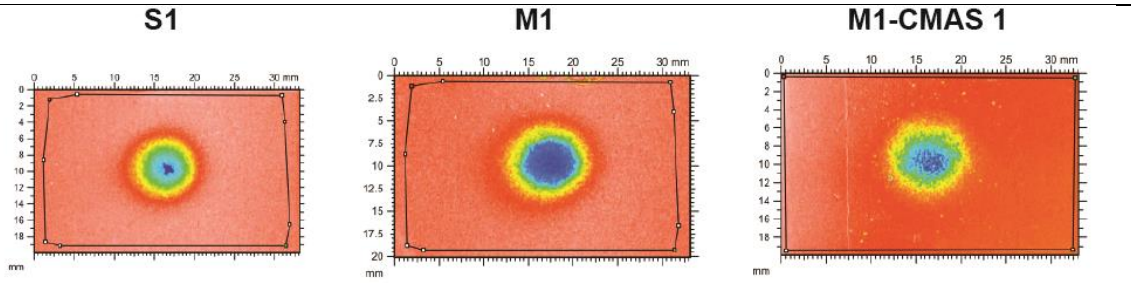

Figure 7.8: Confocal microscope image mapping showing the coating depth difference for the eroded tested coatings after 120 sec.

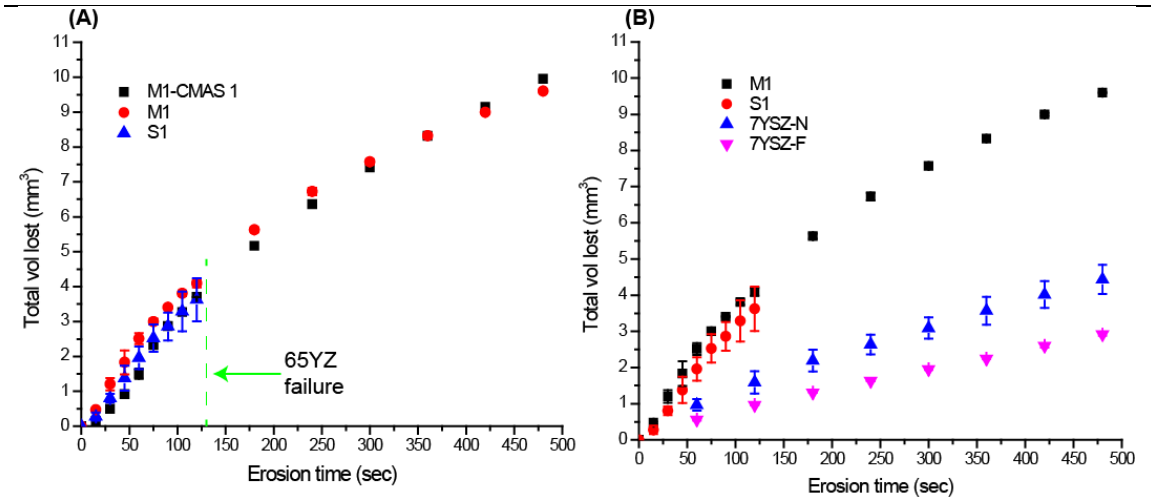

Figure 7.9: (A) erosion plot results for the tested 65YZ samples showing the volume lost vs erosion time. (B) Erosion comparison of the as coated M1 sample with respect to the as coated 7YSZ normal (N) and feathery (F) coatings tested in [114] under the same erosion conditions.

7.3.2 Observations on the Reported Thermal Conductivities for Multiple TBCs.

The produced thermal conductivity maps for the cross-sections have shown in all cases a reduction in the thermal conductivity at the area close to the substrate. It is believed that this reduction is due to the smaller grain size (or smaller columns) from the coating's initial nucleation. Since the thermal conductivity is mostly controlled by the phonon scattering [54], adding more grain boundaries (in this case pores and feather arms) represents a more effective phonon barrier which in principle reduces the thermal conductivity. Additionally, from the plan-section maps in general it would be expected that λ increases slightly towards the bulk compositions λ due to larger grain sizes (since TBC columns usually become coarser with TBC thickness). This assumption is in agreement with the 7YSZ coating which exhibits 43 % increase in λ at the top surface. For the GZO case and 65YZ this increase is not seen and even for the 65YZ case the λ drop to lower overall values than for the cross-section. This difference is believed to be due to the polishing processing from the plan-sections since they had to be polished at the top sections for the measurements. Due to this polishing, some material was removed from the actual coating. The estimations of the actual thickness of the plan-section specimens show that the 7YSZ, 65YZ and

GZO thicknesses were about 350, 20 and 130 μm respectively [11]. Thus, the measured plan-section thermal conductivity for the 65YZ and GZO samples was obtained from areas closer to the substrate owing to that the non-correlation with higher values at the surface as seen for the 7YSZ case. Therefore, the cross-section values provided in **Table 7.1** are believed to be the more realistic values that incorporate all the differences in microstructural features that the TBC exhibit thought their thicknesses. Finally, the close λ that 65YZ exhibited with respect to 7YSZ shows that this material does not significantly sacrifices thermal conductivity in exchange of CMAS resistance.

7.4 Conclusion

The erosion resistance of as coated 65YZ TBCs in single and multi-layer configurations on top of 7YSZ layer were studied. The CMAS 1 infiltrated erosion resistance of 65YZ multi-layer coatings was also studied. In addition, the thermal conductivity of single coatings such as 7YSZ, 65YZ and GZO were analyzed via TDTR in cross-sectioned and plan-sectioned samples. The erosion results showed that the 65YZ represents a very brittle material with an erosion resistance in the as coated configuration about half of the one exhibited by standard normal 7YSZ TBCs. The erosion exhibited for the multi-layer configuration was reduced more due to the weak interface generated from the shadowing controlled conical growth of the samples. This represents a critical zone for microstructural refining for effective multilayer systems. In this context, the CMAS infiltration appeared to be beneficial for the erosion resistance in the case of the multi-layer system by the generated strengthening at the interface that was produced from the CMAS reaction. Additionally, the erosion under CMAS infiltration produced the propagation of large cracks due to the complete densification of the material which made the coating behave as a continuum where the cracks could propagate faster due to the elimination of columnar gaps which represent barriers for crack propagation. The thermal conductivity generated from the cross-sectional mappings exhibited good correlation with the values reported from the literature. The plan-sections λ variations for the 65YZ and GZO appeared to be due to the processing used prior analysis which

[11] The as coated coating thicknesses were 400, 100 and 200 μm for 7YSZ, 65YZ and GZO respectively.

generated thinner coatings. This did not represent a problem for the 7YSZ case since the sample was still thick after polishing. Finally, the reported thermal conductivity for the 65YZ was very close to standard 7YSZ which is beneficial for its potential use in multi-layer TBC systems were CMAS resistance does not come at significant expense of thermal conductivity.

Chapter 8: Concluding Remarks

The overall goal of this project was to study the performance of yttria rich-zirconia based TBCs produced by EB-PVD under a large variety of CMAS/VA sources relevant to the aviation industry. The studies were mainly performed at 1250 °C which represents a critical temperature due to the phase destabilization exhibited for 7YSZ and the melting onset of most of the CMAS compounds. The study focused on gaining a better understanding of the chemical reaction kinetics of TBC with a wide spectrum of CMAS bearing sources, and the kinetics of infiltration under different microstructural configurations. A multi-layer coating system was tested under thermal gradients to assess the most critical parameters that will influence infiltration under real engine simulated conditions. The results showed that coating microstructure plays a more critical role in infiltration than the coating reactivity since a proven CMAS resistant material such as 65YZ was clearly infiltrated under non-favorable microstructural conditions such as large columnar gaps and unfavorable coating nucleation. Furthermore, the results shown under thermal gradients clearly indicated that the dominant nature of CMAS attack is thermo-mechanical creating an urgency to arrest the glass infiltration at shallow zones to avoid cold shock spallation. The erosion testing on the coatings showed that 65YZ represents a brittle material with reduced erosion resistance compared to standard 7YSZ. This was well expected since it is well known that YSZ phases in the cubic ranges are more brittle in nature plus pure yttria also represents a very soft material compared to the *t'* phase generated in 7YSZ. The current studies provided very revealing information critical for the implementation of effective and robust CMAS resistant TBC systems. The main concluding remarks form the different performed studies are as follow.

The studies showed that higher potential for CMAS glass crystallization can be generated with more "free yttria" solute availability in a reaction. Thus, using pure yttria as a CMAS resistant material would maximize the potential for glass crystallization. However, implementing this material is not very practical due to its low toughness and high thermal conductivity compared to 7YSZ. Thus, the use of zirconates is selected as an optimal for CMAS resistant applications being

in our case the 65YZ composition the selected one. The critical parameter for effective crystallization is then correlated with the yttria available to promote silicates formation (being the apatite phase the most critical one) with respect to the yttria retained in the fluorite phase. The addition of other elements into the system such as Ti proved to be of importance for the ICE VA case since it shifted the thermodynamics of reaction to promote formation of other Y retaining phases such as zirconolite. Additionally, the infiltration temperature also seems to be critical since at higher temperatures (above 1300 °C) the fluorite phase field can retain more yttria leaving less free yttria to promote apatite formation.

The kinetics of reaction was studied for a wide range of CMAS/VA compositions for various time regimes and up to 1300 °C to study the phase stability and evolution. The 65YZ sample was compared with GZO under same testing conditions to see infiltration resistance and phase reactions. The results showed that the glass interactions with 65YZ and GZO are very complex systems were several parameters work synergistically to control reaction and infiltration such as: chemistry of the melt, molecular partitioning, glass deposit interaction and TBC microstructure. Both samples exhibited effective apatite formation and in general the 65YZ exhibited higher infiltration resistance than its counterpart GZO. For the 65YZ case the melt chemistry promoted formation of different secondary reaction phases such as garnet, YDS and zircon. Based on the melt composition the use of the BI (correlated with the SiO_2 content) proved to be an effective way to predict reaction product formation at the reaction layer for the CMAS/VA tested sources. The low BI ranges < 1 appear to promote YDS and zircon formation whereas the high ranges ≥ 1 appear to promote garnet formation. Additionally, the BI also showed a good correlation with the melt viscosity which could predict the amount of expected infiltration. From the chemical composition point of view, the Fe and Ti contents represent important elements to promote garnet and zirconolite formation respectively. The sample cooling promoted an enhanced growth for the garnet phase at slow cooling, and formation of dendrites for the ICE VA case. At 1300 °C, no significant shift in reaction phases was found for the tested CMAS/VA compounds. Only in the CMAS 1 case 65YZ exhibited larger growth of garnets and dendrite garnet formation

during the slow cooling of the samples. The results also show that the secondary reaction phases such as garnet and YDS require large glass deposits (such as large columnar gaps or the top glass deposit) to be promoted. However, the apatite formation is promoted in smaller glass pockets where the glass is saturated with the RE cation faster. The Si/Ca ratio in the melt was a good indicator to predict apatite formation for the glass sources since Ca is the most critical element required for apatite formation. Thus, high Ca containing melts can promote faster apatite formation than high Si containing melts. For the infiltration comparison between the 65YZ and GZO, the higher infiltration resistance exhibited in the 65YZ coating was influenced by the chemistry, element partitioning and microstructure. The element partitioning showed the higher potential for Y^{3+} and low ionic radii RE^{3+} cations to stabilize the garnet formation. Where the slower garnet growth in combination with its higher content of glass elements retained appear to be beneficial for long term infiltration and coating recession rate in lab scale tests. Additionally, the experiments which lasted for 50 h showed that the apatite phase formation for the 65YZ layer was able to retain more glass than the Gd-base apatite by showing lower M^{I}:M^{II} ratios. Thus, less coating is required to promote apatite formation in the 65YZ case improving its infiltration resistance. Finally, the GZO microstructure was not favorable to arrest infiltration (large columnar gaps). However, the Gd dissolution into the melt promotes a further decrease in melt viscosity (higher than Y dissolution) owing to an increase infiltration potential.

The microstructural effects of TBC on the CMAS/VA infiltration were studied in detail for single and multi-layer 65YZ/7YSZ coatings. The results showed that microstructure is a critical parameter to maintain lower infiltration over the TBC reactivity. The permeability estimations using the concentric pipe model revealed that intercolumnar gap width is the most critical parameter dictating the infiltration kinetics. Thus, in order for the reaction kinetics to counteract the infiltration kinetics, thin columnar gaps of widths < 1 μm are proposed as an optimal value for effective CMAS arrest. Additionally, the 65YZ top coat nucleation condition represents an important parameter to consider for multi-layer system since un-coherent cauliflower like columnar growth influenced by substrate roughness and porous features (shadowing) promote

enhanced infiltration. This is due to the large number of open gaps generated from the conical columnar growth which also promotes coarser columns. For the case where the 65YZ coating grew epitaxially following the 7YSZ column, it was noted that the new grown 65YZ column followed the same columnar nucleation direction of the lower 7YSZ leaving a continuous columnar gap width. Thus, this creates the urgency to also tune the 7YSZ microstructural parameters to promote small columnar gaps in order for the 65YZ coating to have the same thin intercolumnar gaps. Finally, the dissolution rate is also influenced by microstructure since large columnar gaps require more coating dissolution to reach Y saturation limit precipitating apatite. For the case of long feather arm coatings, these represented high specific surface area zones that are dissolved faster than the column core. Therefore, for the case of Ca deficient melts the column dissolution is excessive since the feather arms are consumed leaving a thicker columnar gap with higher infiltration potential.

The thermal gradient tests on multi-layer 65YZ/7YSZ coatings using a complete TBC system (superalloy, BC and TGO) showed that the as coated system is highly resistant to thermal cyclic loads comparable with standard 7YSZ TBC. This resistance is due to the highly strain tolerant feathery 7YSZ underlying layer used. The CMAS 1/ICE infiltration tests showed that the CMAS attack mechanism under TGT is thermo-mechanical in nature influenced by the stiffening of the coating from infiltration which losses its strain tolerance and upon cooling leads to TBC delamination from cold shock. This showed the urgency for tailoring the microstructure effectively to maintain a shallow infiltration thus, reducing the cold shock effects in case of multi-layer coatings. Additionally, the coating interface generated from the shadowing proved to be a weak zone to promote delamination of the 65YZ top coat. At 1300 °C, the damage was more severe due to the reaction of the glass with the TGO promoting the complete coating delamination. This also shows the high importance to address the challenges of CMAS attack since at higher turbine temperatures the glass infiltration would be increased significantly.

The erosion test of the 65YZ single and multi-layer TBC in the as coated and CMAS 1 infiltrated conditions were performed to assess the degree of damage. The 65YZ sample proved to

be a brittle material compared to standard 7YSZ by showing 2 times higher erosion damage compared to normal 7YSZ. The 65YZ nucleation zone also represented a weak area that promoted crack propagation and increased erosion behavior. In contrast, the multi-layer CMAS 1 infiltrated sample exhibited lower erosion rate compared to the as coated multi-layer due to the chemical strengthening generated at the 65YZ/7YSZ interface from the reaction. The infiltrated samples exhibited very fast crack propagation due to the densification generated from the CMAS 1 infiltration. In addition, the thermal conductivity of the 65YZ coating was estimated experimentally by TDTR approach and compared with the conductivity of standard 7YSZ and GZO. The estimated conductivities for the cross-section samples showed very good agreement with the values from literature for GZO and 7YSZ. Thus, showing the validity of the experimental method used. The exhibited cross-sectional thermal conductivities were 1.4, 1.5 and 1.1 W $m^{-1}K^{-1}$ for 7YSZ, 65YZ and GZO respectively. These results showed that only toughness is sacrificed for CMAS resistance in the case of 65YZ since its thermal conductivity was very close to 7YSZ.

Finally, an ideal CMAS resistant TBC multi-layer system for real aero-engine conditions is proposed considering the most critical parameters observed from this study. A pentagram plot using the critical parameters is given in **Figure 8.1** where microstructure, temperature, coating composition, toughness and reaction time represent them. Since the studies showed that the microstructure plays a critical role by exhibiting full coating infiltration for non-optimized microstructures it is considered as a most important parameter, which means careful tailoring of 7YSZ and 65YZ microstructure and coating transition must be produced for robust operation. Next, the engine temperature at which infiltration takes place is also a critical parameter since current goals for turbine inlet temperatures are targeting 1500 °C the CMAS infiltration will be expected to be very aggressive due to the very low melt viscosity. This is concluded from the TGT infiltration tests where a surface temperature change from 1250 °C to 1300 °C produced significantly higher damage. Thus, the infiltration produced in a temperature increase to 1500 °C would be very challenging to arrest. The CMAS resistant coating composition represents an important parameter with lower influence in infiltration compared relatively to the microstructure

or temperature. This conclusion was drawn based on the results were the CMAS resistant 65YZ coating was completely infiltrated at large columnar gaps showing that the infiltration kinetics are more dominant than the reaction kinetics. Next, toughness also represents an important factor for CMAS resistance mostly for the case scenario were an as coated multi-layer system is exposed to erosion damage which means that the soft 65YZ (for example) will be removed 2 times faster than the tough 7YSZ possibly leaving no more material to react against CMAS infiltration. Since the TGT results showed evidence of very thin glass deposits left after the cold shock due to the spallation of the glass deposit during cooling. This could mean that in general for CMAS resistant coatings no large glass deposit will be left after the cold shock therefore, no extra erosion protection will be provided by the case when a large glass deposit is present on top of the TBC. Finally, the reaction time represents a relevant parameter compared to the other ones. Although, it influences the recession rate of the reaction layer it has been shown that the propensity of the infiltrated coating under TGT to spall off during the cooling engine cycle is very high due to the cold shock. In addition, engine flight regimes do not go over 20 h of constant operation (for long haul flights) i.e. the reaction layer would not be significantly thick. Then, comparing the long-term infiltration results it was seen that for the single layer 65YZ coating the infiltration into the columnar gaps was always deeper than the reaction layer thickness henceforth, during the cooling engine cycle it is expected that the coating will spall off from the deep infiltrated column area instead of the reaction layer.

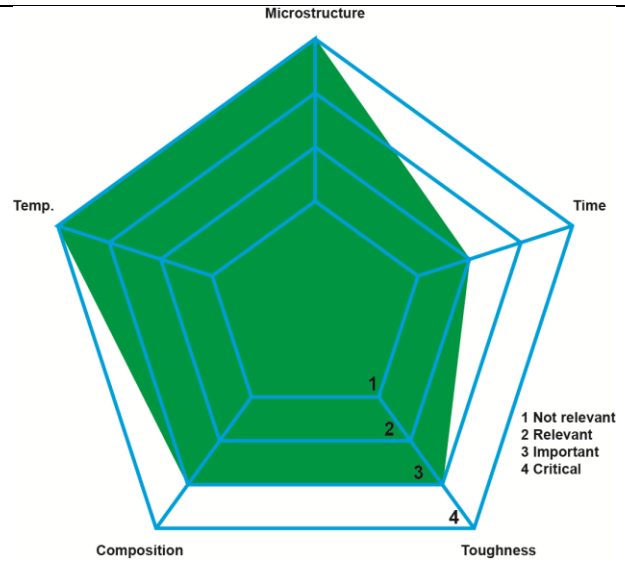

Figure 8.1: Schematic of ideal parameters that a robust CMAS resistant multi-layer system must integrate for real engine conditions.

8.1 Project Outlook

The current studies showed the overall CMAS/VA infiltration performance of 65YZ based TBCs. In general it was shown that for single layer optimized microstructures the CMAS infiltration performance even outperformed GZO which represents a material that is currently in operation [10]. Additionally, this project showed that for non-optimized multi-layers the infiltration significantly increased. Besides, for the TGT testing is was proven that it is very critical to maintain a very shallow infiltration to avoid cold shock failure under real aircraft engine conditions. Therefore, it is urgent to explore in the future more efficient coating methods to produce optimized multi-layer microstructures with parallel columnar growth which incorporates thin columnar gaps < 1 µm wide. This can be achieved by a direct evaporation transition from the underlayer evaporation source (7YSZ) to the CMAS resistant layer evaporation source (e.g. 65YZ). Additionally, a thin 7YSZ underlayer (50-90 µm) could be beneficial to reduce columnar gap thickness and substrate roughness in order to avoid the undesired shadowing-controlled cauliflower like growth. Finally, since the apatite phase represents the primarily reaction phase for CMAS arrest. As it was reported that Ca deficient melts require higher TBC consumption to

promote apatite formation. Therefore, it would be of high significance to explore coatings that work effectively under wide spectrum of CMAS/VA sources. This could be achieved by using a CMAS resistant material such as (65YZ or pure yttria) doped with Ca to provide an extra source for apatite formation when a Ca deficient glass is in interaction with the TBC.

References

1. Padture, N.P., M. Gell, and E.H. Jordan, *Thermal Barrier Coatings for Gas Turbine Engine Applications.* Science, 2002. **296**: p. 280-284.
2. Padture, N.P., *Advanced structural ceramics in aerospace propulsion.* Nature Materials, 2016. **15**: p. 804-809.
3. Clarke, D.R., M. Oechsner, and N.P. Padture, *Thermal-barrier coatings for more efficient gas-turbine engines.* MRS Bulletin, 2012. **37**: p. 891-898.
4. Evans, A.G., D.R. Clarke, and C.G. Levi, *The influence of oxides on the performance of advanced gas turbines.* Journal of the European Ceramic Society, 2008. **28**: p. 1405-1419.
5. Darolia, R., *Thermal barrier coatings technology: critical review, progress update, remaining challenges and prospects.* International Materials Reviews, 2013. **58**: p. 315-348.
6. Schulz, U., et al., *Review on Advanced EB-PVD Ceramic Topcoats for TBC Applications.* International Journal of Applied Ceramic Technology, 2005. **1**: p. 302-315.
7. Clarke, D.R. and S.R. Phillpot, *Thermal barrier coating materials.* Materials Today, 2005. **8**(6): p. 22-29.
8. Levi, C.G., *Emerging materials and processes for thermal barrier systems.* Current Opinion in Solid State and Materials Science, 2004. **8**: p. 77-91.
9. Sampath, S., et al., *Processing science of advanced thermal-barrier systems.* MRS bulletin, 2012. **37**: p. 903-910.
10. Levi, C.G., et al., *Environmental degradation of thermal-barrier coatings by molten deposits.* MRS Bulletin, 2012. **37**: p. 932-941.
11. Poerschke, D.L., R.W. Jackson, and C.G. Levi, *Silicate Deposit Degradation of Engineered Coatings in Gas Turbines: Progress Toward Models and Materials Solutions.* Annual Review of Materials Research, 2017. **47**(1): p. 297-330.
12. Grant, K.M., et al., *CMAS degradation of environmental barrier coatings.* Surface and Coatings Technology, 2007. **202**: p. 653-657.
13. Grant, K.M., et al., *Calcium–Magnesium Alumino-Silicate Interaction with Yttrium Monosilicate Environmental Barrier Coatings.* Journal of the American Ceramic Society, 2010. **93**: p. 3504-3511.
14. Harder, B.J., et al., *Chemical and mechanical consequences of environmental barrier coating exposure to calcium–magnesium–aluminosilicate.* Journal of the American Ceramic Society, 2011. **94**.
15. Poerschke, D.L., et al., *Interaction of yttrium disilicate environmental barrier coatings with calcium-magnesium-iron alumino-silicate melts.* Acta Materialia, 2018. **145**: p. 451-461.
16. Summers, W.D., et al., *Roles of composition and temperature in silicate deposit-induced recession of yttrium disilicate.* Acta Materialia, 2018. **160**: p. 34-46.
17. Mercer, C., et al., *A delamination mechanism for thermal barrier coatings subject to calcium-magnesium-alumino-silicate (CMAS) infiltration.* Acta Materialia, 2005. **53**: p. 1029-1039.
18. Poerschke, D.L., et al., *Stability and CMAS Resistance of Ytterbium-Silicate/Hafnate EBCs/TBC for SiC Composites.* Journal of the American Ceramic Society, 2015. **98**(1): p. 278-286.

19. Poerschke, D.L., G.G.E. Seward, and C.G. Levi, *Influence of Yb:Hf Ratio on Ytterbium Hafnate/Molten Silicate (CMAS) Reactivity.* Journal of the American Ceramic Society, 2016. **99**(2): p. 651-659.
20. Drexler, J.M., et al., *Plasma sprayed gadolinium zirconate thermal barrier coatings that are resistant to damage by molten Ca–Mg–Al–silicate glass.* Surface and Coatings Technology, 2012. **206**: p. 3911-3916.
21. Drexler, J.M., et al., *Jet engine coatings for resisting volcanic ash damage.* Advanced Materials, 2011. **23**: p. 2419-2424.
22. Gledhill, A.D., et al., *Mitigation of damage from molten fly ash to air-plasma-sprayed thermal barrier coatings.* Materials Science and Engineering: A, 2011. **528**: p. 7214-7221.
23. Krause, A.R., et al., *Resistance of 2ZrO2·Y2O3 top coat in thermal/environmental barrier coatings to calcia-magnesia-aluminosilicate attack at 1500°C.* Journal of the American Ceramic Society, 2017. **100**(7): p. 3175-3187.
24. Krause, A.R., et al., *2ZrO2·Y2O3 thermal barrier coatings resistant to degradation by molten CMAS: Part II, Interactions with sand and fly ash.* Journal of the American Ceramic Society, 2014. **97**: p. 3950-3957.
25. Krause, A.R., et al., *2ZrO2·Y2O3 thermal barrier coatings resistant to degradation by molten CMAS: Part I, Optical basicity considerations and processing.* Journal of the American Ceramic Society, 2014. **97**: p. 3943-3949.
26. Naraparaju, R., et al., *Interaction and infiltration behavior of Eyjafjallajökull, Sakurajima volcanic ashes and a synthetic CMAS containing FeO with/in EB-PVD ZrO2-65 wt% Y2 O3 coating at high temperature.* Acta Materialia, 2017. **136**: p. 164-180.
27. Eils, N.K., P. Mechnich, and W. Braue, *Effect of CMAS Deposits on MOCVD Coatings in the System Y2O3–ZrO2: Phase Relationships.* Journal of the American Ceramic Society, 2013. **96**: p. 3333-3340.
28. Schulz, U. and W. Braue, *Degradation of La2Zr2O7 and other novel EB-PVD thermal barrier coatings by CMAS (CaO-MgO-Al2O3-SiO2) and volcanic ash deposits.* Surface and Coatings Technology, 2013. **235**: p. 165-173.
29. Krämer, S., J. Yang, and C.G. Levi, *Infiltration-inhibiting reaction of gadolinium zirconate thermal barrier coatings with CMAS melts.* Journal of the American Ceramic Society, 2008. **91**: p. 576-583.
30. Mechnich, P. and W. Braue, *Volcanic ash-induced decomposition of EB-PVD Gd 2 Zr 2 O 7 thermal barrier coatings to Gd-oxyapatite, zircon, and Gd, Fe-zirconolite.* Journal of the American Ceramic Society, 2013. **96**: p. 1958-1965.
31. Naraparaju, R., et al., *Estimation of CMAS Infiltration depth in EB-PVD TBCs: A new constraint model supported with experimental approach.* Journal of the European Ceramic Society, 2019.
32. Naraparaju, R., et al., *Tailoring the EB-PVD columnar microstructure to mitigate the infiltration of CMAS in 7YSZ thermal barrier coatings.* Journal of the European Ceramic Society, 2017. **37**: p. 261-270.
33. Zaleski, E.M., C. Ensslen, and C.G. Levi, *Melting and crystallization of silicate systems relevant to thermal barrier coating damage.* Journal of the American Ceramic Society, 2015. **98**: p. 1642-1649.
34. Poerschke, D.L. and C.G. Levi, *Effects of cation substitution and temperature on the interaction between thermal barrier oxides and molten CMAS.* Journal of the European Ceramic Society, 2015. **35**(2): p. 681-691.

35. Naraparaju, R., et al. *Criteria for development of new CMAS/volcanic ashes resistant TBCs: Experiments and simulations*. in *Thermal Barrier Coatings V*. 2018. Irsee, Gernamy.
36. Smialek, J. and R. Miller, *Revisiting the Birth of 7YSZ Thermal Barrier Coatings: Stephan Stecura †.* Coatings, 2018. **8**(7).
37. Naraparaju, R., et al., *Integrated testing approach using a customized micro turbine for a volcanic ash and CMAS related degradation study of thermal barrier coatings.* Surface and Coatings Technology, 2018. **337**: p. 198-208.
38. Clarkson, R.J., E.J.E. Majewicz, and P. Mack, *A re-evaluation of the 2010 quantitative understanding of the effects volcanic ash has on gas turbine engines.* Proceedings of the Institution of Mechanical Engineers, Part G: Journal of Aerospace Engineering, 2016. **230**(12): p. 2274-2291.
39. Weber, K., et al., *Airborne in-situ investigations of the Eyjafjallajökull volcanic ash plume on Iceland and over north-western Germany with light aircrafts and optical particle counters.* Atmospheric Environment, 2012. **48**: p. 9-21.
40. Weinzierl, B., et al., *On the visibility of airborne volcanic ash and mineral dust from the pilot's perspective in flight.* Physics and Chemistry of the Earth, Parts A/B/C, 2012. **45-46**: p. 87-102.
41. Kueppers, U., et al., *The thermal stability of Eyjafjallajökull ash versus turbine ingestion test sands.* Journal of Applied Volcanology, 2014. **3**: p. 4.
42. Song, W., et al., *Fusion characteristics of volcanic ash relevant to aviation hazards.* Geophysical Research Letters, 2014. **41**: p. 2326-2333.
43. Song, W., et al., *Volcanic ash melting under conditions relevant to ash turbine interactions.* Nature communications, 2016. **7**.
44. Song, W., et al., *Wetting and spreading of molten volcanic ash in jet engines.* The Journal of Physical Chemistry Letters, 2017. **8**: p. 1878-1884.
45. Borom, M.P., C.A. Johnson, and L.A. Peluso, *Role of environment deposits and operating surface temperature in spallation of air plasma sprayed thermal barrier coatings.* Surface and Coatings Technology, 1996. **86-87**: p. 116-126.
46. Webb, J., et al., *Coal Ash Deposition on Nozzle Guide Vanes—Part I: Experimental Characteristics of Four Coal Ash Types.* Journal of Turbomachinery, 2012. **135**: p. 021033.
47. Cengel, Y.A.B., Michael A *Thermodynamics: An Engineering Approach*. 7th ed. 2011: McGraw Hill.
48. Perepezko, J.H., *The hotter the engine, the better.* Science, 2009. **326**: p. 1068-1069.
49. Reed, R.C., *The Superalloys fundamentals and applications.* The Superalloys: Fundamentals and Applications, 2006. **9780521859**: p. 1-372.
50. Vaßen, R., et al., *Overview on advanced thermal barrier coatings.* Surface and Coatings Technology, 2010. **205**: p. 938-942.
51. Bose, S. and J. DeMasi-Marcin, *Thermal barrier coating experience in gas turbine engines at Pratt & Whitney.* Journal of Thermal Spray Technology, 1997. **6**: p. 99-104.
52. Mercer, C., et al., *On a ferroelastic mechanism governing the toughness of metastable tetragonal-prime (t') yttria-stabilized zirconia.* Proceedings of the Royal Society A: Mathematical, Physical and Engineering Sciences, 2007. **463**: p. 1393-1408.
53. Stecura, S., *Two-layer thermal barrier coating for high temperature components.* American Ceramic Society Bulletin, 1977. **56**: p. 1082-1085.

54. Nicholls, J.R., et al., *Methods to reduce the thermal conductivity of EB-PVD TBCs.* Surface and Coatings Technology, 2002. **151-152**: p. 383-391.
55. Kulkarni, A., et al., *Comprehensive microstructural characterization and predictive property modeling of plasma-sprayed zirconia coatings.* Acta Materialia, 2003. **51**(9): p. 2457-2475.
56. Renteria, A.F., et al., *Effect of morphology on thermal conductivity of EB-PVD PYSZ TBCs.* Surface and Coatings Technology, 2006. **201**: p. 2611-2620.
57. Flores Renteria, A., *A small-angle scattering analysis of the influence of manufacture and thermal induced morphological changes on the thermal conductivity of EB-PVD PYSZ thermal barrier coatings*, in *Fakultät für Georessourcen und Materialtechnik der Rheinisch*. 2007, Westfälischen Technischen Hochschule Aachen. p. 151.
58. Evans, A.G., et al., *Mechanisms controlling the durability of thermal barrier coatings.* Progress in Materials Science, 2001. **46**: p. 505-553.
59. Schulz, U., *Phase transformation in EB-PVD yttria partially stabilized zirconia thermal barrier coatings during annealing.* Journal of the American Ceramic Society, 2000. **83**: p. 904-910.
60. Krogstad, J.A., et al., *In Situ Diffraction Study of the High-Temperature Decomposition of t'-Zirconia.* Journal of the American Ceramic Society, 2015. **98**(1): p. 247-254.
61. Lughi, V. and D.R. Clarke, *High temperature aging of YSZ coatings and subsequent transformation at low temperature.* Surface and Coatings Technology, 2005. **200**(5): p. 1287-1291.
62. Marrow, T.J., S.G. Roberts, and A.K. Pearce-Higgins, *The brittle/ductile transition in cubic stabilised zirconia.* Journal of the European Ceramic Society, 1994. **14**(5): p. 447-453.
63. Chevalier, J., et al., *The tetragonal-monoclinic transformation in zirconia: lessons learned and future trends.* Journal of the American Ceramic Society, 2009. **92**: p. 1901-1920.
64. Bisson, J.-F., et al., *Thermal Conductivity of Yttria-Zirconia Single Crystals, Determined with Spatially Resolved Infrared Thermography.* Journal of the American Ceramic Society, 2004. **83**: p. 1993-1998.
65. Mévrel, R., et al., *Thermal diffusivity and conductivity of Zr1−xYxO2−x/2 (x=0, 0.084 and 0.179) single crystals.* Journal of the European Ceramic Society, 2004. **24**: p. 3081-3089.
66. Subramanian, R., *Highly defective oxides as sinter resistant thermal barrier coating.* 2005.
67. Stott, F.H. and G.C. Wood, *Growth and adhesion of oxide scales on Al2O3-forming alloys and coatings.* Materials Science and Engineering, 1987. **87**: p. 267-274.
68. Gleeson, B., *Thermal Barrier Coatings for Aeroengine Applications.* Journal of Propulsion and Power, 2006. **22**(2): p. 375-383.
69. Stiger, M.J., et al., *Thermal Barrier Coatings for the 21st Century.* Zeitschrift fur Metallkunde, 1999. **12**: p. 1069-1078.
70. Strangman, T., et al., *Damage mechanisms, life prediction, and development of EB-PVD thermal barrier coatings for turbine airfoils.* Surface and Coatings Technology, 2007. **202**: p. 658-664.
71. Pollock, T.M., D.M. Lipkin, and K.J. Hemker, *Multifunctional coating interlayers for thermal-barrier systems.* MRS Bulletin, 2012. **37**: p. 923-931.
72. Schulz, U., et al., *Some recent trends in research and technology of advanced thermal barrier coatings.* Aerospace Science and Technology, 2003. **7**: p. 73-80.

73. Terry, S.G., *Evolution of Microstructure during the Growth of Thermal Barrier Coatings by Electron-Beam Physical Vapor Deposition*, in *Materials Department*. 2001, University if California Santa Barbara. p. 197.
74. Schulz, U., S.G. Terry, and C.G. Levi, *Microstructure and texture of EB-PVD TBCs grown under different rotation modes.* Materials Science and Engineering: A, 2003. **360**(1): p. 319-329.
75. Bernier, J.S., et al., *Crystallographic texture of EB-PVD TBCs deposited on stationary flat surfaces in a multiple ingot coating chamber as a function of chamber position.* Surface and Coatings Technology, 2003. **163-164**: p. 95-99.
76. Rigney, D.V., et al., *PVD thermal barrier coating applications and process development for aircraft engines.* Journal of Thermal Spray Technology, 1997. **6**(2): p. 167-175.
77. Aygun, A., *Novel thermal barrier coatings (TBC) that are resistant to high temperature attack by CaO-MgO-Al2O3-SiO2 (CMAS) glassy deposits*, in *Materials Science and Engineering*. 2008, The Ohio State University. p. 176.
78. Ndamka, N.L., *Microstructural damage of thermal barrier coatings due to CMAS*, in *Surface engineering and nanotechnology institute*. 2013, Cranfield University. p. 332.
79. Cao, X.Q., R. Vassen, and D. Stoever, *Ceramic materials for thermal barrier coatings.* Journal of the European Ceramic Society, 2004. **24**: p. 1-10.
80. Subramanian, M.A., G. Aravamudan, and G.V.S. Rao, *Oxide pyrochlores—a review.* Progress in Solid State Chemistry, 1983. **15**: p. 55-143.
81. Padture, N.P. and P.G. Klemens, *Low Thermal Conductivity in Garnets.* Journal of the American Ceramic Society, 2005. **80**: p. 1018-1020.
82. Joshi, M.M. and S. Lee, *Integrated Gasification Combined Cycle— A Review of IGCC Technology.* Energy Sources, 1996. **18**(5): p. 537-568.
83. Christou, C., I. Hadjipaschalis, and A. Poullikkas, *Assessment of integrated gasification combined cycle technology competitiveness.* Renewable and Sustainable Energy Reviews, 2008. **12**(9): p. 2459-2471.
84. Stott, F.H., D.J. de Wet, and R. Taylor, *Degradation of Thermal-Barrier Coatings at Very High Temperatures.* MRS Bulletin, 1994. **19**(10): p. 46-49.
85. De Wet, D., R. Taylor, and F. Stott, *Corrosion mechanisms of ZrO2-Y2O3 thermal barrier coatings in the presence of molten middle-east sand.* Le Journal de Physique IV, 1993. **3**(C9): p. C9-655-C9-663.
86. Dean, J., C. Taltavull, and T.W. Clyne, *Influence of the composition and viscosity of volcanic ashes on their adhesion within gas turbine aeroengines.* Acta Materialia, 2016. **109**: p. 8-16.
87. Casadevall, T.J., *The 1989–1990 eruption of Redoubt Volcano, Alaska: impacts on aircraft operations.* Journal of Volcanology and Geothermal Research, 1994. **62**: p. 301-316.
88. Taltavull, C., J. Dean, and T.W. Clyne, *Adhesion of volcanic ash particles under controlled conditions and implications for their deposition in gas turbines.* Advanced Engineering Materials, 2016. **18**: p. 803-813.
89. Li, L. and D.R. Clarke, *Effect of CMAS Infiltration on Radiative Transport Through an EB-PVD Thermal Barrier Coating.* International Journal of Applied Ceramic Technology, 2008. **5**(3): p. 278-288.
90. Evans, A.G. and J.W. Hutchinson, *The mechanics of coating delamination in thermal gradients.* Surface and Coatings Technology, 2007. **201**: p. 7905-7916.

91. Bacos, M.P., et al., *10 Years-Activities at ONERA on Advanced Thermal Barrier Coatings.* AerospaceLab, 2011(3): p. p. 1-14.
92. Braue, W., *Environmental stability of the YSZ layer and the YSZ/TGO interface of an in-service EB-PVD coated high-pressure turbine blade.* Journal of Materials Science, 2009. **44**(7): p. 1664.
93. Braue, W. and P. Mechnich, *Recession of an EB-PVD YSZ coated turbine blade by CaSO4 and Fe, Ti -Rich CMAS-Type deposits.* Journal of the American Ceramic Society, 2011. **94**: p. 4483-4489.
94. Chen, X., *Calcium-magnesium-alumina-silicate (CMAS) delamination mechanisms in EB-PVD thermal barrier coatings.* Surface and Coatings Technology, 2006. **200**: p. 3418-3427.
95. Krämer, S., et al., *Mechanisms of cracking and delamination within thick thermal barrier systems in aero-engines subject to calcium-magnesium-alumino-silicate (CMAS) penetration.* Materials Science and Engineering A, 2008. **490**: p. 26-35.
96. Krämer, S., et al., *Thermochemical interaction of thermal barrier coatings with molten CaO-MgO-Al 2O 3-SiO 2 (CMAS) deposits.* Journal of the American Ceramic Society, 2006. **89**: p. 3167-3175.
97. Krause, A.R., et al., *Calcia-magnesia-alumino-silicate (CMAS)-induced degradation and failure of air plasma sprayed yttria-stabilized zirconia thermal barrier coatings.* Acta Materialia, 2016. **105**: p. 355-366.
98. Mechnich, P., W. Braue, and U. Schulz, *High-temperature corrosion of EB-PVD yttria partially stabilized zirconia thermal barrier coatings with an artificial volcanic ash overlay.* Journal of the American Ceramic Society, 2011. **94**: p. 925-931.
99. Naraparaju, R., et al., *The Accelerating Effect of CaSO sub4sub Within CMAS (CaO-MgO-Al sub2sub O sub3sub -SiO sub2sub) and Its Effe.* Journal of the American Ceramic Society Ceramic Society, 2016. **99**: p. 1398-1403.
100. Naraparaju, R., et al., *Degradation study of 7wt.% yttria stabilised zirconia (7YSZ) thermal barrier coatings on aero-engine combustion chamber parts due to infiltration by different CaO-MgO-Al2O3-SiO2 variants.* Surface and Coatings Technology, 2014. **260**: p. 73-81.
101. Pujol, G., et al., *Step-by-step investigation of degradation mechanisms induced by CMAS attack on YSZ materials for TBC applications.* Surface and Coatings Technology, 2013. **237**: p. 71-78.
102. Vidal-Setif, M.H., et al., *Calcium-magnesium-alumino-silicate (CMAS) degradation of EB-PVD thermal barrier coatings: Characterization of CMAS damage on ex-service high pressure blade TBCs.* Surface and Coatings Technology, 2012. **208**: p. 39-45.
103. Vidal-Sétif, M.H., et al., *Microstructural characterization of the interaction between 8YPSZ (EB-PVD) thermal barrier coatings and a synthetic CAS.* Surface and Coatings Technology, 2014. **239**: p. 41-48.
104. Wellman, R., G. Whitman, and J.R. Nicholls, *CMAS corrosion of EB PVD TBCs: Identifying the minimum level to initiate damage.* International Journal of Refractory Metals and Hard Materials, 2010. **28**: p. 124-132.
105. Wu, J., et al., *Evaluation of plasma sprayed YSZ thermal barrier coatings with the CMAS deposits infiltration using impedance spectroscopy.* Progress in Natural Science: Materials International, 2012. **22**: p. 40-47.
106. Zhao, H., C.G. Levi, and H.N.G. Wadley, *Molten silicate interactions with thermal barrier coatings.* Surface and Coatings Technology, 2014. **251**: p. 74-86.

107. Rai, A.K., et al., *CMAS-Resistant Thermal Barrier Coatings (TBC).* International Journal of Applied Ceramic Technology, 2010. **7**: p. 662-674.
108. Mohan, P., et al., *Electrophoretically deposited alumina as protective overlay for thermal barrier coatings against CMAS degradation.* Surface and Coatings Technology, 2009. **204**: p. 797-801.
109. Aygun, A., et al., *Novel thermal barrier coatings that are resistant to high-temperature attack by glassy deposits.* Acta Materialia, 2007. **55**: p. 6734-6745.
110. Drexler, J.M., et al., *Air-plasma-sprayed thermal barrier coatings that are resistant to high-temperature attack by glassy deposits.* Acta Materialia, 2010. **58**: p. 6835-6844.
111. Naraparaju, R., et al., *EB-PVD alumina (Al2O3) as a top coat on 7YSZ TBCs against CMAS/VA infiltration: Deposition and reaction mechanisms.* Journal of the European Ceramic Society, 2018. **38**(9): p. 3333-3346.
112. Jackson, R.W., et al., *Response of molten silicate infiltrated Gd2Zr2O7 thermal barrier coatings to temperature gradients.* Acta Materialia, 2017. **132**: p. 538-549.
113. Kumar, R., et al., *Influence of microstructure on the durability of gadolinium zirconate thermal barrier coatings using APS & SPPS processes.* Surface and Coatings Technology, 2018. **337**: p. 117-125.
114. Steinberg, L., et al., *Erosion behavior of EB-PVD 7YSZ coatings under corrosion/erosion regime: Effect of TBC microstructure and the CMAS chemistry.* Journal of the European Ceramic Society, 2018. **38**(15): p. 5101-5112.
115. Zeng, J., et al., *Heat-treated lanthanum magnesium hexaaluminate coatings exposed to molten calcium-magnesium-alumino-silicate.* Ceramics International, 2019.
116. Doebber, P. and F. Seidel, *Thermal barrier coating with high corrosion resistance*. 2017, Google Patents.
117. Naraparaju, R., *CMAS-Resistant Protective Layer*. 2019, Google Patents.
118. Ott, A., *CMAS/Volcanic ash resistant coatings for TBC and EBC applications based on a novel Y-Si-Fe oxide system*, in *Mathematisch-Naturwissenschaftliche Fakultät*. 2018, Universität zu Köln. p. 153.
119. Poerschke, D.L. and C.G. Levi, *Phase equilibria in the calcia-gadolinia-silica system.* Journal of Alloys and Compounds, 2017. **695**: p. 1397-1404.
120. Poerschke, D.L., T.L. Barth, and C.G. Levi, *Equilibrium relationships between thermal barrier oxides and silicate melts.* Acta Materialia, 2016. **120**: p. 302-314.
121. Bronson, A. and G.R. St. Pierre, *Electric Furnace Slags*, in *Electric Furnace Steelmaking*, C.R. Taylor, Editor. 1985: Warrendale, PA. p. 321-355.
122. Craig, M., et al., *CMAS degradation of EB-PVD TBCs: The effect of basicity.* Surface and Coatings Technology, 2015. **270**: p. 145-153.
123. Kucuk, A., A.G. Clare, and L. Jones, *An estimation of the surface tension for silicate glass melts at 1400° C using statistical analysis.* Glass Technology, 1999. **40**: p. 149-153.
124. Krause, A.R., X. Li, and N.P. Padture, *Interaction between ceramic powder and molten calcia-magnesia-alumino-silicate (CMAS) glass, and its implication on CMAS-resistant thermal barrier coatings.* Scripta Materialia, 2016. **112**: p. 118-122.
125. White, T.J., *The microstructure and microchemistry of synthetic zirconolite, zirkelite and related phases.* American Mineralogist, 1984. **69**: p. 1156-1172.
126. Rossell, H.J., *Solid solution of metal oxides in the zirconolite phase CaZrTi2O7. I. Heterotype solid solutions.* Journal of Solid State Chemistry, 1992. **99**: p. 38-51.

127. Ringwood, A.E., et al., *Immobilisation of high level nuclear reactor wastes in SYNROC.* Nature, 1979. **278**: p. 219-223.
128. Medraj, M., et al., *High temperature neutron diffraction study of the Al2O3–Y2O3 system.* Journal of the European Ceramic Society, 2006. **26**(16): p. 3515-3524.
129. Turcer, L.R., et al., *Environmental-barrier coating ceramics for resistance against attack by molten calcia-magnesia-aluminosilicate (CMAS) glass: Part I, YAlO3 and γ-Y2Si2O7.* Journal of the European Ceramic Society, 2018.
130. Gell, M., et al., *Higher Temperature Thermal Barrier Coatings with the Combined Use of Yttrium Aluminum Garnet and the Solution Precursor Plasma Spray Process.* Journal of Thermal Spray Technology, 2018. **27**(4): p. 543-555.
131. Tarasi, F., et al., *Amorphous and crystalline phase formation during suspension plasma spraying of the alumina–zirconia composite.* Journal of the European Ceramic Society, 2011. **31**(15): p. 2903-2913.
132. Schulz, U., K. Fritscher, and C. Leyens, *Two-source jumping beam evaporation for advanced EB-PVD TBC systems.* Surface and Coatings Technology, 2000. **133-134**: p. 40-48.
133. Andrievskaya, E.R., *Phase equilibria in the refractory oxide systems of zirconia, hafnia and yttria with rare-earth oxides.* Journal of the European Ceramic Society, 2008. **28**(12): p. 2363-2388.
134. TRUBELJA, M.F. and V.S. STUBICAN, *Phase Equilibria and Ordering in the System Zirconia-Hafnia-Yttria.* Journal of the American Ceramic Society, 1988. **71**(8): p. 662-666.
135. Fabrichnaya, O., et al., *Phase equilibria and thermodynamic properties of the ZrO2-GdO1.5-YO1.5 system.* Journal of Phase Equilibria and Diffusion, 2005. **26**(6): p. 591-604.
136. Fantozzi, G., et al., *Effect of nonstoichiometry on fracture toughness and hardness of yttrium oxide ceramics.* Journal of the American Ceramic Society, 1989. **72**: p. 1562-1563.
137. DELLA VENTURA, G., F. BELLATRECCIA, and C.T. WILLIAMS, *ZIRCONOLITE WITH SIGNIFICANT REEZrNb (Mn, Fe) O7 FROM A XENOLITH OF THE LAACHER SEE ERUPTIVE CENTER, EIFEL VOLCANIC REGION, GERMANY.* The Canadian Mineralogist, 2000. **38**: p. 57-65.
138. Stefanovsky, S.V., et al., *XRD, SEM and TEM Study of the Gd-Doped Zirconolites.* MRS Online Proceedings Library Archive, 2002. **713**.
139. Bayliss, P., et al., *Mineral nomenclature: zirconolite.* Mineral. Mag, 1989. **53**: p. 565-569.
140. Jackson, R.W., et al., *Interaction of molten silicates with thermal barrier coatings under temperature gradients.* Acta Materialia, 2015. **89**: p. 396-407.
141. Lenz Leite, M., et al., *Synthesis and characterization of yttrium and ytterbium silicates from their oxides and an oligosilazane by the PDC route for coating applications to protect Si 3 N 4 in hot gas environments*. 2017.
142. Sun, Z., M. Li, and Y. Zhou, *Recent progress on synthesis, multi-scale structure, and properties of Y–Si–O oxides.* International Materials Reviews, 2014. **59**(7): p. 357-383.
143. Parmentier, J., et al., *Influence of iron on the synthesis and stability of yttrium silicate apatite.* Solid State Sciences, 2001. **3**(4): p. 495-502.
144. Shannon, R., *Revised effective ionic radii and systematic studies of interatomic distances in halides and chalcogenides.* Acta Crystallographica Section A, 1976. **32**: p. 751-767.
145. Shannon, R.D.T. and C.T. Prewitt, *Effective ionic radii in oxides and fluorides.* Acta Crystallographica Section B: Structural Crystallography and Crystal Chemistry, 1969. **25**: p. 925-946.

146. Drexler, J.M., A.L. Ortiz, and N.P. Padture, *Composition effects of thermal barrier coating ceramics on their interaction with molten Ca–Mg–Al–silicate (CMAS) glass.* Acta Materialia, 2012. **60**: p. 5437-5447.
147. Ito, J., *Silicate apatites and oxyapatites.* American Mineralogist, 1968. **53**(5-6): p. 890-907.
148. Poerschke, D.L., et al., *Phase equilibria and crystal chemistry in the calcia–silica–yttria system.* Journal of the European Ceramic Society, 2016. **36**(7): p. 1743-1754.
149. Speight, J.G., *Chapter 6 - Introduction Into the Environment*, in *Environmental Organic Chemistry for Engineers*, J.G. Speight, Editor. 2017, Butterworth-Heinemann. p. 263-303.
150. Risbud, A.S., et al., *Enthalpies of formation of lanthanide oxyapatite phases.* Journal of Materials Research, 2001. **16**: p. 2780-2783.
151. Sudarsanan, K. and R.A. Young, *Significant precision in crystal structural details. Holly Springs hydroxyapatite.* Acta Crystallographica Section B, 1969. **25**(8): p. 1534-1543.
152. Giordano, D., J.K. Russell, and D.B. Dingwell, *Viscosity of magmatic liquids: A model.* Earth and Planetary Science Letters, 2008. **271**: p. 123-134.
153. Fluegel, A., *Glass viscosity calculation based on a global statistical modelling approach.* Glass Technology-European Journal of Glass Science and Technology Part A, 2007. **48**(1): p. 13-30.
154. Wang, M., et al., *Viscosity and thermal expansion of soda-lime-silica glass doped with Gd2O3 and Y2O3.* Solid State Sciences, 2012. **14**(8): p. 1233-1237.
155. Zhang, B., W. Song, and H. Guo, *Wetting, infiltration and interaction behavior of CMAS towards columnar YSZ coatings deposited by plasma spray physical vapor.* Journal of the European Ceramic Society, 2018. **38**(10): p. 3564-3572.
156. Schulz, U., et al. *Lifetime evaluation of various new EB-PVD and APS TBCs in thermal in thermal gradient and FCT*. in *Thermal Barrier Coatings V*. 2018. Irsee, Germany.
157. Faulhaber, S., et al., *Buckling delamination in compressed multilayers on curved substrates with accompanying ridge cracks.* Journal of the Mechanics and Physics of Solids, 2006. **54**(5): p. 1004-1028.
158. Liu, D., P.E.J. Flewitt, and K.R. Hallam, *Residual Stress Evolution and Failure Modes in a Thermal Barrier Coating Deposited on a Curved Substrate.* Oxidation of Metals, 2014. **81**(1): p. 69-82.
159. Hochstein, L., *Lebensdauer von 7YSZ EB-PVD Wärmedämmschichten in Flugtriebwerken mit lokaler CMAS-Belastung: Ausfallmechanismen und Modellierung*, in *Mechanical Engineering*. 2017, Technische Universität Dresden: Germany. p. 98.
160. O'Hara, K.E., X. Hu, and D.G. Cahill, *Characterization of nanostructured metal films by picosecond acoustics and interferometry.* Journal of Applied Physics, 2001. **90**(9): p. 4852-4858.
161. Thomsen, C., H.J. Maris, and J. Tauc, *Picosecond acoustics as a non-destructive tool for the characterization of very thin films.* Thin Solid Films, 1987. **154**(1): p. 217-223.
162. Tojo, T., et al., *Heat capacity and thermodynamic functions of zirconia and yttria-stabilized zirconia.* The Journal of Chemical Thermodynamics, 1999. **31**(7): p. 831-845.
163. Moskal, G., A. Iwaniak, and A. Rozmysłowska-Grund. *Characterization of thermal properties of micro-sized ceramic powders for APS deposition of ceramic layers*. in *Key Engineering Materials*. 2011. Trans Tech Publ.
164. Lide, D.R., *CRC handbook of chemistry and physics*. Vol. 85. 2004: CRC press.

165. Huxtable, S., et al., *Thermal conductivity imaging at micrometre-scale resolution for combinatorial studies of materials.* Nature Materials, 2004. **3**(5): p. 298-301.
166. Zheng, X., D.G. Cahill, and J.-C. Zhao, *Thermal Conductivity Imaging of Thermal Barrier Coatings.* Advanced Engineering Materials, 2005. **7**(7): p. 622-626.

Glossary

λ: Thermal conductivity

65YZ: 65 wt % Y_2O_3-ZrO_2 balanced

7YSZ: Yttria stabilized zirconia

A: Apatite reaction product

An: Anorthite reaction product

BC: Bond coat

CA: Contact angle

CTE: Coefficient of thermal expansion

EBC: Environmental barrier coating

F: Fluorite reaction product

FOD: Foreign object damage

G: Garnet reaction product

GZO: Gadolinium zirconate

IN 100: Inconel 100

TBC: Thermal barrier coating

TC: Thermo couple

TDTR: Time-domain thermoreflectance

TGO: Thermally grown oxide

TGT: Thermal gradient testing

U: Unidentified reaction product

Z: Zirconolite reaction product

Zi: Zircon reaction product

Appendix A

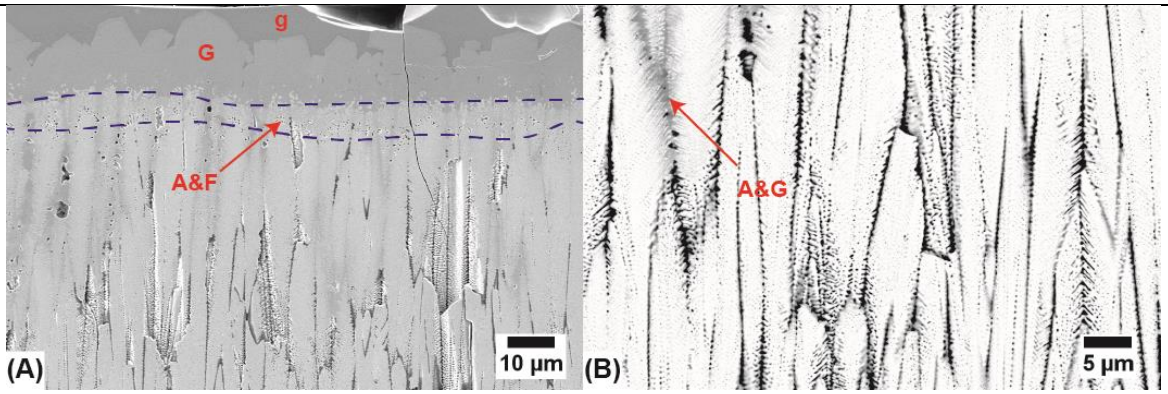

Figure A1: (A) low magnification SEM cross-sectional image of the CMAS 2 infiltrated sample after 50 h at 1250 °C (air quenched) and (B) high-magnification at the deepest infiltrated columnar gaps

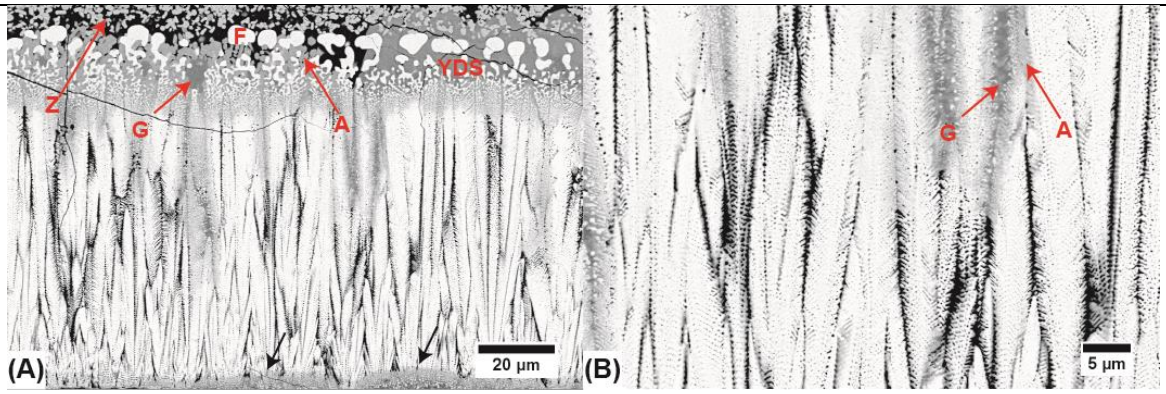

Figure A2: (A) low magnification SEM cross-sectional image of the ICE infiltrated sample after 50 h at 1250 °C (air quenched) and (B) high-magnification at the deepest infiltrated columnar gaps. Black arrows in (A) show reaction with substrate impurity elements.

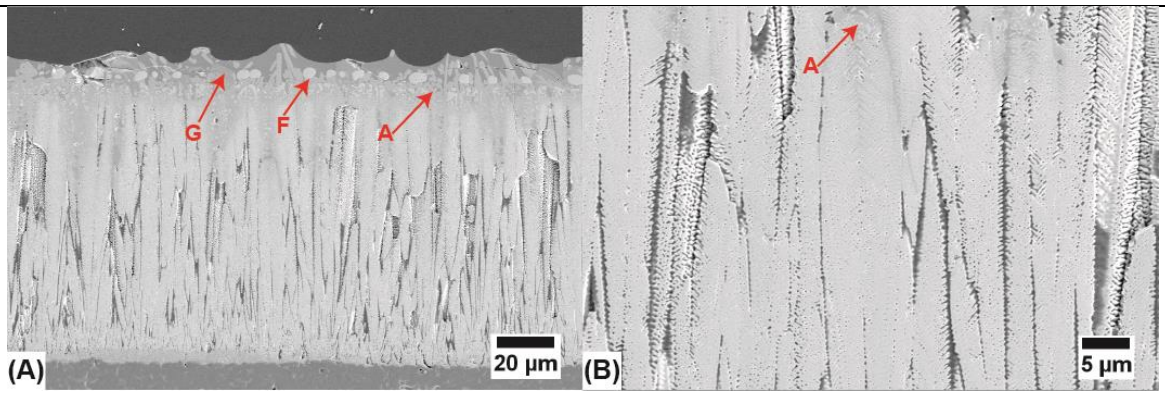

Figure A3: (A) low magnification SEM cross-sectional image of the UCSB infiltrated sample after 50 h at 1250 °C (air quenched) and (B) high-magnification at the deepest infiltrated columnar gaps.

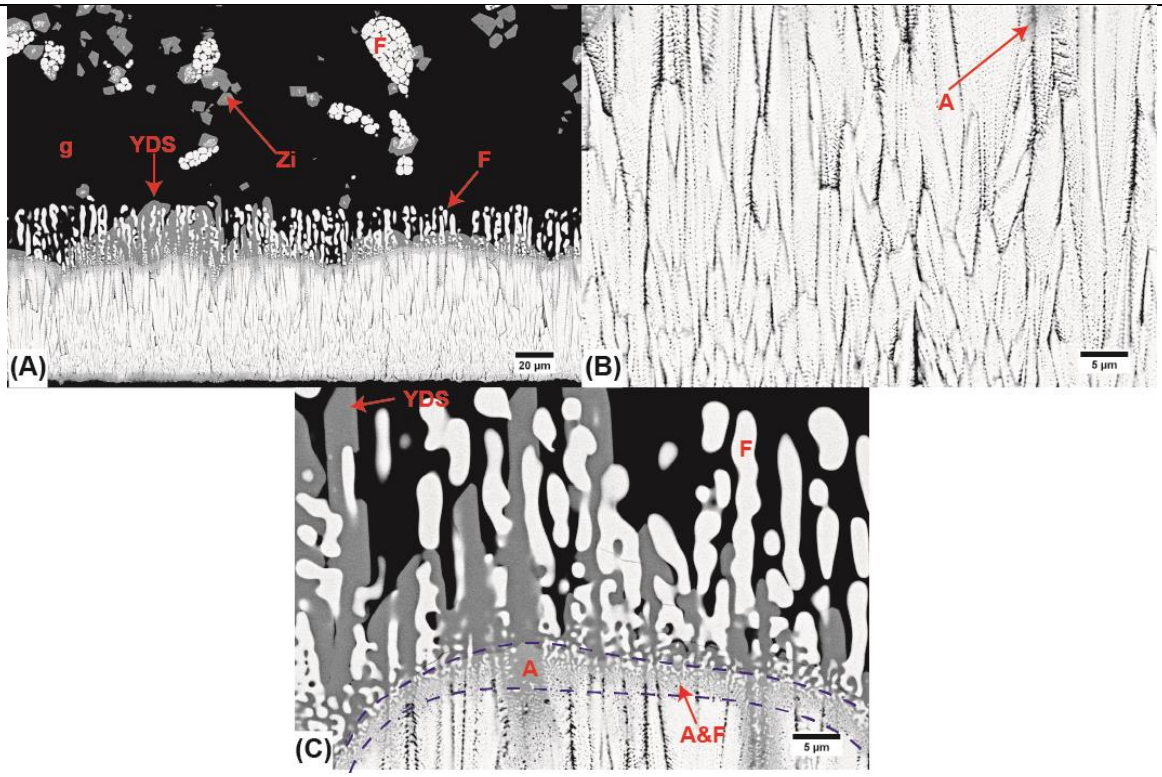

Figure A4: (A) low magnification SEM cross-sectional image of the Popo infiltrated sample after 50 h at 1250 °C (air quenched) and (B) high-magnification at the deepest infiltrated columnar gaps. (C) high-magnification of the reaction layer.

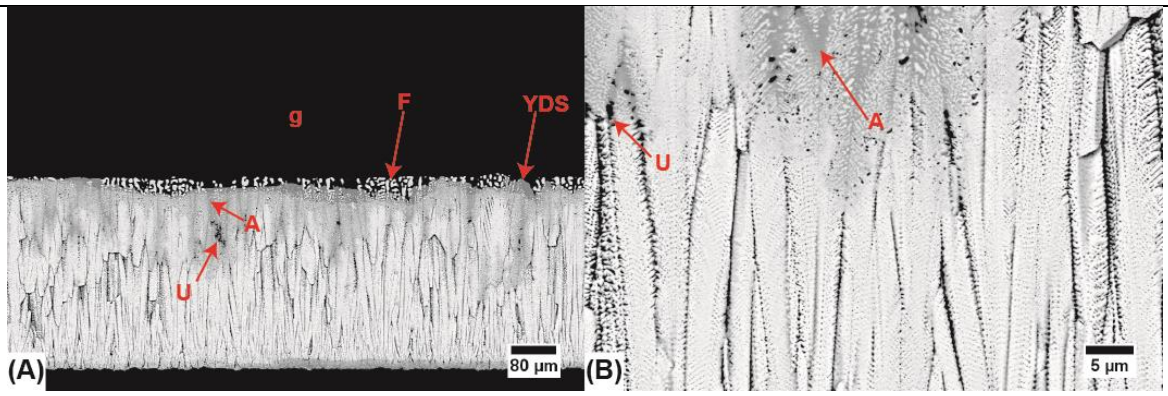

Figure A5: (A) low magnification SEM cross-sectional image of the COL infiltrated sample after 50 h at 1250 °C (air quenched) and (B) high-magnification at the deepest infiltrated columnar gaps.

Appendix B

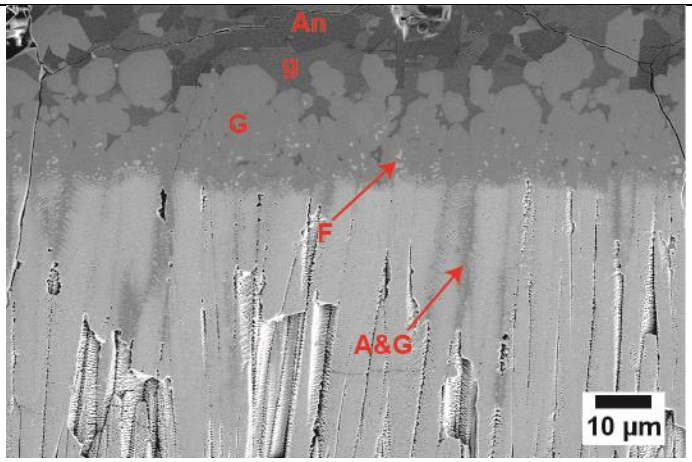

Figure B1: SEM cross-sectional image of the reaction layer of the CMAS 1 infiltrated sample after 50 h at 1250 °C (slow cooled).

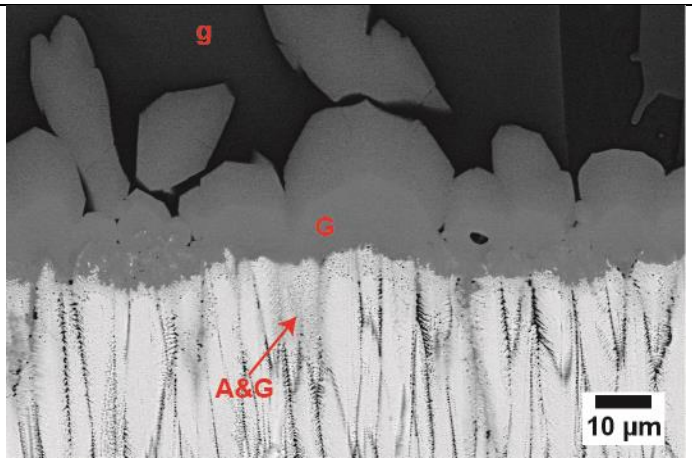

Figure B2: SEM cross-sectional image of the reaction layer of the CMAS 2 infiltrated sample after 50 h at 1250 °C (slow cooled).

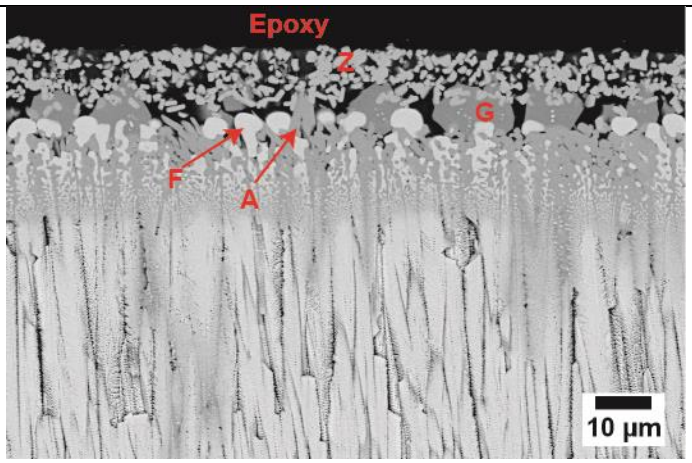

Figure B3: SEM cross-sectional image of the reaction layer of the ICE infiltrated sample after 50 h at 1250 °C (slow cooled).

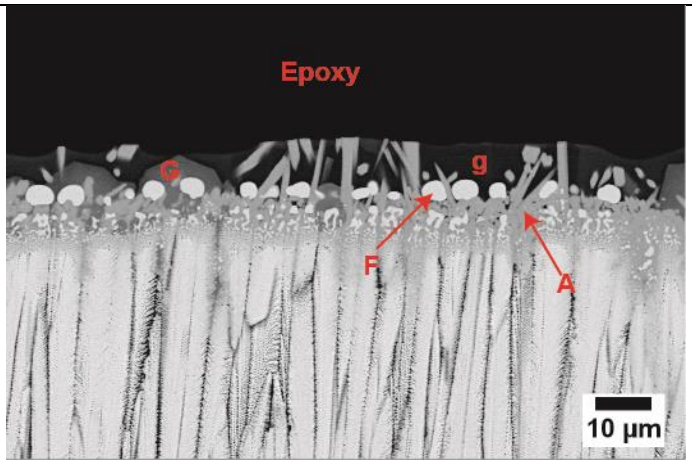

Figure B4: SEM cross-sectional image of the reaction layer of the UCSB CMAS infiltrated sample after 50 h at 1250 °C (slow cooled).

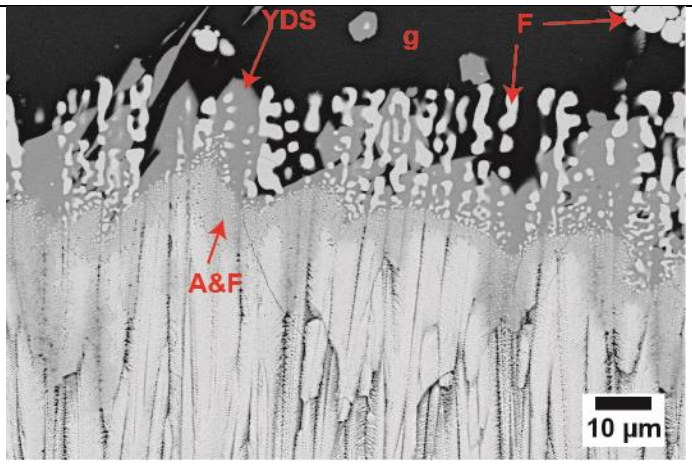

Figure B5: SEM cross-sectional image of the reaction layer of the Popo infiltrated sample after 50 h at 1250 °C (slow cooled).

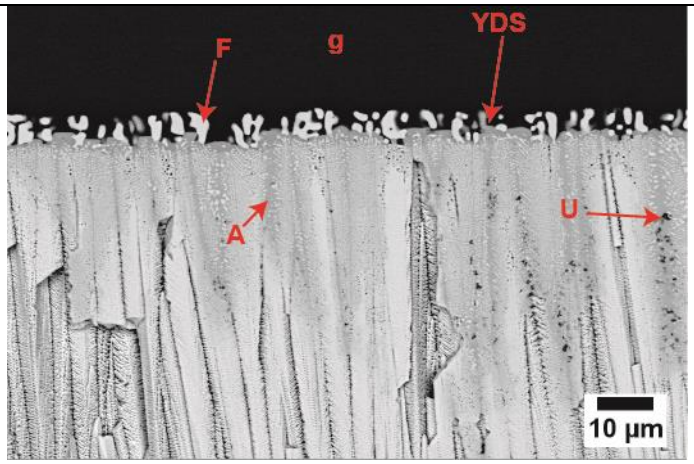

Figure B6: SEM cross-sectional image of the reaction layer of the COL infiltrated sample after 50 h at 1250 °C (slow cooled).

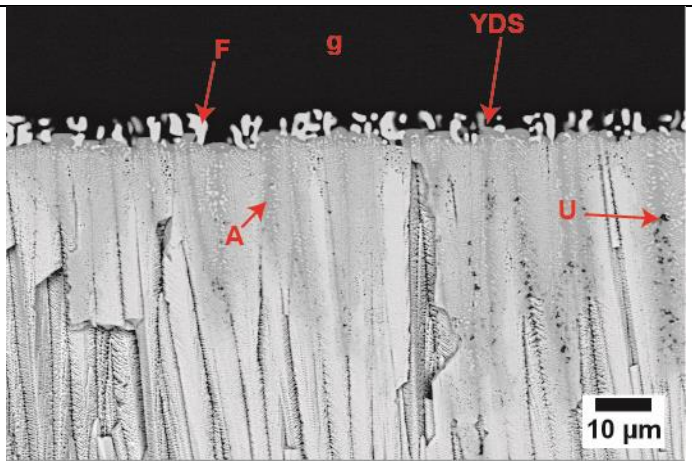

Figure B7: SEM cross-sectional image of the reaction layer of the COL infiltrated sample after 50 h at 1250 °C (slow cooled).

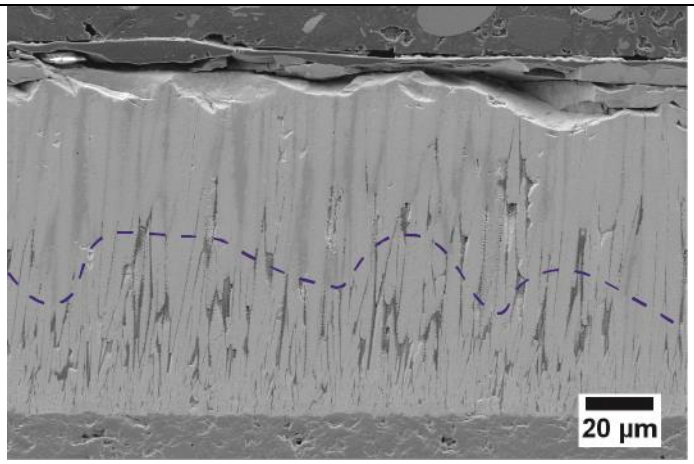

Figure B8: SEM cross-sectional image of the reaction layer of the CMAS 2 infiltrated sample after 5 h at 1300 °C (slow cooled) showing the uneven infiltration zone.

Appendix C

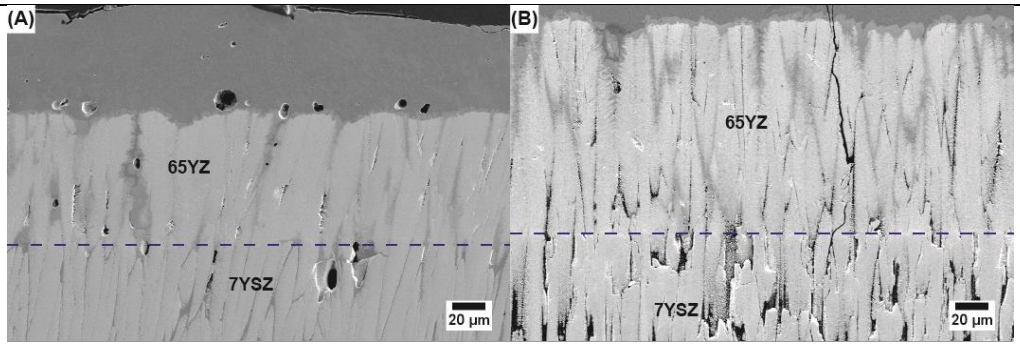

Figure C1: SEM cross-sectional image of the CMAS 2 infiltrated multi-layer samples at 1250 °C for 5 min for (A) M1and (B) M2.

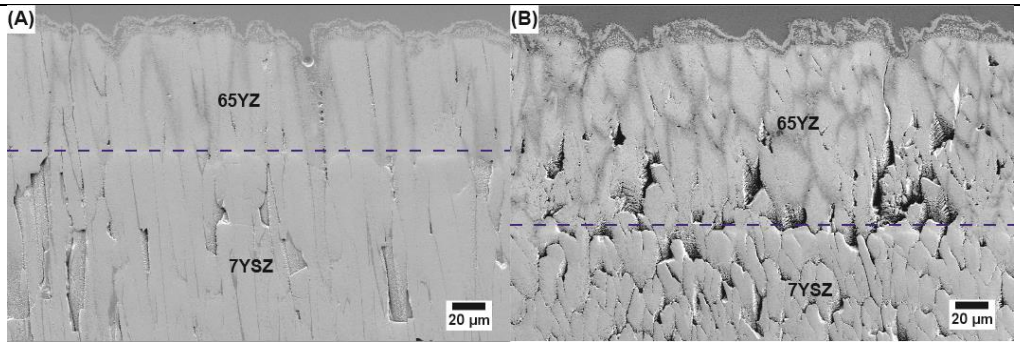

Figure C2: SEM cross-sectional image of the ICE infiltrated multi-layer samples at 1250 °C for 5 min for (A) M1and (B) M2.

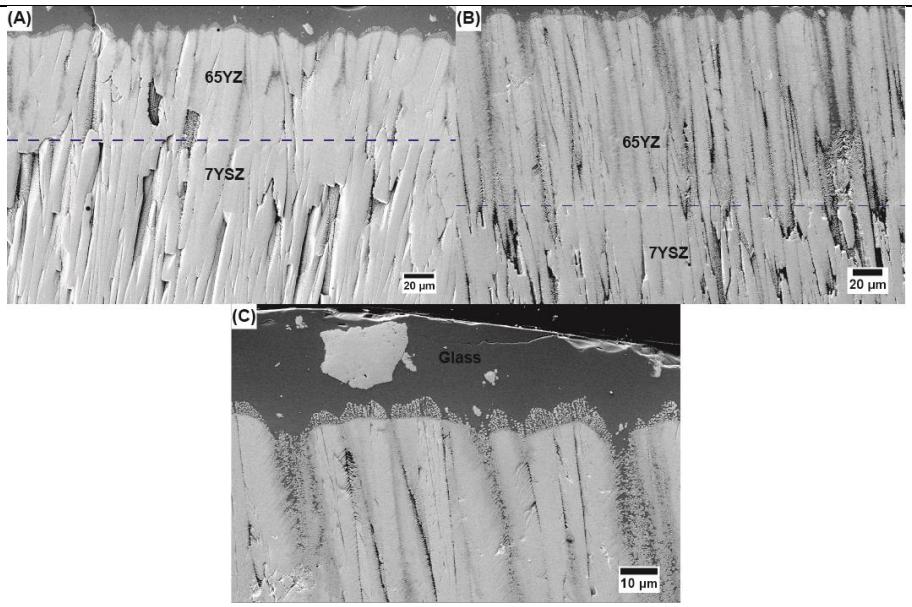

Figure C3: SEM cross-sectional image of the ICE infiltrated multi-layer samples at 1250 °C for 5 min for (A) M1and (B) M2. (C) High magnification image of the M2 sample 65YZ layer showing column degradation.

Vita

Juan Jose Gomez Chavez earned his Bachelor of Science degree in Mechanical Engineering from UTEP in 2014. In 2016, he received his Master of Science degree in Mechanical Engineering from UTEP. Dr. Gomez Chavez was the first UTEP student to graduate from the international research collaboration program between UTEP and the German Aerospace Center (DLR) in Cologne, Germany where he spent 1 ½ years between his Master and Ph.D. studies working as a research fellow. He has presented his research at several international conferences including the prestigious Thermal Barrier Coatings V held every 4 years in Irsee, Germany. His work has been published in prestigious Materials Science Journals including Acta Materialia and the Journal of the European Ceramic Society. While pursuing his Ph.D., Dr. Gomez Chavez worked as a research associate in the Department of Mechanical Engineering at UTEP and the Materials Research Institute at DLR. In 2017 he also had an internship at Boeing research and development in Ladson, South Carolina as well as W. Silver inc in 2014 in Vinton, Texas and Solar Turbines in 2013 in Mabank, Texas. Dr. Gomez Chavez will join Blue Origin in June 2019 as a full-time testing engineer.

Email: jjgomez2@miners.utep.edu

This thesis/dissertation was typed by Juan Jose Gomez Chavez